Non-Equilibrium Dynamics of Ultracold Atoms in Optical Lattices

Jens Philipp Ronzheimer

Dissertation
an der Fakultät für Physik
der Ludwig–Maximilians–Universität
München

vorgelegt von
Jens Philipp Ronzheimer
aus Aurich

München, Oktober 2013

Erstgutachter: Prof. Dr. Immanuel Bloch
Zweitgutachter: Prof. Dr. Ulrich Schollwöck
Tag der mündlichen Prüfung: 30. Januar 2014

Zusammenfassung

Das Gebiet der Nichtgleichgewichtsdynamik stark korrelierter Quantensysteme beinhaltet eine Vielzahl interessanter Fragestellungen, erweist sich dabei allerdings oftmals als schwer zugänglich für gängige numerische und analytische mathematische Methoden. In den letzten Jahren hat sich durch die experimentelle Realisierung gut kontrollierbarer quantenmechanischer Systeme die Möglichkeit eröffnet, Experimente als Quantensimulatoren für das Verhalten komplexer Vielteilchensysteme zu benutzen. Ultrakalte Atome in optischen Gittern eignen sich hervorragend als Simulatoren für simple Festkörpersysteme, da sich sämtliche Parameter der zugrunde liegenden Hamiltonoperatoren präzise kontrollieren lassen und der Zustand der Systeme mit einer Vielzahl an Messmethoden untersucht werden kann.

In unseren Experimenten realisieren wir Bose-Hubbard Systeme durch ultrakalte ^{39}K Atome in blau verstimmten optischen Gittern. Zusätzliche optische Dipolpotenziale und magnetische Feshbach-Resonanzen erlauben es uns dabei, die Parameter der Systeme zu jedem Zeitpunkt beliebig zu variieren. Dadurch sind die von uns erzeugten Systeme in besonderem Maße dazu geeignet, Nichtgleichgewichtseffekte zu untersuchen. Unser Hauptaugenmerk liegt auf der Untersuchung der Expansionsdynamik wechselwirkender Atome in homogenen Gittern. Wir beginnen unsere Experimente mit einem Anfangszustand im tiefen Gitter, der aus lokalisierten Atomen auf maximal einfach besetzten Gitterplätzen besteht. Durch gleichzeitiges schnelles Verringern der Gittertiefe und der externen Potenziale werden die Atome in ein homogenes Gitter entlassen und die Zeitentwicklung ihrer Dichteverteilung wird durch Absorptionsabbildungen festgehalten.

Es zeigt sich, dass sowohl die Wechselwirkung zwischen den Atomen als auch die Dimensionalität der Gitter einen starken Einfluss auf die Dynamik haben. In allen integrablen Grenzfällen des Bose-Hubbard Modells verhalten sich die Atome ballistisch und expandieren mit hoher Geschwindigkeit, doch sobald sich das System außerhalb der integrablen Regime befindet verringert sich die Expansionsgeschwindigkeit drastisch. Diese verringerte Geschwindigkeit geht einher mit der Ausbildung charakteristischer bimodaler Dichteverteilungen, die auf eine diffusive Dynamik schließen lassen. Für stark wechselwirkende Systeme können wir einen dimensionalitätsabhängigen Übergang zwischen ballistischer Dynamik im 1D *hard-core*-regime und diffusiver Dynamik im 2D Fall beobachten sowie eine starke Verringerung der Expansionsgeschwindigkeit, wenn der Anfangszustand des Systems mehrfach besetzte Gitterplätze enthält. Des Weiteren beobachten wir die Erzeugung solcher Mehrfachbesetzungen nach dem Entlassen der Atome, deren schnelle Entwicklung auf eine lokale Relaxationsdynamik hin zu quasistationären Werten deuten lässt.

Als Letztes untersuchen wir die Entwicklung der Quasiimpulsverteilung stark wechselwirkender expandierender Atome, die laut theoretischer Vorhersagen eine vorübergehende Quasikondensation zeigen sollen, bei der sich scharfe lokale Maxima

in der Quasiimpulsverteilung bei endlichen Quasiimpulsen bilden. Wir beobachten die Entstehung nicht-thermischer Quasiimpulsverteilungen die Maxima an den vorhergesagten Positionen zeigen. Allerdings sind die von uns beobachteten Maxima wesentlich breiter als die vorhergesagten und wir diskutieren eine Reihe möglicher Erklärungen für diese Verbreiterung sowie Vorschläge zur Verbesserung zukünftiger Experimente.

Abstract

The field of non-equilibrium dynamics of strongly correlated quantum systems encompasses some of the most interesting questions about quantum mechanical behavior, but is particularly challenging for established numerical methods. However, recent advances in the experimental control over certain quantum mechanical systems have paved the way towards the quantum simulation of dynamics previously beyond the reach of theoretical investigations. Among the most successful candidates for the implementation of quantum simulators are ultracold atoms in optical lattices, which combine an excellent control over the Hamiltonians governing their evolution with a multitude of methods to measure a diverse range of observables.

In our experiments, we use ultracold ^{39}K atoms in blue-detuned optical lattices to implement Bose-Hubbard systems. Employing optical dipole potentials to adjust the external confinement as well as Feshbach resonances to change the interaction strength between the atoms, we are able to control all parameters of the Bose-Hubbard Hamiltonian individually and in real-time, which makes our setup particularly well suited to investigate the time evolution of non-equilibrium systems in a wide range of parameter regimes. Our main experimental results are concerned with the expansion dynamics in homogeneous Hubbard systems. We create initial states of localized atoms in a deep lattice, described by a product of Fock states with no more than one atom per lattice site. These atoms are released into homogeneous lattices by simultaneous quantum quenches in the external confinement as well as the tunneling coupling along the expansion directions.

We find that both dimensionality and interaction strength crucially influence the non-equilibrium dynamics. While the atoms expand ballistically in all integrable limits of the Bose-Hubbard model, deviations from these limits dramatically suppress the expansion and lead to the appearance of almost bimodal cloud shapes, indicating diffusive dynamics in the center surrounded by ballistic wings. For strongly interacting bosons, we observe a dimensional crossover of the dynamics from ballistic in the one-dimensional hard-core case to diffusive in two dimensions, as well as a strong suppression of the expansion dynamics upon introducing higher occupancies into the initial state. Furthermore, we investigate the fast relaxation of the system after the sudden quenches and observe a buildup of higher occupancies on a timescale of less than a tunneling time, indicative of local relaxation to quasi-equilibrium values.

Finally, we also study the evolution of the quasimomentum distribution of expanding 1D hard-core bosons, which is predicted to acquire sharp peaks at finite quasimomenta while the system undergoes a transient dynamical quasi-condensation. We do observe the formation of a non-thermal quasimomentum distribution with peaks at the correct quasimomenta. However, these peaks are much broader than those predicted by theory. Thus, we discuss multiple possible effects that could hinder the formation or detection of quasi-condensation, as well as methods to experimentally investigate and mitigate these issues.

Contents

Chapter 1

Introduction

Quantum mechanics provides an elegant formalism to describe the behavior of atoms, electrons and all constituents of matter on atomic length scales. Unfortunately, the beauty and simplicity that is inherent to this theory is in general accompanied by the absolute unfeasibility of calculating exact time evolutions. As the Hilbert space of a quantum many-body system grows exponentially with the number of its constituents, obtaining analytic or numerically exact solutions can become virtually impossible already for small systems.

One solution to this problem was famously pointed out by Richard P. Feynman already in 1982 [1]: In order to accurately calculate the properties of a certain quantum-mechanical system, one can try to find another quantum system that is both easier to control and experimentally more accessible and use it as a quantum simulator. The realization of a universal quantum simulator, as envisaged by Feynman, that can be used to emulate arbitrary Hamiltonians, remains challenging [2]. Nevertheless, recent progresses in various areas of experimental quantum physics have shown that it is indeed possible to recreate certain Hamiltonians with a high degree of precision and conduct well controlled simulations of quantum dynamics [3–7].

A promising candidate for the realization of a quantum simulator are ultracold atoms [4]. The idea is to realize Hubbard models with atoms in an optical lattice in order to simulate fundamental aspects of the dynamics of solid-state systems. The groundbreaking experimental realization of the first Bose-Einstein condensates (BEC), almost 20 years ago [8–10], paved the way for this line of physics. Early experiments confirmed long-predicted properties of BEC, such as macroscopic phases revealed in matter-wave interference experiments [11, 12], the existence of superfluidity and vortices [13–15], and the validity of the predictions of Bogoliubov theory [16, 17].

In order to reach the regime of strong correlations, where the systems cannot be described in simple mean field approximations and interactions between the atoms play a crucial role, it was suggested in 1998 by Jaksch et al. [18] to use optical lattices to implement the Bose-Hubbard Hamiltonian [19]. In a hallmark experiment in 2002, this technique was used to observe a quantum phase transition between a superfluid

(SF) and a Mott insulating (MI) state of bosons in three dimensional optical lattices [20].

Since then, a multitude of experiments have contributed to the extraordinary growth of the field of ultracold atoms in optical lattices and extended the tools available for controlling such systems and detecting their properties. The SF-MI transition was realized for bosons in lower dimensional systems [21, 22] and MI states were also observed for two-component Fermi gases in lattices [23, 24]. The flexibility of optical lattice setups was used to recreate other simple quantum mechanical models, like the Tonks-Girardeau gas [25, 26], and to extend the Hubbard model with the addition of superlattices [27–29] or the creation of triangular and hexagonal lattice geometries [30, 31].

The first observation of Feshbach resonances [32, 33] in ultracold atoms [34] opened up an additional method of changing the system parameters, by allowing to control the interaction strength between atoms using homogeneous magnetic fields [35]. In continuous systems of ultracold fermions, this allowed for the first creation of ultracold molecules [36], Bose-Einstein condensation of molecules [37–39] and the observation of superfluidity in the crossover between the BEC and the Bardeen-Cooper-Schrieffer (BCS) regime [40–42]. For bosons in the continuum, Feshbach resonances have been used to, e.g., create squeezed states [43] or to observe the long predicted Efimov resonances [44–46]. In Hubbard systems, Feshbach resonances allow for an independent control over the on-site interaction strength and lead to, e.g., the realization of tunable Mott Insulator states [47] and Mott insulators at attractive interactions [48].

A wide array of methods for the detection of many-body states in optical lattices has been developed over the years. Absorption and phase contrast imaging [49] can be used to detect *in-situ* density distributions [50], momentum distributions in time-of-flight [51] and noise correlations [52, 53]. Other notable methods include spectroscopic techniques (see, e.g., [21, 54, 55]) or the use of an electron beam as a scanning microscope [56]. Recently, it has become possible to optically detect atoms in lattices with single-site resolution [57, 58] and to manipulate many body states in the lattice on a single atom level [59], which opened up a whole new range of possible experiments [4].

While a large body of experimental work has been concerned with the investigation of the equilibrium states in optical lattices, fewer studies exist to date that experimentally investigate the non-equilibrium and relaxation dynamics of ultracold atoms. The non-equilibrium dynamics of closed quantum systems has become a topic of renewed interest in recent years, due to the experimental realization of quantum systems with a high degree of controllability [60]. Simple effective models, such as the Hubbard model [61], were originally derived to qualitatively understand the fundamental aspects of much more complex solid state systems. Nowadays, such models can be faithfully recreated in experiments, e.g., with ultracold atoms in optical lattices [62], and the theoretical analysis of these systems can be complemented

by directly measuring their equilibrium properties and time evolution. A prominent example of non-equilibrium dynamics was studied in the context of Tonks-Girardeau gases in 1D systems [63]. Here, two clouds of atoms were observed to collide repeatedly with each other without showing signs of thermalization, a behavior that is directly related to the integrability of the system. Actual relaxation dynamics were observed in experiments investigating the evolution of 1D condensates after being split in two [64], which were later shown to exhibit fast pre-thermalization dynamics [65]. The influence of optical lattice potentials on transport phenomena was investigated in [66, 67] and recently, optical potentials have been used to study the transport dynamics of fermions in 2D channels [68, 69]. In Hubbard systems, non-equilibrium dynamics were studied, e.g., in the form of transport phenomena [70, 71], dynamics after quenches from the MI to the SF regime [72] and the relaxation of density waves in optical superlattices [73].

On the theoretical side, non-equilibrium dynamics in the Hubbard model have been studied extensively, especially using time-dependent density-matrix renormalization-group methods (t-DMRG) [74–76] for 1D systems as well as exact diagonalization methods for small or integrable systems (see, e.g., [77]). Among many investigated topics are the dynamics after quantum quenches [78–82] , transport properties [83–86], and the important role of non-integrability in the ability of a system to thermalize [77, 87–89] (see chapter 3.4 for more details). Despite the broad progress that has been achieved on the theoretical side, the efficient simulation of non-equilibrium dynamics remains challenging and stresses the importance of developing novel approaches, such as quantum simulators.

In this thesis, we show how Hubbard Hamiltonians can be implemented using ultracold atoms. In particular, we focus on experiments investigating the non-equilibrium dynamics of ultracold atoms in optical lattices in the context of their expansion dynamics. The recent advances in controlling and manipulating the internal states of the atoms and their interactions as well as the possibility to individually change lattice depths and external potentials provide us with a full control over all parameters of the system. We present results for expanding fermions and bosons in varying lattice geometries and with varying interaction strength and observe the dynamics of density distributions in real space and momentum space as well as the evolution of higher occupancies in the lattice. Our main findings include the observation of a crossover between ballistic and diffusive dynamics depending on dimensionality and interactions, fast local relaxation of the higher occupancies in the lattice, and first steps towards the observation of quasi-condensation of expanding hard-core bosons.

Outline of this Thesis

In chapter 2, we summarize the fundamental properties of atoms in periodic potentials, introduce the Bose-Hubbard Hamiltonian and discuss its equilibrium states in

different parameter regimes as well as the SF-MI phase transition between them.

Chapter 3 provides a brief introduction into the equilibration dynamics of closed quantum systems. In the first part, we elaborate on the intricacies that arise when translating concepts like thermalization, ergodicity and integrability into the quantum regime and discuss recent advances in the theoretical description and experimental observation of relaxation dynamics in quantum systems. The second part is devoted to relaxation dynamics in the Bose-Hubbard model, focusing on the role of its integrable limits as well as on theoretical results on its time evolution after quantum quenches.

In chapter 4, we present the experimental setup used to create Bose-Einstein condensates of ^{39}K. This includes a brief description of the magneto-optical traps, sympathetic evaporative cooling of ^{87}Rb and ^{39}K in magnetic quadrupole traps and optical dipole traps, as well as the available Feshbach resonances to manipulate the inter- and intra-species interactions. This is followed by a description of the optical lattice setup in chapter 5, where we discuss the properties of the lattices, methods to accurately calibrate them, and how to minimize light induced losses. We then introduce some methods for the detection of density and momentum distributions of the prepared many-body states and present results on the observation of equilibrium states in the lattice. These include the SF-MI transition of ^{39}K, driven by the manipulation of both the tunneling and the interaction strength, and the creation of thermodynamically stable states with negative absolute temperature.

Chapter 6 sets the scope for the main experimental results of this work, the expansion dynamics of atoms in homogeneous lattices. We present our scheme for the preparation of the initial states of the experiments and the expansion dynamics expected for non-interacting atoms. After describing the experimental optimization of the homogeneity of our lattice potentials and the desired properties of the initial state, we introduce the fundamental quantities used in the analysis of our experiments throughout the rest of the thesis and show the agreement between theory and experiment for the expansion dynamics of non-interacting atoms.

While the main focus of this thesis lies on the expansion dynamics of bosons, results obtained with a two-component Fermi gas in earlier experiments [71] already showed some of the key characteristics of interacting atoms expanding in 2D and 3D homogeneous lattices. These results are presented in chapter 7, where we start by describing the experiment and investigating the behavior of free fermions, which is in excellent agreement with theoretical predictions. The main result of this chapter is the observed onset of diffusive dynamics when interactions are introduced into the system: These lead to the appearance of characteristic bimodal density distributions and can be qualitatively reproduced by a semi-classical Boltzmann equation. In addition, we find the dynamics to be invariant under a change of the sign of the interaction, a direct consequence of the symmetries of the Hubbard Hamiltonian and the initial state.

In chapter 8, we present the main experimental results of this thesis, the investi-

gation of multiple aspects of the expansion dynamics of interacting bosons in homogeneous lattices. We find the expansion dynamics to be analogous to the fermionic results when the atoms move in a 2D lattice geometry. In 1D lattices, however, the behavior of strongly interacting atoms is markedly different. Due to the approach of an integrable limit for hard-core bosons in 1D, we find ballistic dynamics when the interactions are strong and a minimum of the expansion velocity at intermediate interactions, in very good agreement with t-DMRG calculations. The flexibility of tuning the tunneling along individual axes allows us to investigate the dynamics in the crossover between 1D and 2D, and we can observe how breaking the integrability by introducing tunneling along a second axis continuously drives the system towards diffusive dynamics. Furthermore, we investigate the formation of double occupancies during the expansion, which happens on a timescale that is consistent with fast local relaxation in the system and well reproduced by t-DMRG calculations. Finally, we also investigate the effects of double occupancies introduced into the initial state, which not only break the integrability of strongly interacting atoms in 1D but already alter the dynamics significantly even for small interactions.

After being mainly concerned with the evolution of density distributions in chapters 7 and 8, we turn our attention to the evolution of the momentum distribution of systems of strongly interacting expanding bosons in chapter 9. For appropriate initial conditions, such systems are expected to undergo a quasi condensation during the expansion [90], signaled by the development of sharp peaks in their momentum distribution. We do observe the onset of such effects, however, the peaks remain much broader than predicted by theory. Thus, we devote a large part of this chapter to the analysis of experimental effects that could limit the formation of quasi-condensates and our ability to detect them.

In chapter 10, we summarize our results and provide a brief outlook on future experiments.

Chapter 2

Ultracold Atoms and the Hubbard Model

In this chapter, we give a brief introduction into the fundamental properties of quantum systems in periodic potentials, especially those relevant in the context of ultracold atoms in optical lattices. As these have already been treated in a multitude of publications, we try to limit the discussion to the aspects most relevant in the context of this thesis. Parts of this chapter closely follow the treatments in [91] and [92], a more thorough introduction to the concepts discussed in this chapter can be found in, e.g., [62] and references therein.

First, we discuss the properties of single particles in periodic potentials to establish the concepts of Bloch waves and the band structure, Wannier states, and the tight binding limit. As quantum mechanics in periodic potentials lies at the heart of modern solid state theory, these concepts have been established already in the early days of quantum mechanics and can be found in any modern textbook on solid state physics (see, e.g., [93, 94]).

We then introduce the Bose-Hubbard Hamiltonian [19, 61], which is particularly suited to describe the behavior of ultracold atoms in optical lattices [18], and discuss its superfluid and Mott insulating limits as well as the quantum phase transition between them in homogeneous and inhomogeneous systems.

2.1 Quantum Mechanics in Periodic Potentials

We will start by discussing a simple realization of a quantum mechanical system in a periodic potential, limiting ourselves for now to the non-interacting 1D case. For non-interacting systems, the essential properties are captured in the single-particle behavior, so we can investigate the Schrödinger equation for a particle of mass m in a periodic potential

$$\hat{H}\Psi_q^{(n)}(x) = E_q^{(n)}\Psi_q^{(n)} \quad \text{with} \quad \hat{H} = -\frac{\hbar^2}{2m}\frac{\partial^2}{\partial x^2} + V(x), \tag{2.1}$$

where $V(x)$ has the periodicity d, i.e. $V(x) = V(x+d)$.

2.1.1 Bloch Waves and Band Structure

According to the Bloch theorem, the solutions to this Schrödinger equation, the so-called Bloch waves, can be expressed as the product of a plane wave and a periodic function $u_q^{(n)}(x) = u_q^{(n)}(x+d)$ as

$$\Psi_q^{(n)}(x) = e^{iqx} u_q^{(n)}(x). \tag{2.2}$$

Here, we already introduce the two fundamental quantum numbers, the quasimomentum q and the band index n, which will be discussed in more detail below. Substituting eq. 2.2 into eq. 2.1 results in an eigenvalue problem for the $u_q^{(n)}(x)$ of the form

$$\hat{H} u_q^{(n)}(x) = \left(\frac{\hbar^2}{2m} \left(-\mathrm{i}\frac{\partial}{\partial x} + q \right)^2 + V(x) \right) u_q^{(n)}(x) = E_q^{(n)} u_q^{(n)}(x). \tag{2.3}$$

Both the potential $V(x)$ and the functions $u_q^{(n)}(x)$ are periodic in x with the same periodicity d, and they can thus be expanded as discrete Fourier sums

$$V(x) = \sum_\mu V_\mu e^{\mathrm{i}2\mu k x} \quad \text{and} \quad u_q^{(n)}(x) = \sum_\nu c_\nu^{(n,q)} e^{\mathrm{i}2\nu k x}, \tag{2.4}$$

with $k = \pi/d$ and $\nu, \mu \in \mathbb{Z}$. With these substitutions, the kinetic energy term becomes

$$\frac{\hbar^2}{2m} \left(-\mathrm{i}\frac{\partial}{\partial x} + q \right)^2 u_q^{(n)}(x) = \sum_\nu \frac{\hbar^2 (q + 2k\nu)^2}{2m} c_\nu^{(n,q)} e^{\mathrm{i}2k\nu x} \tag{2.5}$$

and the potential energy term becomes

$$V(x) u_q^{(n)}(x) = \sum_\mu \sum_\nu V_\mu e^{\mathrm{i}2(\mu+\nu)kx} c_\nu^{(n,q)}. \tag{2.6}$$

Assuming a sinusoidal periodic potential, typical for optical lattice potentials (see chapter 5.1), of the form

$$V(x) = -V_x \cos^2(kx) = -\frac{V_x}{4} \left(e^{\mathrm{i}2kx} + e^{-\mathrm{i}2kx} + 2 \right) \tag{2.7}$$

shows that only three terms of the Fourier sum in eq. 2.4 are nonzero, namely $V_{-1} = V_1 = -V_x/4$ and $V_0 = -V_x/2$, and we can rewrite the Schrödinger equation 2.3 as

$$\sum_\nu H_{\nu,\nu'} \cdot c_\nu^{(n,q)} = E_q^{(n)} c_\nu^{(n,q)}, \tag{2.8}$$

with

$$H_{\nu,\nu'} = \begin{cases} (q/k + 2\nu)^2 E_r & \text{for } |\nu - \nu'| = 0 \\ -V_x/4 & \text{for } |\nu - \nu'| = 1 \\ 0 & \text{for } |\nu - \nu'| > 1 \end{cases} \tag{2.9}$$

where we have set V_0 to zero, as it just provides a constant energy offset. $E_r = \hbar^2 k^2/(2m)$ is called the recoil energy, and is a convenient unit when dealing with optical lattices (see chapter 5). This Hamiltonian is the matrix representation of $\hat{H}$ in eq. 2.3 in the plane wave basis basis $\{|\nu\rangle\}$, where $\langle x|\nu\rangle = e^{\mathrm{i}2k\nu x}$. While it can not be solved analytically [95], its eigenstates can easily be calculated numerically by truncating the Hamiltonian for large $|\nu|$.

The wavefunctions $\Psi_q^{(n)}(x)$ corresponding to quasimomenta q and q' which differ by exactly one reciprocal lattice vector $q' = q + 2k$ are identical, and we can thus restrict the analysis of the single particle states in the lattice to quasimomenta within the first Brillouin zone, $q \in [-\pi/d, \pi/d]$. For a certain q, the eigenvalues $E_q^{(n)}$ then represent the eigenenergies in the energy bands indicated by the index n. The corresponding Bloch waves are given by the $c_\nu^{(n,q)}$ through equations 2.4 and 2.2.

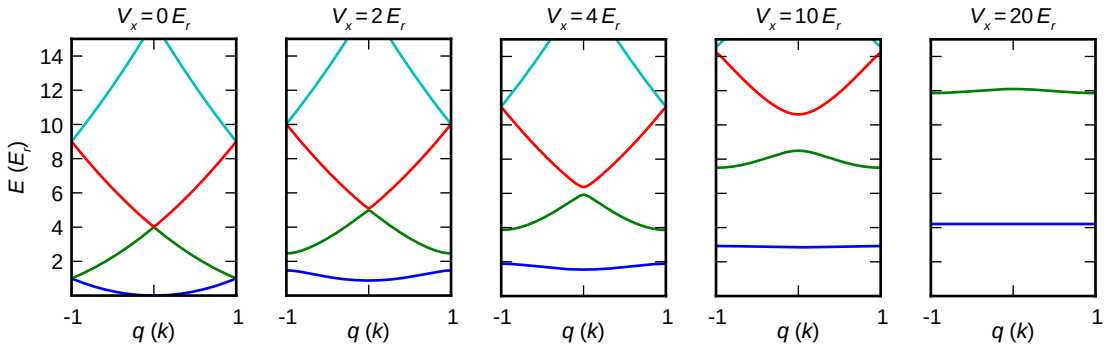

Figure 2.1: Structure of the eigenenergy bands of eq. 2.8 for a sinusoidal lattice with varying depth V_x, reduced to the first Brillouin zone.

In figure 2.1, we plot the band structure for the four lowest bands at varying lattice depths V_x, calculated by truncating eq. 2.8 at $|\nu| \leq 6$. For $V_x = 0$, the band structure corresponds to the free particle dispersion relation, reduced to the first Brillouin zone. For increasing V_x, an energy gap opens at the edges of the Brillouin zone, and the structure of the eigenenergies separates into distinct energy bands. These bands become narrower in energy for larger V_x and the energy gap between them increases.

2.1.2 Wannier States

A Bloch wave with a fixed quasimomentum q describes a completely delocalized single-particle wavefunction, essentially providing a description of the dynamics in

momentum space. In situations where one wants to describe localized states in a lattice, it is often more convenient to use a representation in real space, which can be obtained by a transformation into the so called Wannier basis.

The Wannier function of a particle localized to site i at position x_i in the n^{th} energy band is given by

$$w_n(x - x_i) = \frac{1}{\sqrt{\mathcal{N}}} \sum_q e^{iqx_i} \Psi_q^{(n)}(x), \tag{2.10}$$

where the sum runs over all possible quasimomenta q within the first Brillouin zone and $\mathcal{N}$ is the number of lattice sites. For a finite $\mathcal{N}$, the possible quasimomenta q are discrete and spaced equidistantly over the first Brillouin zone. In the limit of infinitely large lattices, q becomes continuous and the summation is replaced by an integral over the first Brillouin zone. A Bloch wave can in turn be represented in the Wannier basis as

$$\Psi_q^{(n)} = \frac{1}{\sqrt{\mathcal{N}}} \sum_i e^{\mathrm{i}qx_i} w_n(x - x_i). \tag{2.11}$$

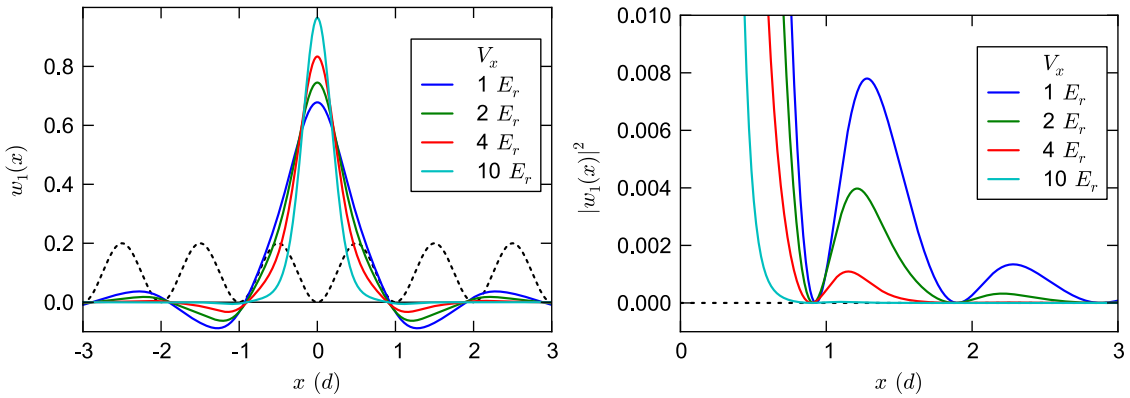

(a) Wannier functions $w_1(x)$ in the lowest bands of lattices with varying potential depth V_x. The dashed black line depicts the shape of the lattice potential.

(b) Probability amplitudes $|w_1(x)|^2$ of the Wannier functions shown in fig. 2.2a, limited to $x > 0$ and truncated to $|w_1(x)|^2 < 0.01$ to highlight the overlap with neighboring lattice sites.

Figure 2.2

In the limit of sufficiently deep lattice potentials and low energies, we can restrict the description of a particle to the lowest band and omit the index n, i.e., $w_1(x-x_i) \equiv w(x - x_i)$. In figure 2.2a, we show the Wannier functions of the lowest band for varying lattice depth V_x. The x-axis is given in units of the lattice constant d and the dashed black line shows the shape of the lattice potential. For small V_x, the Wannier functions extend well into the potential barriers between the lattice wells. As V_x is

increased, the peak around $x = 0$ becomes narrower and the Wannier state becomes more localized to a single lattice site, as it becomes energetically unfavorable to have a large overlap with the potential barriers. This effect is highlighted in figure 2.2b, which shows the probability amplitude $|w_1(x)|^2$ for the Wannier functions of fig. 2.2a. Here, we can clearly see how the side lobes of the Wannier functions are strongly suppressed for deep lattices.

Representing a single particle wave function $\Psi(x)$ in the Wannier basis in the lowest band,

$$\Psi(x) = \sum_i c_i w(x - id), \tag{2.12}$$

we can rewrite the Hamiltonian in second quantization as

$$\hat{H} = -\sum_{i,j} J_{i,j} \hat{c}_i^\dagger \hat{c}_j + \sum_i E_i \hat{c}_i^\dagger \hat{c}_i, \tag{2.13}$$

where $\hat{c}_i^\dagger$ and $\hat{c}_i$ are the creation and annihilation operators for a particle in a Wannier function on site i, E_i is the on-site energy of a single particle on site i, given by the lattice potential, and $J_{i,j}$ is the tunneling matrix element between sites i and j. It can be calculated by determining the wavefunction overlap between the Wannier functions on site i and site j as

$$J_{i,j} = -\int_{-\infty}^{\infty} w^*(x - x_i) \left(-\frac{\hbar^2}{2m} \frac{\partial^2}{\partial x^2} + V(x) \right) w(x - x_j) dx. \tag{2.14}$$

In the lowest energy band, the value of the nearest neighbor tunneling matrix element $J = J_{i,i+1}$ is directly related to the band width of the lowest band, given by $J = (E^{(1)}_{q=\pi/d} - E^{(1)}_{q=0})/4$ [96].

2.1.3 The Tight-Binding Limit

As it can be seen from the Wannier functions shown in figure 2.2b, for sufficiently deep lattices, the overlap of a Wannier function on a site i with that on a site j becomes negligible for $|i - j| > 1$. In this case, we can assume all $J_{i,j}$ to vanish for $|i - j| > 1$ and restrict the description of the system to nearest neighbor tunneling. This approximation is called the tight-binding limit, and is generally assumed to be valid for lattice depths exceeding $5\,E_r$ [18]. The Hamiltonian of eq. 2.13 can then be further simplified by noting that $J = J_{i,i+1}$ is independent of i, and the on-site energy E_i is constant and can be neglected, resulting in

$$\hat{H} = -J \sum_{\langle i,j \rangle} \hat{c}_i^\dagger \hat{c}_j, \tag{2.15}$$

where the summation index $\langle i, j\rangle$ runs over all nearest neighbor sites.

By applying this Hamiltonian to the Bloch waves of eq. 2.11, the single particle dispersion relation in the tight-binding can be determined as

$$\epsilon_q = -2J\cos(qd). \tag{2.16}$$

Thus, in the lowest band, the kinetic energy of a single particle is bounded to values between $-2J$ and $2J$. Furthermore, the cosine form of the dispersion relation leads to a characteristic shape of the group velocity of a single particle

$$v_g = \frac{1}{\hbar}\frac{\partial \epsilon_q}{\partial q} = \frac{2d}{\tau}\sin(qd), \tag{2.17}$$

where $\tau = \hbar/J$. A particle has the maximum absolute group velocity $2d/\tau$ at momenta $q = \pm\pi/(2d)$ and a group velocity of zero at $q = 0$ as well as at $q = \pm\pi/d$. These simple relations are sufficient to predict the dynamics of the density distribution of non-interacting atoms evolving freely in homogeneous lattice, which we will investigate in more detail in chapter 6 and can easily be extended to incorporate external potentials (see chapter 6.3.1 and 9.5.3).

2.2 The Bose-Hubbard Model

The Hubbard Hamiltonian was originally derived by J. Hubbard in its fermionic form as a simple approximation for the description of electrons in narrow bands [61]. The implementation of a corresponding bosonic version, the Bose-Hubbard model [19], using ultracold bosonic atoms in optical lattices was proposed in 1998 by Jaksch et. al. [18]. This proposal was realized in [20] and has laid the foundation to an ever growing field of research, the simulation of condensed matter systems with ultracold atoms in optical lattices [62].

The Bose-Hubbard Hamiltonian for atoms in the lowest band of an optical lattice can be written as

$$H = -J\sum_{\langle i,j\rangle}\hat{b}_i^\dagger\hat{b}_j + \frac{U}{2}\sum_i \hat{n}_i(\hat{n}_i - 1) + \sum_i V_{\text{ext}}(\mathbf{r}_i)\hat{n}_i. \tag{2.18}$$

Here, $\hat{b}_i^\dagger$ and $\hat{b}_i$ are the creation and annihilation operators for a boson on site i, obeying the usual bosonic commutation relation $[\hat{b}_i, \hat{b}_j^\dagger] = \delta_{i,j}$, and $\hat{n}_i = \hat{b}_i^\dagger\hat{b}_i$ is the number operator on site i. In the first term, which describes the tunneling between lattice sites, the sum over $\langle i, j\rangle$ runs over all nearest neighboring sites and J is the tunneling coupling between the lattice sites. The second term describes the on-site interaction, with the interaction strength U, where the sum runs over all lattice sites. The third term includes effects of external global potentials $V_{\text{ext}}(\mathbf{r}_i)$ that depend on

the position $\mathbf{r}_i$ of the lattice sites.

The tunneling matrix element is determined from the overlap of the Wannier functions on adjacent sites as given in eq. 2.14. The on-site interaction U is calculated from the interaction energy of two Wannier functions on the same site as

$$U = \frac{4\pi\hbar a_s}{m} \int_{-\infty}^{\infty} |w_1(x)|^4 \, dx, \tag{2.19}$$

where a_s is the s-wave scattering length. Note that this is only an approximation, as the presence of more than one atom on a lattice site modifies the shape of the wavefunction and can lead to deviations, especially at large a_s and for large occupation numbers [97].

2.2.1 Phases of the Bose-Hubbard Model

For simplicity, we will first investigate the Bose-Hubbard Hamiltonian in a 3D lattice without external global potentials, which only consists of the tunneling and interaction terms

$$\hat{H} = -J \sum_{\langle i,j \rangle} \hat{b}_i^\dagger \hat{b}_j + \frac{U}{2} \sum_{i=1}^{L} \hat{n}_i(\hat{n}_i - 1). \tag{2.20}$$

The behavior of a system described by this Hamiltonian can be characterized by three parameters, the tunneling matrix element J, the on-site interaction U and the average filling factor $\overline{n}$ which is given by the number of atoms N and the number of available lattice sites L as $\overline{n} = N/L$.

The Superfluid $\mathbf{U/J \to 0}$ Limit

In the limit of large tunneling J and vanishing interactions U, the tunneling term in the Bose-Hubbard Hamiltonian dominates and the atoms delocalize over the complete lattice. The ground state of this system is a superfluid state where all atoms occupy the lowest energy mode of $\mathbf{q} = 0$. For N particles on L lattice sites, it is given by

$$|\Psi_{\mathrm{SF}}\rangle = \left(\frac{1}{\sqrt{L}} \sum_{i=1}^{L} \hat{b}_i^\dagger \right)^N |0\rangle \, . \tag{2.21}$$

In the limit of large lattices and atom numbers, this state can be approximated by a product of coherent states [62]

$$|\Psi_{\mathrm{SF}}\rangle \approx \prod_{i=1}^{L} |\alpha_i\rangle \, , \tag{2.22}$$

where the coherent states are the eigenstates of the destruction operator

$$\hat{b}_i \left|\alpha_i\right\rangle = \alpha_i \left|\alpha_i\right\rangle \tag{2.23}$$

and can be expressed as a superposition of Fock states $\left|n\right\rangle_i$ [98]

$$\left|\alpha_i\right\rangle = e^{-|\alpha_i|^2/2} \sum_{n=0}^{\infty} \frac{\alpha_i^n}{\sqrt{n!}} \left|n\right\rangle_i . \tag{2.24}$$

The average atom number on a site i for this state is given by $\overline{n} = \langle \hat{n}_i \rangle = N/L$ and the atom number fluctuations follow a Poissonian statistics, with a variance of $\sigma^2 = \overline{n}$.

The Mott Insulating U/J $\rightarrow \infty$ Limit

In the limit of strong interactions, small tunneling, and commensurate fillings, i.e. $\overline{n} \in \mathbb{N}$, the ground state of the system is called Mott insulating, and behaves very differently from the superfluid state discussed above. The tunneling term in the Hamiltonian can be neglected and the atoms localize to individual lattice sites. Instead of representing the system using coherent states, the many-body wavefunction can now be expressed in terms of local Fock states

$$\left|\Psi_{\mathrm{F}}\right\rangle = \prod_i \frac{1}{\sqrt{\eta_i!}} \left(\hat{b}_i^\dagger\right)^{\eta_i} \left|0\right\rangle , \tag{2.25}$$

where the η_i give the occupation number, or number of atoms, on an individual lattice site i. In the Mott insulating regime, the mean occupation is again $\langle n_i \rangle = \overline{n}$, but the fluctuations completely vanish, $\sigma^2 = 0$, and $\eta_i = \overline{n}$ for all sites i.

Phase Transitions and External Potentials

For a system at finite U/J and at $\overline{n} = 1$, the superfluid limit is connected to the Mott insulating limit via a quantum phase transition that occurs at a critical ratio $(U/J)_c$. While the simple wavefunctions mentioned above are only valid in the limits $U/J = 0$ and $U/J \rightarrow \infty$, the characteristics of these phases persist up to the transition point. As this transition is driven by quantum fluctuations, it even occurs at $T = 0$, and the Bose-Hubbard model provides one of the simplest implementations of a system which exhibits a quantum phase transition that can not be mapped onto previously studied classical phase transitions [99].

In a mean field approximation, the quantum critical point $(U/J)_c$ is determined to be [19, 100–102]

$$(U/J)_c = 5.8z, \tag{2.26}$$

where z is the number of nearest neighbors, depending on the lattice geometry. However, in low dimensional systems, the actual value for $(U/J)_c$ differs significantly from this prediction. More precise values have been determined using numerical techniques like exact diagonalization, density-matrix renormalization group (DMRG) methods and Quantum Monte Carlo simulations. For a mean atom number of $\overline{n} = 1$, $(U/J)_c \approx 3.4$ in 1D [103–105], $(U/J)_c \approx 16.9$ in 2D [106], and in 3D, $(U/J)_c \approx 29.4$ [107].

Note that technically, the phase transition from a superfluid to a Mott insulating state in homogeneous systems only appears when $\overline{n} \in \mathbb{N}$. As an example, take a mean density of $\overline{n} + \epsilon$, where $\epsilon \ll 1$. Even in the limit of $U/J \to \infty$, the small fraction of additional atoms will reside on top of a $\overline{n} = 1$ Mott insulator and form a superfluid, lowering its kinetic energy by delocalizing over many lattice sites [62]. Thus, The complete system can never be fully Mott insulating. This situation, however, is usually mitigated in experimental realizations by the presence of an overall harmonic confinement.

We can write the Bose-Hubbard model with the inclusion of an external potential as

$$H = -J \sum_{\langle i,j \rangle} \hat{b}_i^\dagger \hat{b}_j + \frac{U}{2} \sum_i \hat{n}_i(\hat{n}_i - 1) + \sum_i (\epsilon_i - \mu_0)\hat{n}_i. \tag{2.27}$$

Here, we have introduced the chemical potential μ_0, which can be used to control the number of atoms in the system in a grand-canonical ensemble. The single particle energy ϵ_i is given by the external potential $V_{\text{ext}}(\mathbf{r}_i)$, where $\mathbf{r}_i$ is the position of site i. In practice, the density distribution of an inhomogeneous system can be calculated using a local density approximation, where the density on site i is determined from the local chemical potential $\mu = \mu_0 - \epsilon_i$. In a mean field approximation, the boundary between the superfluid and the Mott insulating regime is given by [102]

$$\left(\frac{J}{U}\right)_c = \frac{1}{z} \frac{(n - \frac{\mu}{U})(1 - n + \frac{\mu}{U})}{1 + \frac{\mu}{U}}. \tag{2.28}$$

On the left side of figure 2.3, we show the behavior of $(J/U)_c$ with changing μ. The shaded areas at small J/U are the Mott insulating regimes with the respective atom number n per site indicated, while the area at larger J/U shows the superfluid regime. A system with a given J/U will exhibit local chemical potentials μ that lie on vertical lines in the plot up to a maximum value $\mu_{\max}$

For a system at small J/U where a vertical line does not intersect the Mott insulating lobes, the density of the system varies slowly over its extension. At intermediate J/U (dashed line b), however, the system is composed of a Mott insulating shell structure, where the shells are separated by superfluid regions. A visualization of such a density distribution for a 2D system is shown on the right side of fig. 2.3 (label b). Such wedding cake structures of regions that are flat in density,

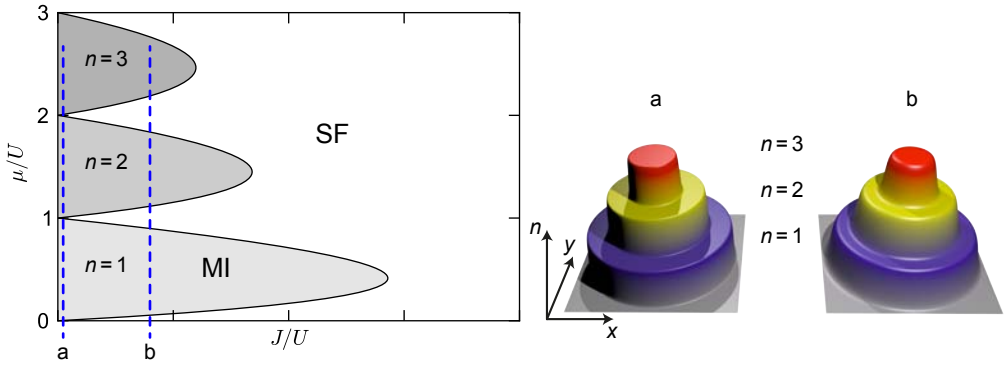

Figure 2.3: Left: Phase Diagram of the Bose-Hubbard model with an external potential. The solid black line is the boundary between the superfluid and the Mott insulating phase. Right: Schematic visualization of the density distribution in a 2D lattice with harmonic confinement and J/U as indicated by the dashed lines in the phase diagram.

interspersed by superfluid regions, occur as soon as J/U is smaller than the critical $(J/U)_c$ at $n = 1$. For very small J/U (line a), the superfluid regions become smaller and smaller, leading to steep transitions between regions with integer numbers of n, as shown in the center of fig. 2.3. The formation of such shell structures was first observed in [108] and has recently been imaged directly, using fluorescence imaging with single site resolution [58, 109]. In chapter 5.3.1, we present the observation of the superfluid to Mott insulator transition using ^{39}K in an optical lattice, where we can tune U and J individually.

Chapter 3

Integrability and Thermalization in Closed Quantum Systems

Statistical mechanics is one of the pillars of modern physics. It demonstrates beautifully how the microscopic properties of the constituents of large systems are intrinsically related to macroscopically observable quantities like temperature, pressure etc. The extension of the classical statistical mechanics to the quantum regime, where the prediction of such extraordinary states as Bose-Einstein condensates results from first principles about the exchange characteristics of individual atoms, proved equally fruitful in connecting microscopic behavior with macroscopic observables.

At the heart of statistical mechanics lies the postulate of equal *a priori* probabilities, which states that a macroscopic system in thermodynamic equilibrium can be found with equal probability in any microscopic state that satisfies the macroscopic conditions of the system. For a closed system with a fixed total energy between E and $E + \delta E$, the macroscopic behavior can be determined by averaging over the microcanonical ensemble that includes all microscopic states with an energy in this range. For the description of a system that is weakly coupled to a bath with which it can exchange energy, the canonical ensemble is used in which the temperature of the system in thermal equilibrium is determined by the temperature of the bath. If the system can exchange energy as well as particles with the bath, it can be described by a grand-canonical ensemble with a temperature T and a chemical potential μ that determines the average number of particles in the system.

These ensembles can not always be applied directly to quantum-mechanical systems. For a closed system, there is no exchange with a bath and thus only the microcanonical ensemble can be suitable to describe the full system. Especially after a quantum quench in the parameters of the Hamiltonian, however, a quantum-mechanical system could be in a superposition of multiple eigenstates with a large variation of eigenenergies, and the microcanonical ensemble could not be applied. When investigating the thermalization of closed systems, one approach is to partition the system into small subsystems, which can exchange energy and particles. In thermal equilibrium, all other subsystems then act as a bath for the investigated sub-

system, however, the coupling in this case is much stronger than the weak coupling usually assumed in statistical mechanics.

The validity of the postulate of equal *a priori* probabilities is the foundation of the description of systems in terms of these ensembles, and the most fundamental question regarding the thermodynamical behavior of closed systems is thus: under what conditions does a system that starts in a given initial state relax towards thermodynamic equilibrium, where the postulate of equal *a priori* probabilities holds and its macroscopic properties are defined by the predictions of statistical mechanics? And if these conditions are not met, will the system still show some form of relaxation dynamics and what defines the final state of a system in which the postulate does not hold?

In this chapter, we try to elaborate on these questions and on how they are relevant in our experimental situation. First, we will briefly discuss the question of thermalization in classical physics. We then turn to quantum mechanical systems and elaborate on the notion of integrability, ergodicity, and the meaning of thermalization in terms of the eigenstate thermalization hypothesis (ETH) [110, 111]. For integrable systems, we also introduce the description of relaxed states in terms of the generalized Gibbs ensemble (GGE) [87]. After discussing recent advances in the theoretical description and experimental observation of relaxation and thermalization in closed quantum systems in general, we focus on the Bose-Hubbard Hamiltonian and discuss its integrable and non-integrable parameter regimes as well as recent results on its relaxation dynamics.

3.1 Classical Thermalization

The key to understanding thermalization in isolated classical systems lies in the effects that cause a system to behave ergodically. Ergodicity implies that a closed system of particles with a given total energy E will, over time, explore the full phase space on a fixed energy surface. For sufficiently long times, the probabilities of the system to be in any microscopic state at a given energy will then become equal and general thermodynamic relations can be derived.

As a simple gedankenexperiment, one can think of a large number N of particles released into a box of volume V with perfectly reflecting walls. All these particles start with the same initial velocity $\mathbf{v}_{\mathrm{in}}$ but at different coordinates $\mathbf{r}_{\mathrm{in}}$, such that the total energy of this system is given by $E = Nm/2|v_{\mathrm{in}}|^2$, where m is the mass of the particles. Let us first assume these particles to be non-interacting. In this case, there is no possibility of exchanging momentum with other particles and each particle will retain the absolute value of its velocity throughout all times. Accordingly, the multitude of allowed states that have the same E but varying individual velocities is not accessible during the evolution and the assumption of equal probabilities is invalid, leading to a distinctively non-thermal behavior of this system.

If we now add interactions to the system, e.g., in the form of a hard sphere potential with radius a

$$V_{\text{int}}(r_{i,j}) = \begin{cases} \infty & \text{for } r_{i,j} \leq a \\ 0 & \text{for } r_{i,j} > a \end{cases}, \tag{3.1}$$

where $r_{i,j}$ is the distance between two particles, the dynamics change drastically. The particles can now collide with each other and redistribute their momentum. This system is known to be fully chaotic and will explore the full phase space on a constant energy surface for any value of E [111, 112]. Note that, if the initial conditions are perfectly well defined, two separate realizations of such a gedankenexperiment will in principle still result in the exact same state after a fixed evolution time. If, however, we allow for a small spread in the initial conditions or measure at different times, the system will be equally likely in any possible microstate with energy E and fulfill the postuale of equal *a priori* probabilities. After a short evolution time, independently of its initial state, the system will be in full agreement with the predictions of classical statistical mechanics.

3.1.1 Integrability and Chaos

The two examples above highlight the central question about the ability of a classical system to thermalize: Under what conditions does a system behave ergodically?

Clearly, a system of non-interacting particles, as discussed above, does not behave ergodically. This is related to the notion of integrability of a system in the sense of Liouville (see, e.g., [113]). If a system with s degrees of freedom, occupying a $2s$-dimensional phase-space, possesses s independent integrals of motion, it is considered integrable. The solutions of the equations of motion then display a periodic motion in phase space, rendering the system non-ergodic. Such a system will thus only explore a very small region of the available phase-space and will not thermalize.

Conversely, for a system that exhibits full dynamical chaos, the motion on any constant energy surface in phase space is ergodic (see, e.g., [114]). This is the case for the interacting system described above and in general also for most interacting many-body systems. However, for a given system, ergodicity is not at all trivial to prove.

The mere presence of interactions or, more generally, a nonlinearity in a system is not sufficient to result in ergodic behavior. This was famously observed in the Fermi-Pasta-Ulam experiment [115–117], which led to the realization that a lot of non-linear equations can be solved exactly and that ergodic behavior can even depend on the initial conditions (see [118] and references therein). Another notable contribution to the limitations of establishing ergodicity for a classical system comes from the theory of Kolmogorov, Arnold, and Moser [119–121] (KAM theory), which

shows that many-body systems that are only weakly disturbed by a nonlinearity will exhibit quasi-periodic tori in phase space and thus in general behave non-ergodic.

A thorough treatment of the theoretical work on classical ergodicity and thermalization is beyond the scope of this thesis. The examples above shall mainly serve as a reminder that the connection between the microscopic dynamics of a system and its thermal behavior still pose open problems even in the classical regime and remain a topic of active research (see, e.g., [122]).

3.2 Thermalization in Closed Quantum Systems

3.2.1 Quantum Ergodicity

Extending the notion of ergodicity to the quantum mechanical case is not at all straightforward. A first attempt was given in von Neumann's seminal paper on quantum ergodicity [123], restated in a more modern notation in [124]:

For a Hamiltonian H with eigenenergies E_α and corresponding eigenvectors $|\Phi_\alpha\rangle$, the micro-canonical density matrix $\hat{\rho}_{\mathrm{mc}}$ at energy E is defined as

$$\hat{\rho}_{\mathrm{mc}} = \frac{1}{D} \sum_{\alpha : E_\alpha \in [E, E+\delta E]} |\Phi_\alpha\rangle \langle \Phi_\alpha| \,, \tag{3.2}$$

where D is the number of eigenstates with energies between E and $E + \delta E$. Let $|\Psi_0\rangle$ be a generic initial state sufficiently narrow in energy that can be written as

$$|\Psi_0\rangle = \sum_{\alpha : E_\alpha \in [E, E+\delta E]} c_\alpha |\Phi_\alpha\rangle \,. \tag{3.3}$$

The closest analogon to classical ergodicity would now be to require that the time average over the density matrix of the time evolved state $|\Psi_t\rangle$ fulfills

$$\overline{|\Psi_t\rangle \langle \Psi_t|} = \hat{\rho}_{\mathrm{mc}}. \tag{3.4}$$

However, assuming that the Hamiltonian is non-degenerate, we can easily calculate the time average as

$$\overline{|\Psi_t\rangle \langle \Psi_t|} = \sum_{\alpha,\beta} \overline{e^{\left(-i(E_\alpha - E_\beta)t/\hbar\right)}} c_\alpha c_\beta^* |\Phi_\alpha\rangle \langle \Phi_\beta| = \sum_\alpha |c_\alpha|^2 |\Phi_\alpha\rangle \langle \Phi_\alpha| \,, \tag{3.5}$$

with $\alpha, \beta : E_\alpha, E_\beta \in [E, E+\delta E]$. Thus, if ergodicity was defined by eq. 3.4, it would be required that $|c_\alpha|^2 = 1/D$ for all α, which is only satisfied for a very specific class of initial states and thus almost never realized. Von Neumann already realized that, in order to define ergodicity as a foundation of quantum statistical mechanics, one

can not look at the evolution of the state itself but rather at the observables of interest.

A definition of quantum ergodicity that is nowadays widely agreed upon [60, 77, 110, 125] was suggested in [126] as

$$\langle\langle\Psi_t|A|\Psi_t\rangle\rangle_t = \frac{1}{D}\sum_\alpha \langle\Phi_\alpha|A|\Phi_\alpha\rangle \equiv \langle A\rangle_{\mathrm{mc}}(E_0). \tag{3.6}$$

In words, a system is ergodic in an observable A, if the time average of the expectation value of A is equal to its microcanonical ensemble average. This raises the question what kind of observables are relevant for the characterization of systems as ergodic. Obviously, observables like the occupation of individual energy eigenstates are stationary in closed quantum systems and will never show thermalization, so it would be certainly too much to require eq. 3.6 to hold for all possible observables. In general, local observables like densities or short range correlation functions and macroscopic observables that are based on local observables, such as the magnetization of spin chains or global density distributions of cold atoms are investigated in the context of thermalization in closed quantum systems. Such observables are commonly referred to as natural observables of the system.

From an experimentalist's point of view, it is reasonable to consider those observables that can be directly measured. In ultracold quantum gases experiments, these are predominantly density distributions $n(\mathbf{r})$, but also the behavior of short range correlations has been studied extensively [73, 78, 79].

3.2.2 Thermodynamic Universality

Assuming that we are looking at an observable A that does thermalize, expressed in the energy eigenbasis of the systems Hamiltonian, we can directly see from eqns. 3.5 and 3.6 that

$$\sum_\alpha |c_\alpha|^2 A_{\alpha,\alpha} = \frac{1}{D}\sum_{\substack{\alpha \\ E_\alpha\in[E,E+\delta E]}} A_{\alpha,\alpha}. \tag{3.7}$$

This is a central equation in the discussion of thermodynamical behavior of quantum mechanical systems as it directly encompasses the thermodynamical universality: The left hand side depends directly on the microscopic details of the individual quantum states via the coefficients c_α while the right hand side depends only on the total energy E of the system.

For a quantum system obeying eq. 3.7, there are three possible explanations for this universality [77]. The first two explanations rely on assumptions about the typical initial states: First, for physically interesting initial conditions, the fluctuations of the $A_{\alpha,\alpha}$ as well as those of the $|c_\alpha|^2$ for different eigenstates are large but uncor-

related. Any initial state then gives an unbiased sampling over the distribution of the $A_{\alpha,\alpha}$, which leads to eq. 3.7. Second, the eigenstate occupation numbers $|c_\alpha|^2$ hardly fluctuate at all for physically interesting initial states (that are sufficiently narrow in energy). This immediately gives eq. 3.7 but requires that all $|c_\alpha|^2 \approx 1/D$, which is a rather strong constraint on the possible initial states. While thermodynamic universality of systems can be explained under the two assumptions above, both rely on properties of the $|c_\alpha|^2$ in non-integrable systems. Thus, thermalization would depend on the choice of the initial state, and it would always be possible to engineer special states that do not thermalize.

The third possible explanation circumvents this problem. It is based on assumptions about the behavior of the eigenstate expectation values $A_{\alpha,\alpha}$ as a function of energy E_α and is commonly referred to as the eigenstate thermalization hypothesis (ETH) [111].

3.2.3 Eigenstate Thermalization Hypothesis

It was first suggested in [126] that in systems which show thermalization, certain observables expressed in the eigenbasis of the Hamiltonian behave as if they were Gaussian random variables. This was elaborated on by Deutsch and Srednicki [110, 111], resulting in the eigenstate thermalization hypothesis which can be expressed in the following way: In a large interacting many-body system, the expectation values of a natural observable on an eigenstate $|\Phi_\alpha\rangle$, $A_{\alpha,\alpha}$, are given by a smooth function of the eigenenergy E_α, and are thus essentially constant in the narrow energy range $[E, E+\delta E]$. In this case, eq. 3.7 holds for all initial states that are narrow in energy.

The ETH can also be expressed as

$$A_{\alpha,\alpha} = \langle A \rangle_{\mathrm{mc}}\,, \tag{3.8}$$

which highlights a remarkable property of systems that adhere to the ETH: The knowledge of a single eigenstate of the system is sufficient to compute the microcanonical averages of observables.

There is no general theoretical argument for the validity of the ETH, but for specific systems, it has been shown to hold. In [110], it was shown to be valid for an integrable Hamiltonian perturbed by a real, symmetric matrix with elements chosen from a random Gaussian ensemble. Furthermore, it was shown to be valid for certain quantum systems with chaotic classical counterparts [111, 127]. A very thorough analysis of the ETH is given in [77] for a system of bosons released into a 2D lattice and compared to an integrable system of hard-core bosons on a 1D lattice, where the ETH is not satisfied. In that work, it was also shown that the distribution of the $|c_\alpha|^2$ in the investigated system fluctuates strongly, ruling out the assumption that $|c_\alpha|^2 \approx 1/D$. These examples, combined with other results (see [77] and references therein) make a strong case for the assumption that the ETH is

the fundamental mechanism for thermalization in general isolated quantum systems, however, a formal proof remains elusive.

3.3 Quantum Integrability

After discussing thermalization in the context of closed quantum systems, a remaining question is: Under what circumstances can we expect quantum mechanical systems to behave ergodically and show such thermalization? As in the classical case, this question involves the concept of integrability, which, in the quantum mechanical case, can not be defined as straightforwardly as its classical counterpart. Any quantum-mechanical system in a finite-dimensional Hilbert space that is governed by an arbitrary Hermitian Hamiltonian can easily be shown to fulfill criteria rather similar to those demanded for classical integrability. Even though it might be computationally unfeasible, any Hermitian Hamiltonian can be diagonalized, leading to a set of orthonormal eigenvectors $|\Phi_\alpha\rangle$ to energy eigenvalues E_α. Every initial state of the system can be expressed in this eigenbasis as

$$|\Psi_{\text{in}}\rangle = \sum_\alpha c_\alpha |\Phi_\alpha\rangle . \tag{3.9}$$

From the Schrödinger equation

$$i\hbar \frac{d}{dt} |\Phi_\alpha\rangle = H |\Phi_\alpha\rangle = E_\alpha |\Phi_\alpha\rangle \tag{3.10}$$

follows the simple time evolution for the state $|\Psi(t)\rangle$, starting from the initial state $|\Psi_{\text{in}}\rangle$, as

$$|\Psi(t)\rangle = \sum_\alpha c_\alpha \exp\left(-\frac{i}{\hbar} E_\alpha\right) \Phi_\alpha. \tag{3.11}$$

For a Hamiltonian that is defined on a Hilbert space of dimension D_H, we can thus immediately find a set of D_H conserved quantities, e.g., the set of projectors onto the eigenstates $P_\alpha = |\Phi_\alpha\rangle \langle\Phi_\alpha|$. Following this simple argument, one would have to consider every quantum mechanical system that is governed by a Hermitian Hamiltonian as being fully integrable. This is not a practical point of view, as we certainly expect strong differences in the behavior of, e.g., non-interacting and interacting quantum systems.

The above argument, however, can be incorporated into a second definition of integrability by requiring that the system can be solved exactly and the full set of eigenstates can indeed be constructed explicitly [128]. Further definitions of quantum integrability that have been discussed in the literature rely on demanding that the scattering supported by a system is non-diffractive [129] or that its energy

level statistics is Poissonian [130]. An overview over various attempts at defining quantum integrability and the problems associated with them can be found in [128], a full discussion of the advantages and disadvantages of certain definitions is beyond the scope of this thesis. In general, there is no universally agreed upon way of defining quantum integrability, and definitions are usually suited to specific kinds of problems.

For our purposes, it shall suffice to note that all free theories can be considered integrable. In these cases, it is usually trivial to achieve exact diagonalization of the Hamiltonian via a Fourier transformation and the integrals of motion can be directly constructed from the operators representing the occupation of the Fourier modes [128]. In general, integrable models are characterized by the existence of many non-trivial integrals of motion that significantly influence their dynamics.

A notable example of an integrable interacting system are hard-core bosons in 1D optical lattices. As discussed below (sect. 3.4.2), they can be mapped onto a system of free fermions, which is completely integrable. Consequently, the system also possesses many non-trivial integrals of motion and will not show thermalization. Relaxation dynamics in this system can nevertheless be observed, but they will generally result in non-thermal equilibration states (see sect. 3.5.1).

3.3.1 Equilibrium States of Integrable Quantum Systems

Concerning integrable systems that possess many non-trivial integrals of motion, a general question to ask is whether such systems will show some kind of equilibration during the evolution from a given initial state that is not an eigenstate of the Hamiltonian. If so, the next question is what kind of equilibrium state will be reached, as it generally will not be the state expected from the predictions of typical statistical mechanics for ergodic systems.

An intuition of how relaxation dynamics can arise in integrable systems comes from the investigation of quantum quenches, sudden changes to a parameter of the Hamiltonian, e.g., the interaction strength (see, e.g., [78, 131, 132]). One can typically observe relaxation dynamics in these systems, even when they are completely integrable in the sense discussed above, but the resulting states can in general not be described by a microcanonical ensemble. The key to understanding such dynamics lies in considering only small subsystems of a large quantum system after a quench. For such small subsystems, one can then regard the rest of a system as a reservoir that allows the subsystems to locally equilibrate with respect to each other [133]. In contrast to usual statistical mechanics with a weak coupling, the reservoirs here are strongly coupled to the system. In order to predict the final states after such relaxation, the constraints imposed by the integrability of the system have to be taken into account.

A conjecture about the equilibration states of generic quantum systems constrained by a given set of integrals of motion $\{\hat{\mathcal{I}}_m\}$ is that, during an evolution

starting in a specific initial state, the system should maximize its entropy S while obeying the constraints. This results in a many-body density matrix of the form

$$\hat{\rho} = Z^{-1} \exp\left(- \sum_m \lambda_m \hat{\mathcal{I}}_m \right), \tag{3.12}$$

first introduced in [134], which is now mostly referred to as the generalized Gibbs ensemble (GGE) [87]. Here, the λ_m are the Lagrange multipliers, their values are determined by the initial $\langle \mathcal{I}_m \rangle$.

In [87], it was shown that the momentum distribution of the relaxed state of a system of hard-core bosons in the 1D Hubbard model can be described by the GGE. The validity of the GGE in this case was shown to be the consequence of a generalized eigenstate thermalization hypothesis [135].

While there is no formal proof that establishes the validity of the GGE in general for integrable systems, recent studies reveal a broad range of systems in which the predictions of the GGE are valid: the GGE was shown to be valid for, e.g., local observables in free bosonic and fermionic theories [133, 136], local observables after a magnetic field quench in the transverse field Ising chain [137], simple correlation functions after an interaction quench in the Luttinger model [138], momentum distribution functions at small momenta in the Lieb-Liniger model [139], and many more (see, e.g. , [140–142] and references in [143])

3.3.2 Breaking of Integrability and Relaxation Dynamics

As a general statement about the presence of full thermalization in closed quantum systems, we can conclude that it does not occur in fully integrable systems, while most macroscopic many-body systems with interactions can be expected to show thermalization and are likely to agree with the ETH. A remaining question that has not found a definitive answer to date is, how far from integrability a system needs to be in order to exhibit thermal behavior. This is closely related to a second open question regarding the time-scales on which a system relaxes towards an equilibrium state, be it thermal or determined by the generalized Gibbs ensemble.

Multiple recent publications deal with these question in various systems. In [78], the behavior of 1D and 2D Hubbard systems after a quench from the superfluid to the Mott insulating phase is investigated theoretically, showing a strong dependence of the equilibration on the final interaction strengths. An interaction quench in Hubbard models is also investigated in [81, 82], showing that the relaxation exhibits a prethermalization on a fast time scale followed by a slow relaxation towards thermal equilibrium. Ref. [144] shows the relaxation of different initial states of fermions on 1D lattices with next-nearest neighbor interaction towards a common non-thermal final state. In [88], the effect of weakly breaking the integrability of a system of hard-core bosons on a 1D lattice is investigated by introducing a next-nearest neighbor

tunneling and interaction. It is shown that the system is continuously driven further away from thermodynamic predictions, the closer it comes to being integrable.

On the experimental side, there has been a lot of progress using ultracold atoms to investigate the thermalization behavior of quantum systems. The absence of thermalization in integrable systems is convincingly demonstrated in the "*Quantum Newtons Cradle*" experiment [63], where collisions of two clouds of bosons close to the Tonks-Girardeau regime (see sect. 3.4.2) where observed on long time scales, with no indication of thermalization.

Recently, an experiment investigating the relaxation of density waves in optical lattices that was suggested in [79, 80] was realized using ^{87}Rb in an optical superlattice [73]. The relaxation is observed for the quasi-local densities and currents, which are shown to retain information about the initial state of the system, as well as nearest neighbor correlators, which relax to values compatible with thermodynamical predictions.

Another line of experiments [64, 65, 145] investigates relaxation dynamics by coherently splitting a 1D Bose gas into two phase coherent gases and then observing the decay of phase coherence between the two clouds over time. The fast decay observed in [64] for completely decoupled 1D gases was shown in [65] to be an instance of prethermalization dynamics. The thermal correlations induced during this prethermalization stage were shown to emerge locally and spread in a light-cone like fashion throughout the system [145].

There are numerous other experiments using ultracold gases as well as solid state systems to investigate the non-equilibrium dynamics and thermalization properties of closed quantum systems. For a more detailed overview over a wide range of experiments, please refer to [60].

3.4 Integrability in the Bose-Hubbard Hamiltonian

The system we are mainly concerned with in this thesis is that of bosons in homogeneous optical lattices. As discussed in chapter 2, in the absence of external global potentials, this system can be described by the Bose-Hubbard Hamiltonian of the form

$$H = -J \sum_{\langle i,j \rangle} \hat{b}_i^\dagger \hat{b}_j + \frac{U}{2} \sum_i \hat{n}_i(\hat{n}_i - 1), \tag{3.13}$$

with tunneling J, bosonic creation and annihilation operators $\hat{b}_i^\dagger$ and $\hat{b}_i$ on site i, on-site interaction U and the on-site number operators $\hat{n}_i = \hat{b}_i^\dagger \hat{b}_i$. While it is in general non-integrable [62], two integrable limits exist, namely the non-interacting limit and the limit of infinitely strong interactions in 1D.

3.4.1 The Non-Interacting Limit

In the non-interacting limit, the term describing the interaction energy in the system vanishes and we are left with the Bose-Hubbard Hamiltonian for free particles in a lattice. As discussed, this Hamiltonian can be easily diagonalized using a basis transformation into Fourier space, which results in an eigenstate basis of Bloch waves with quasimomenta q. Due to the absence of interactions, the dynamics of any given initial state is then simply given by the sum over the evolution of all individual Bloch waves. Thus, non-interacting atoms in any dimensionality constitute a completely integrable system and we do not expect any form of global relaxation or thermalization to be present.

Quantum quenches in this model can only affect the tunneling J. This does not alter the eigenstates of the system but only the eigenenergies, leaving the overall dynamics identical except for a change in timescales. As we will see in chapter 6, dynamics in this system can be investigated by, e.g., confining atoms to few sites and then releasing them into a larger lattice. These dynamics, however, can always be understood in terms of ballistic single particles and do not pose any unanswered questions.

3.4.2 The $|U/J| \to \infty$ Limit

The more interesting limit of the Bose-Hubbard Hamiltonian is that of infinite interactions, $|U| \to \infty$. The behavior now depends strongly on the initial state of the system. Let us assume that $n_i = 2$ on a single site i. This would, in the case of $U \to -\infty$, constitute a bound object of infinitely large binding energy. In the case $U \to +\infty$, the two atoms would form a repulsively bound pair [146]. As the rest of the system can neither provide the energy necessary to break up such a pair in the $U < 0$ case, nor take up the energy released in the dissolving of a pair in the $U > 0$ case, in both situations a doubly occupied site is a stable object. Dynamically, this object behaves completely static at $|U| \to \infty$. At finite U/J, the two atoms can only move to a neighboring site in a second order process where both atoms tunnel simultaneously in order to conserve their interaction energy. The effective hopping matrix element for such a process is proportional to J^2/U [27], which becomes zero in the limit $|U/J| \to \infty$. The same holds for any sites with occupation $n_i > 2$. Thus, an initial state that consists solely of sites with $n_i = 2$ in the $|U/J| \to \infty$ limit would constitute a rather uninteresting system from the dynamical perspective. A system consisting of a mixture of sites $n_i = 1$ and $n_i = 2$ can exhibit some interesting dynamics. The different mobility of singly and doubly occupied sites can lead to quantum distillation effects in expanding states, where doubly occupied sites accumulate in the center while singly occupied sites leave the system [83, 147].

Regarding the integrability of Bose-Hubbard systems, the most peculiar consequences arise from the effects of large interactions on an initial state with all $n_i \leq 1$.

In this case, the wavefunction of the system can never have a contribution from $n_i > 1$, due to the energetic constraints. Thus, even though $|U|$ is infinitely large, the system does not contain any interaction energy as $n_i(n_i - 1)$ is always zero. This reduces the Hamiltonian again to that of free particles in a lattice but imposes an additional constraint on the hopping term. The strong interaction acts as an effective Pauli blocking that prevents two bosons from occupying the same lattice site. Even though we can not simply substitute the bosonic creation and annihilation operators by the fermionic ones, as the particles still obey the bosonic commutation relations, the system does nevertheless exhibit a characteristically fermionic behavior.

Bose-Fermi Mapping

The connection between hard-core bosons and fermions was first realized by Girardeau [148] for impenetrable bosons in 1D (without additional lattices). Take a system of bosons in a 1D geometry with arbitrary interactions. The only constraint on the form of the interactions is that is must posses an impenetrable nature, i.e., the probability of finding two bosons at a distance smaller than the hard-core diameter a must vanish:

$$\Psi(x_1, \ldots, x_N) = 0 \quad \text{if} \quad |x_i - x_j| \leq a, \quad 1 \leq i, j \leq N, \tag{3.14}$$

where $x_1 \ldots x_N$ are the coordinates of the N particles. It can then be shown that if the bosonic wave function Ψ^B is a solution to the Schrödinger equation of the system, the fermionic wave function Ψ^F given by

$$\Psi^B = \Psi^F \cdot \prod_{i>j} \operatorname{sgn}(x_i - x_j) \tag{3.15}$$

is also a solution. This establishes a one-to-one mapping between impenetrable bosons and free fermions in 1D geometries that has profound consequences for certain observables. In particular, quantities like the density distributions or density-density correlations behave in exactly the same way as those of a system of free fermions. Also the energy spectrum and the chemical potential are exactly the same in both cases. There are, however, profound differences in non-diagonal quantities like the momentum distribution [149] and the one-particle reduced density matrix [150].

The possibility of creating such systems with ultracold atoms was first pointed out in [151], making use of the increased scattering between atoms in the presence of a strong transverse confinement. First experimental realizations of Tonks-Girardeau gases were produced with the help of optical lattices [25, 63] to supply the transverse confinement (and to increase the effective mass of the atoms in [25]). The experiments in [63] are of particular interest regarding the question of thermalization in these systems. In repeated collisions of two clouds of impenetrable bosons, no signs of damping or relaxation towards a thermal equilibrium could be observed. This can

be seen as a direct consequence of the existence of a mapping onto free fermions. As discussed in sect. 3.3, free systems are integrable and do not equilibrate to thermal states. In a theoretical study, this behavior was confirmed under conditions similar to the experimental ones. Here, it was shown that a momentum distribution consisting of distinct peaks will preserve these peaks throughout all times [87]. There is, however, some initial relaxation that leads to a broadening of the peaks in momentum space consistent with predictions of the GGE, but on a scale that is below the experimental resolution in [63].

Hard-Core Bosons in 1D Lattices

The same kind of one-to-one mapping to free fermions can be constructed for a system of impenetrable bosons in 1D lattices. Such a system can be described by the standard Bose-Hubbard Hamiltonian for free particles

$$H = -J \sum_{\langle i,j \rangle} \hat{b}_i^\dagger \hat{b}_j, \tag{3.16}$$

where $\hat{b}_i^\dagger$ and $\hat{b}_i$ obey the usual bosonic commutation relations and the additional on-site constraints

$$\hat{b}_i^{\dagger 2} = \hat{b}_i^2 = 0 \quad \text{and} \quad \{\hat{b}_i, \hat{b}_i^\dagger\} = 1. \tag{3.17}$$

The additional constraints ensure the hard-core behavior of the bosons by requiring a maximum population of one atom per lattice site. In order to rewrite the Hamiltonian with fermionic creation and annihilation operators, one can use a Jordan-Wigner transform [152] of the form [153]

$$\hat{b}_i^\dagger = \hat{f}_i^\dagger \prod_{\beta=1}^{i-1} e^{-i\pi \hat{f}_\beta^\dagger \hat{f}_\beta}, \; \hat{b}_i = \prod_{\beta=1}^{i-1} e^{i\pi \hat{f}_\beta^\dagger \hat{f}_\beta} \hat{f}_i. \tag{3.18}$$

Here, $\hat{f}_i^\dagger$ and $\hat{f}_i$ are the fermionic creation and annihilation operators of the Hamiltonian for non-interacting fermions

$$H_F = -J \sum_{\langle i,j \rangle} \hat{f}_i^\dagger \hat{f}_j. \tag{3.19}$$

From eq. 3.18 we can directly see that the density distribution of the bosonic representation is exactly the same as that of the fermionic representation:

$$\hat{n}_i^b = \hat{b}_i^\dagger \hat{b}_i = \hat{f}_i^\dagger \hat{f}_i = n_i^f. \tag{3.20}$$

Thus, when investigating the non-equilibrium evolution of the density distribution of bosons in 1D lattices (see chapter 8.2) with strong interactions, its evolution is

indistinguishable from that of free fermions. Note that we do not specify the nature of the interaction between the bosons. It is easy to see that infinitely strong on-site repulsion leads to the conditions of eq. 3.17. However, in a system with infinitely attractive on-site interactions, $U \to -\infty$, the formation of doubly occupied sites is equally forbidden by energetic constraints. Thus, when starting from an initial state with singly occupied sites in the limit of $|U| \to \infty$, the expected dynamics are the same, regardless of the sign of the interaction.

It is clear that the limit of $|U| \to \infty$ can experimentally never be fully achieved. However, this is not necessary in order to observe the fermionization of a system of bosons in 1D. The criterion for the applicability of the mapping from hard-core bosons to free fermions is the suppression of the formation of doubly occupied sites. The energy of such a doubly occupied site is proportional to U. Thus, as long as U is large compared to the kinetic energies available in the system, the formation of double occupancies will be strongly suppressed and can be neglected. The bandwidth of the lowest band in the 1D Bose-Hubbard model is $4J$, which is the maximum energy a single particle can possibly release or take up in a collision with other particles. For interaction strengths in the range of $U/J = 20$, which are easily achievable in our experiments, the formation of a single double occupancy would thus require at least a 5-body process in order to guarantee the conservation of energy. This shows that already at $U/J = 20$, an approximation in terms of a hard-core behavior of 1D lattice bosons is well justified.

3.5 Relaxation Dynamics in the Bose-Hubbard Model

3.5.1 Relaxation in the Integrable Regimes

While a non-interacting system of Bosons will not show global thermalization, one can still expect to observe relaxation dynamics when looking at local observables (see sect. 3.3.1). This is demonstrated in [133], where the evolution of a system of bosons after a quench in U from the Mott insulating regime to $U = 0$ is investigated. It is shown that the state on a single site, obtained by tracing out the rest of the system, evolves towards a state that maximizes the local entropy. In chapter 8.4.1, we experimentally investigate the formation of sites with occupation $n_i > 1$ after a quantum quench in U/J and find a very fast relaxation dynamics for non-interacting as well as interacting atoms.

The dynamics in the $|U| \to \infty$ regime can also exhibit relaxation that can be observed by investigating the momentum distribution. As mentioned above, a system of hard-core bosons in 1D can be mapped onto a system of free fermions. Naturally, the quasimomentum distribution of free fermions in a 1D Hubbard system is conserved and provides as many conserved quantities as there are lattice sites in the system. However, expressing these conserved quantities in the terms of the bosonic

operators $\hat{b}_i^\dagger$ and $\hat{b}_i$ reveals that they become non-trivial many-body operators in the bosonic representation [87] and can indeed exhibit relaxation dynamics towards equilibrium states.

In [90], the evolution of an initial Fock state of hard-core bosons released into a homogeneous 1D lattice is investigated. During this evolution, the density distribution of the bosons behaves exactly as it is expected for free particles, as a direct consequence of the bose-fermi mapping. The quasimomentum distribution n_q, which is initially flat over the first Brillouin zone, shows a much more interesting behavior. Dynamically, n_q acquires strong peaks at finite quasimomenta $q = \pm\pi/(2d)$, reflecting a quasi-condensation occurring in this system. This is a transient behavior, the peaks in n_q decay in the long time limit and n_q approaches its initial shape again as the density becomes lower and lower during the expansion. This quasi-condensation effect is investigated experimentally in chapter 9, where we also discuss the theoretical predictions in more detail.

A second study investigates the expansion dynamics of the ground state of hard-core bosons in a 1D lattice with an external confinement and a low characteristic density [154]. The quasimomentum distribution of this system before expanding is characterized by a strong peak around $q = 0$. Shortly after the expansion is initiated by removing the confinement, this strong peak disappears and during the course of the expansion, n_q becomes broader and broader and approaches the quasimomentum distribution of free fermions in the limit of long expansion durations.

The two studies discussed above already show that, even though the system of hard-core bosons can be mapped to a fully integrable system of free fermions, a lot of interesting dynamics in momentum space can be observed. However, these dynamics are investigated in the distinctly non-equilibrium situation of an expanding system without boundaries, where no long term equilibration can take place.

The relaxation of a system of hard-core bosons towards an equilibrium state in a bounded system is investigated in [87]. Here, the expansion of a ground state of hard-core bosons in a 1D lattice is investigated after releasing them from a small box potential. At the beginning of the numerical experiment, the small box is replaced by a larger box and the evolution of the momentum distribution of the hard-core bosons is recorded over time. In this evolution, relaxation dynamics can be clearly observed and after a short period of changes, a new equilibrium distribution is reached. This equilibrium distribution shows very good agreement with the predictions of the GGE that takes the constraints imposed by the integrability of the system into account, as discussed in section 3.3.1.

A similar study was conducted with the inclusion of an additional confining or anti-confining potential after a quench in the tunneling J from zero to a finite value. In this setting, the system is also observed to equilibrate towards GGE predictions, which can have positive as well as negative effective temperatures, depending on the nature of the external potential [89].

3.5.2 Relaxation in the non-integrable Bose-Hubbard Model

Thermalization in the 2D Hubbard Model

In 2D and 3D lattices, a mapping from hard-core bosons to free fermions is not possible and these systems do not become integrable even in the limit of $U \to \infty$. In a theoretical study of the dynamics of hard-core bosons released into a 2D lattice, it was convincingly demonstrated that such a system does not only relax to an equilibrium state, but that the expectation values of observables like the momentum distribution in this state are with a high accuracy predicted by a microcanonical ensemble [77].

The evolution of bosons in 2D lattices after a quench in the interaction strength is investigated using exact diagonalization in [78]. In a 2D Bose-Hubbard system, the interaction U is suddenly increased, bringing the system from the superfluid into the Mott insulating regime. A fast relaxation of the next-neighbor correlations to an equilibrium state is observed in the following evolution. However, the final state of this relaxation is only found to agree with thermodynamic predictions for small final U while for large $U \gg J$, the final state bears a strong memory of the initial conditions. The absence of full thermalization is attributed to the large gap deep in the Mott insulating regime that restricts the equilibration between quasi-particles due to energetic constraints. Note, however, that higher order processes might still induce thermalization on longer timescales that are not accessible in the calculations and the state observed in [78] could be an example of pre-thermalization [155].

The dynamics of 2D Bose-Hubbard systems are experimentally investigated in chapter 8 in the context of expansions in homogeneous lattices. In these experiments, we find dynamics that appear distinctly diffusive, indicating fast local relaxation processes to be present already at small interactions. We furthermore study the transition from 1D systems to 2D systems and observe how the breaking of integrability via additional degrees of freedom drives the system from ballistic to diffusive dynamics. Similar studies were also recently conducted using time dependent density matrix renormalization group calculations for hard-core bosons on two leg ladders [86], which showed a qualitatively similar behavior to the experimental results.

Thermalization in the 1D Hubbard Model

While the 2D (and 3D) Hubbard models are generally non-integrable for finite U, the 1D Hubbard model constitutes a special case due to the integrable limit at $U \to \infty$. The effects of approaching the integrable limit are studied in [88] by introducing next-nearest neighbor hopping and interaction terms into the 1D Bose-Hubbard Hamiltonian for hard-core bosons, which break the integrability of the system. For a strong breaking of integrability, the expectation values of few body observables relax quickly to thermal values. By decreasing the integrability breaking, it can then

be seen that the predictions of statistical mechanics become continuously worse the closer the system comes to integrability.

The interaction quenches in [78], as discussed above for 2D systems, are also investigated in 1D Bose-Hubbard models in the same publication, using t-DMRG methods. They show a qualitatively similar behavior, with two distinct non-equilibrium regimes depending on the final interaction strength. For small final U, the systems relax to thermal states, while for $U \gg J$, the relaxed states show a distinctly non-thermal behavior. In the 1D case, this agrees well with the observations of [88] that the predictions of statistical mechanics become less applicable the closer a system comes to integrability. However, this study was again limited to rather small evolution times and the observations could also indicate fast pre-thermalization, followed by a much slower regular thermalization.

A study of the relaxation dynamics of a density wave in the non-integrable 1D Bose-Hubbard systems that is suggested in [79, 80] is conducted experimentally in [73]. Here, a patterned initial density distribution is created using an optical superlattice setup. After the preparation, the lattice potential is transformed into a single-wavelength lattice in a rapid quench and the evolution of various observables like quasi-local densities, currents, and coherences is monitored. The system shows a fast relaxation of all observed quantities, in good agreement with theoretical predictions. The only non-trivial equilibrium value, that of the nearest neighbor correlators, is observed to agree well with thermodynamic predictions, supporting the assumption of thermalization in this system.

In chapter 8, we experimentally investigate the effects of integrability breaking on the expansion dynamics in the homogeneous 1D Bose-Hubbard model by changing the interaction strength as well as the dimensionality of the system.

Chapter 4

Experimental Setup - Making Quantum Degenerate Gases

In this chapter, we present the experimental setup used to create ultracold quantum gases and the employed cooling techniques to reach quantum degeneracy. Most of these techniques have by now become standard tools in atomic physics and are not described in full detail, but can be found in textbooks about experimental physics with cold atoms, e.g., [156]. A more thorough treatment of the experimental details can be found in [92, 157, 158].

The cooling of the atoms is conducted in three distinct steps. In the first step, hot ^{87}Rb and ^{39}K atoms are trapped and cooled using a magneto-optical trap (MOT) [156, 159]. After pumping the atoms into magnetically trappable states, they are magnetically transported into a second vacuum chamber where forced evaporation in an optically plugged magnetic quadrupole trap takes place. Finally, the atoms are transferred into optical dipole traps. Further evaporative cooling is conducted where we employ a Feshbach resonances between ^{87}Rb and ^{39}K for sympathetic cooling, as well as an intra-species Feshbach resonance for ^{39}K in the final cooling step, until we obtain Bose-Einstein condensates in the optical dipole traps.

The structure of this chapter follows the experimental procedure. We first describe the vacuum chamber and the MOT. Then we discuss magnetic trapping of neutral atoms and methods for forced evaporative cooling. Finally, we briefly introduce optical dipole potentials and our dipole trap setup, before investigating the relevant inter- and intra-species Feshbach resonances.

4.1 Vacuum System and Atom Sources

The vacuum system consists of two separate main chambers, connected by a differential pumping stage as shown in fig. 4.1. The Rb and K atoms used in our experiments are introduced into the system by heating the Alvatec dispensers, which are thin metal tubes filled with alloys that contain Rb and K and release it through a small slit facing towards the MOT chamber when they are heated by an electrical current. Additionally, we use light emitting diodes with a wavelength centered around

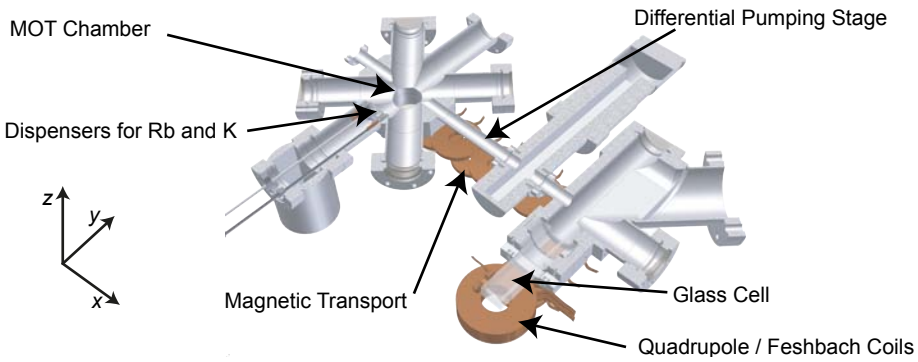

Figure 4.1: Cross sectional view of the vacuum system, including the most important magnetic field coils. The coordinate system used throughout this thesis is shown in the lower left corner.

365 nm (UV LEDs) for light induced desorption of atoms [160] stuck to the walls and windows of the MOT chamber, which increases the background pressure of the alkali atoms.

In the MOT chamber, shown on the left side, the measured background pressure ranges from approximately $1 \cdot 10^{-9}$ mbar to $1 \cdot 10^{-8}$ mbar. Within this range, the pressure increases when the dispensers are heated and the UV LEDs are turned on during the first seconds to release hot atomic Rb and K and decreases during the rest of the experimental cycle. Note that due to the unknown composition of the background gas that determines a correction factor for the measured pressure, the actual background pressure could be well below these values.

The MOT chamber is connected to the experimental chamber via a differential pumping stage of 70 mm length with an inner diameter of 8 mm, which allows to keep a constant pressure gradient between the two chambers while both are being pumped using ion pumps. In the experimental chamber, which is connected to the glass cell in which the final stage of the experiment takes place, the pressure is below $1 \cdot 10^{-11}$ mbar.

4.2 Magneto-Optical Trapping and Cooling

Magneto-optical trapping of atoms relies on a combination of the dissipative forces of near-resonant light in combination with magnetic fields [161, 162]. The laser beams used for the magneto-optical trap are red-detuned relative to the atomic transition lines, which leads to an increased scattering between atoms and photons that are propagating in opposite directions due to the Doppler effect and slows down the atoms. A magnetic quadrupole field is used to introduce a position dependence of the scattering cross section via the Zeeman shift. By carefully choosing the right polarization of the laser beams, atoms displaced from the center of the quadrupole

field absorb light predominantly from those laser beams that push them back towards the center of the field, which results in an effective spatial confinement. For more details on magneto-optical trapping, refer to, e.g., [156].

We use the D2 transitions of ^{87}Rb and ^{39}K for magneto-optical cooling and trapping. Due to the similar structure of both atoms, the hyperfine level structure of the transition lines is qualitatively the same, but differs in the energy splitting between the separate levels, as shown in fig. 4.2.

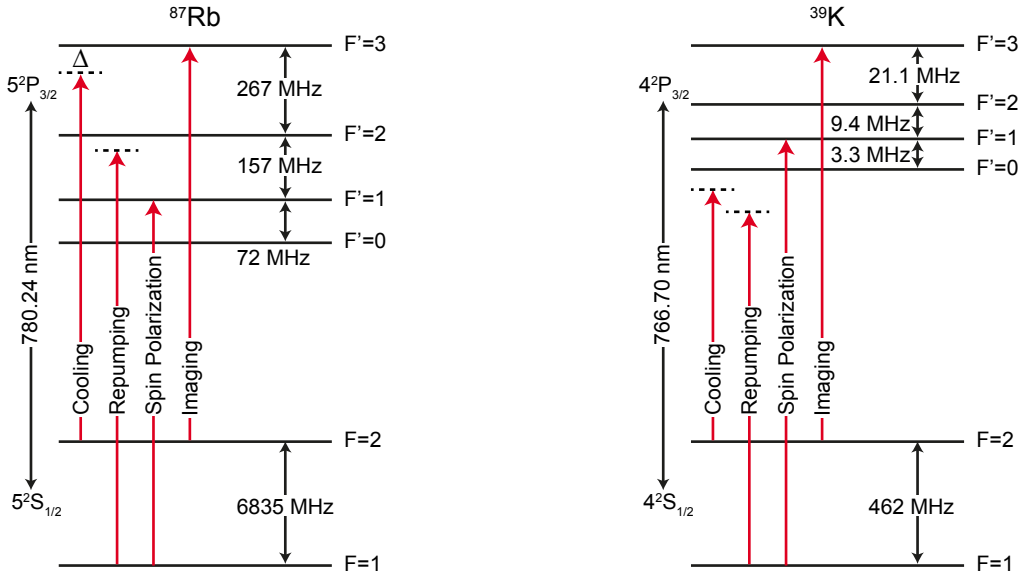

Figure 4.2: Hyperfine structure of the D2 lines of ^{87}Rb and ^{39}K and the transitions used in our experiments. All data taken from [163, 164].

In the case of ^{87}Rb, we use the closed transition from the $|5^2S_{1/2}, F = 2\rangle$ to the $|5^2P_{3/2}, F' = 3\rangle$ states as the main cooling line, indicated by the red arrow labeled "Cooling" in fig. 4.2. The term "closed" refers to the fact that, due to the selection rules for the quantum numbers in optical dipole transitions, an atom that is excited into the $|5^2P_{3/2}, F' = 3\rangle$ state can only decay back into the $|5^2S_{1/2}, F = 2\rangle$ state. In the case of off-resonant excitations into the $|5^2P_{3/2}, F' = 2\rangle$ manifold, however, atoms can decay to the $|5^2S_{1/2}, F = 1\rangle$ ground state and leave the cooling cycle. In order to pump them back into the $|5^2S_{1/2}, F = 2\rangle$ state, the "Repumping" laser (see fig. 4.2) is slightly red detuned to the $|5^2S_{1/2}, F = 1\rangle \rightarrow |5^2P_{3/2}, F' = 2\rangle$ transition. This scheme is in principle also valid for the cooling of ^{39}K, however, due to the significantly smaller level splitting between the hyperfine sublevels of the $|4^2P_{3/2}\rangle$ state of ^{39}K, the roles of the cooling light and the repumping light are not as clearly defined. As can be seen in fig. 4.2, the splitting between the $|4^2P_{3/2}, F' = 3\rangle$ and the $|4^2P_{3/2}, F' = 2\rangle$ states is only 21.1 MHz. The typical detunings Δ that are necessary to achieve efficient Doppler cooling of atoms, are on the same scale (in our

experiment, Δ ranges from $\Delta \approx -40\,\mathrm{MHz}$ to $\Delta \approx -20\,\mathrm{MHz}$). Thus, the assumption of a closed transition $|4^2S_{1/2}, F = 2\rangle \rightarrow |4^2P_{3/2}, F = 3\rangle$ is by no means valid in this situation. Conversely, the amount of atoms decaying into the $|4^2S_{1/2}, F = 1\rangle$ state is significantly larger for ^{39}K than for ^{87}Rb and a much higher intensity of the repumping light is needed. As a second consequence, the distinction between cooling and repumping light is rather arbitrary, since both beams need to be red-detuned to their respective transition frequencies in order to provide sufficient Doppler cooling, and the detuning is in general larger than the hyperfine splitting of the excited state.

In our experiment, we observe the magneto-optical cooling and trapping of ^{39}K to be less efficient than that of ^{87}Rb. One reason for this difference is the smaller hyperfine splitting of the $|4^2P_{3/2}\rangle$ state for ^{39}K, which necessitates the use of more repumping light. A second reason could be a larger partial pressure of ^{87}Rb in the MOT chamber due to its higher vapor pressure at room temperature [165]. In order to trap and cool enough ^{39}K atoms, the duration of the MOT for ^{39}K is typically on the order of 10 s, while the light for the ^{87}Rb MOT is only switched on during the last few seconds, which is long enough to load a sufficient amount of ^{87}Rb atoms.

4.2.1 Laser Setup for ^{87}Rb

The laser setup that provides the frequency stabilized light for the magneto-optical trap for ^{87}Rb consists of three laser. One of the lasers, the reference and imaging laser, is stabilized to a Doppler free absorption spectroscopy [166]. This laser is not used for the MOT, but provides some of the resonant light used in the spin-polarization phase (see below) and the imaging of ^{87}Rb in later stages of the experiment. The laser that provides the cooling light is a tapered amplifier laser, seeded by a diode laser, that produces an output power on the order 1 W, while the repumping laser is a diode laser with an output power on the order of 50 mW. Both these lasers are frequency stabilized by overlapping a small portion of their light with separate beams from the reference laser and detecting the combined light on photo diodes. This allows to detect the frequency difference between the lasers as a beating signal of the measured intensity, which can be used as a feedback signal for the lock electronics.

4.2.2 Laser Setup for ^{39}K

We employ a similar frequency stabilization scheme for the ^{39}K laser setup. In this case, a dedicated reference laser, whose only purpose is to provide a reference signal, is stabilized to a Doppler free absorption spectroscopy. The light for the MOT is provided by two tapered amplified lasers, with output powers on the order of 1W each, which are stabilized to the reference laser as described above. The light used for imaging ^{39}K as well as some of the light used in the spin-polarization sequence

is provided by a third laser, a diode laser with an output power on the order of 50 mW, which is also stabilized to the reference laser.

4.3 Magnetic Transport and Evaporation in a Plugged Quadrupole Trap

4.3.1 Magnetic Trapping and Spin Polarization

In order to magnetically trap both ^{87}Rb and ^{39}K, the atoms need to be in a low field seeking state, i.e. a state whose energy increases when the magnetic field increases. In the $|^2S_{1/2}\rangle$ states of these atoms, both the $|F=1\rangle$ and the $|F=2\rangle$ hyperfine states exhibit Zeeman sublevels which are magnetically trappable. For weak magnetic fields, the change of potential energy due to the field is given by:

$$E_{\mathrm{mag}} = g_F m_F \mu_B |\mathbf{B}(\mathbf{r})|, \tag{4.1}$$

where the g_F is the Landé g-factor for the hyperfine state F, m_F the Zeeman sublevel, μ_B is Bohr's magneton and $\mathbf{B}$ denotes the magnetic field. For $dE_{\mathrm{mag}}/dB > 0$, the atoms can be trapped in a local minimum of a magnetic field. Such a local minimum can be easily created by superimposing the magnetic fields created by two coils with counter-propagating currents (anti-Helmholtz configuration) [167].

In our experiments, we magnetically trap both the ^{87}Rb atoms as well as the ^{39}K atoms in the $|^2S_{1/2}, F=1, m_F=-1\rangle$ states. In order to transfer the atoms into these states after the cooling in the MOT and a short optical molasses phase [156], we use a spin polarization sequence that is similar for both ^{87}Rb and ^{39}K. We apply a homogeneous magnetic field along the vertical axis, to ensure a fixed quantization axis for atomic transitions, and shine in circularly polarized light along this direction. The light is resonant to the $|^2S_{1/2}, F=1\rangle \rightarrow |5^2P_{3/2}, F'=1\rangle$ transition and the polarization is chosen so that $m'_F = m_F - 1$, which drives the population into the states with smaller m_F. As it is possible that atoms start in, or decay into, the $|^2S_{1/2}, F=2\rangle$ states, a second laser is used that is resonant to the $|^2S_{1/2}, F=2\rangle \rightarrow |^2P_{3/2}, F'=2\rangle$ transition. This laser is left on for a slightly longer time at the end of the spin polarization sequence, which ensures that all population ends up in the $|^2S_{1/2}, F=1\rangle$ states. While we can not transfer atoms with 100% efficiency into the $|F=1, m_F=-1\rangle$ state, atoms in states with $m_F = 0$ or $+1$ are not magnetically trappable and do not remain in the system.

4.3.2 Magnetic Transport

After the spin polarization sequence, the current in the coils above and below the MOT chamber is turned on rapidly in an anti-Helmholtz configuration, which creates

the magnetic quadrupole field used for the trapping. The atoms are then transported through the differential pumping stage by moving the magnetic minimum in space using the fields created by multiple pairs of coils along the transport path. By carefully manipulating the currents in these overlapping coils, the atoms can be transported smoothly around the corner and into the glass cell, where they are finally trapped in the magnetic field created by the quadrupole coils (see fig. 4.1). For more details about this transport process, please refer to [91, 92].

4.3.3 Evaporative and Sympathetic Cooling

The effect of evaporative cooling is often illustrated by envisioning a steaming pot of coffee. Here, the hottest molecules transition from the liquid phase into the gaseous phase, which allows them to leave the system. The remaining molecules rethermalize by colliding with each other. As the molecules that leave the system have an energy higher than the average energy of all particles, the temperature after rethermalization is lower than the initial temperature. This example illustrates the two mechanisms that need to be present in order to efficiently cool atoms using evaporation, namely interactions to ensure thermalization and a way to remove the particles with the largest energies from the system. Evaporation as a means of cooling trapped atoms was first suggested and realized in the context of magnetically trapped hydrogen [168, 169] and has been used in every experiment that reached quantum degenerate regimes with neutral atoms to date.

In our setup, it is much easier to trap large amounts of ^{87}Rb atoms and their number at the beginning of the evaporative cooling phase is typically more than a factor of 100 larger than the number of ^{39}K atoms. However, we want to conduct our experiments in optical lattices using ultracold ^{39}K and thus have to make sure that we retain the largest amount of ^{39}K possible during evaporative cooling. We thus rely on sympathetic cooling, where we mainly evaporate ^{87}Rb atoms and rely on thermalization between ^{87}Rb and ^{39}K to cool the ^{39}K atoms, a technique that has already been shown to work reliably with ^{87}Rb and ^{39}K in other experiments [170, 171].

4.3.4 Forced Evaporation in a Magnetic Trap

For evaporative cooling in trapping potentials with a finite depth, as it is the case for optical dipole traps (see section 4.4), any particle can leave the trapping potential as soon as it has an energy that is larger than the potential depth. The situation is different for atoms trapped in magnetic quadrupole fields. At typical field strengths required to produce a dense cloud of atoms, the potential depth can be thought of as being effectively infinity and atoms can not simply leave the trap when they have a large energy. Instead, a mechanism for forced evaporation is introduced that allows to selectively remove atoms with large energies from the system. This

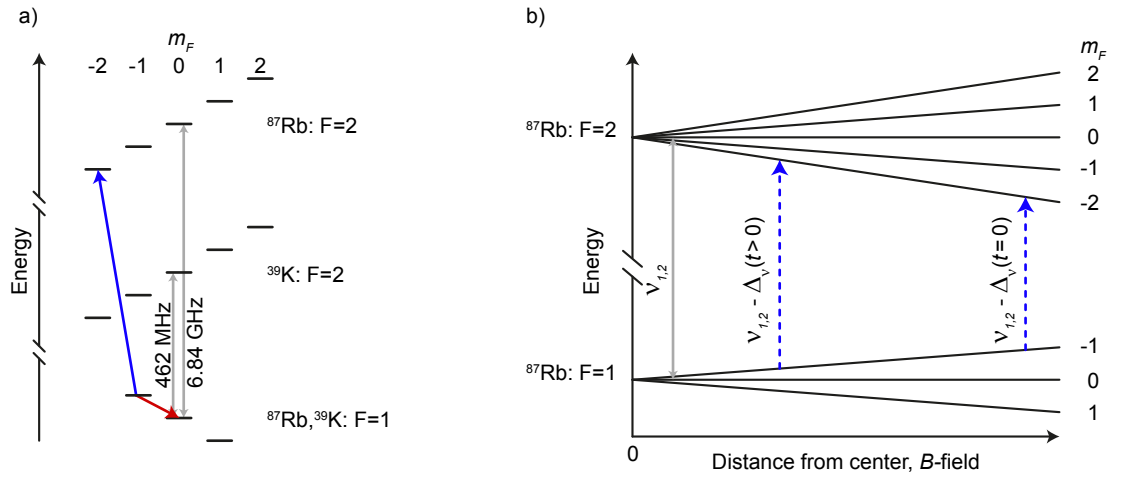

Figure 4.3: a): Zeeman splitting of the $F = 1$ and $F = 2$ hyperfine states of ^{87}Rb and ^{39}K. The red arrow indicates the RF transition that can be used for evaporative cooling and the blue arrow the MW transition, which, in addition to being sensitive to the B-field, is also species selective. b): Schematic depiction of the spatially varying resonance frequency for MW transitions at two different times t during the evaporation (dashed arrows). The gray arrow shows the transition frequency at $B = 0$.

is done by introducing electromagnetic radiation that drives transitions between the trapped and untrapped ($dE_{\mathrm{mag}}/dB < 0$) internal states of the atoms. The resonance frequency of these transitions depends on the magnetic field strength and by choosing appropriate frequencies, we can selectively remove atoms from the trap a certain positions in the field. This method is commonly referred to as radio frequency (RF)-evaporation and was first demonstrated in [172]. It was used in all the early realizations of Bose-Einstein condensates of ultracold atoms [8–10] and is still used in the vast majority of experiments dealing with ultracold quantum gases to date.

For ^{87}Rb, there are two possible types of transitions that can be used to selectively transfer atoms into magnetically untrapped states and thus force their evaporation. In figure 4.3a, we show the splitting of the Zeeman sublevels at a fixed magnetic field for the $F = 1$ ground state of ^{39}K and ^{87}Rb as well as the splitting of the respective $F = 2$ hyperfine states. The different signs of E_{mag}/dB in the $F = 1$ and $F = 2$ are determined by g_F, which is $-1/2$ in the $F = 1$ state and $+1/2$ in the $F = 2$ state. One possibility would be to drive a transition from the $|F = 1, m_F = -1\rangle$ state to the $|F = 1, m_F = 0\rangle$ state (red arrow), using a radio frequency field with a frequency of $\nu_{\mathrm{RF}} = 1/(2h)\mu_B|B(r)|$, where $B(r)$ is the field at a distance r from the center of the trap. While this transition would allow to selectively remove atoms from the

trap at positions with a certain B-field value, the Zeeman splitting is the same for ^{87}Rb and ^{39}K, and we would thus evaporate both kinds of atoms indiscriminately. As discussed above, we are interested in evaporating only the ^{87}Rb atoms, and it is possible to do so by making use of the different hyperfine splitting between the $|F = 1, m_F = -1\rangle$ and $|F = 2, m_F = -2\rangle$ states of the two atoms. When driving a transition between these two hyperfine states for ^{87}Rb (blue arrow), the transition frequency is given by $\nu_{\mathrm{MW,Rb}} = -3/(2h)\mu_B|B(r)| + 6.83\,\mathrm{GHz}$, while for ^{39}K, it would be $\nu_{\mathrm{MW,K}} = -3/(2h)\mu_B|B(r)| + 462\,\mathrm{MHz}$. This allows for selectively evaporating ^{87}Rb atoms with a certain potential energy (given by their position in the B-field), without driving transitions for the ^{39}K atoms, which remain in the $|F = 1, m_F = -1\rangle$ state throughout the evaporation.

The evaporation itself is conducted by introducing microwave (MW) radiation into the system with a time dependent frequency $\nu_{\mathrm{MW}} = \nu_{1,2} - \Delta_\nu(t)$. $\nu_{1,2}$ is the transition frequency between the two hyperfine states without an external magnetic field, given by $\nu_{1,2} = 6.834682\,\mathrm{GHz}$ [173] and $\Delta_\nu(t)$ is the time dependent detuning that determines the magnetic field value B, at which the transition is resonant. At the beginning of the evaporation ($t = 0$), we start with a large detuning, and transitions are driven at large magnetic field, far away from the center of the trap (see figure 4.3b). During the course of approximately 9 s of evaporation, $\Delta_\nu(t)$ is slowly decreased and the point where transitions occur moves towards positions where the atoms have lower potential energy, leading to colder and colder atoms being left in the center of the trap.

After evaporative cooling in the quadrupole trap, we typical obtain on the order of a few 10^6 ^{87}Rb atoms and about $1 \cdot 10^6$ ^{39}K atoms at temperatures of a few μK.

4.3.5 Plugged Quadrupole Trap

In order for the atoms to stay trapped in a magnetic quadrupole potential, it is necessary that their magnetic moment adiabatically follows the magnetic field vector. This is given as long as the rate of change of the magnetic field direction Φ satisfies [49]

$$\frac{d\Phi}{dt} < E_{\mathrm{mag}}/\hbar \equiv \omega_L. \tag{4.2}$$

If this condition is violated, however, the atoms can undergo spin-flips, so called "Majorana flops" [174] into untrapped magnetic states and are lost from the trap [167]. In a purely magnetic quadrupole potential, condition 4.2 is always violated in the center of the trap, where the B-field is zero but increases linearly in all directions [175]. The Majorana losses become particularly important when the atoms reach low temperatures, and the density becomes large in the center of the trap. In our experiment, we circumvent these losses by adding an additional repulsive potential in the center of the magnetic quadrupole field. This is done by shining a tightly focused blue-detuned laser beam (wavelength $\lambda_p \approx 760\,\mathrm{nm}$) through the center of the

trap, as first demonstrated in [10], which creates a local potential energy maximum (see next section) and prevents atoms from entering the region of low magnetic field.

4.4 Optical Dipole Traps

4.4.1 Optical Dipole Potentials

We can not only use dissipative forces introduced by near resonant light to trap atoms, but also the conservative forces exerted on neutral atoms by light that is far detuned to the atomic transition. These forces arise from the interaction between the light and the light-induced dipole moments of the neutral atoms. The possibility of using such optical dipole forces for the manipulation of neutral atoms was already suggested in [176, 177] and in [178], it was first experimentally demonstrated that they can be used to trap neutral atoms. Since then, optical dipole potentials have become a standard tool for the trapping and manipulation of neutral atoms [156, 179].

In a semi-classical oscillator model, the potential created by a laser beam with frequency ω_D that is detuned by $\Delta = \omega_D - \omega_0$ from the atomic transition frequency ω_0 of a two-level atom is given by [179]

$$V_{\mathrm{dip}}(\mathbf{r}) \approx \frac{3\pi c^2}{2\omega_0^3}\frac{\Gamma}{\Delta} I(\mathbf{r}), \tag{4.3}$$

where c is the speed of light, Γ is the natural linewidth of the atomic transition, and $I(\mathbf{r})$ is the light intensity at position $\mathbf{r}$. The residual scattering rate for absorption processes is given by

$$\Gamma_{\mathrm{sc}} \approx \frac{3\pi c^2}{2\hbar\omega_0^3}\left(\frac{\Gamma}{\Delta}\right)^2 I(\mathbf{r}). \tag{4.4}$$

The optical dipole potential is thus proportional to the intensity $I(\mathbf{r})$ and inversely proportional to the detuning Δ. The residual scattering rate, which causes a heating of the atoms in the dipole potential due to a momentum transfer between the photons and the atoms in the absorption and spontaneous emission processes involved, is also proportional to $I(\mathbf{r})$, but inversely proportional to Δ^2. In order to minimize the heating rates it is thus favorable to work at detunings that are as large as possible. However, as also the intensity of the laser has to be increased at larger detunings, in order to reach sufficient potential depths, the choice of suitable lasers is limited. In our experiments, we use two lasers with a wavelength $\lambda_{\mathrm{D}} \approx 1064\,\mathrm{nm}$ and a combined output power of approximately 46 W to create the optical dipole potentials used for trapping the atoms.

For alkaline atoms like ^{87}Rb and ^{39}K, there are typically two transition lines with optical frequencies in the near-infrared regime. For ^{87}Rb, the D_2 line, which is

used for the magneto optical cooling, corresponds to light with a wavelength of $\lambda_{D2}^{\mathrm{Rb}} \approx 780.2\,\mathrm{nm}$ [180] while the D_1 line of the transition from the $5^2S_{1/2}$ to the $5^2P_{1/2}$ state corresponds to a wavelength of $\lambda_{D1}^{\mathrm{Rb}} \approx 795.0\,\mathrm{nm}$ [181]. The situation is similar for ^{39}K, where $\lambda_{D2}^{\mathrm{K}} \approx 766.7\,\mathrm{nm}$ and $\lambda_{D1}^{\mathrm{K}} \approx 770.1\,\mathrm{nm}$ [182]. For wavelengths of our optical dipole traps around $\lambda_{\mathrm{D}} \approx 1064\,\mathrm{nm}$, this results in slightly different contributions from the two lines and eq. 4.3 has to be extended to incorporate the two transitions. The hyperfine splitting of the two lines themselves, however, is small enough so that the detuning can be assumed as constant and the individual transitions between the various hyperfine states can be summed up into a common transition linewidth Γ. The contributions of the two fine-structure lines can then be summed into a combined potential as [179]

$$V_{\mathrm{dip}}(\mathbf{r}) = \frac{1 - \mathcal{P} g_F m_F}{3} V_{\mathrm{Dip},D1} + \frac{2 + \mathcal{P} g_F m_F}{3} V_{\mathrm{Dip},D2}, \tag{4.5}$$

Where $V_{\mathrm{Dip},D1}$ and $V_{\mathrm{Dip},D2}$ are the dipole potentials of eq. 4.3 for the parameters of the D_1 and D_2 line, respectively. $\mathcal{P}$ is a polarization factor that is 0 for linear polarization and ± 1 for $\sigma^{\pm}$ polarization, respectively.

4.4.2 Gaussian Beams as Dipole Traps

For red-detuned beams, i.e., $\Delta < 0$, the Potential created by a laser beam is attractive and the potential energy of the atoms decreases with increasing intensity $I(\mathbf{r})$. Thus, atoms can be trapped in local maxima of the light intensity, which can in principle already be created by a single focused laser beam. The intensity profile of a focused laser beam, propagating along the x direction, is given by

$$I_x(\mathbf{r}) = \frac{2P}{\pi w_y(x) w_z(x)} e^{\left(-\frac{2y^2}{w_y^2(x)} - \frac{2z^2}{w_z^2(x)}\right)}, \tag{4.6}$$

where P is the total power of light in the beam, and w_y and w_z are the radii of the beams, defined as the distance from the beam axis where the intensity drops to $1/e^2$ of the intensity on the axis.

For a Gaussian beam, $w_{y,z}$ vary along the propagation direction x as

$$w_{y,z}(x) = w_{0;y,z} \sqrt{1 + \left(\frac{x}{R_{y,z}}\right)}. \tag{4.7}$$

$w_{0;y,z}$ are the beam radii in the focus of the beam, i.e., the smallest radii the beam reaches along the respective direction during its propagation, and are referred to as

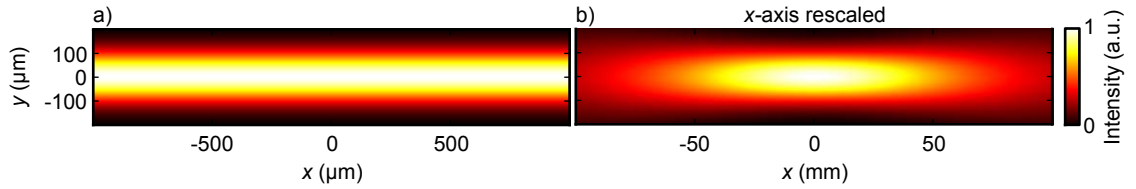

Figure 4.4: a) Intensity distribution at $z = 0$ of a Gaussian beam propagating along x with beam waist $w_{0,y} = 150\,\mu$m and $\lambda_D = 1064\,$nm. b) The same intensity distribution as in a), but the x-axis is scaled by a factor of 100.

the beam waists. $R_{y,z}$ are the so-called Rayleigh lengths, given by

$$R_{y,z} = \frac{\pi w_{0;y,z}^2}{\lambda_D}, \tag{4.8}$$

which determines how quickly the beam diverges after reaching its smallest extension.

Figure 4.4a shows the intensity distribution at $z = 0$ of a Gaussian beam with beam waist $w_{0,y} = 150\,\mu$m and wavelength $\lambda_D = 1064$nm. While the Gaussian shape of the beam along the y-direction can be clearly observed, the intensity decay along the x-direction becomes only visible when rescaling the x-axis by a factor of 100 (fig. 4.4b).

We can use a Taylor expansion around the point of largest intensity to approximate the potential created by the beam as

$$V_x(\mathbf{r}) \approx V_{0,x}\left(1 - \frac{1}{2}\left(\frac{x}{R_y}\right)^2 - \frac{1}{2}\left(\frac{x}{R_z}\right)^2 - 2\left(\frac{y}{w_{0,y}}\right)^2 - 2\left(\frac{z}{w_{0,z}}\right)^2\right). \tag{4.9}$$

This results in trapping frequencies for atoms of mass m given by

$$\omega_x = \sqrt{\frac{V_0}{m}\left(\frac{1}{R_y^2} + \frac{1}{R_z^2}\right)}, \tag{4.10}$$

$$\omega_{y,z} = \sqrt{\frac{4V_0}{m w_{0;y,z}^2}}. \tag{4.11}$$

As the Rayleigh length is typically much larger than the beam waists (see fig. 4.4), a single gaussian beam provides a much smaller confinement along its propagation axis. In order to create trapping potentials that are more isotropic, multiple beams can be overlapped to create combined optical dipole potentials.

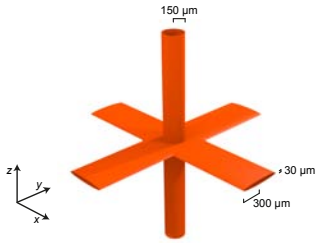

Figure 4.5: Schematic layout of the three optical dipole trap beams with their beam waists indicated by the labels.

4.4.3 Crossed Optical Dipole Trap

In our experiment, we use a dipole trap configuration that consists of three laser beams propagating along mutually orthogonal axes. The individual focal points of these beams meet at one point in space, where the combined optical dipole potential of the three beams creates the confinement used for trapping the ^{87}Rb and ^{39}K atoms after the evaporative cooling in the magnetic quadrupole trap. In order to prevent inteference between two beams originating from the same laser, their polarizations are chosen to be linear and mutually orthogonal and a frequency offset of approximately 160 MHz is introduced using acousto-optical modulators.

The beams propagating along the horizontal (x, y) axes both have beam waists of approximately 30 μm along the vertical (z) and 300 μm along the horizontal axes. The beam propagating along the z direction is cylindrically symmetric with a beam waist of approximately 150 μm. The layout of these beams is shown schematically in figure 4.5. The small beam waists along the vertical axis create a large trap frequency along this direction, which minimizes the differential gravitational sag introduced due to the different masses of ^{87}Rb and ^{39}K atoms [92]. The beam waist of the vertical dipole trap beam is chosen to be identical to the beam waists of the optical lattice beams, in order to be able to compensate the global potentials caused by the lattice, which is necessary for the creation of homogeneous systems (see chapters 5.1.2 and 6.3.1).

The atoms are transferred from the magnetic quadrupole trap into the dipole trap by simultaneously increasing the laser intensities of the dipole trap beams and reducing the currents in the anti-Helmholtz coils. A homogeneous magnetic field along the vertical axis is simultaneously ramped up which shifts the point of zero field along the plug beam and out of the trap region and we can turn off the plug laser beam once the atoms are confined by the dipole trap. This field also serves as a quantization axis for the atoms in order to preserve the spin polarization.

After loading the atoms into a deep optical dipole trap, we transfer all atoms from the $|F = 1, m_F = -1\rangle$ state into the $|F = 1, m_F = 1\rangle$ state using an adiabatic RF sweep, which, due to the identical level splitting between the magnetic sublevels, works simultaneously for ^{87}Rb and ^{39}K. We then reduce the trap depth over a time

span of approximately 4 s, which results in evaporative cooling. Due to the influence of the gravitation potential, the trap depths is lowest along the direction of gravity, and atoms are predominantly expelled from the trap in this direction. This also facilitates the desired sympathetic cooling in the final stages of the evaporation where we aim to predominantly evaporate the ^{87}Rb atoms. As the mass of ^{87}Rb is more than twice as large as that of ^{39}K, for low enough dipole trap intensities the larger gravitational force on ^{87}Rb significantly increases its evaporation [92].

4.5 Feshbach Resonances of ^{87}Rb and ^{39}K

During the evaporative cooling in the dipole trap, it is useful to be able to control the interaction strength between the atoms in order to ensure a fast thermalization while preventing losses due to three-body collisions. The interaction between atoms in the low energy limit, where only s-wave collisions are relevant, can be characterized by the s-wave scattering length a_s that determines the scattering amplitude (see, e.g., [183]), and the scattering cross section between the atoms is proportional to a_s^2. In the Bose-Hubbard model, the interaction parameter U is directly proportional to a_s (see eq. 2.19) and for $a_s < 0$, there is an attractive interaction between two atoms, leading to a decrease in energy when multiple atoms occupy the same lattice site, while for $a_s > 0$, the interaction is repulsive.

In certain cases, it is possible to change the scattering length between two atoms by modifying the energy of the last bound states supported by the interaction potential. This possibility was first noted in [32, 33], and the resulting resonances that can be observed in the scattering length are generally referred to as Feshbach resonances. In the context of ultracold atoms, the possibility of tuning the scattering length using homogeneous magnetic fields [35], which was first observed in [34], is of particular importance and has become a standard tool in many-body physics with cold atoms [184].

In the presence of a Feshbach resonance, the scattering length is given phenomenologically as a function of the magnetic field B as [185]

$$a_s(B) = a_{\mathrm{bg}} \cdot \left(1 - \frac{\Delta B}{B - B_0}\right), \tag{4.12}$$

where a_{bg} is the unperturbed background scattering length, far away from the Feshbach resonance, B_0 is the resonance position, where the scattering length diverges, and ΔB is the width of the resonance, given by the difference in B between the B_0 and the point where $a_s(B) = 0$. For more details on Feshbach resonances in ultracold atomic gases, see, e.g., [184, 185].

Figure 4.6a shows such a Feshbach resonance for scattering between a ^{87}Rb atom in the $|5^2S_{1/2}, F = 1, m_F = 1\rangle$ and a ^{39}K atom, also in the $|4^2S_{1/2}, F = 1, m_F = 1\rangle$

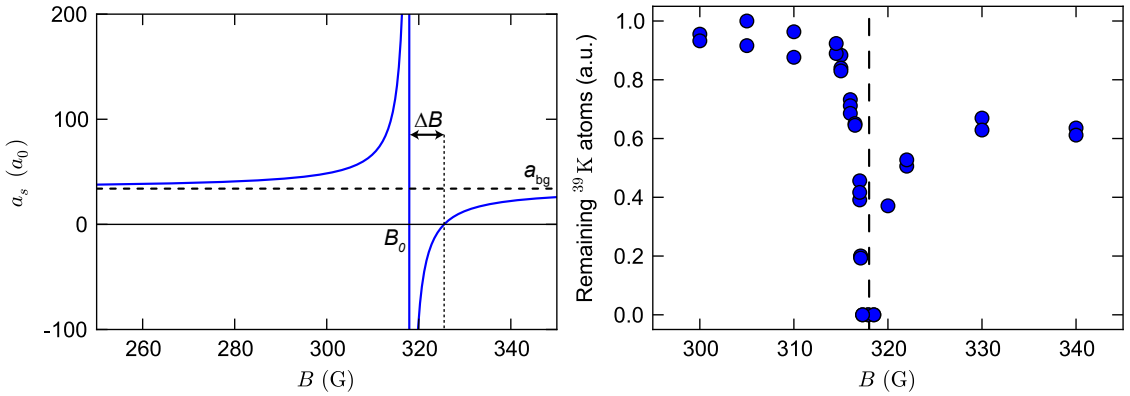

(a) Inter-species Feshbach resonance for ^{87}Rb and ^{39}K in the absolute ground state.

(b) Qualitative measurement of B_0 by observing the three-body losses at varying magnetic fields.

Figure 4.6: Inter-species Feshbach resonance for ^{87}Rb and ^{39}K in the absolute ground state.

state, using the parameters predicted in [186]. The resonance position is at $B_0 = 318 \pm 3\,\mathrm{G}$, $\Delta B = 7.6\,\mathrm{G}$ and $a_{\mathrm{bg}} = 28.7 \pm 0.5\,a_0$, where a_0 is Bohr's radius. In figure 4.6b, we show a qualitative measurement of the resonance position. The measurement is conducted using ^{87}Rb and ^{39}K in an optical dipole trap. The magnetic field B is ramped to various values and then kept constant for a few ms. As the rate of inelastic three-body collisions at large scattering lengths scales with a_s^4 [187], the position of the Feshbach resonance is indicated by strongly enhanced losses that are observed in our measurement by monitoring the number of ^{39}K atoms left after the hold time. The vertical dashed line indicates the prediction of $B_0 = 318\,\mathrm{G}$, which agrees well with the position of the observe loss resonance.

During the major part of the evaporation, the magnetic field is set to $B \approx 314\,\mathrm{G}$, which results in an inter-species scattering length between ^{87}Rb and ^{39}K of $a_s \approx 100\,a_0$, sufficiently large to ensure a fast thermalization of the two species while low enough to prevent excessive three-body losses.

At the later stages of the evaporation, most of the ^{87}Rb has left the trap, while the number of ^{39}K atoms stays approximately constant, due to the smaller gravitational sag that prevents their evaporation. At this point, it becomes necessary to change the magnetic field in order to adjust the intra-species scattering length of ^{39}K. The background scattering length between ^{39}K atoms in the absolute ground state ($|4^2S_{1/2}, F = 1, m_F = 1\rangle$) is $a_s = -29.3(0)\,a_0$ [188], resulting in an overall attractive mean field interaction that would lead to a collapse of a ^{39}K condensate above a critical density [189–191]. In order to prevent this collapse, we can use an intra-species Feshbach resonance for ^{39}K at 402.5(3) G that has a width of $\Delta B = -52.1(1)\,\mathrm{G}$ [46]. Figure 4.7a shows the behavior of a_s for varying B around the Feshbach resonance

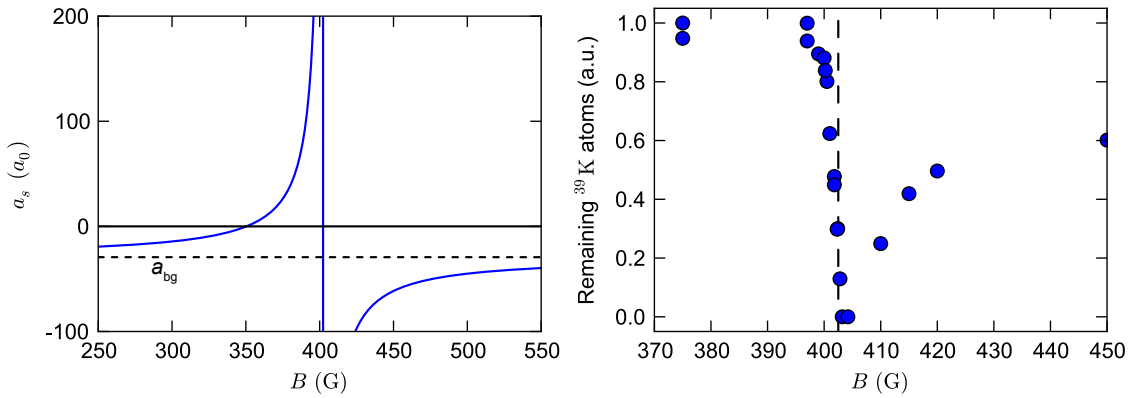

(a) Intra-species Feshbach resonance for ^{39}K in the absolute ground state.

(b) Qualitative measurement of B_0 by observing the three-body losses at varying magnetic fields.

Figure 4.7: Intra-species Feshbach resonance for ^{39}K in the absolute ground state.

and figure 4.7b shows a measurement similar to that shown in figure 4.6b, but in this case without ^{87}Rb present in the experiment. The loss resonance again shows a good qualitative agreement with the position of the Feshbach resonance, indicated by the dashed vertical line.

We typically conduct the final part of the evaporative cooling at a magnetic field of $B \approx 395.5\,\mathrm{G}$, which corresponds to an intra-species scattering length for ^{39}K of $a_s \approx 189\,a_0$.

4.6 Bose-Einstein Condensates of ^{39}K

After the full evaporation cycle, which takes about 30 s, we can create Bose-Einstein condensates of ^{39}K in the optical dipole trap that contain typically on the order of 10^5 atoms with no thermal component visible in absorption images after time-of-flight (TOF, see chapter 5.2.1 for details about the imaging process). As an example, we show images of condensates of ^{39}K released from an optical dipole trap with trap frequencies $\omega_x \approx \omega_y \approx 10\,\mathrm{Hz}$ and $\omega_z \approx 140\,\mathrm{Hz}$, imaged using absorption imaging after 16 ms TOF. The shape of the cloud after the expansion during TOF shows the characteristic inversion of the shape of the initial density distribution expected for Bose-Einstein Condensates. The dipole trap from which the atoms are released has a much larger trap frequency along the vertical direction, leading to an increased curvature of the initial wavefunction and thus a much broader momentum distribution along this axis. Before releasing the atoms from the dipole trap, the interaction was changed using the ^{39}K intra-species Feshbach resonance. The effects of increasing repulsive interactions can be observed in the broadening of the cloud for large a_s, as the increased mean-field energy of the atoms is converted into kinetic

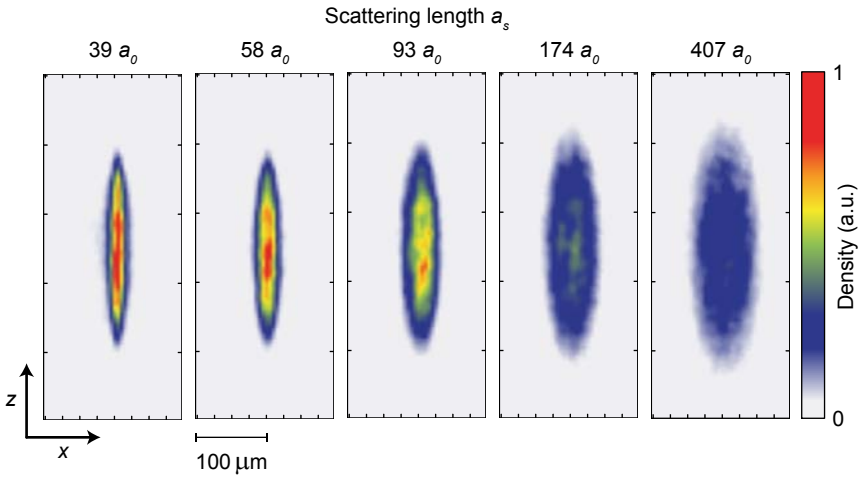

Figure 4.8: Bose-Einstein condensates of about 10^5 ^{39}K atoms after 16 ms TOF, released from an optical dipole trap with trap frequencies $\omega_x \approx \omega_y \approx 10\,\text{Hz}$ and $\omega_z \approx 140\,\text{Hz}$ at varying scattering length a_s.

energy during an expansion.

Chapter 5

Ultracold Atoms in Optical Lattices

In this chapter, we discuss how to use optical lattices in experiments with ultracold atoms to realize the Bose-Hubbard Hamiltonian and how we can independently control all of its parameters. We review the properties of the lattice potentials and methods to properly calibrate them, as well as global potentials created by the lattice beams. We also briefly discuss loss mechanism introduced by the lattice light and methods to minimize these losses. Furthermore, we describe various methods for the detection and characterization of the many-body states in the lattice that rely on directly imaging atomic density distributions using resonant light. Most of the techniques described in this chapter have become standard tools for the manipulation and detection of cold atoms in recent years [62] and we will only discuss the most fundamental aspects relevant in our work. For a more detailed discussion of the techniques employed in our experiment, please refer to [92, 157].

The final part of this chapter briefly presents some results on equilibrium states of ^{39}K that can be created in our setup. Here, we first discuss the observation of the superfluid to Mott insulator transition, driven by changing the lattice depth as well as the interaction strength between the atoms. Finally, we also present our results on the creation of equilibrium states with negative absolute temperatures [192], which relies on the possibility to tune all parameters of the Bose-Hubbard Hamiltonian individually and highlights the flexibility of our experimental setup.

5.1 Optical Lattices

The optical lattices in our experiment are created by retro-reflecting linearly polarized laser beams with a wavelength $\lambda_l \approx 740\,\mathrm{nm}$ created by a titanium-sapphire laser. To create an optical lattice along one axis, a collimated beam is focused onto the atoms, recollimated upon exiting the experimental chamber and finally focused onto a retro reflecting mirror. By focusing the beam onto the retro-reflecting mirror, the propagation of the beam is inverted and the returning beam has approximately the same beam waist as the incoming beam when it reaches the atoms again. To create a three dimensional optical lattice, beams are sent in along all three spatial directions with Gaussian beam waists of approximately $150\,\mu\mathrm{m}$.

5.1.1 Lattice Potentials

The superposition of two counter-propagating running waves, traveling along the x and $-x$ directions, creates a standing wave with an intensity distribution

$$I_{1\mathrm{D}}(x,y,z) = I_x e^{-2\frac{y^2+z^2}{w_x^2}} \cos^2(kx), \tag{5.1}$$

where $k = 2\pi/\lambda_l$. The maximum intensity (for a perfectly reflecting retro-mirror and no losses during the beam propagation) is given by $I_x = 4I_0$, where I_0 is the intensity of the incoming beam. The term $\exp(-2(y^2+z^2)/w_x^2)$ describes the Gaussian shaped intensity distribution of the beam perpendicular to the propagation direction (see chapter 4.4.2). Here, we assume the Rayleigh length to be much larger than w_x so that we can assume w_x to be constant over the extension of the cloud of atoms. Superimposing three standing waves along three perpendicular directions then leads to a 3D periodic potential of the form

$$\tilde{V}_{3\mathrm{D}}(\mathbf{r}) = \tilde{V}_x e^{-2\frac{y^2+z^2}{w_x^2}} \cos^2(kx) + \tilde{V}_y e^{-2\frac{x^2+z^2}{w_y^2}} \cos^2(ky) + \tilde{V}_z e^{-2\frac{x^2+y^2}{w_z^2}} \cos^2(kz), \tag{5.2}$$

where the potential depths $\tilde{V}_{x,y,z}$ can be determined from the intensity of the light as discussed in chapter 4.4.1. Cross interference between lattice beams along perpendicular axes is avoided by adjusting the polarization of the individual laser beams to be linear along mutually orthogonal directions. Furthermore, a frequency difference between the three laser beams on the order of tens of MHz is introduced using acousto-optical modulators (AOMs). Any residual cross interference between the beams, caused by imperfections in the polarization, thus oscillates with a large frequency and averages out on the dynamical time scales relevant for atoms in the optical lattice.

The potential depth $\tilde{V}_{x,y,z}$ along the different directions is determined from the intensities of the laser beams along the respective directions and the detuning of the lasers with respect to the atomic transitions, as discussed in chapter 4.4. We typically state the potential in units of the recoil energy $E_r = \hbar^2 k^2/(2m)$, where m is the atomic mass. In cases where we want to refer to the specific E_r of one of the atomic species, E_r^K refers to the recoil energy for ^{39}K and E_r^{Rb} to that for ^{87}Rb. As we are only dealing with blue-detuned lattices in the scope of this thesis, we can assume all $\tilde{V}_{x,y,z}$ to be positive. The Wannier states in such a lattice are thus centered around the nodes of the standing-wave potential, where the intensity is minimal.

The geometry of the created lattices is determined by the ratio of the individual potential depths $\tilde{V}_{x,y,z}$. In particular, it is possible to create effectively 1D and 2D lattice geometries by choosing some intensities very large to suppress tunneling along certain directions. This is demonstrated in figure 5.1, which shows the potential energy isosurfaces of lattices with varying intensities along the three spatial

directions.

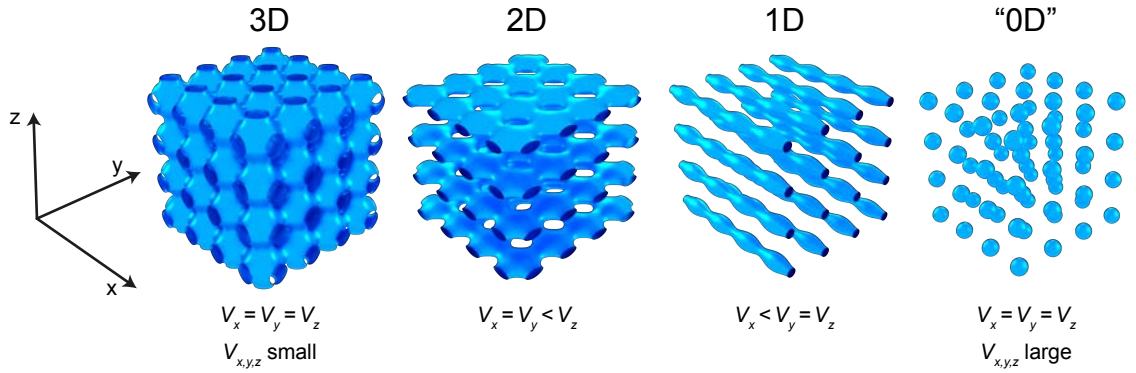

Figure 5.1: Isosurfaces of lattice potentials for varying depths $V_{x,y,z}$ of the individual lattice axes.

For $V_x = V_y = V_z$, the lattice structure is that of a 3D cubic crystal, where the atoms can tunnel equally along all three directions. If the intensity is now strongly increased along one direction (here: $V_x = V_y < V_z$), the tunneling is inhibited along this direction and the system effectively decouples into a stack of 2D lattices. If two lattices are very strong compared to the third ($V_x < V_y = V_z$), only tunneling along one direction is relevant and the system is further decoupled into an array of individual 1D systems. If all three beams have the same, but very large, intensity, tunneling is suppressed along all directions. The system then has the same cubic crystal structure as in the 3D case, but all individual wells are decoupled and no tunneling dynamics take places. Note that the difference between the 3D configuration and the effectively "0D" configuration in figure 5.1 is only the time scale for tunneling in the lattice. But as this time scale can be made large compared to the duration of the experiments, we can regard the tunneling dynamics as essentially frozen out.

In the experimental realization, the intensity of the incoming and the retro-reflected beams are not exactly equal. Due to reflection and absorption by optical elements in the beam path as well as a sub-unity reflectivity of the retro mirror, the incoming intensity I_{in} is always slightly higher than the retro-reflected intensity I_{re}, which decreases the contrast of the sinusoidal lattice potential.

With $R_x = I_{\mathrm{re},x}/I_{\mathrm{in},x}$, the intensity distribution of a single lattice beam pair along, e.g., x is then given by

$$V(x,y,z) = \frac{V_x}{4} e^{-2\frac{y^2+z^2}{w_x^2}} \left(1 + R_x - 2\sqrt{R_x} + 4\sqrt{R_x}\cos^2(kx)\right). \tag{5.3}$$

Thus, the lattice depth relevant for the tunneling dynamics of atoms in our ex-

periments is given by

$$V_x = \sqrt{R_x}\tilde{V}_x. \tag{5.4}$$

5.1.2 Global Potentials

Not only is the effective depth of the sinusoidal potential reduced when $R_x < 1$, but the potential also does not vanish anymore in the nodes of the standing wave. At the points where $\cos^2(kx) = 0$, e.g. $x = \pi/(2k)$, the overall potential along y and z is given by

$$V(y,z) = \frac{V_x}{4} e^{-2\frac{y^2+z^2}{w_x^2}} \left(1 + R_x - 2\sqrt{R_x}\right) \tag{5.5}$$

and results in an overall anti-confining Gaussian potential along the y- and z-direction. Note that for large $R \lesssim 1$, this anti-confining potential is much weaker than the corresponding confining potential for red-detuned lattices, where the positions of the atoms inside the wells are centered around the points of maximum intensity.

We can use a harmonic approximation to obtain an effective trap frequency of this global potential along the axes perpendicular to the propagation direction, which is given by

$$\omega_{y,z}^2 = \frac{4}{m} \frac{(-\tilde{V}_x(1 + R_x - 2\sqrt{R_x})}{w_x^2}. \tag{5.6}$$

In the blue-detuned case, where $\tilde{V_x} > 0$, $\omega_{y,z}^2$ is smaller than zero and the trap frequencies $\omega_{y,z}$ are imaginary, describing overall anti-confining potentials.

The varying lattice depth perpendicular to the propagation direction leads to an additional effective global potential. This can be seen by approximating a lattice well locally with a harmonic potential and calculating the total energy of the ground-state wavefunction. In a harmonic approximation, the trap frequency for an atom of mass m in a sinusoidal potential of the form $V(x) = V_x \cos^2(kx)$ is given by

$$\omega_{\text{latt}}^2 = |V_x| \frac{2k^2}{m}. \tag{5.7}$$

The spatial variation of the lattice depth along the perpendicular direction now decreases the local trap frequencies further away from the center of the beam according to eq. 5.1 as

$$\omega_{\text{latt}}^2(y,z) = e^{-2\frac{y^2+z^2}{w_x^2}} |V_x| \frac{2k^2}{m} \tag{5.8}$$

and thus leads to a variation of the ground state energy of

$$E_{\text{gs}} = \frac{1}{2}\hbar\omega_{latt} \Rightarrow E_{\text{gs}}(y,z) = \frac{1}{2}\hbar e^{-\frac{y^2+z^2}{w_x^2}} \sqrt{|V_x| \frac{2k^2}{m}}, \tag{5.9}$$

which results in a second effectively anti-confining potential. In a harmonic approximation, this potential has an effective trap frequency of

$$\omega_{y,z}^2 = -\frac{2}{m\omega_z^2}\sqrt{|V_x|E_r}. \tag{5.10}$$

This potential is always anti-confining, as the depth of the potential wells always decreases further away from the center of the beam, independent of the detuning of the lattice.

For blue-detuned lattices and reasonable values of R_x, the dominant contribution to the anti-confining global potential is given by eq. 5.10, while eq. 5.6 contributes only very little. For a 3D lattice configuration, the potential along each axes is given by the sum of the global potentials created by the two lattices perpendicular to that axes.

In order to create homogeneous lattice potentials, the overall anti-confining potential created by the blue-detuned lattice beams has to be compensated. In our experiment, this is achieved using the red-detuned dipole trap beams, which are carefully aligned to overlap with the lattice beams. However, as the shapes of the dipole trap beams propagating along the two horizontal directions do not match the shape of our lattice beams, we can only use the dipole trap beam along the vertical axis for a compensation on large scales. As this beam does not create any significant confinement along its propagation direction, compensation in our setup is thus only possible along the horizontal plane. In chapter 6.3.1, we describe the optimization of the homogeneity of the lattice for our expansion experiments in more detail.

5.1.3 Calibration of Lattice Depth

While it is in principle possible to measure the properties of the lattice laser beams accurately, reflection losses as well as the optimal alignment of the beams are hard to determine from direct measurements, and it is not easy to infer the precise lattice depths from the beam intensities. Fortunately, as it is so often the case in experiments dealing with ultracold atoms, we can use the atoms themselves as a probe to determine the depth of the lattice at a given laser intensity.

Frequency Modulation Spectroscopy

For deep lattices, the Bloch bands become very narrow in energy while the energy gap between them becomes large (compare figure 2.1) and we can measure this band gap using a type of parametric excitation spectroscopy [193]. In our case, the frequency of the lattice laser ω_l is weakly modulated using an AOM, such that $\omega_\mathrm{l}(t) = \omega_\mathrm{l}(0) + \Delta\omega \sin(\nu_\mathrm{mod} t)$, where $\Delta\omega$ is typically on the order of a few MHz. As the retro-mirror in our setup constitutes a fixed point in space for the first node of the optical lattice, a changing ω_l leads to a time dependence in the position of the potential wells,

which amounts to a sinusoidal shaking along the lattice direction (see figure 5.2a). When $h\nu_{\mathrm{mod}}$ is equal to the energy difference between the first and the second Bloch band, $h\nu_{\mathrm{mod}} = E_q^{(2)} - E_q^{(1)}$, the atoms are resonantly excited into the higher band. We detect these atoms in time-of-flight imaging using a band mapping technique (cf. 5.2.3). Figure 5.2 shows such a measurement, where we plot the amount of atoms

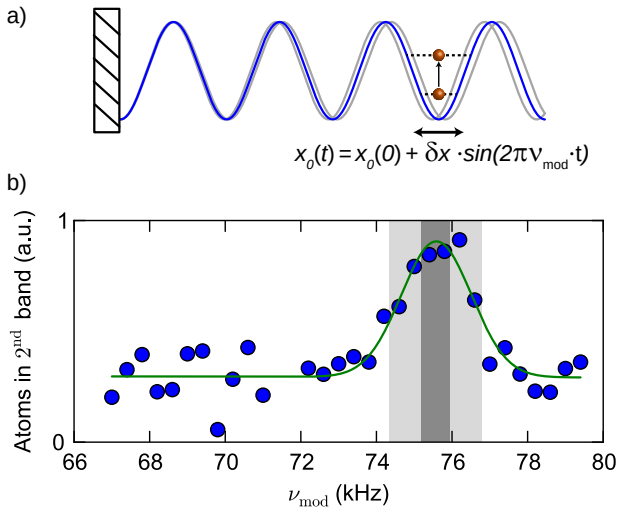

Figure 5.2: a) Sketch of the effects of frequency modulation on the position of the lattice wells. b) Number of ^{87}Rb atoms in the second band for varying modulation frequencies ν_h. The solid line is a Gaussian peak fit function to the observed resonance. The dark gray area indicates the combined bandwidths of the first and second band at a lattice depth $V_x = 27.1\, E_r^{\mathrm{Rb}}$, the light gray area the experimental uncertainty.

in the upper band over the modulation frequency ν_h. We can observe a resonance around 75.6(1.3) kHz, which corresponds to a lattice depth $V_x = 27.1(8)\, E_r^{\mathrm{Rb}}$. The dark gray shaded area indicates the combined bandwidths of the first and second band, given by the difference of the band gaps at quasimomenta $q = 0$ and $q = \pi/d$. A second broadening of the transition results from the finite extension of the atomic cloud within the slightly inhomogeneous lattice. The overall experimental error, given by the width of the Gaussian peak fit function used to determine ν_h, is indicated by the light gray shaded area. This method is only suitable for deep lattices, typically for lattice depths $V_x > 20\, E_r$, where the interband distance is large compared to the bandwidth. For lower lattice depths, the bandwidth increases and at $V_x = 5\, E_r$, the difference between the band gaps at $q = 0$ and at $q = \pi/d$ is approximately half as large as the band gap itself at $q = 0$, rendering this method very inaccurate for small lattice depths.

Lattice Diffraction

For lower lattice depths, we can use a method that relies on the diffraction of the atoms in a pulsed lattice to determine the lattice depth [194]. We start such measurements with a Bose-Einstein condensate of ^{87}Rb in an optical dipole trap and then rapidly switch on the lattice for a brief duration on the order of tens of μs. This leads to a projection of the ground state wavefunction of the BEC, which can be written as a plane wave state $|\phi(t=0)\rangle = |q_0\rangle$ with a momentum $q_0 = 0$, onto the Bloch states $|\Psi_{q_0}^{(n)}\rangle$

$$|\phi(t=0)\rangle = \sum_{n=1}^{\infty} |\Psi_{q_0}^{(n)}\rangle \langle\Psi_{q_0}^{(n)}|q_0\rangle \,. \tag{5.11}$$

A Bloch wave in band n with momentum q can be written in the plane wave basis as

$$|\Psi_q^{(n)}\rangle = \sum_{\mu=-\infty}^{\infty} a_\mu^{(n,q)} e^{\mathrm{i}(q+2k\mu)x} \tag{5.12}$$

(see eq. 2.2 and 2.4) and thus, the projection $\langle\Psi_{q_0}^{(n)}|q_0\rangle = (a_0^{(n,q_0)})^*$. From this, we can deduce that the time evolution after the projection onto the basis of Bloch waves becomes

$$|\phi(t)\rangle = \sum_{n=1}^{\infty} (a_0^{(n,q_0)})^* e^{-\mathrm{i}E_{q_0}^{(n)}t/\hbar} |\Psi_{q_0}^{(n)}\rangle \,. \tag{5.13}$$

By switching off the lattice after an evolution time t_B, the wavefunction is projected back onto the free-space momentum states, given by the plane wave basis states $|q_0 + 2k\mu\rangle$. The time evolution leads to an oscillation of the relative occupation of the plane wave basis states, which can be detected experimentally in time-of-flight (TOF) imaging (see section 5.2.3). Due to the symmetry of the initial state with $q_0 = 0$, only states with the same symmetry can be populated, which lie in bands with odd indices n.

Figure 5.3 shows the oscillation between population in the first and third band, observed in TOF imaging as distinct peaks. The oscillation frequency is given by the energy difference between the $q = 0$ states in the first and the third Bloch band, $\nu_R = (E_0^{(3)} - E_0^{(1)})/h$. In the case shown here, ν_R is determined from a simple sinusoidal fit to be 48.6(3) kHz, which corresponds to a lattice depth of 6.63(8) E_r^{Rb}.

Note that for lattice depths larger than $8\,E_r$, the population in Bloch bands with $n \geq 5$ becomes significant and the oscillation dynamics become more complicated, leading to deviations in the observed frequencies from the simple assumption above. However, using the diffraction method for low lattice intensities and the frequency modulation method for high lattice intensities, we can obtain a calibration of the lattice depth with respect to the laser intensity for the full range of accessible lattice

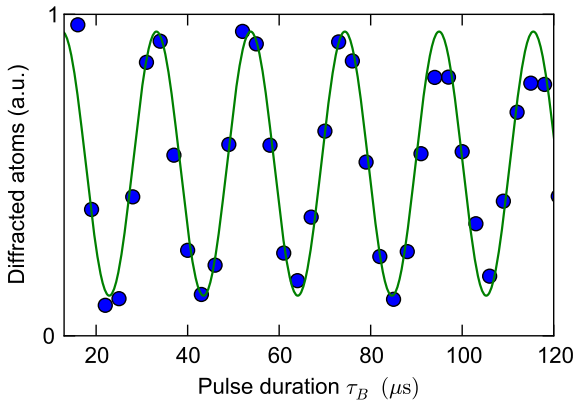

Figure 5.3: Oscillation between population in the $n = 1$ and $n = 3$ Bloch bands, induced by applying the lattice with a fixed intensity onto a BEC of ^{87}Rb for a duration τ_B.

depths.

5.1.4 Light-Assisted Collisions

The interaction between the light of the lattice and the atoms can lead to losses due to the absorption of photons. For a single atom on a lattice site, the absorption of lattice light photons is strongly suppressed due to the large detuning between the frequency of the lattice light and the resonance frequencies of the atomic transitions for ^{87}Rb and ^{39}K. However, when two atoms are situated on the same lattice site, the presence of the lattice photons can additionally lead to light-assisted collisions. We will only sketch the most fundamental concepts relevant to minimize the losses induced by light-assisted collisions in this section. A more thorough analysis can be found in, e.g., [195] and detailed experimental observations of the properties of light-assisted collisions in blue-detuned optical lattices are presented in [196].

The interaction between two atoms and a light field can lead to an excitation of the atoms into molecular states consisting of one excited atom and one ground state atom. Figure 5.4a shows a sketch of the fundamental process and the general shape of the molecular potentials involved.

For red-detuned light, the excitation can only happen into a bound molecular state. Such an excited molecule typically decays into lower lying vibrational levels, which are typically untrapped, resulting in a loss of the atoms [195]. However, due to the discrete energy spectrum of the bound states of the molecular potential, this process is strongly suppressed as long as the frequency of the lattice light is not resonant to a transition into a bound state.

The situation is different for blue-detuned light, where the relevant excited molecular potential is of a repulsive nature and does not support bound states. In this

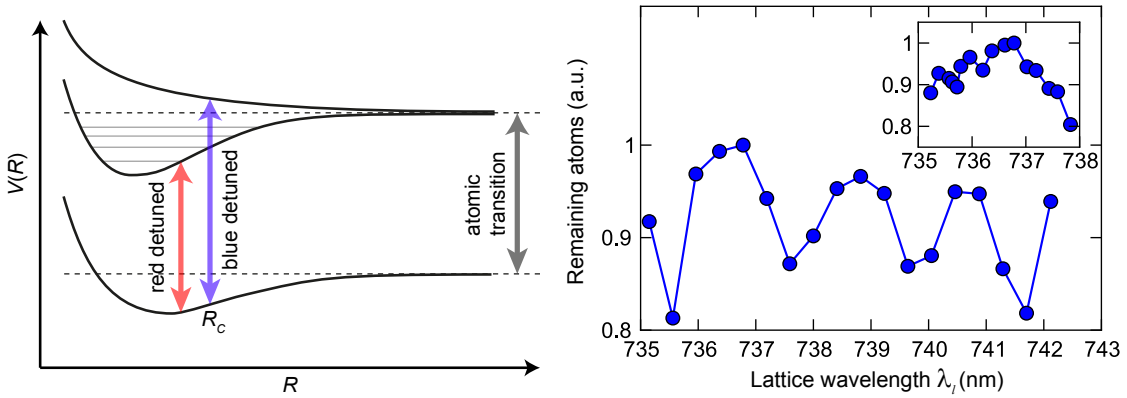

(a) Schematic drawing of the molecular potentials involved in light-assisted collisions (solid lines). The thin gray lines depict the energies of some of the bound states that can be excited by red-detuned light. The arrows indicate possible transitions.

(b) Number of remaining atoms after holding ^{39}K in the lattice for a fixed duration at variable lattice wavelength λ_l. The maxima indicate that the wavefunction overlap between $|\Psi_g\rangle$ and $|\Psi_e\rangle$ is small at the corresponding Condon points and losses are minimized. The inset shows a finer scan of the first maximum.

Figure 5.4

case, the accessible excited states form a continuum and excitations are possible for all light frequencies. Atoms excited into such a state will be repelled by each other and gain kinetic energy before decaying back into the ground state, which leads to a loss of both atoms [195].

The rate of excitation from the ground state into the excited state is proportional to the Franck-Condon factor (FC), which is given by the overlap of the ground state wavefunction $|\Psi_g(R)\rangle$ and the excited state wavefunction $|\Psi_e(R)\rangle$, where R is the internuclear distance, as

$$\mathrm{FC} \propto |\langle \Psi_g(R) | \Psi_e(R) \rangle|^2 . \tag{5.14}$$

For a given detuning of the light, there exist certain internuclear distances R_C (see fig. 5.4a) where the energy of a photon is equal to the potential energy difference between the ground and the excited molecular potentials, called the Condon points. The region around these Condon points typically gives the largest contribution to FC. We can move R_C by changing the detuning of the lattice light and as the wavefunctions of the molecular ground states oscillate strongly for small R, we can find a point where the wavefunction has a node and the overlap is minimized. This effect can be used to minimize the effects of light-assisted collisions by measuring loss rates while varying the lattice wavelength.

Results for this kind of optimization for ^{39}K are shown in fig. 5.4. We hold the ^{39}K

atoms in the lattice and record the number of remaining atoms after a fixed hold time before changing the wavelength of the lattice and repeating the measurement. We vary the wavelength over a range of several nm and observe multiple minima and maxima of the number of remaining atoms. The points where the most atoms remain corresponds to an R_c where the overlap between $|\Psi_g\rangle$ and $|\Psi_e\rangle$ is minimal and excitations into unbound molecular states are suppressed. The inset of fig. 5.4 shows a finer scan of the region around the first peak. From this finer scan, we determine $\lambda_l = 736.6\,\text{nm}$ to be a good choice for the lattice wavelength when working with ^{39}K. Note that for a different species of atoms, the optimal wavelength will vary. For experiments using the fermionic ^{40}K, which are described briefly in chapter 7, the lattice wavelength was chosen to be 738 nm [196]

5.2 Detecting Density and Momentum Distributions

For the detection of the atoms in our experiments, we rely on direct imaging techniques using resonant light. The imaging is either conducted while the atoms are still trapped inside the optical potentials (*in-situ*), which provides information about their density distribution, or after a free time-of-flight (TOF) evolution after switching off the external potentials, which provides information about their momentum distribution.

5.2.1 Absorption Imaging

The most widely used and conceptually simplest method of investigating the density distribution of atoms in the optical lattice or after TOF is that of absorption imaging [49]. A collimated beam of light, resonant with an atomic transition, impedes on the cloud of atoms and the density dependent absorption is recorded on a camera.

For a beam of light with a low intensity I_0 before entering the cloud, the change of intensity while propagating through a medium of density $n(z)$ is given by

$$\frac{dI(z)}{dz} = -n(z)\sigma_0 I(z), \tag{5.15}$$

where σ_0 is the scattering cross section for the atomic transition, given by

$$\sigma_0 = \frac{\hbar\omega_a\Gamma_a}{2I_{\text{sat}}}, \tag{5.16}$$

with the atomic transition frequency ω_a, the atomic transition linewidth Γ_a and the saturation intensity I_{sat}. I_{sat} is the intensity at which the scattering cross section drops to 50% of its value at $I \to 0$ and incorporates details about the atomic dipole transitions (see, e.g., [197] for a more detailed discussion on light-atom interac-

tions). For ^{87}Rb, using σ^+ polarized light resonant to the $|5^2S_{1/2}, F = 2, m_F = 2\rangle \rightarrow |5^2P_{3/2}, F' = 3, m_{F'} = 3\rangle$ transition, the saturation intensity is $I_{\text{sat}} = 16.69(2)\, W/m^2$ [164], while the same transition for ^{39}K has a saturation intensity of approximately $17.5\, W/m^2$ [163]. Varying the polarization of the imaging light can lead to strongly varying saturation intensities when additional hyperfine states can participate in the transition. Experimentally, the saturation intensity for a given (and possibly unknown) polarization can be determined by investigating the intensity dependence of the scattering cross section for large imaging intensities [198, 199].

The density distribution of atoms is determined by taking two images consecutively, one with the atoms present (resulting in an intensity distribution $I(x, y)$ on the camera) and a second at a later time without any atoms ($I_0(x, y)$). At each coordinate (x, y) of the image, we can then determine the local column density of atoms $n_{\text{col}}(x, y) = \int n(x, y, z)dz$ by integrating eq. 5.15 along the imaging (z) direction:

$$n_{\text{col}}(x, y) = -\frac{1}{\sigma_0} \ln\left(\frac{I(x, y)}{I_0(x, y)}\right). \tag{5.17}$$

On the camera chip, we do not measure actual intensities, but the integrated intensity over one pixel. The area of one pixel corresponds to a an area element A in the focal plane that is given by the magnification of the imaging system. With this information, we can calculate the number of atoms at a given position as

$$N(x, y) = -\frac{A}{\sigma_0} \ln\left(\frac{I(x, y)}{I_0(x, y)}\right). \tag{5.18}$$

5.2.2 In-Situ Imaging

We can use absorption imaging to directly determine the density distribution of atoms in the optical lattice. We typically use the vertical axis as the imaging axis for *in-situ* measurements, as our cloud has a smaller extension along the vertical direction due to the elliptical shape of our dipole trap beams (cf. chapter 4.4), which makes it easier to obtain unsaturated images. Furthermore, in this thesis we are mostly interested in the dynamics of atoms along the horizontal directions of the lattice, so imaging along the vertical direction is the natural choice as imaging along a horizontal direction would lead to the loss of information about dynamics along this axis.

Recently, it has become possible to image the density distribution of atoms in optical lattices with such a high resolution that the number of atoms on individual sites of 2D lattices can be detected [57, 58]. These experiments rely on fluorescence imaging with high numerical aperture optics, and necessitate the use of Doppler cooling during the imaging to gather enough fluorescence light without altering the distribution of atoms in the lattice. In our experimental setup, we are not

able to resolve individual lattice sites, as the resolution of our imaging system is on the order of about $3\,\mu$m, and thus significantly larger than the lattice spacing of $d = 368.3\,$nm. Furthermore, even though we use a highly elliptical dipole trap configuration before loading atoms into our lattices, we always populate many layers of the lattice along the vertical direction, which are averaged when imaging along this direction. Nevertheless, we can use *in-situ* imaging to get information about the overall density distribution in the lattice, which we use heavily in chapter 8 to investigate the expansion dynamics of interacting bosons in 1D and 2D lattice geometries.

The exponential scaling of the absorption with the density in eq. 5.15 can cause problems when imaging clouds with very high densities, e.g., large Bose-Einstein condensates. When the transmitted intensity becomes exponentially small and can not be distinguished from the background noise, we can not obtain information about the density distribution anymore. In these cases, imaging techniques like phase contrast imaging [49] can be used, which do not use resonant light but rely on the refractive index of the atoms for detuned imaging light. While we do not rely on the use of phase-contrast imaging in this thesis, we do have the option of using it to investigate states with large densities in our experiment. Details on the experimental realization of phase contrast imaging can be found in [157].

5.2.3 Time-of-Flight Measurements

Allowing the atoms to freely evolve for a certain time t_{TOF} before taking an absorption image gives insight into the momentum distribution of the state. This method is commonly referred to as time-of-flight imaging, and has been used extensively in the context of ultracold atoms, e.g., in the first observations of Bose-Einstein condensation [8, 10].

To initiate the TOF, all confining potentials are instantaneously switched off and the atoms begin to fall downwards under the influence of gravity. If no additional potentials are present and interactions between the atoms can be neglected, the cloud of atoms evolves according to its initial momentum distribution. In the limit of very large t_{TOF}, the initial density distribution of the cloud can be neglected, and the density distribution observed on the TOF images is directly proportional to the momentum distribution of the atoms. For shorter t_{TOF}, the initial density distribution has to be taken into account. A more detailed description of the reconstruction of momentum distributions from TOF images is given in chapter 9.3, for a thorough analysis of how to determine coherence properties from TOF images, refer to [200].

Detecting Coherence

When switching off the lattices abruptly before the time-of-flight evolution begins, the Bloch waves in the lattice are projected onto free space momenta, as discussed in

section 5.1.3. In the case of a superfluid state in the lattice, which macroscopically occupies the Bloch state with $q = 0$, this leads to the appearance of narrow peaks in the density observed after TOF, where the spacing between the peaks is given by $2\hbar k$. Conversely, when the atoms are in a Mott insulating state, being effectively localized in real space and thus occupying many Bloch waves with different momenta, the density distribution after TOF will not show any sharp features, but will instead be given by a broad peak, the so called Wannier background. This has been used in [20] to investigate the superfluid to Mott insulator transition of ^{87}Rb in a 3D optical lattice and has become a standard tool to investigate the coherence of atoms in optical lattices (see, e.g., [97, 201, 202]).

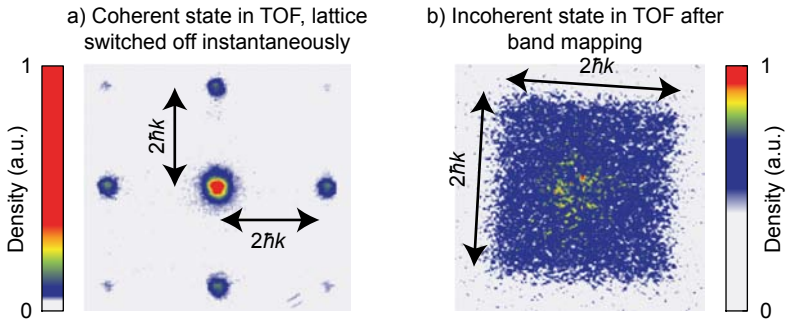

Figure 5.5: a) Coherent state in TOF, released by switching off the lattice. b) Incoherent state in TOF that occupies the complete first Brillouin zone, released using a band mapping technique.

In figure 5.5a, we show the density distribution after 12 ms TOF of ^{39}K in a superfluid state, released from a 3D lattice potential with a lattice depth of $10\,E_r$ along all axes. We can clearly observe the central peak of atoms with momentum $p = 0$ and the higher order lattice peaks.

Band Mapping

A second method for the investigation of momentum distributions of atoms in optical lattice is the so called band mapping technique. In this case, the lattice is not switched off instantaneously but rather gradually lowered on a time scale that is fast compared to the many-body dynamics in the lattice, in order to preserve the quasimomentum distribution of the state under investigation, but slow enough to be adiabatic with respect to transitions between the Bloch bands [51, 203]. Under these circumstances, the Bloch waves are adiabatically transformed into the corresponding free space plane waves. The quasimomenta of the atoms are preserved and an atom in the lowest Bloch band with quasimomentum q is mapped onto a free space momentum $p = \hbar q$. Atoms in higher Bloch bands are mapped to free space momenta

in the respective higher Brillouin zones , and the occupation of these Brillouin zones can be observed in the TOF images.

Figure 5.5a shows a state of ^{39}K in a 2D lattice with a momentum distribution that completely occupies the first Brillouin zone. In this case, the lattice intensity is ramped down within 500 μs from a lattice depth of $(10, 10, 20)\, E_r$ along (x, y, z), before the free evolution in TOF starts.

5.3 Equilibrium States in the Bose-Hubbard Model

Using blue-detuned laser beams to create lattice potentials of varying depths and being able to compensate the resulting anti-confining potentials with the addition of red-detuned dipole trap beams, we can independently control the tunneling J and the external confinement of the Bose-Hubbard Hamiltonian. Using ^{39}K in the $|5^2S_{1/2}, F = 1, m_F = 1\rangle$ ground state, we can then employ the intra-species Feshbach resonance discussed in chapter 4.5 to change the on-site interaction U between the atoms. This allows us to independently modify all relevant parameters of the Bose-Hubbard Hamiltonian. Being able to adjust the tunneling of the individual lattice axes independently as well as the individual axes of the dipole traps, we can even control the dynamics along all axes separately, and have full control over the Hamiltonian

$$H = -\sum_{\mu} \left(J_\mu \sum_{\langle i,j \rangle_\mu} \hat{b}_i^\dagger \hat{b}_j \right) + \frac{U}{2} \sum_i \hat{n}_i(\hat{n}_i - 1) + \sum_\mu \sum_i V_{\mathrm{ext},\mu}(\mathbf{r}_i)\hat{n}_i, \tag{5.19}$$

where μ indicates the three spatial axes, J_μ the tunneling matrix elements and the summation index $\langle i, j \rangle_\mu$ runs over all nearest neighbor sites along axis μ. $V_{\mathrm{ext},\mu}(\mathbf{r}_i)$ are the contributions from the global potentials along each axis to the total potential at the position $\mathbf{r}_i$ of site i.

This flexibility allows us to study all aspects of the equilibrium states as well as the dynamics in the Bose-Hubbard model. The main scope of this thesis lies on the investigation of expansion dynamics, which will be discussed extensively in the following chapters. In the remainder of this chapter, we will give a brief overview over studies concerning equilibrium states of the system. First, we will demonstrate the effects of changing U and J on the coherence properties of ground states in the lattice, which are indicative of the superfluid to Mott insulator transition. Second, we will show more exotic equilibrium states that are supported in this model, namely states with negative absolute temperatures, which are the only thermodynamically stable states of the attractive Bose-Hubbard model.

5.3.1 Superfluid - Mott Insulator Transition of ^{39}K

As discussed in chapter 2.2.1, the Bose-Hubbard model exhibits a quantum phase transition from a superfluid (SF) to a Mott insulating (MI) phase. The transition point depends on the ratio between the tunneling J and the interaction U as well as on the external confinement, which sets the local chemical potential in the lattice. This phase transition has first been observed for ^{87}Rb in optical lattices [20]. As there are no practical intra-species Feshbach resonances available for ^{87}Rb, the scattering length was fixed in these experiments, and the SF-MI transition was driven by varying the lattice intensities, thus mainly changing the tunneling coupling J. Using experiments with single site resolution [57, 58], it recently became possible to directly image the formation of the wedding cake structure of Mott insulator domains with varying occupation numbers [58, 109].

In figure 5.6, we show TOF images of ^{39}K atoms released from 3D lattices at varying lattice depths and varying interaction strengths, given in terms of the intra-species scattering length a_s. We can clearly observe the loss of coherence in the system for increasing interactions as well as increasing lattice depth. The black line shows the prediction for $(U/J)_c \approx 29.4$, which marks the SF-MI transition in 3D for a filling of $n = 1$ [107]. Even though the system, being harmonically trapped by optical dipole traps in addition to the lattice potentials, does not exhibit a constant density of $n = 1$ atom per lattice site, the line does qualitatively separate the graph into a region of coherent states with high visibility peaks after TOF and a region of low visibility, which indicates incoherent, localized states.

5.3.2 Negative Temperature States

Being able to choose the magnitude as well as the sign of all parameters in the Bose-Hubbard Hamiltonian allows for the creation of equilibrium states with negative absolute temperatures. Here, we will only briefly discuss the fundamental concepts involved as well as some of the experimental results obtained. For a more detailed treatment, please refer to [192] and the PhD thesis of S. Braun [204].

The possibility for the creation of stable states with negative temperature depends on the presence of an upper bound on the energy per particle E/N, where E is the total energy of the system [205, 206]. If such an upper bound exists, the absolute temperature, defined as

$$1/T = \frac{\partial S}{\partial E}, \tag{5.20}$$

where S is the Boltzmann entropy, becomes negative as the system approaches this upper bound and all constituents of the system start to occupy the highest possible energy states, leading to a decreasing entropy with increasing energy.

This effect is sketched in figure 5.7 for the occupation of states with quasimomentum q and corresponding kinetic energy E_q in the tight binding dispersion relation

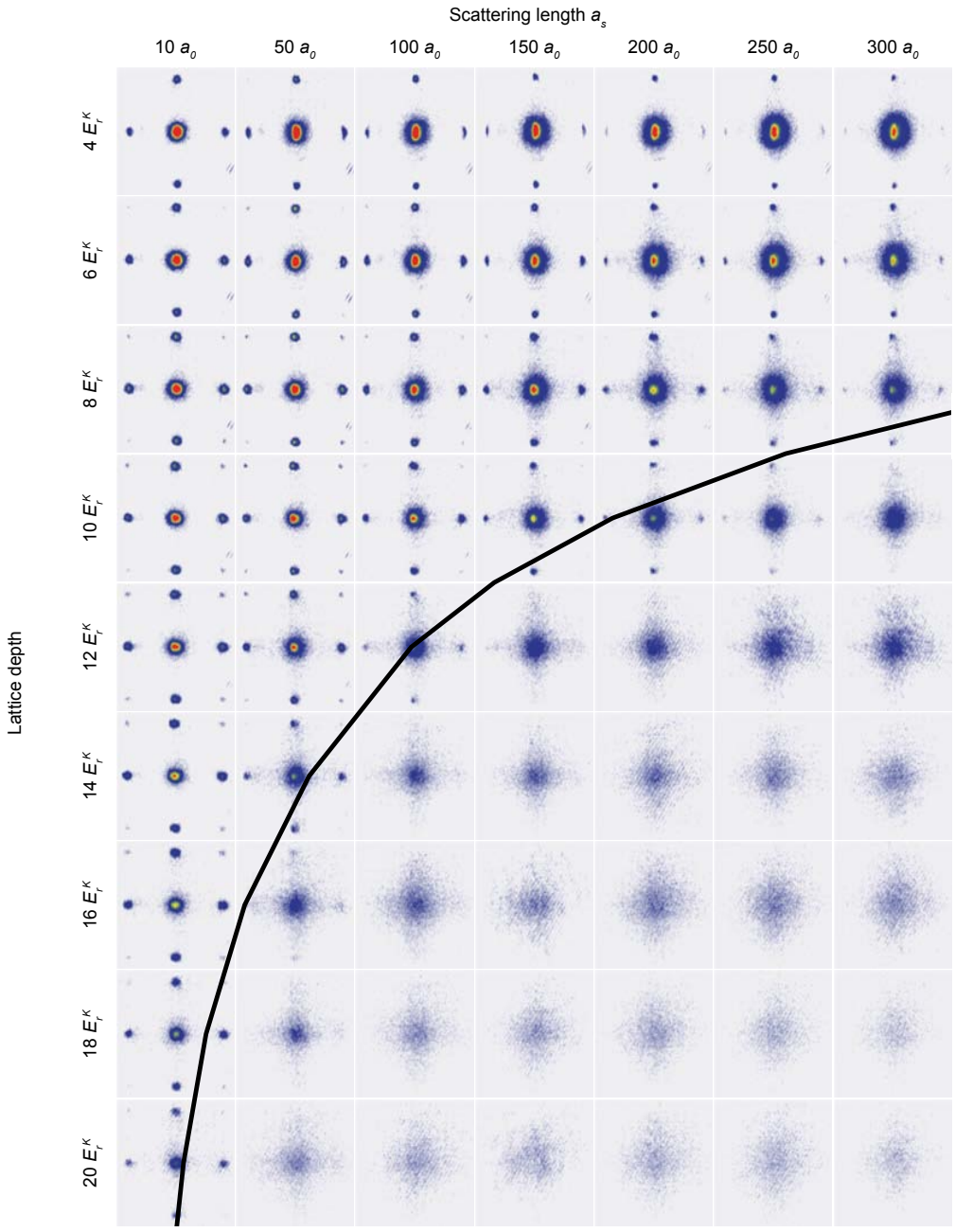

Figure 5.6: SF-MI transition of ^{39}K (see text).

of a 1D optical lattice. For simplicity, we use the canonical ensemble for distinguishable particles, and the populations are thus given by the canonical Boltzmann distribution at temperature T. For positive T close to $T = 0$, only the lowest energy states at $q = 0$ are occupied, resulting in a state with low entropy. As T is increased, higher momenta become occupied and at $T = \infty$, all energy states are

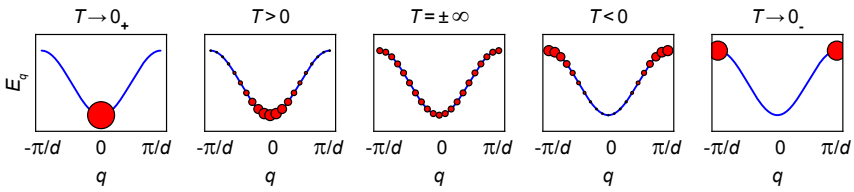

Figure 5.7: Sketch of the occupation of quasimomentum states at varying temperature T for a non-interacting system of distinguishable particles. The area of the circles represents the occupation.

occupied evenly, resulting in a maximum entropy. A further increase in total energy now leads to a population inversion and the entropy decreases for increasing E, resulting in negative temperatures.

Negative temperatures have so far been realized only in systems of localized spins [207–209], where the position of the spins was stationary. In our setup, we can create the first negative temperature system with motional degrees of freedom. We follow the proposals of [210, 211] and first load a BEC of ^{39}K into an optical lattice at repulsive interactions $U > 0$ with a harmonic confinement present ($V > 0$). Deep in the Mott insulating regime, these parameters can be inverted so that $U < 0$ and the global potential is anti-confining ($V < 0$). If the state in the deep lattice, where tunneling is negligible, does not contain any sites with more than one atom, the entropy generation during this parameter change is only very small [211] as a state of localized particles on singly occupied sites at $|U/J| \to \infty$ is an eigenstate of the Hamiltonian both at U and $-U$. We then decrease the lattice intensities again to bring the system back to the superfluid regime. Depending on the parameters of the final Hamiltonian, we obtain states with finite positive temperatures for $U > 0$ and $V > 0$ and states with finite negative temperatures for $U < 0$ and $V < 0$.

In figure 5.8, we show the momentum distribution of two states in TOF imaging, revealing the changes introduced to the momentum distribution of the system when the parameters of the Hamiltonian are changed. For the density distribution shown on the left side, the final U and V are positive, resulting in a state with small positive temperature T. The peaks in momentum space are observed at $p = 0$ and the corresponding higher lattice momenta (see section 5.2.3), as expected for a state with a momentum distribution that is centered around $q = 0$. On the right side, we show the final state after inverting U and V. The peaks in momentum space are now situated at momenta at the edge of the Brillouin zone ($q_x = \pm\pi/d, q_y = \pm\pi/d$), corresponding to a macroscopic occupation of the highest kinetic energy states, as expected for a state with negative temperature.

We were able to show that the created negative temperature states had approximately the same absolute value of temperature $|T|$ as the positive temperature states and were stable on the same time scales, as long as the external anti-confinement after the inversion was adapted to match the magnitude of the initial confining

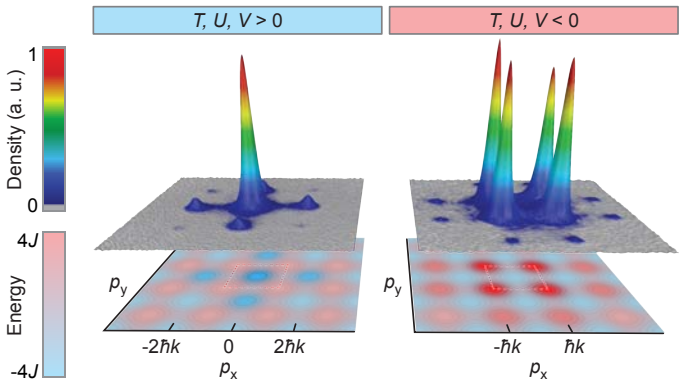

Figure 5.8: Momentum distribution of a positive temperature state (left) and a negative temperature state (right) after 7 ms TOF. Both images are averages over 20 experimental realizations. The contour plots below show the 2D tight-binding dispersion relation, where momenta with large occupation are highlighted by a stronger saturation of the colors. The white squares indicate the first Brillouin zone. Figure reprinted from [192].

potential [192].

5.4 Summary

In this chapter, we have shown how to realize the Bose-Hubbard Model using ultracold atoms in optical lattices and fundamental aspects regarding additional global potentials created by the lattices as well as the minimization of light-assisted collisions have been addressed. We have further discussed observables that can be measured using absorption imaging, namely the *in-situ* density distributions and momentum distributions using TOF methods. Finally, we briefly reported on using the flexibility of our realization of the Bose-Hubbard Model to create various equilibrium states, by observing the SF-MI transition as well as negative temperature states in the lattice.

After establishing the fundamental requirements for the investigation of physics in the Hubbard model, the following part of this thesis will be devoted to studying non-equilibrium dynamics of ultracold atoms in homogeneous optical lattices.

Chapter 6

Expansion Dynamics of Noninteracting Bosons in Optical Lattices

In this chapter, we first sketch an experimental procedure employed to induce expansion dynamics of ultracold atoms in optical lattices. This sets the scope of the main experimental work in this thesis. We then discuss the dynamics expected for free bosons in homogeneous lattices and the necessary optimization of the experimental system to ensure the creation of suitable initial states and lattice geometries. This includes a study of the influence of external potentials on the dynamics as well as an investigation of higher occupancies in the system. Finally, we discuss suitable quantitative measures for the investigation of the dynamics, along with experimental results for the expansion of non-interacting bosons in homogeneous lattices.

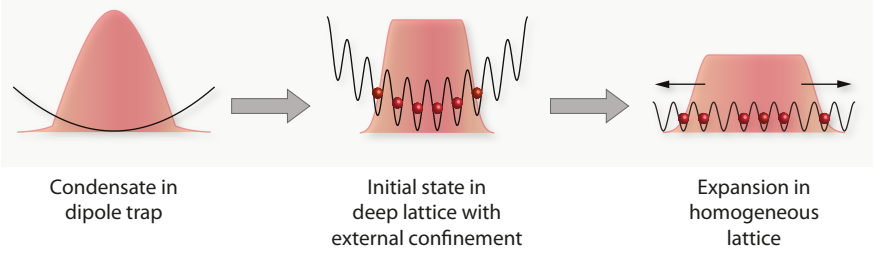

Figure 6.1: Schematic of the measurement sequence for the expansion dynamics of atoms in homogeneous lattices. Starting with a condensate in an optical dipole trap, the lattice is ramped up to create an initial state of dephased, singly occupied sites. In a simultaneous quench of U/J and the trapping potential, the expansion into the homogeneous lattice is then initiated.

To outline the scope of this discussion, we show the envisaged experimental setup in fig. 6.1. We first load a Bose-Einstein condensate of ^{39}K atoms from an optical dipole trap into a deep optical lattice potential in order to create a large Mott

insulating core with $n = 1$ in the center of the cloud. Our main goal is to ensure that each lattice site is only occupied by at most one atom, as the presence of higher occupancies can severely alter the expansion dynamics (see chapter 8.4). In the deep lattice, where J is very small, any residual potential leads to a dephasing between the different lattice sites, which localizes all atoms to individual sites [97], leading to a completely flat quasimomentum distribution $n_q = \text{const.}$ over the first Brillouin zone (BZ). This is the initial state for our expansion measurements, which are initiated by lowering the lattice depth along the expansion directions and compensating external potentials to make the lattices as homogeneous as possible.

6.1 Preparation of the Initial State and Start of the Expansion

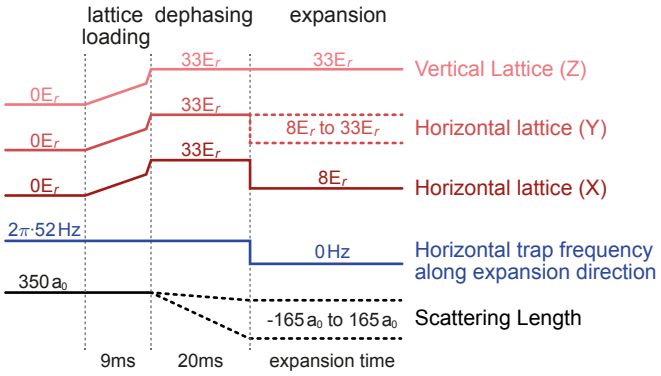

Figure 6.2: Sketch of the experimental sequence for the creation of the initial states and the initiation of the expansion.

We start the experiments with Bose-Einstein condensates of ^{39}K containing on the order of 10^5 atoms in the $|4^2S_{1/2}, F = 1, m_F = 1\rangle$ state in an optical dipole trap with trap frequencies $\omega_x \approx \omega_y \approx 52\,\text{Hz}$ and $\omega_z \approx 120\,\text{Hz}$. For details on the preparation of condensates of ^{39}K, please refer to chapter 4. Figure 6.2 gives an overview of the changes in the significant parameters of the system during the initial state preparation. The condensate is prepared at a magnetic field of $B \approx 398.4\,\text{G}$, which corresponds to a scattering length a_s of approximately $350\,a_0$, set by the intra-species Feshbach resonance at 402.5(3) G [46] (see chapter 4.5 for more details). This strongly repulsive interaction is chosen in order to prevent the formation of higher occupancies in the lattice. The optical lattices are then ramped up to a depth of $20\,E_r$ within 8 ms. For experiments with ^{39}K, we use a lattice with a wavelength of $\lambda = 736.6\,\text{nm}$ (see chapter 5.1.4), which yields a lattice constant $d = \lambda/2 = 368.3\,\text{nm}$. For some of the experiments performed, the atoms are kept in the $20\,E_r$ deep lattice,

while for other experiments, we additionally ramp up the lattice within 1 ms to a depth of $33\,E_r$ along all directions. The tunneling time τ_D in the deep lattice is 6.8 ms in the $20\,E_r$ case and 58 ms in the $33\,E_r$ case. The atoms are held in the deep lattice in combination with the harmonic potential for a dephasing time of 20 ms, during which all residual correlations between the atoms are lost and they become effectively localized to individual lattice sites [97]. We designed the ramps to generate as few double occupancies in the system as possible to ensure that the initial state can indeed be described by mixture of products of local Fock states, where the individual terms have the form

$$|\Psi_{\text{initial}}\rangle = \prod_i \frac{1}{\sqrt{\eta_i!}} \left(\hat{b}_i^\dagger\right)^{\eta_i} |0\rangle\,, \tag{6.1}$$

with an occupation $\eta_i \in \{0, 1\}$ on each site i. For more details on the detection of double occupancies and the optimization of the loading procedure, refer to section 6.3.2. During the dephasing period, the magnetic field is changed to set the scattering length to values between $-165\,a_0$ and $+165\,a_0$. Due to the suppressed tunneling, the changing interaction does not influence the density distribution of the state after the preparation procedure.

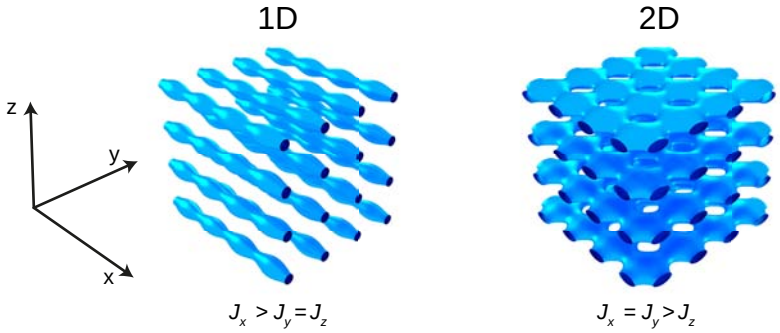

Figure 6.3: Potential energy isosurfaces of a 1D lattice configuration (left) and a 2D lattice configuration (right).

After changing the scattering length, the expansion is initiated. This is done by ramping down the intensity of the lattice beams within 150 μs to increase J and allow tunneling. Depending on the geometry we want to investigate, we either ramp down only the lattice along the x-direction to a depth $V_x = 8\,E_r$, which creates a geometry of 1D tubes with a weaker lattice along the tubes, or both the x- and the y-lattices, to allow tunneling in 2D lattice planes. Note that it is also possible to operate in a crossover regime between 1D and 2D by choosing values for the tunneling $J_x < J_y < J_z$. The z-lattice is always kept at a high depth to inhibit tunneling along the vertical direction. The resulting lattice geometries are shown in terms of their potential energy isosurfaces in figure 6.3. Simultaneously with the

lattice intensities, the dipole trap beams along the x- and y-direction are turned off by linearly ramping down their intensities in 150 μs. The atoms are now supported against gravity only by the strong lattice potential along the z-direction. The small tunneling amplitude $J_d \approx h \times 2.7\,\mathrm{Hz}$ in a $33E_r$ deep lattice in combination with the effects of gravity lead to Bloch oscillations with an amplitude of approximately 11 nm, which is much smaller than the lattice constant d, confining the atoms to individual lattice planes. The dipole trap beam along the z-direction, which creates a confinement along the horizontal axes, is at the same time adjusted to an intensity that precisely compensates the overall anti-confining potential of the blue-detuned lattices in order to create a homogeneous lattice system (see section 6.3.1).

We investigate the expansion dynamics in these homogeneous lattices by allowing the atoms to evolve for a certain time t_E and then image their density distribution using *in-situ* absorption imaging along the z-direction (see chapter 5.2.1). This procedure is repeated multiple times for varying t_E to determine the complete time evolution of the atomic density.

6.2 Dynamics of Non-Interacting Atoms in Homogeneous Lattices

In order to investigate the expansion dynamics of atoms in optical lattices, it is instructive to first consider the example of non-interacting atoms in one dimensional (1D) homogeneous lattices. As discussed in chapter 3.4.1, the dynamics of non-interacting atoms reduce to single particle dynamics, as the Hamiltonian can be decomposed into a sum of single-particle Hamiltonians which can be solved individually. In the ideal experimental situation, the dynamics are generally described by the Bose-Hubbard Hamiltonian without interactions and external potentials, given by

$$H = -J \sum_{\langle i,j \rangle} \hat{b}_i^\dagger \hat{b}_j. \tag{6.2}$$

The single particle dynamics can now be calculated by assuming an initial wavefunction, in our case that of a completely localized particle, and calculating its evolution over time. A measurement of the particle density in the lattice would then project the wavefunction onto a position in real space, revealing that the dynamics in the lattice can be seen as an example of a continuous quantum walk [212, 213]. This allows for a simple interpretation of eq. 6.2, where the tunneling J gives a timescale for tunneling events in the lattice, the tunneling time $\tau = \hbar/J$. In a classical random walk, where the dynamics result from a succession of individual tunneling events, one would expect the distance $|\mathbf{r}(t_E) - \mathbf{r}(0)|$ of the atom from its initial position $\mathbf{r}(0)$ to scale with the square root of the evolution time t_E, $|\mathbf{r} - \mathbf{r}_0| \propto \sqrt{t_E}$. But

due to the quantum nature of the random walk, the atom tunnels simultaneously in all directions, as given by the spreading of the wavefunction over time, and the distance instead scales linearly with t_E [59, 214].

In order to extract the dynamics of several localized particles in the lattice, instead of calculating the evolution of the individual wavefunctions it is sufficient to turn to a semi-classical description, using the effective dispersion relation of atoms in optical lattices in the tight-binding limit. According to chapter 2.1.3, the dispersion relation for a single particle with momentum q is given by

$$\epsilon_q = -2J\cos(qd) \tag{6.3}$$

(see top panel of figure 6.4a) and the corresponding group velocity is given by

$$v_g(q) = \frac{1}{\hbar}\frac{\partial \epsilon_q}{\partial q} = \frac{2d}{\tau}\sin(qd) \tag{6.4}$$

(see bottom panel of fig. 6.4a). We can then simply calculate the trajectories of many atoms in the lattice, starting at positions within the extension of the initial state with quasimomenta q according to their initial quasimomentum distribution n_q, and sum up the trajectories to get the evolution of the overall density distribution.

The sinusoidal shape of the group velocity as a function of quasimomentum has direct consequences for the dynamics of atoms in a lattice. Our given initial state consists of singly occupied lattice sites with completely localized particles that are released into a homogeneous lattice. For localized atoms, all quasimomentum states are occupied equally, corresponding to an evenly filled first Brillouin zone. Calculating the group velocity distribution of this state shows that the number of atoms with high positive or negative velocities is much larger than the number of atoms with vanishing velocities. This is due to the fact that the bounded group velocity has a vanishing derivative with respect to q at the largest velocities, leading to a higher number of states.

The lower panel of fig. 6.4a shows the group velocity distribution of a uniformly occupied Brillouin zone. The colors indicate different velocity classes, showing clearly the dominance of high velocity states (red circles) compared to the low velocity states (blue circles). To show this effect more clearly, we can calculate the distribution of group velocities, n_{v_g}, for a given quasimomentum distribution n_q. In the top panel of fig. 6.4b, we show two distinct n_q, one that is completely flat over the first Brillouin zone (solid line) and one that is peaked around $q = 0$ (dashed line). In the panel below, we plot the corresponding n_{v_g}. While n_{v_g} has a rather broad peak around $v_g = 0$ if n_q is peaked around zero (dashed line), in the case of $n_q = \text{const.}$, n_{v_g} shows two narrow peaks at the maximum absolute group velocities $v_g = \pm 2d/\tau$ (solid line).

Given these calculated group velocities, we can now easily determine how the

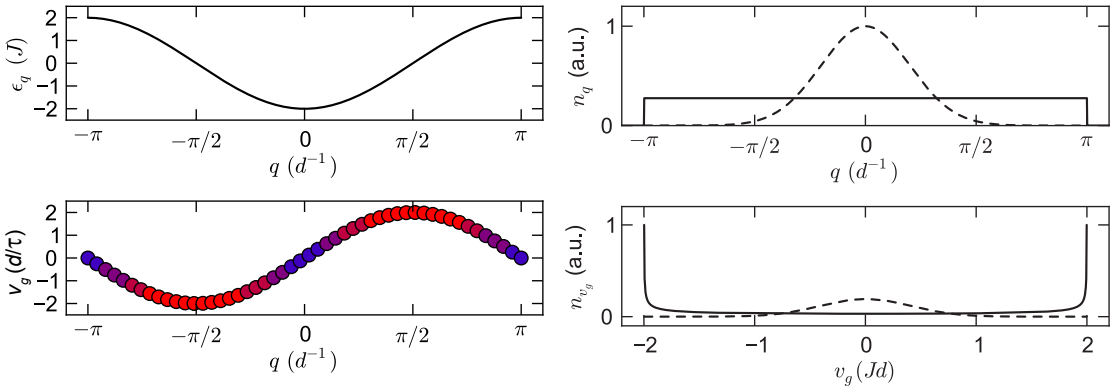

(a) Top panel: Dispersion relation in the optical lattice. Bottom panel: Group velocity in the optical lattice. Points indicate states equally spaced in quasimomentum space. The colors indicate different velocity classes.

(b) Top panel: Quasimomentum distributions with n_q = const. (solid line) and n_q peaked around $q = 0$ (dashed line). Bottom panel: The corresponding group velocity distributions n_{v_g}.

Figure 6.4

evolution of the real space density distribution of a given initial state of atoms in a homogeneous lattice looks like. We do this for a state of atoms that initially evenly occupies the range in position $x \in [-30, 30]d$ and show the results in fig. 6.5, where each horizontal line corresponds to the 1D density distribution at evolution time t_E. Panel (a) shows the evolution for n_q = const. (solid line in the top panel of fig. 6.4b). The effect of the peaks in n_{v_g} are immediately obvious from the two distinct lobes of high density traveling outwards with maximum group velocity $v_g^{\max} = 2d/\tau$. These are the expansion dynamics we expect for non-interacting atoms in our experiments. Panel (b) shows the evolution for the n_q peaked around $q = 0$ (dashed line in the top panel of fig. 6.4b). In this case there is only one peak visible in the density

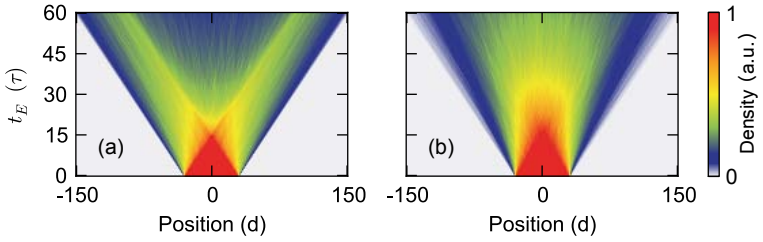

Figure 6.5: Evolution of the density distribution during the expansion for (a): n_q = const and (b): n_q peaked around $q = 0$ (see top panel of fig. 6.4b. The initial density distributions are constant over the central 60 sites.

distribution centered around $x = 0$ and the overall evolution is much slower.

As the evolution along different lattice axes decouples for non-interacting atoms, the expansion in a 2D or 3D lattice geometry is simply given by the superposition of the 1D dynamics along all expansion directions.

6.3 Optimizing the Expansion

6.3.1 Homogeneity

The goal of these measurements is to investigate the expansion dynamics of bosons in a homogeneous Hubbard system. In our setup, the blue-detuned lattice beams always create an anti-confining potential perpendicular to their propagation direction (cf. chapter 5.1.2). In order to compensate these anti-confining potentials on large scales, we have to employ red-detuned dipole trap beams with similar beam waists. As outlined in chapter 4.4, the dipole trap beams along the x- and y-direction have a highly elliptical shape and their beam waists differ greatly from those of the lattice beams. Thus they cannot be used for the compensation. The dipole trap beam along the z-direction, however, is circular and has approximately the same beam waist as the lattice beams. Since this vertical dipole trap beam creates a significant confinement only along the two horizontal directions, we are not able to create a homogeneous potential along all spatial directions. This is not a problem in our experiments, since we only investigate the expansion dynamics in 1D and 2D and choose the expansion directions to be along the x-direction in 1D and along the x- and y-directions in the 2D case, disregarding any dynamics along the vertical direction.

The approximate beam waists of the lattice beams and the z-dipole trap beam are given in table 6.1. Note that we specify two waists for each beam, along the two axes perpendicular to the propagation direction, as the beams are not perfectly symmetric. All Gaussian waists are close to $150\,\mu$m and by adjusting their overlap carefully, the anti-confining nature of the lattice beams can be approximately compensated by the confining dipole trap potential along the horizontal directions. Note, however, that there are deviations in the beam waists on the order of about 10 percent, which can cause residual potentials especially further away from the center of the system.

In order to optimize the homogeneity of the lattice system, we need to optimize the relative alignment of the beams. The procedure relies on monitoring the displacement of the clouds that is induced by the confining and anti-confining potentials of the beams, using *in-situ* absorption imaging.

A second optimization has to be conducted to find the correct intensity of the z-dipole beam. For too strong dipole trap intensities I_d, there is an overall confining potential present, as shown on the left side of figure 6.6, which leads to a decreasing

Beam	w_x	w_y	w_z
x-lattice	–	149.1 μm	148.6 μm
y-lattice	149.3 μm	–	144.6 μm
z-lattice	163.5 μm	155.8 μm	–
z-dipole	152.7 μm	147.0 μm	–

Table 6.1: Approximate Gaussian waists (w_x, w_y, w_z) along (x, y, z), respectively, of the lattice and dipole trap beams that are present during the expansion measurements.

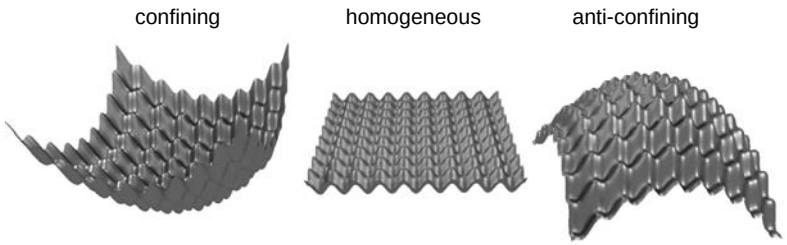

Figure 6.6: Visualization of a 2D lattice with additional harmonic confinement (left), optimally compensated external potentials (center) and overall anti-confinement (right).

quasimomentum q of the expanding atoms while traveling outwards, effectively reducing the expansion velocity of the cloud. For a too small I_d, the anti-confinement created by the blue-detuned lattice beams is not fully compensated and results in an overall anti-confining potential (right side of figure 6.6), which leads to an increasing q of the expanding atoms but also to a reduction of the expansion velocity.

The effects of the confining and anti-confining global potentials lead to changes in the quasimomentum distribution $n_q(t_E)$ over time and could in principle decrease as well as increase the observed expansion velocities. However, in an expansion starting in a state with $n_q(0) = \text{const}$, there are two reasons why global potentials generally lead to slower expansions. First, atoms in a lattice cannot be accelerated indefinitely. Increasing the quasimomentum of an atom to a value $q = \pi/d$ will result in a Bragg reflection that maps its quasimomentum to $-\pi/d$, which is the fundamental mechanism for Bloch oscillations in optical lattices [215, 216]. Second, the group velocity has a local maximum at quasimomenta $q = \pi/(2d)$ (see figure 6.4a). Atoms with these quasimomenta are the ones that travel fastest in real space and will thus be the atoms to experience the strongest effects of residual potentials. Any change in q for these atoms, be it positive or negative, will result in a decreasing group velocity. To investigate this effect, we look at the 1D Bose-Hubbard Hamiltonian

with an additional harmonic potential

$$H = -J \sum_{\langle i,j \rangle} \hat{b}_i^\dagger \hat{b}_j + \sum_i \frac{\omega^2}{2} (i - i_0)^2 d^2, \tag{6.5}$$

where i_0 is the index of the site in the center of the harmonic potential with trap frequency ω (given in units of $J^{-1/2}$) and d is the lattice constant. To incorporate anti-trapping potentials, ω can be chosen to be purely imaginary, resulting in a negative sign for the second term in eq. 6.5.

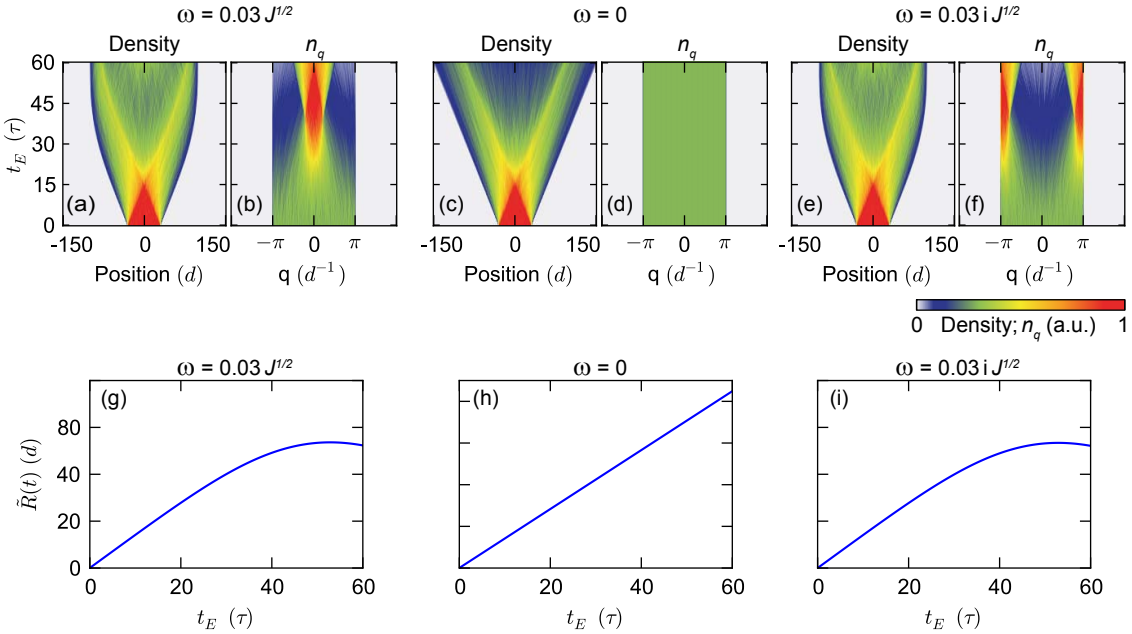

Figure 6.7: (a),(c),(e): Evolution of the 1D density distribution during the expansion, calculated from eq. 6.5 for various ω, stated in units of $J^{1/2}$. Imaginary values for ω result in anti-confining potentials. The initial states have a constant density for $x \in [-30d, 30d]$ and a constant n_q in the first BZ. (b),(d),(f): Quasimomentum distribution n_q during the same evolutions. (g),(h),(i): Evolution of the rescaled radius $\tilde{R}(t_E)$, calculated from the evolution of the density distribution in (a),(c),(e), respectively.

In figure 6.7, we show the effects of such harmonic potentials on the evolution of atoms in optical lattices. We calculate trajectories of individual atoms starting from an initial state with a constant density in the range of $x \in [-30d, 30d]$ and constant n_q in the first Brillouin zone, as described in section 6.2. Figs. 6.7c and d show the evolution of the density distribution and of n_q, respectively, without any additional potentials present. The density distribution shows the typical bal-

listic behavior already shown in fig. 6.5(a), while n_q stays constant throughout the complete evolution.

As a measure of the size of the cloud, we calculate the rescaled radius $\tilde{R}(t_E) = \sqrt{R^2(t_E) - R^2(0)}$, where $R^2(t_E) = 1/N \sum_n (x_n(t_E))^2$, N is the number of atoms and $x_n(t_E)$ is the distance of the n-th atom from the center of the harmonic potential [1]. For more details on this quantity and the determination of cloud sizes in general, please refer to section 6.4.2. Without external forces, $\tilde{R}(t_E)$ increases linearly with time, as shown in fig. 6.7h.

The effects of a confining potential on the 1D density $n_x(t_E)$ and on $n_q(t_E)$ can be observed in figs. 6.7a and b. The trajectories of the fastest atoms are visibly bent inwards as a direct consequence of the confining potential that decreases their quasimomentum, leading to lower velocities. This effect can be observed even more clearly in the evolution of the quasimomentum distribution, which exhibits a strong redistribution of momentum towards smaller $|q|$ during the first $45\,\tau$ of the evolution. The effects on the expansion velocity can be seen in fig. 6.7g, where the initially linear increase of $\tilde{R}(t_E)$ is slowed down for large t_E and for $t_E \gtrsim 50\tau$, $\tilde{R}(t_E)$ even starts to decrease over time.

The changes in n_q during an expansion in the anti-confining potential (fig. 6.7f, $\omega = 0.03\mathrm{i}J^{1/2}$) are exactly the opposite as in the confining case. During the evolution, n_q increases at large $|q|$ and decreases around $q = 0$. However, the effect on the evolution of the density distribution is exactly the same in both cases, due to the high symmetry of the group velocity relation (see fig. 6.4a). This is also reflected in the evolution of $\tilde{R}(t_E)$, which is exactly the same in figs. 6.7g and 6.7i.

As a side remark, it should be noted that for even stronger harmonic confinements or longer expansion durations, the atoms complete several oscillation periods. Without the lattice potential, such oscillations in a purely harmonic geometry would lead to a rephasing of the atomic trajectories and a completely periodic oscillation pattern of the density distribution. In the optical lattice, this behavior is modified by the cosine dispersion relation that introduces an amplitude dependence of the oscillation frequency, leading to a rapid dephasing of the individual trajectories.

The fact that the evolution of the density distribution only depends on the strength of the global potential but not on its sign allows for an easy method of optimizing the homogeneity of the system. We conduct an expansion measurement up to a long expansion duration $t_E > 40\tau$ and record the size of the clouds, which is determined assuming a function of the form

$$n(x) = A \exp\left(-\frac{(x - x_0)^2}{2\sigma_x^2}\right) \tag{6.6}$$

[1] Here, we treat the atoms in a semi-classical continuum approximation and their position is not discretized. For the investigation of dynamics in the actual Hubbard Hamiltonian, $\tilde{R}(t_E)$ is redefined in a discrete version in eq. 6.9.

for the atomic density integrated along the y-direction and using a least-squares fitting algorithm to determine the best value for the Gaussian waist σ_x. As both confining as well as anti-confining potentials decrease the final size of the cloud, maximizing σ_x with respect to the intensity of the optical dipole trap beam results in the most homogeneous lattice potentials. Figure 6.8 shows such an optimization measurement for a 1D expansion along x in a lattice with depths $(8, 20, 20)\, E_r$ along (x, y, z), respectively.

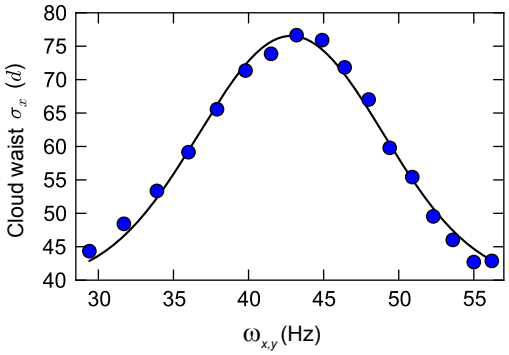

Figure 6.8: Gaussian waist σ_x of the clouds after an expansion for $t_E = 54\,\tau$ in a lattice of depth $(8, 20, 20)\, E_r$ along (x, y, z), respectively, for varying intensities of the z-dipole trap. The dipole trap intensity is given as the bare trap frequency $\omega_{x,y}$ that the beam would create along the horizontal directions if no other potentials were present. The solid line is a Gaussian fit to the data. The maximum in σ_x indicates the best homogeneity along the expansion direction.

Here, the intensity of the dipole trap beam is given as the bare harmonic trap frequency it would create without other potentials present. For a bare trap frequency of $\omega_{x,y} \approx 43\,\mathrm{Hz}$, the anti-confinement of the lattice beams is optimally compensated and the cloud reaches its largest extension after the expansion.

6.3.2 Double Occupancies

A second concern is the presence of sites with an occupation of more than one atom (higher occupancies) in the initial state. For non-interacting atoms, these higher occupations do not behave differently from singly occupied sites. As soon as interactions are present, however, the dynamics of sites with initial $\eta_i > 1$ are different from those of singly occupied sites. The difference between the dynamics is especially strong for large interactions, where doubly occupied sites are essentially stable objects that slow down the dynamics. For a complete discussion of the effects of higher occupancies in the initial state, see chapter 8.4.4.

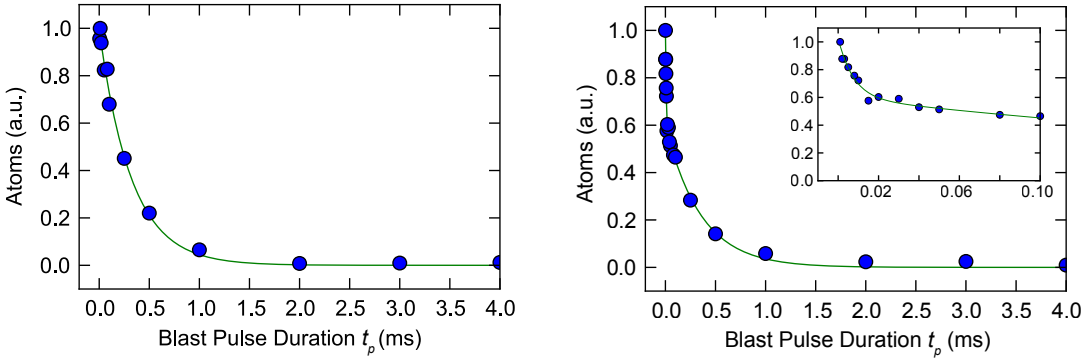

(a) Few sites with $\eta_i > 1$

(b) Many sites with $\eta_i > 1$. The inset highlights the data at small times.

Figure 6.9: Decay of atom number under the influence of a near-resonant light pulse of duration t_p for states with different amounts of sites with $\eta_i > 1$. The light is approximately 110 MHz red-detuned to the high-field imaging transition (see text).

6.3.3 Imaging Double Occupancies

In order to determine the amount of doubly and higher occupied sites in the lattice, we first freeze out the on-site number distribution by ramping up the lattice in 50 μs to a depth of 33.0(5) E_r along all three axes. In the deep lattice, where tunneling is strongly suppressed (tunneling time $\tau_d = \hbar/J_d \approx 58$ ms), we set the magnetic field within 10 ms to a fixed value of $B \approx 400$ G, where the scattering length is large. This freezing out and the decoherence due to differences in the on-site energies leads to a projection of the wavefunction in the lattice onto a mixture of products of local Fock states, as discussed in section 6.1 in the context of the initial state preparation. Each local Fock state is defined by its occupation number η_i (see eq. 6.1). The strongly repulsive interaction between the atoms further stabilizes the sites with higher occupancy in the deep lattice, due to the energy offset between sites with different η_i.

We then apply a near-resonant light pulse with a duration t_p of a few μs. On multiply occupied sites, this near-resonant light pulse gives rise to a fast two-body loss process caused by light-assisted inelastic scattering of atoms [58, 109, 217, 218]. This loss acts as a parity projection of the on-site atom number η_i and results in the loss of all atoms for even atom numbers and the loss of all but one atom for odd atom numbers.

In fig. 6.9, we present two typical decay curves of the total atom number in the presence of the near-resonant light for varying pulse durations. Figure 6.9a shows the decay for a state that contains only a negligible fraction of sites with

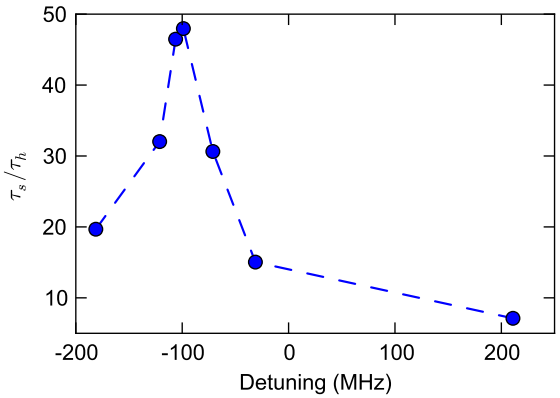

Figure 6.10: Ratio between the loss rate caused by off resonant scattering (τ_s) and by light assisted collisions (τ_h) for a varying detuning of the laser relative to the high-field imaging transition.

$\eta_i > 1$. In this case, the evolution of the atom number follows a simple exponential decay which is caused by off-resonant scattering of photons. If there is, however, a significant fraction of sites with a higher occupancy present, the decay curves look qualitatively different, as shown in fig. 6.9b. In this case, there is a very fast decay present during the first few microseconds in addition to the slower loss caused by off-resonant scattering. The inset of fig. 6.9b shows a close-up of the fast part of the decay, which clearly exhibits a time-constant much shorter than the slower part. We use the sum of two exponential decay functions as a model

$$N(t_p) = \frac{1}{N_{\text{total}}} \left(N_h \exp\left(-\frac{t_p}{\tau_h}\right) + N_s \exp\left(-\frac{t_p}{\tau_s}\right) \right), \tag{6.7}$$

where τ_h is the fast decay constant associated with the higher occupancies, τ_s is the slow decay time associated with off-resonant excitations and $N_{\text{total}} = N_h + N_s$ is the total atom number before the pulse. This fit function is plotted as the green line in figure 6.9b, with decay times $\tau_h = 7.6(1.2)\,\mu$s and $\tau_s = 355(36)\mu$s. As we are only interested in the losses on sites with $\eta_i > 1$, it is desirable that the decay caused by light-assisted collisions is much faster than the decay due to off-resonant excitations. We investigate the ratio of the two time constants τ_s and τ_h for various detunings and find an optimal ratio approximately 110 MHz red-detuned relative to the high-field imaging transition from the $\left|4^2S_{1/2}, m_I = +3/2, m_J = -1/2\right\rangle$ state to the $\left|4^2P_{3/2}, m_I = +3/2, m_J = -3/2\right\rangle$ state (see figure 6.10).

We extract a measure of the higher occupancy by comparing the number of atoms with (N_{pulse}) and without (N_{total}) a near-resonant light pulse with a duration of $t_{\text{pulse}} = 50\,\mu$s. In the presence of the near-resonant pulses, the parity projection on multiply occupied sites has taken place and only atoms on singly occupied sites as well as the remaining atoms from sites with $\eta_i = 3, 5, \ldots$ are left in the system.

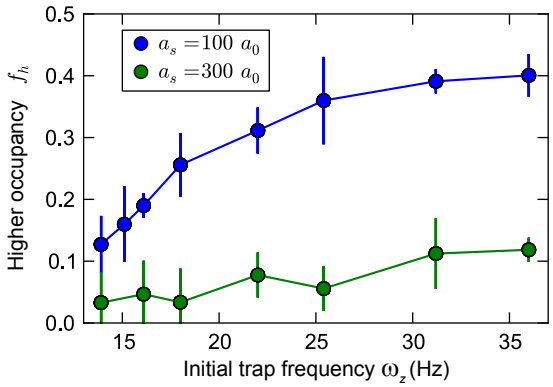

Figure 6.11: Higher occupancy f_h after loading the lattice for varying initial vertical trap frequencies ω_z. The blue data was taken at a scattering length $a_s = 100\,a_0$, the green data at $a_s = 300\,a_0$. The error bars are the standard deviation of the mean value of four measurements per point.

The measured atom number N_{pulse} is extrapolated to a pulse duration of $0\,\mu$s using the measured slow decay time: $N_{\text{par}} = N_{\text{pulse}} \exp(t_p/\tau_s)$. We then calculate an approximate measure of the fraction of atoms on multiply occupied sites

$$f_h = (N_{\text{total}} - N_{\text{par}})\,/N_{\text{total}}. \tag{6.8}$$

Note that, strictly speaking, f_h is only a lower bound on the fraction of atoms on multiply occupied lattice sites, because N_{par} also contains one atom per site with $\eta_i = 3, 5, \ldots$. While being exact for singly and doubly occupied sites, the measured fractions will be systematically too low whenever a significant amount of sites with $\eta_i \geq 3$ is present in the system. However, sites with an occupation of $\eta_i \geq 3$ are dynamically formed only in the weakly interacting regime, and even at $U/J = 0$, the difference between f_h and the real fraction of atoms on sites with $\eta_i > 1$ is small (see chapter 8.4.1).

6.3.4 Optimizing the Amount of Double Occupancies

The amount of double (and higher) occupancies in the initial state depends strongly on the interaction strength while loading the lattice as well as on the density of the condensate before ramping up the lattices. This can be seen in figure 6.11, which shows the higher occupancy f_h in the initial state depending on the initial trap frequency along the vertical axis before ramping up the lattice. One curve was taken at a scattering length $a_s = 100\,a_0$ (blue circles), while the other curve was taken at $a_s = 300\,a_0$ (green circles). In both curves, we can observe that f_h increases with increasing initial trap frequencies, highlighting the influence of a

higher initial density on f_h. Comparing the two curves, it can also be seen that a stronger repulsive interaction between the atoms leads to a suppression of higher occupancies. This effect is directly related to the higher interaction energy of a doubly occupied site at increasing U. For an adiabatic loading, the atoms stay in the lowest energy state and thus avoid forming doubly occupied sites. Note that if the interaction was attractive, $a_s < 0$, the formation of pairs would be energetically favorable. For fermions, attractive interactions were observed to lead to a strongly increased number of double occupancies in the system [219]. For bosons, attractive interactions can lead to a collapse of the BEC before loading the lattice [190, 191].

In the daily routine of conducting experiments, we do not directly measure the amount of double occupancies in the system to ensure their absence in the initial state. Instead, we rely on the fact that the presence of higher occupancies strongly suppresses the expansion dynamics of strongly interacting atoms (see chapter 8.4.4). We can thus simply determine the expansion velocity at large U/J to check whether fluctuations in the initial atom number or beam alignments might have increased the number of higher occupancies in the initial state.

6.4 Recording the Expansion Dynamics

6.4.1 Imaging Density Distributions

To record the expansion dynamics, we use *in-situ* imaging along the vertical (z) axis. Since the expansion dynamics in our experiments take place along the two horizontal axes, the evolution of the density distribution over time along these axes can be monitored simultaneously when imaging along the third, vertical axis.

Typical images of an evolution during the experiment are shown in fig. 6.12. The top row shows the column density of non-interacting atoms in a 1D lattice of depth $(8, 33, 33)E_r$ along (x, y, z), respectively. The second row shows non-interacting atoms in a 2D lattice of depth $(8, 8, 33)E_r$. In the second row, we can clearly see the limitations of the approximation of having a homogeneous lattice. For expansion durations t_E larger than $40\,\tau$, the square shape expected for non-interacting atoms becomes distorted due to residual potentials. We can also observe the tendency of the cloud to become "pillow shaped", i.e. the density distribution in the corners of the square shape tends to extend slightly further than at the edges. This is due to the finite size of the lattice beams. Perpendicular to the lattice axis, the lattice beams exhibit a Gaussian shaped intensity profile, with decreasing intensity at points further away from the beam axis (see chapter 5.1.2). This decreasing intensity leads to a decreasing lattice depth away from the axis, causing a faster absolute expansion velocity.

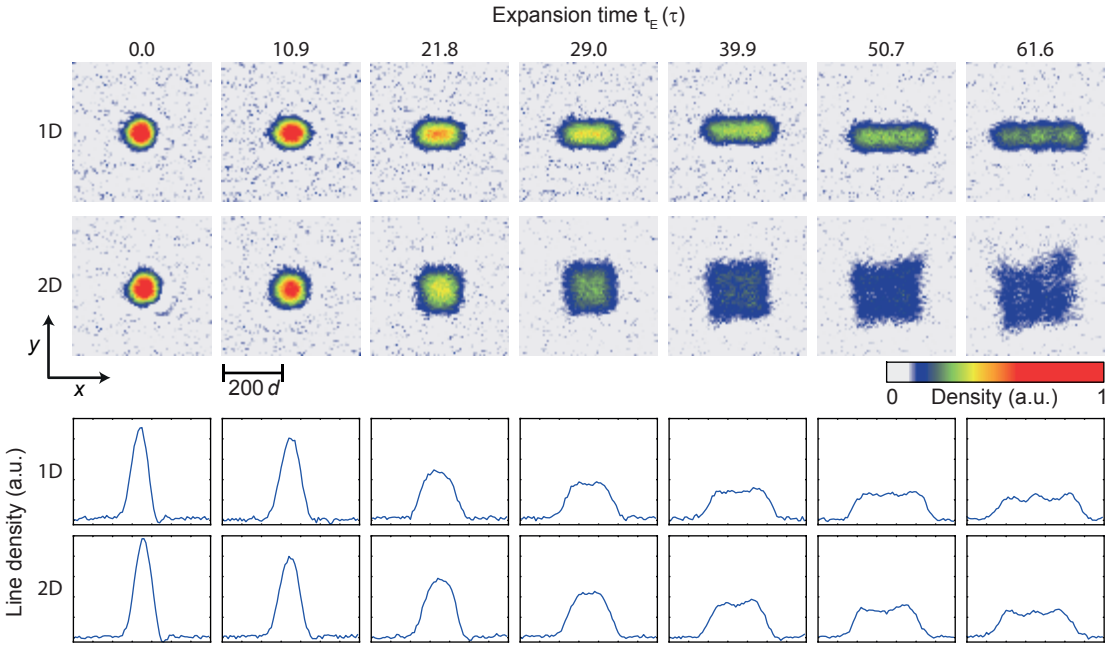

Figure 6.12: *In-situ* density distributions (Top two rows) during the expansion in an (8,33,33) E_r lattice (1D) and an (8,8,33) E_r lattice (2D) and the corresponding line density profiles (bottom two rows), obtained by integrating along the y-direction.

6.4.2 Extracting Cloud Sizes

In order to compare the expansion dynamics for varying parameters, we want to extract a measure for the size of the clouds from the density profiles. To do so, we first integrate the density distributions along one axis to obtain line density profiles $n_x(t_E)$. In the cases of expansions in one dimension, where the expansion takes place along the x-axis, we integrate along the y-axis of the distributions. In the 2D case, the expansion takes place along both axes and we can freely choose which axis to integrate over. Since we want to compare the expansion velocities in the 1D and 2D cases, we choose to also integrate along the y-axis. Such line density profiles, extracted from the absorption images shown in the two upper rows of fig. 6.12, are shown in the two lower rows of fig. 6.12.

In the following, we discuss two different measures for the cloud size that can be used to determine expansion velocities. The first measure is that of the half-width-at-half-maximum (HWHM) of the clouds, which is a reliable quantity when working with experimental data. The second measure is the rescaled cloud radius $\tilde{R}$, which is more sensitive to the detailed shape of the density profiles and will be used when investigating calculated density profiles, but can not be applied directly to our experimentally observed density distributions due to its sensitivity to imaging noise.

The Half-Width-at-Half-Maximum

To determine the evolution of the HWHM during the expansion, we use the following procedure: for each line density profile, we determine the maximum density $n_{\max}$. Starting from the outer edges of the profiles, we then move inwards in both directions and determine the positions where the density first reaches $n_{\max}/2$, using linear interpolation between the points. Half of the distance between these two positions is recorded as the HWHM of the cloud. Figure 6.13a shows some of the line density profiles of an expansion series in one dimension with an interaction $U/J = 0$ at various expansion durations t_E. The points where n_x reaches $n_{\max}/2$ are indicated by the dashed lines.

The HWHM has the disadvantage of being insensitive to the detailed shape of the cloud. However, since it is not *a priori* clear how the shape of the cloud will evolve during expansion experiments with varying interactions, any measure that relies on explicit assumptions about the cloud shape would not be suitable.

The Rescaled Radius $\tilde{R}$

The ideal measure for the cloud size would be that of the rescaled radius

$$\tilde{R}(t_E) = \sqrt{R^2(t_E) - R^2(0)}, \tag{6.9}$$

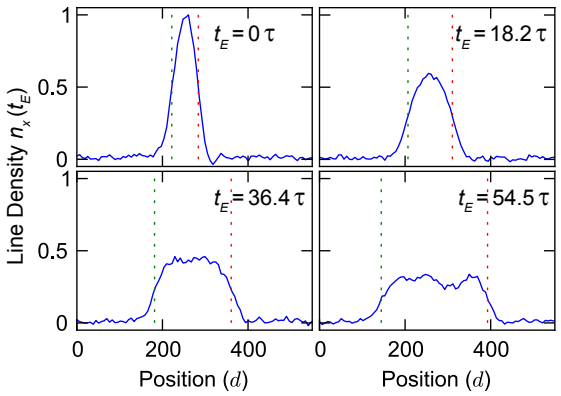

(a) Line density profiles n_x after various expansion durations. The positions where $n_x = n_{\max}/2$ are indicated by the dashed lines. Half of the distance between the dashed lines is recorded as the HWHM of the cloud.

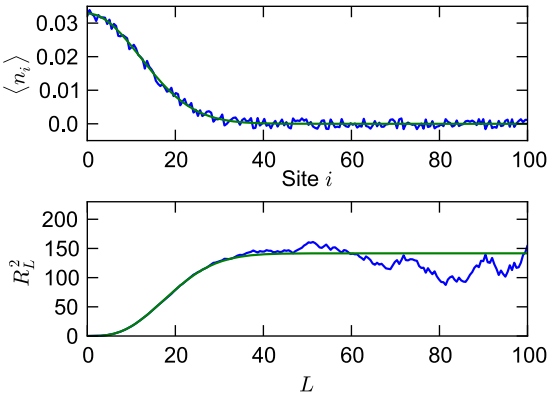

(b) Top panel: Gaussian density distribution (green) and the same distribution with added random noise (blue). Bottom panel: $R_L^2 = \sum_{i=1}^{L} \langle \hat{n}_i \rangle \, i^2$ with varying summation limit L for the two distributions. For large L, R_L^2 corresponds to R^2.

Figure 6.13

where $R^2(t_E)$ in a 1D lattice is given by

$$R^2\left(t_E\right) = \frac{1}{N} \sum_{i=1}^{L} \langle \hat{n}_i \rangle \left(t_E\right) \cdot \left(i - i_0\right)^2 d^2. \tag{6.10}$$

The sum runs over all L sites, $\langle \hat{n}_i \rangle$ is the expectation value (or measured value) of the atomic density on site i, i_0 is the center of the initial state and N is the total atom number. $\tilde{R}(t_E)$ has the advantage that it takes the full shape of the cloud into account by explicitly including the density at each lattice site.

The rescaled cloud radius $\tilde{R}(t_E)$ is a widely used measure to extract cloud sizes of calculated density distributions and to investigate their dynamics. However, it is not well suited for experimental data, due to the presence of noise at large distance. Any noise will be weighted with the square of the distance from the cloud center (see eq. 6.13), and thus will in general not average out for large distances.

In fig. 6.13b, we demonstrate this problem for an assumed Gaussian shaped density distribution (only one half of the distribution is shown). The top panel shows two density distributions, one with a simple Gaussian shape (green) and one with additional random noise added to it (blue). In the lower panel, the result of the summation $R_L^2 = \sum_{i=1}^{L} \langle \hat{n}_i \rangle \, i^2$ is shown for varying limits L. For the density distribution without noise, the value of R_L^2 becomes independent of L at large L and can be associated with the true value of R^2. This is possible because the density

distribution decays to zero for large i. For the density distribution with additional noise (blue), this is not the case. R_L^2 fluctuates strongly for large L, even though the random noise is centered around $\langle \hat{n}_i \rangle = 0$, due to the fact that it is weighted with the square of the distance $|i - i_0|$.

Thus, $\tilde{R}(t_E)$ is not suited for the analysis of experimental data. One can overcome this limitation by first fitting a peak function to the data that is guaranteed to approach zero for large i and then calculating $\tilde{R}(t_E)$ from these fit functions. This, however, only works if we have a pre-existing knowledge about the evolution of the shape of the density distribution during the expansion. For non-interacting atoms, this method is used in chapter 7.2 to verify that their expansion velocity agrees with theoretical predictions, but in the more general case of interacting atoms it is not easily applicable and requires a model for the expected cloud shapes. We will, however, use $\tilde{R}(t_E)$ when investigating the evolution of calculated density profiles in chapter 8, as it is more sensitive to the exact shapes of the distributions than the HWHM.

6.4.3 Extracting Expansion Velocities

The Radius Expansion Velocity v_r

As discussed above, the rescaled radius $R(t_E)$ can be used to investigate the dynamics of calculated density distributions. We can then define the radius expansion velocity v_r as

$$v_r(t_E) = \frac{d\tilde{R}(t_E)}{dt_E}. \tag{6.11}$$

For non-interacting atoms, v_r is equal to a more intuitive quantity, namely the average velocity

$$v_{\mathrm{av}}(t_E) = \sqrt{\frac{1}{N\hbar} \sum_q \left(\frac{\partial \epsilon_q}{\partial q} \right)^2 n_q(t_E)}, \tag{6.12}$$

with the one-particle dispersion relation $\epsilon_q = -2J \cos(qd)$. This quantity is simply the average over the group velocity at a certain q, weighted by the respective density in quasimomentum space. For non-interacting atoms, $v_{\mathrm{av}}(t_E)$ is constant over time because no redistribution in $n_q(t_E)$ takes place during the evolution and its value can be directly calculated from the initial quasimomentum distribution. In the case of $n_q(0) = \text{const.}$ in the first Brillouin zone and an expansion in 1D, it is given by $v_{\mathrm{av}} = \sqrt{2}(d/\tau)$.

Comparing v_r and v_{av} allows for some further insight into the expansion dynamics. In the non-interacting case, v_r is always equal to the average velocity v_{av}. For interacting atoms, however, this relation is in general not satisfied. Even if $n_q(t_E)$ were to stay constant during the evolution, the fact that scattering events can exchange

the momenta of two atoms while leaving n_q unchanged can lead to a significantly different evolution of $\tilde{R}(t_E)$, and hence to a different v_r, than predicted by the average velocity v_{av}. Thus, deviations between v_r and v_{av} are an indication of the effects of scattering on the evolution dynamics of interacting atoms, which will be discussed in further detail in chapter 8.4.3. Very large differences between v_r and v_{av} arise in the hard-core boson regime in 1D, where quasi-condensation leads to a strong increase in v_{av} which is not reflected in the evolution of the density distribution (see chapter 9).

Note that we can generalize the definition of $\tilde{R}(t_E)$ to dimensions higher than one by defining

$$R^2\left(t_E\right) = \frac{1}{N}\sum_{i=1}^{N}\left\langle\hat{n}_i\right\rangle\left(t_E\right)\left|\mathbf{r}_i - \mathbf{r}_0\right|^2, \tag{6.13}$$

where $|\mathbf{r_i} - \mathbf{r}_0|$ is the distance between site i and the center of the initial state. $\tilde{R}(t_E)$ is again defined as $\sqrt{R^2(t_E) - R^2(0)}$ and, in the non-interacting case, we expect it to behave as

$$\tilde{R}(t_E) = v_r t_E. \tag{6.14}$$

The radius expansion velocity for our given initial state of completely localized atoms is then given as

$$v_r = \sqrt{2D}\frac{d}{\tau}, \tag{6.15}$$

where D is the dimensionality of the investigated system.

The Core Expansion Velocity v_c

For the experimental data, we determine the cloud size using the HWHM, as $R(t_E)$ cannot be determined reliably due to the noise on the images. To extract the core expansion velocities v_c, we apply linear fits to the time evolution of the HWHM. For non-interacting atoms, where the dynamics during an expansion are dominated by the atoms with the largest group velocities (see section 6.2), we expect the expansion velocity of the HWHM to be given by $v_c = 2d/\tau$.

Figure 6.14 shows the time evolution of the HWHM extracted from the data partly shown in fig. 6.13a with the linear fit plotted as the solid line. We use an equation of the form

$$\mathrm{HWHM}(t_E) = r_0 + v_c t_E, \tag{6.16}$$

where r_0 is a second, free parameter. The fitted velocity is $v_c = 2.20(5)d/\tau$, where the error is given by the standard deviation of the fit. The residual deviation from the theoretically predicted value of $v_c = 2d/\tau$ can be accounted for by noting that we observe long term fluctuations in the lattice depths on the order of 5% over several days. These fluctuations are most likely caused by small thermal drifts in the beam alignment. We do not specify these fluctuations as statistical errors in our

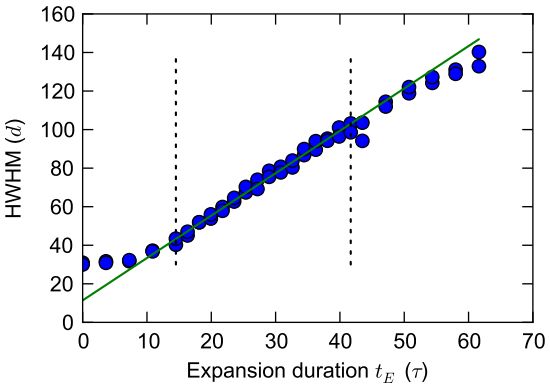

Figure 6.14: Time evolution of the HWHM during an expansion in one dimension at U/J=0. The solid line is a linear fit to the data with a fit range indicated by the dashed lines.

measurements, as they are in general highly correlated for measurements taken on the same day, but they add an overall uncertainty in the absolute value of the lattice depth. Taking this into account, the agreement between our experiments and the theoretical prediction is very good.

The linear fit is not applied to the complete data set, but instead within a certain fit range. Points at times shorter than the fit range are left out, as well as points at times larger than the fit range. The reasons for this are as follows: for times larger than the fit range, the atoms with the highest group velocities will already reach the outskirts of the lattice potential, where the assumption of homogeneity is not valid anymore. This is due to residual global potentials caused by slight mismatches between the beam sizes of the lattice beams and the dipole trap beams as well as due to the fact that the lattice depth is given by the local intensity of the lattice beams. Since these beams have an overall Gaussian shaped intensity distribution, the lattice will be less deep the further away the atoms are from the center of the beam. For short expansion durations, the cloud shape is not determined by the evolution dynamics, but rather by the initial cloud shape given by the initial confining potential. This convolution with the initial size leads to a slower evolution of the HWHM during the first tunneling times. For the investigation of $\tilde{R}(t_E)$, this initial size effect is mitigated by subtracting $R^2(0)$ in eq. 6.9. The evolution of the HWHM does not in general follow the same square-root behavior as $R(t_E)$, and a subtraction of the initial size cannot be done as easily.

Figure 6.15 demonstrates the effects of an initial state with a finite extension $R_c(0)$, given by the initial HWHM of the atom cloud, on the evolution of the density distribution during the expansion. The top row shows the density distributions, calculated as described in section 6.2, for initial states of localized atoms with a varying initial extension. For very small initial states, the characteristic density

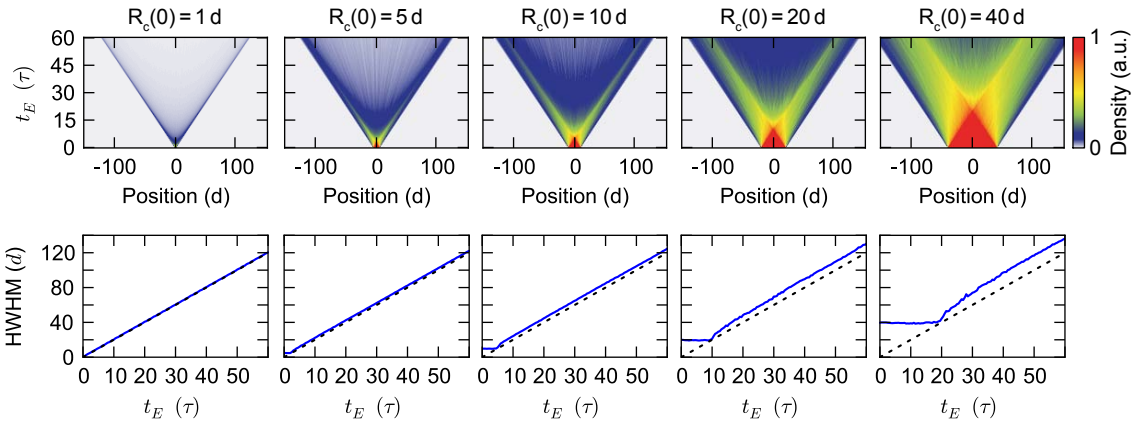

Figure 6.15: Top row: Calculated density profiles for states with varying initial radius $R_c(0)$. Bottom row: Evolution of the extracted HWHM (solid blue lines). For comparison, the dashed lines show an evolution $\mathrm{HWHM}(t_E) = v_c t_E$ with $v_c = 2d/\tau$.

maxima, traveling outwards with a velocity of $2d/\tau$, form immediately as narrow peaks. For larger initial states, these maxima become broader and are formed only after the initial high density core has dissolved, but are moving with the same high velocity.

This behavior can be investigated more quantitatively by extracting the evolution of the HWHM of the calculated density distributions, which is plotted in the bottom row (blue lines) for each initial $R_c(0)$. For comparison, the dashed line in each plot shows an expansion starting at zero with the maximum velocity $v_c = 2d/\tau$. The evolution of the HWHM is consistent with a simple linear scaling with $R_c(0)$. The HWHM stays approximately constant until $t_E \approx \tau R_c(0)/(2d)$, then evolves faster than $2d/\tau$ for a few tunneling times before approaching the asymptotic core expansion velocity of $v_c = 2d/\tau$. The HWHM at large t_E is then approximately $R_c(0)/2$ larger than that observed in an expansion with $R_c(0) = 0$.

6.5 Summary

In this chapter, we have shown that it is indeed possible to use ultracold atoms in optical lattices to investigate expansion dynamics in homogeneous 1D and 2D Bose-Hubbard systems. We can create initial states that are products of local Fock states with all $\eta_i \in \{0, 1\}$, release them into the lattice and investigate the evolution of the density distribution over time. The global external potentials can be compensated by additional dipole trap beams, and the expansion dynamics are in good agreement with the theoretical expectations for non-interacting atoms. We have furthermore introduced the HWHM and the core expansion velocity v_c as appropriate measures

for the quantitative analysis of the dynamics, which we will use in the following chapters to investigate the expansion of interacting fermions (chapter 7) and bosons (chapter 8).

Chapter 7

Expansion Dynamics of Fermions in the Hubbard Model

The main focus of this thesis is on the dynamics of ultracold bosons in optical lattices. However, results obtained earlier on the dynamics of a two-component Fermi gas in homogeneous lattices [71] are very instructive in comparison to later results for the bosonic case. In this chapter, we first briefly discuss the experimental procedure used to investigate the expansion dynamics of interacting fermions in the Fermi-Hubbard model. A more detailed description of the experimental procedures and results can be found in [71, 196]. The creation of the ultracold Fermi gases is discussed extensively in [92] and will be omitted here.

We then investigate the behavior of non-interacting fermions during expansions in the lattice, which is shown to be directly analogous to that of the non-interacting bosons discussed in chapter 6. This is a direct consequence of the initial states of both systems consisting of completely localized atoms.

Finally, we turn to the dynamics of interacting fermions in 2D lattices and find a strong reduction of expansion velocities with increasing interaction strength accompanied by the appearance of strongly bimodal density distributions. This behavior is completely symmetric with respect to the sign of the interaction, as a consequence of a dynamical symmetry of the Hubbard Hamiltonian. In a collaboration with the group of Prof. Achim Rosch, a semi-classical theory based on a Boltzmann equation in relaxation time approximation was developed that successfully describes the behavior of interacting atoms in terms of diffusive dynamics.

7.1 Initial State and Experimental Sequence

The preparation of the initial state is analogous to the procedure described in chapter 6.1 for the expansion experiments with bosons. However, instead of preparing a state of localized atoms with no doubly occupied sites, we create a two component band insulator state consisting of one fermion of each component per lattice site.

The spin states used are the $|F = 9/2, m_F = -9/2\rangle$ and the $|F = 9/2, m_F = -7/2\rangle$ states of ^{40}K in an equal mixture with a total of $N \approx 1 - 1.5 \times 10^5$ atoms. The initial

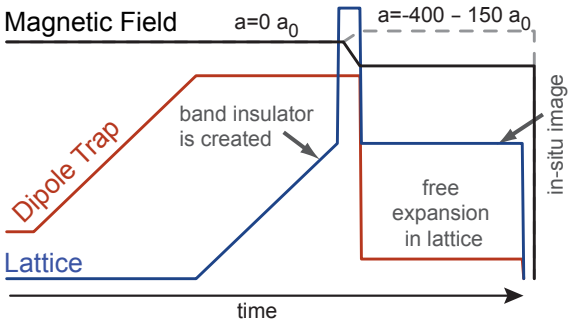

Figure 7.1: Sketch of the experimental sequence for the preparation of the initial states and the expansion measurements. Figure reprinted from [71].

temperature T of the cloud of Fermions before loading it into the optical lattice, given in units of the Fermi temperature T_F, is $T = 0.13(2)\,T_F$.

Figure 7.1 shows a sketch of the employed experimental sequence for the initial state preparation and the expansion measurements. Starting in an optical dipole trap, the trap frequency is first increased to approximately $2\pi \times 100\,\mathrm{Hz}$ along the horizontal (x, y) directions and $2\pi \times 400\,\mathrm{Hz}$ along the vertical (z) direction to increase the density of the cloud of atoms. Then, the intensity of the blue-detuned lattice beams with a wavelength $\lambda = 738\,\mathrm{nm}$[1] is linearly increased over 56 ms to a depth of $8\,E_r$ along all directions. In a second ramp of only $200\,\mu s$ duration, the lattice depth is further increased to $20\,E_r$. The atoms are kept in this deep 3D lattice, combined with a strong harmonic potential, for 40 ms to induce a complete dephasing of all lattice sites with respect to each other [97] and effectively localize the atoms. During the hold time in the deep lattice, the interaction between the two species of fermions is adjusted using a Feshbach resonance located at $B_0 = 202.1\,\mathrm{G}$ [220]. While loading the lattice, the field is at $B = 209.1\,\mathrm{G}$, corresponding to vanishing interactions. For the expansion measurements, the field is changed to values between 206 G and 260 G, corresponding to scattering lengths in the range of $-400\,a_0$ to $+150\,a_0$. Due to the suppressed tunneling in the deep lattice, the state after this preparation procedure has a well defined density distribution, independent of the final interaction between the atoms. This ensures that the following expansion measurements always start from the same initial state.

The expansion dynamics are initiated by a simultaneous quench in the lattice depth and the external confining potential. The lattice depth is ramped down linearly within $200\,\mu s$ to values between $4\,E_r$ and $15\,E_r$ and the intensities of the dipole trap beams are simultaneously adjusted to compensate the anti-confinement induced by the lattice beams (see 6.3.1). The expansion then takes place in a homogeneous

[1] A slightly different wavelength compared to the experiments with ^{39}K is used to minimize the light induced losses (see chapter 5.1.4)

lattice, governed by the Fermi-Hubbard Hamiltonian

$$\hat{H}_{\mathrm{FH}} = -J \sum_{\langle i,j\rangle\sigma} \hat{c}^{\dagger}_{i\sigma}\, \hat{c}_{j\sigma} + U \sum_{i} \hat{n}_{i\uparrow}\hat{n}_{i\downarrow}, \tag{7.1}$$

where J denotes the tunneling, U the on-site interaction between the two species, and i and j are site indices. $\langle i,j\rangle$ indicates a summation over nearest neighbors and the index $\sigma \in \{\uparrow,\downarrow\}$ denotes the two different species of fermions. $\hat{c}^{\dagger}_{i\sigma}$ and $\hat{c}_{i\sigma}$ are the creation and annihilation operators for a fermion of species σ at site i while $\hat{n}_{i\sigma} = \hat{c}^{\dagger}_{i\sigma}\hat{c}_{i\sigma}$ is the density of species σ on site i. In the following discussion, τ refers to the tunneling time $\hbar/J$, while d is the lattice constant, given by $\lambda/2$.

For the data shown in figures 7.2, 7.3, and 7.4, the expansion takes place in a 3D lattice geometry. Note that due to the gravitational potential, the dynamics along the vertical axis are influenced by the acceleration due to gravity and Bloch oscillations in addition to the expansion dynamics [221]. As the vertical axis is also our imaging axis, we always average along this direction when taking experimental data and expect no qualitative differences to be visible in our results. However, For the data that is quantitatively compared to theoretical predictions (shown in figure 7.7), the experiment is conducted in a 2D geometry. In this case only the two lattice axes along the x- and y-direction are ramped down at the start of the expansion, while the vertical lattice is kept at a depth of $20E_r$ to inhibit tunneling along this direction. In these case, we use $J_{2\mathrm{D}}$ to denote the tunneling along the x- and y-directions and neglect tunneling along the z-direction.

7.2 Noninteracting Fermions in 2D

Figure 7.2 shows the evolution of the fermions in the 3D lattice at $U = 0$. Completely analogous to the evolution of noninteracting bosons in 2D (see fig. 6.12), we can observe how the round shape of the initial density distribution is changed into the characteristic square shape given by a ballistic expansion with the group velocity distribution of the initial state. Both in the bosonic expansions (see chapter 6.2) and in this case of expanding fermions, the initial state consists of completely localized atoms, with a quasimomentum distribution n_q that is flat over the first Brillouin zone. Without interactions, n_q remains constant throughout the complete evolution in the lattice and the density distribution after a given expansion time t_E is simply given by the sum over all expanded single particle wave-functions. As the evolution of these single-particle wavefunctions is identical in the bosonic and the fermionic case, the density distributions necessarily look the same for non-interacting particles starting from identical initial states, regardless of the bosonic or fermionic nature of the system.

For long expansion durations ($t_E > 50\,\tau$), the two characteristic effects that limit

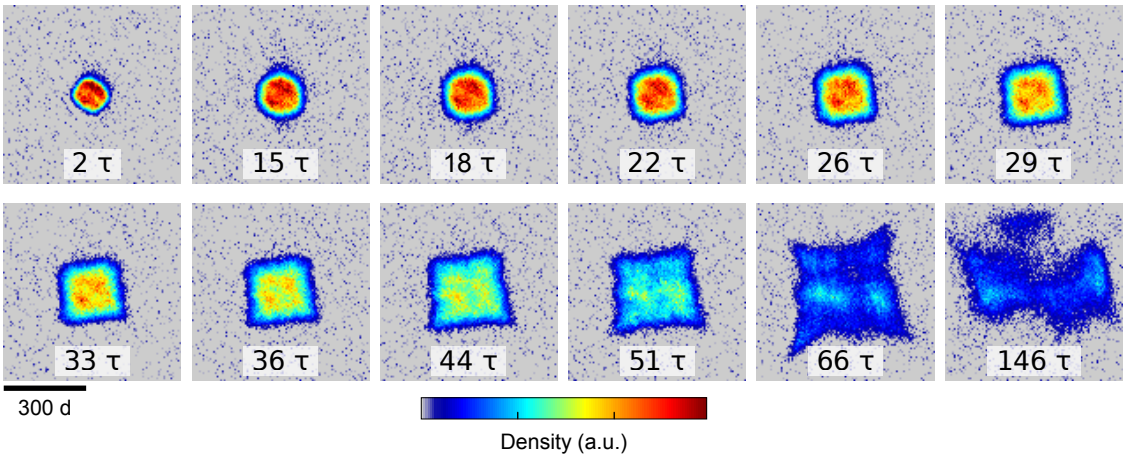

Figure 7.2: Column density profiles of expanding fermions in a 3D, $8E_r$ deep lattice for $U = 0$, imaged along the z-direction. The evolution time t_E is indicated in each density plot. Figure adapted from [196] with kind permission of the author.

the accessible time scales of the expansion measurements become visible. In the density plot for $t_E = 66\,\tau$, we can observe the characteristic *pillow shape* of the cloud of atoms, where the evolution appears to be faster along the diagonals than along the main axes. This is due to the finite size of the lattice beams, as discussed in chapter 6.4.1. In the plot for $t_E = 146\,\tau$, another experimental limitation becomes obvious. Due to slight mismatches in the beam waists of the dipole trap beams and the lattice beams, as well as misalignments of these beams, the overall global potential can never be made completely flat. The residual inhomogeneities lead to a distortion of the cloud shape for large expansion durations. For a quantitative analysis of the evolution, we thus only use the data for $t_E \lesssim 45\,\tau$.

To confirm that the evolution of non-interacting fermions indeed follows the quantum-mechanical predictions, we determine the radius R of the clouds. As discussed in chapter 6.4.2, this cannot be done straightforwardly from the measured data, due to experimental noise. In this case, a 2D gaussian fit function is used, from which the radius can be extracted (see [196] for more details). The total evolution is then fitted with a function $\tilde{R}(t_E) = \sqrt{R(t_E) - R(0)} = v_r t_E$ to determine the radius expansion velocity v_r (see chapter 6.4.2 for more details).

In fig. 7.3, we plot v_r of non-interacting expansions for various lattice depths. As expected, the expansion velocity is directly proportional to the tunneling J and agrees with the quantum-mechanical prediction of eq. 6.15, shown as the black line.

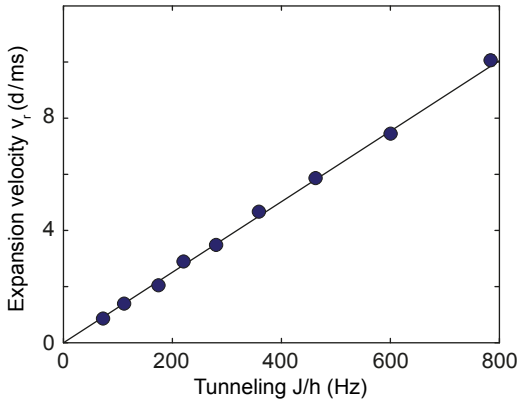

Figure 7.3: Expansion velocity v_r for various lattice depths (circles). Fit errors are comparable to the size of the data points. The black line is the quantum-mechanical prediction. Figure reprinted from [71].

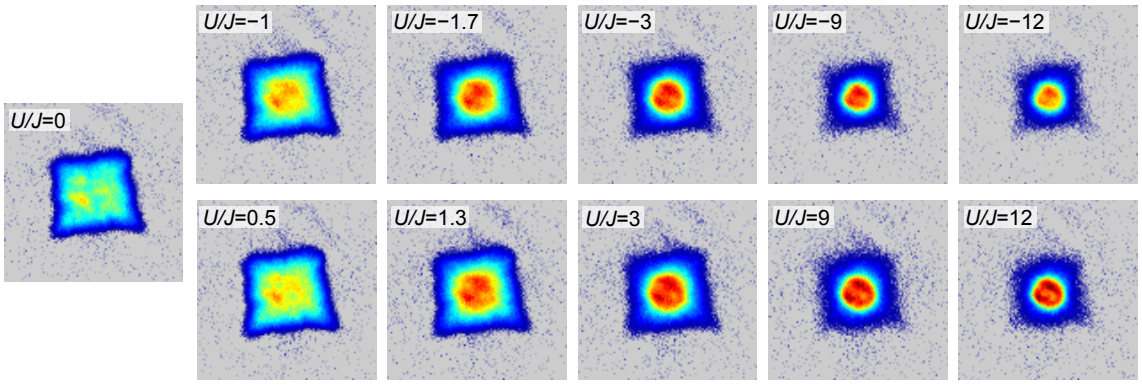

Figure 7.4: Column density profiles of fermions in a 3D, $8E_r$ deep lattice after an expansion for $t_E = 45.5\,\tau$ at various interactions U/J. Figure adapted from [71].

7.3 Interaction Effects

The observed dynamics of the expanding fermions change dramatically when interactions are introduced into the system. This can be seen in fig. 7.4, which shows the density distribution after an expansion for $t_E \approx 45.5\,\tau$ for various interactions U/J in a 3D lattice with a depth of $8\,E_r$. The density distribution for $U/J = 0$ shows the aforementioned square shape of ballistically expanding, free particles. For increasing $|U/J|$, the dynamics gradually change to an almost bimodal expansion. Already at a moderate $|U/J| \approx 3$, a significant amount of atoms remains in the center of the distribution and retains the round shape of the initial state while only a few atoms are visible in a square shaped ballistic background.

This behavior is directly related to the breaking of integrability in this system.

While it is integrable in the non-interacting case (see chapter 3.4), a system of interacting fermions in 2D or 3D is non-integrable and can thermalize. The frequent collisions occurring in the high density region of the cloud then drive the system to an approximate local thermal equilibrium [77, 222], leading to diffusive dynamics. As the diffusion equations governing these dynamics are rotationally invariant, the main portion of the cloud keeps its round initial shape.

In the outer parts of the cloud, the density becomes so low that scattering events between two particles become very rare. Here, the assumption of local thermalization breaks down and the particles behave ballistically again, as their mean free path becomes larger than the cloud size. This leads to the square shaped background that is always present in fig. 7.4.

Interestingly, the onset of the bimodal evolution dynamics is independent of the sign of U. At first glance, this seems counterintuitive, as repulsive interactions increase the total energy of the initial state while attractive interactions reduce it. One could thus naïvely expect faster dynamics in the repulsive case. However, due to the high symmetry of the dispersion relation in the lattice, combined with a highly symmetric initial state, it can be shown that the behavior has to be exactly equal for positive and negative U.

7.3.1 $U \leftrightarrow -U$ Symmetry

The apparent symmetry of the expansion velocities for various interactions with respect to a transformation $U \to -U$ observed in fig. 7.4 reflects a fundamental dynamical symmetry of the Hubbard Hamiltonian for certain initial states and observables. If both the initial state as well as the observable in question are invariant under time reversal, the dynamics of the observable remain unchanged by the transformation $H \to -H$. In the homogeneous case, the Hamiltonian consists only of the kinetic term and the interaction term:

$$H = H_{\text{kin}} + H_{\text{int}}, \quad H_{\text{kin}} \propto J, \quad H_{\text{int}} \propto U. \tag{7.2}$$

From this, we can infer that a time inversion of the system, achieved by inverting the sign of the Hamiltonian, is equivalent to exchanging the signs of U and J:

$$H \to -H \Leftrightarrow J \to -J \text{ and } U \to -U. \tag{7.3}$$

Thus, if the evolution is also invariant under the transformation $J \to -J$, it necessarily follows that it has to be invariant under the transformation $U \to -U$. Due to the bipartite nature of the lattice and the resulting symmetry of the dispersion relation in the tight binding approximation, $\epsilon_{\mathbf{q}} = -2\sum_m \cos(q_m d)$ (here, the sum runs over the spatial dimensions), changing the sign of the tunneling J can be expressed by shifting all momenta $\mathbf{q} \to \mathbf{q} + (\pi, \pi, \pi)/d$. Thus, if the initial state $|\Psi_{\text{init}}\rangle$ and the observable are invariant under time reversal as well as under the transformation

$\mathbf{q} \to \mathbf{q} + (\pi, \pi, \pi)/d$, it follows that the evolution of the observable is invariant under a transformation $U \to -U$.

A rigorous proof of this dynamical symmetry can be found in [71] and [196]. Note that the proof does not rely on the fermionic nature of the system and can thus be directly applied to bosonic systems as well, which will be relevant in chapter 8.

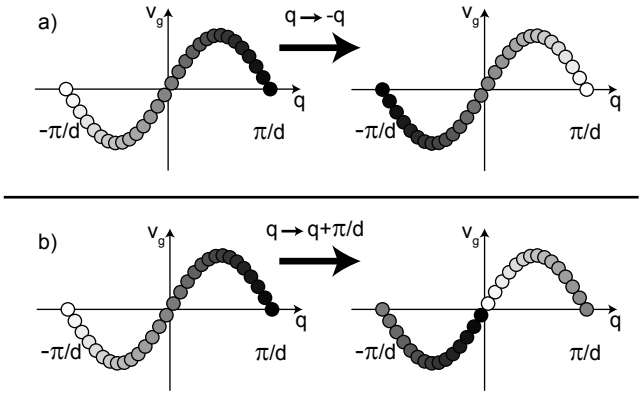

Figure 7.5: Visualization of the effects of the transformations $q \to -q$ (a) and $q \to q + \pi/d$ (b) on the quasimomentum distribution of a state with $n_q = \text{const}$. Each plot shows the group velocities of quasimomentum states spaced evenly in q. The color of the circles indicates where a point in q of the initial distributions is mapped to. For states with $n_q = \text{const.}$, no net redistribution of momentum takes place under the two transformations.

The initial state of our experiment is always one with completely localized atoms, resulting in a quasimomentum distribution n_q that is constant over the first Brillouin zone. This implies that n_q is symmetric about $\mathbf{q} = 0$. For such a distribution, the condition of time-reversal symmetry is always fulfilled, as the transformation $t \to -t$ can be represented by exchanging all momenta $\mathbf{q} \to -\mathbf{q}$. For distributions symmetric about $\mathbf{q} = 0$, this transformation does not change the overall distribution of momenta. The effect of such a transformation on the initial state with $n_q = \text{const.}$ is visualized in fig. 7.5 (a), where each circle represents one state in momentum space. While the transformation changes the position of each point in momentum space, the overall distribution stays constant and results in exactly the same time evolution.

The second requirement of symmetry with respect to the transformation $\mathbf{q} \to \mathbf{q} + (\pi, \pi, \pi)/d$ is also fulfilled for the initial states of fully localized atoms. Figure 7.5(b) shows the effect of such a transformation on the aforementioned initial state. Again, even though each individual state is shifted in q, due to the high symmetry of the global initial state no net change to the quasimomentum distribution takes place.

The observable we are concerned with in this and the next chapter is the atomic

density $\hat{n}_i(t) = \hat{c}^\dagger_{i\uparrow}\hat{c}_{i\uparrow} + \hat{c}^\dagger_{i\downarrow}\hat{c}_{i\downarrow}$. This observable neither depends on $\mathbf{q}$ nor on t and thus also fulfills the conditions stated above.

Note that another important observable, namely the quasimomentum distribution n_q, does not fulfill the criteria for the dynamical symmetry. As n_q depends explicitly on $\mathbf{q}$, it is in general not invariant under either of the two discussed transformations. Considering the limit of long evolution times for our given initial state for positive and negative U, it can be seen straightforwardly that different quasimomentum distributions have to emerge. In the case of $U < 0$, the initial band insulator state has a negative interaction energy E_{int}. For long evolution times, however, all doubly occupied lattice sites will dissolve and $E_{\mathrm{int}} \to 0$. As the total energy of the system is conserved, this must be accompanied by a reduction in kinetic energy which leads to an accumulation of density in quasimomentum space around $q = 0$. For $U > 0$, however, the initially positive E_{int} has exactly the opposite effect. In the long time limit, this energy is converted into an increased kinetic energy, which results in an accumulation in quasimomentum space around $q = \pi$. It is only due to the symmetry of the group velocity relation in the lattice that these two states result in the same evolution of the density distributions in real space.

7.3.2 Diffusive Dynamics from the Boltzmann Equation

The description of the observed dynamics of interacting fermions in terms of diffusive dynamics was developed in collaboration with the group of Prof. Achim Rosch [71].

When speaking about diffusion, one usually considers the motion of a particle inside a medium. In these cases, diffusion constants, which in general are inversely proportional to the density of the medium, are usually assumed to be constant during the evolution of the particle. In our experiment, however, we are looking at an entirely different situation. For a two-component fermi gas, one species acts as the scattering medium for the other species, and in a non-equilibrium situation changes in the density of either species modify the diffusion constant for the other. It is thus necessary to explicitly include the dependence of the diffusion constant on the density $D = D(n)$ into the diffusion equation of the form:

$$\delta_t n = \nabla D(n) \nabla n. \tag{7.4}$$

Here, we assume the evolution for the densities n_σ of the individual species to be equal, so we can describe the evolution in terms of the total density $n = n_\uparrow + n_\downarrow$. The asymptotic behavior of $D(n)$ for small n can be understood by considering that D is proportional to the time τ_{sc} between scattering events, which is proportional to $1/n$ for small densities. Thus, $D(n)$ diverges as $1/n$ for small densities. This makes eq. 7.4 a highly singular *superfast* diffusion equation, leading to curious, but rather unphysical consequences [71, 223]. Far away from the center of the cloud, however, such a hydrodynamical approach breaks down and the expansion is no longer

governed by the diffusion equation but by the dynamics in the low density tails. Here, the atoms scatter so rarely that their dynamics become completely ballistic again, with a maximum group velocity of $v_g = 2d/\tau$ along each spatial dimension. This crossover from diffusive to ballistic dynamics regularizes the singular diffusion equation and re-establishes a physically meaningful behavior.

To describe the dynamics in the diffusive regime as well as in the ballistic tails, a semi-classical Boltzmann equation in relaxation time approximation of the form

$$\delta_t f_{\mathbf{q}} + \mathbf{v}_{\mathbf{q}} \nabla_{\mathbf{r}} f_{\mathbf{q}} + \mathbf{F}(\mathbf{r}) \nabla_{\mathbf{q}} f_{\mathbf{q}} = -\frac{1}{\tau(\mathbf{n})} \left(f_{\mathbf{q}} - f^0_{\mathbf{q}}(\mathbf{n}) \right) \tag{7.5}$$

can be used, where $\mathbf{n}$ is a vector (n, e) consisting of the density $n(\mathbf{r}, t)$ and the local energy $e(\mathbf{r}, t)$. The equation describes the time evolution of the semi-classical momentum distribution $f_{\mathbf{q}}(\mathbf{r}, t)$ as a function of time t and position $\mathbf{r}$ under the influence of a force $\mathbf{F}$. The transport scattering time $\tau(\mathbf{n})$, which describes the relaxation of the system towards an equilibrium momentum distribution $f^0_{\mathbf{q}}$, is determined from a microscopic calculation of the diffusion constant for small interactions (see supplementary information to [71]). Results of numerical simulations based on eq. 7.5 are shown in fig. 7.6.

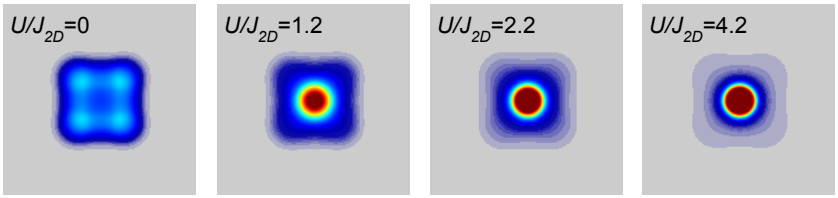

Figure 7.6: Density profiles from numerical simulations of the Boltzmann equation (eq. 7.5) in 2D for various interactions $U/J_{2\mathrm{D}}$ at $t_E = 45.5\,\tau$. The calculations were performed by S. Mandt and the figure is adapted from [71].

The profiles resulting from the numerical simulations capture the qualitative features of the expanding fermions very well. The square shape of ballistically expanding atoms at $U/J_{2\mathrm{D}} = 0$ already develops a round high density core region for small interactions ($U/J_{2\mathrm{D}} = 1.2$). For increasing interaction strength, the dynamics become completely dominated by the high density region and only very few atoms leave the core and enter the ballistic low density regions.

7.4 Core Expansion Velocities

In order to investigate the effects of increasing interaction strengths more quantitatively and allow for a more detailed comparison, we extract expansion velocities

from the density profiles. While fitting a 2D Gaussian function to the distributions works reasonably well for the profiles of non-interacting atoms, it becomes rather arbitrary for the cloud shapes observed for interacting atoms. This is due to the bimodal nature of the profiles with a high density peak and low density ballistic wings, which cannot be captured by a simple 2D Gaussian peak. As discussed in chapter 6.4.2, extracting the radius R directly from the measured density profiles is not possible, due to the strong susceptibility of this quantity on imaging noise far away from the center of the cloud. Thus we choose the core width R_c, given by the HWHM of the cloud, as a robust measure for the cloud size (see 6.4.2). This quantity is very sensitive to the shape of the cloud. Without a strong central core present, the HWHM tracks the evolution of the ballistic atoms but for a significant fraction of atoms in a central core, it tracks the evolution of this high density region.

The expansion velocities v_c in this case are extracted by fitting the evolution of R_c with a function $R_c(t_E) = \sqrt{R_c(0)^2 + v_c^2 t_E^2}$, where R_0 and v_c are free parameters. The resulting core expansion velocities for expansions in 2D lattice geometries at varying lattice depths J_{2D} and interaction strengths U/J_{2D} are shown in fig. 7.7 as circles. The lattice depth along the x- and y-direction is indicated by the color of the circles.

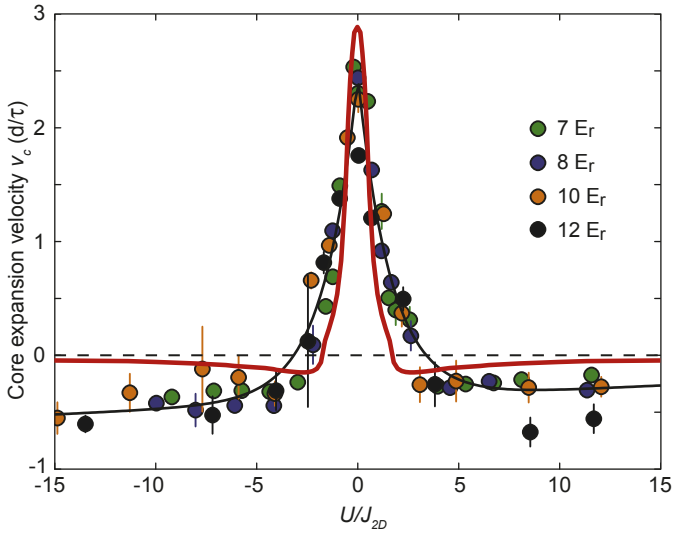

Figure 7.7: Core expansion velocities v_c vs. interaction U/J_{2D} for expanding fermions in 2D lattices with varying lattice depth (indicated by the color of the circles). The red line is the result of 2D numerical simulations of eq. 7.5. The numerical simulations were performed by S. Mandt [71], the figure is adapted from [196] with kind permission of the author

As expected, all data points for different lattice depths fall on one curve, when the units are chosen as the natural units of the Hamiltonian (eq. 7.1), which only

depends on U and J_{2D}. For small values of $|U/J_{2D}|$, v_c is large and agrees with the maximum group velocity possible in a lattice, $v_g^{\max} = 2d/\tau$. As soon as the interaction strengths is increased, however, v_c is drastically reduced. Such a reduction is naturally expected for large $|U/J_{2D}| > 8$, where the interaction energy of a doubly occupied site is on the order of the band-width and the dissolution of these double occupancies becomes energetically suppressed. However, we observe that v_c already drops to zero at $|U/J_{2D}| \approx 3$, reflecting the significant qualitative change in the dynamics already observed in the density profiles shown in fig. 7.4. For even larger $|U/J_{2D}|$, the core starts to shrink over time, leading to negative values for v_c. This can be interpreted as an essential freezing of the dynamics of the core, which only dissolves by emitting particles. As R_c follows the evolution of the edges of the core, this leads to a decreasing R_c over time and results in negative values for v_c.

The evolution of v_c with changing $|U/J_{2D}|$ is captured very well by the results obtained from numerical simulations of the Boltzmann equation (eq. 7.5) shown as the red line in fig. 7.7. Both the fast decay of v_c as well as the negative expansion velocities can be observed. The full quantum dynamics is certainly more complex than the description in terms of a semi-classical Boltzmann equation, including, e.g., the formation of long distance entanglement in the system [81, 224] and the existence of (repulsively) bound pairs [146]. However, the good agreement between the semi-classical model and our experiments are a clear indication that the interpretation of the dynamics in terms of local thermalization and diffusion does indeed give an adequate description of the main features observed in our experiments.

7.5 Summary

In this chapter, we investigated the dynamics of interacting fermions in optical lattices. We showed that the possibility of creating homogeneous lattice potentials in our experiment provides a versatile setup for studies on the non-equilibrium dynamics of quantum systems. As a main conclusion, we established that the dynamics of fermions in 2D lattices can be well described by a theory based on diffusive dynamics in a Boltzmann equation. This supports the notion that the effects of local relaxation and thermalization play a significant role in 2D Hubbard systems, which we also investigate in the next chapter in the context of the Bose-Hubbard Hamiltonian.

Chapter 8

Expansion Dynamics of Interacting Bosons in Optical Lattices

In this chapter, we investigate the dynamics of interacting bosons during expansions in homogeneous Hubbard systems in one and two dimensions. We start by investigating the dynamics of bosons in 2D, due to the conceptual similarity to expanding fermions in 2D, discussed in chapter 7. We find that bosons also behave diffusively when interactions are introduced into the system and exhibit bimodal density distributions that closely resemble those observed in the fermionic expansions.

We then focus on the dynamics in one dimensional systems. At large interactions, we find strong deviations from the diffusion present in higher dimensional systems. These deviations are shown to be a direct consequence of the system approaching the integrable limit, where it can be mapped onto a system of free fermions (see chapter 3.4.2).

At intermediate interaction strengths in 1D, where the integrability of the system is broken, we find a pronounced minimum of the expansion velocity accompanied by bimodal density distributions reminiscent of the diffusive dynamics observed in the 2D case. This behavior is in good agreement with time-dependent density matrix renormalization group (t-DMRG) calculations that were carried out by Stephan Langer et al. [225].

The high flexibility of the optical lattice setup allows us to investigate the dynamics not only in 1D and 2D, but also in the crossover regime between these two limits. Breaking the integrability of 1D hard-core bosons by increasing the tunneling along a second axes is found to continuously drive the system towards diffusive dynamics.

We further investigate the role of dynamically formed doubly (and higher) occupied sites, and find a fast relaxation dynamics taking place after the quenches in U/J. The effects of changes in the quasimomentum distribution introduced during this relaxation are shown to be small compared to the observed reduction of expansion velocities, and we conclude that scattering processes during the expansion are mainly responsible for slowing down the expansion.

Lastly, we investigate how changes to the initial state of the system change the dynamics by introducing higher occupancies during the initial state preparation.

We find that these higher occupancies can significantly slow down the dynamics, especially in the strongly interacting limit.

8.1 Expanding Bosons in 2D

8.1.1 Initial State Preparation and Optimization

The goal is to study the expansion of an initial $n = 1$ Mott insulator, prepared using the sequence presented in chapter 6.1. In short, initial states of localized bosons confined to the center of an optical lattice are created, and the expansion is initiated by a simultaneous quench in J and the harmonic confinement. We take special care to avoid any higher occupancies in the initial state (see chapter 6.3.2), except for the experiments discussed in the last part of this chapter, where we explicitly investigate their effects on the dynamics. The atoms are held in a deep lattice for 20 ms before the expansion is initiated, leading to a complete dephasing of the wave functions on individual lattice sites and ensuring an initial quasimomentum distribution $n_q(t_E = 0)$ that is flat over the first Brillouin zone. During this hold time, the interaction is set to the desired values using a homogeneous magnetic field at field strengths in the vicinity of the ^{39}K intra-species Feshbach resonance (see chapter 4.5). The intensity of the dipole trap beam which ensures the homogeneity of the lattice system is optimized with respect to the expansion along the x-direction as described in chapter 6.3.1. Due to slight asymmetries in the alignment and size of the lattice beams, it is not always possible to optimally compensate the global potential along both expansion directions, which can be seen in fig. 8.1.

The width of the cloud along the x-direction (blue circles) and along the y-direction (red circles) is shown for varying intensities of the dipole beam along the z-direction. The intensity of the dipole trap is given as the effective trap frequency that would be created along the horizontal axes if no other potentials were present. The width of the cloud has maxima at two different dipole trap intensities for the two different axes, indicating slightly different anti-confining potentials along these two axes. In order to compare our results for expansions in 2D to those for expansions in 1D, we ensure that the potential is as homogeneous as possible along the x-direction, and accept a small overall anti-confining potential along the other.

8.1.2 Expansion Dynamics and Interaction Effects

In figure 8.2, we show the density distributions during the evolution in the homogeneous lattice for various interactions U/J and expansion durations t_E. Note that throughout this chapter, J denotes the tunneling matrix element along the investigated expansion directions. In the 2D cases, $J = J_x = J_y$ while in the 1D cases discussed below, $J = J_x$ and tunneling along y is neglected.

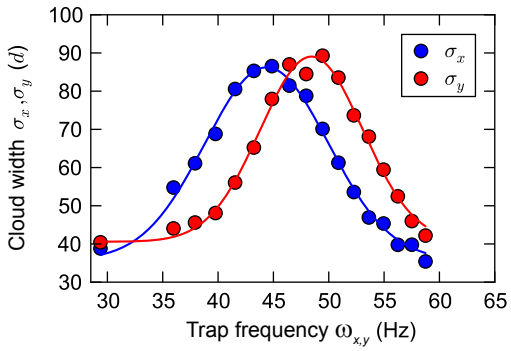

Figure 8.1: Gaussian waists σ_x and σ_y of the non-interacting cloud after an expansion for $54\,\tau$ in a lattice of depth $(8, 8, 20)\,E_r$ along (x, y, z), respectively, for varying intensities of the z-dipole trap. The dipole trap intensity is given as the bare trap frequency ω_z that would be created by the beam if no other potentials were present. The position of the peaks indicate optimal homogeneity for expansions along the respective axes.

The density distributions at $U/J = 0$ show the typical square symmetry of the first Brillouin zone, as expected for ballistic expansions starting from a state of completely localized atoms (see 6.4.1). Starting from a round shape given by the harmonic confinement during the creation of the initial state, the whole cloud expands according to the group velocity distribution of the single-particle wave functions (see chapter 6.2). At intermediate expansion durations ($t_E = 14\tau$ and $t_E = 22\tau$), the square shape becomes already recognizable, but the convolution with the initial shape is easily seen in the rounded off corners.

By increasing the interaction strength to $U/J = 0.5$, we can already observe a qualitative change in the evolution of the density distribution. For large expansion durations, there is a region of higher density in the center of the trap, which evolves more slowly than the fast ballistic atoms in the square shaped background.

Already at $U/J = 1$, the higher density region in the center becomes dominant at large t_E and clearly exhibits the round shape of the initial distribution. At even larger U/J, it becomes very hard to make out the faint background of fast atoms around the stable high density core region.

This formation of a high density core that is stable on the observable time scales already for moderate interaction strengths is directly analogous to the behavior observed in the expansions of a two-component Fermi gas (see chapter 7.3). Since both expansions start from an initial state with a quasimomentum distribution $n_q(t_E = 0)$ that is completely flat in the first Brillouin zone, this qualitative similarity is not surprising. There is no reason why the diffusive dynamics observed in the fermionic

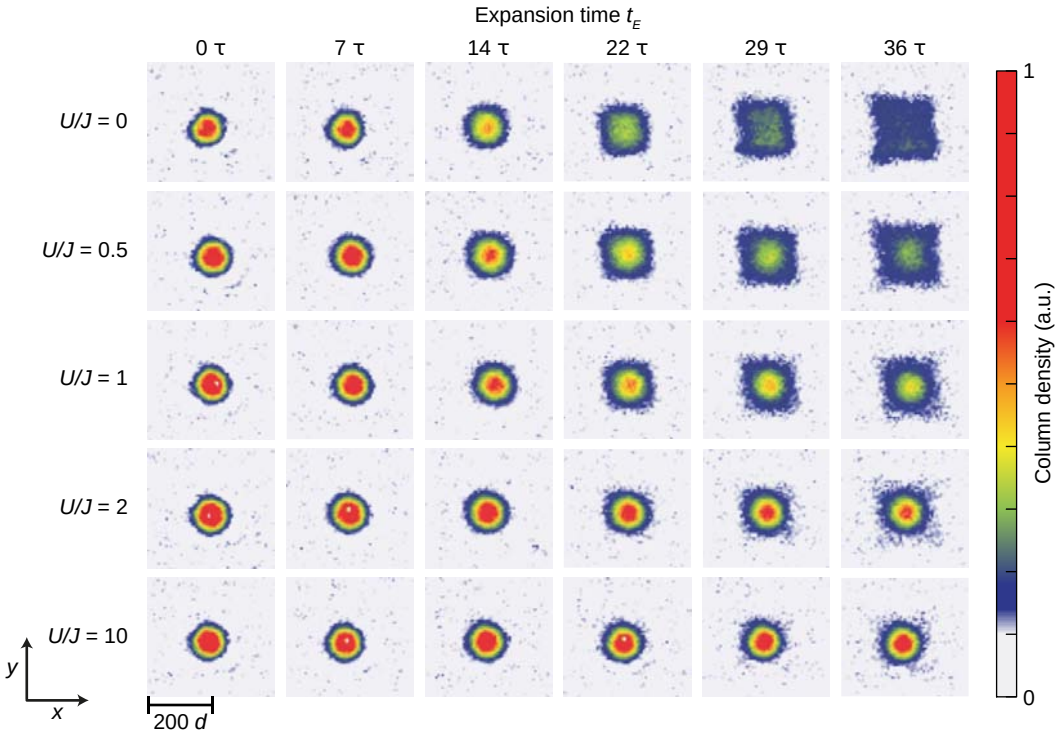

Figure 8.2: Absorption images of the *in-situ* density distributions during expansions in 2D for various interactions U/J and expansion durations t_E.

case should not take place in the bosonic case. Quantitative differences, however, could arise from from differences in the initial states and scattering properties, which we will discuss below.

In the top row of fig. 8.3, we show the evolution of the line density profiles $n_x(t_E)$ of the expanding bosons for various interaction strengths, obtained by integrating along the y-direction (see chapter 6.4.2). This highlights the drastic differences between non-interacting and interacting atoms and the stability of the high density core already for moderate interaction strengths ($U/J = \pm 2$). From these profiles, we can extract the core expansion velocity v_c of the expanding atoms by determining the HWHM for all expansion durations t_E. These are plotted in the bottom row of fig. 8.3 along with linear fits applied to intermediate t_E used to determine v_c (see sect. 6.4.2). The effect of the stable high density core is clearly visible in the evolution of the HWHM. While it increases linearly with increasing t_E in the non-interacting case, there is hardly any evolution at all in the interacting cases. As the HWHM is very sensitive to large densities, a stable high density core with a peak density $n_{\max}$ that sits atop a background of atoms with densities smaller than $n_{\max}/2$ will completely dominate the evolution of the HWHM, and the few atoms with high velocities that can be observed as a faint background in the line density

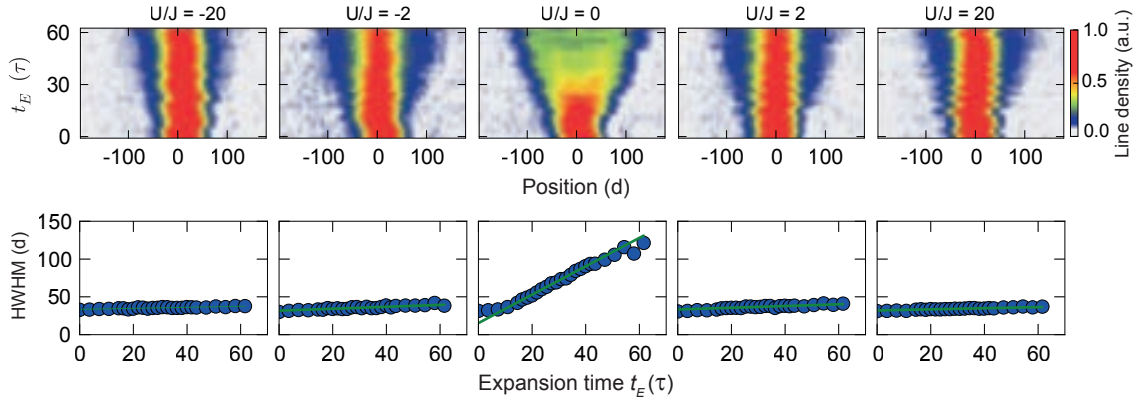

Figure 8.3: Top Row: Evolution of line densities $n_x(t_E)$ during expansions in 2D at various interactions U/J. Bottom row: corresponding evolution of the extracted HWHM (circles) and linear fits to extract the core expansion velocity v_c (solid lines).

evolutions (top row of fig. 8.3) are not taken into account.

To investigate the effects of interactions on the dynamics more quantitatively, we plot v_c over U/J in fig. 8.4 for expansions in a 2D lattice with depths $(8, 8, 33)E_r$ along the (x, y, z) directions.

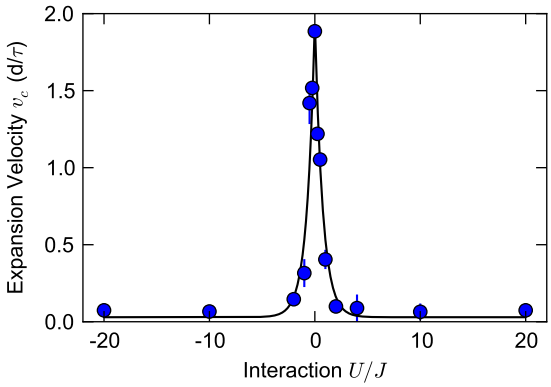

Figure 8.4: Core expansion velocity v_c along the x-direction over interaction U/J for expanding bosons in a 2D lattice at depth $(8, 8, 33)E_r$ along (x, y, z). Black lines are guides to the eye. The error bars are the standard deviation of the linear fits used to determine v_c.

The first thing to observe is the invariance of v_c under a sign change of U. As discussed in sect. 7.3.1, the time evolution of an observable in a homogeneous lattice is invariant under the transformation $U \to -U$ if the observable as well as the initial state are invariant under time-reversal and under a boost of all quasimomenta $\mathbf{q} \to \mathbf{q}+(\pi/d, \pi/d, \pi/d)$. The observable in this case is again the density distribution

$n(\mathbf{r})$, which neither depends explicitly on the time nor on the quasimomentum. The initial state for the bosonic expansions is very similar to the fermionic case. In the same way as discussed for the fermions, the quasimomentum distribution n_q of the atoms is flat over the first Brillouin zone due to their localization to individual lattice sites. Thus, the initial state is invariant under the transformation $\mathbf{q} \rightarrow \mathbf{q} + (\pi/d, \pi/d, \pi/d)$ as well as under the transformation $\mathbf{q} \rightarrow -\mathbf{q}$ and fulfills the conditions for the dynamical $U \leftrightarrow -U$ symmetry.

Second, there is a very strong reduction in the expansion velocity already at small values of U/J. The overall shape of the curve is very similar to the changes of v_c in the fermionic case (figure 7.7). This behavior, together with the characteristic bimodal cloud shapes shown in fig. 8.2, is a clear indication of the onset of diffusive dynamics also in the bosonic case as soon as interactions are turned on in the system.

A remaining discrepancy in the behavior of v_c with changing U between the fermionic case and the bosons in 2D is the fact that for the fermions, v_c becomes slightly negative for large U, which is not the case for the bosons. However, there are a few differences between the two situations that could potentially lead to this observed discrepancy: First, the fact that only inter-species scattering is allowed in the fermionic case, while there is only one component with intra-species interactions present in the bosonic case, reduces the amount of potential scattering partners in the fermionic case. However, this effect could be compensated by the fact that the fermionic expansion starts from an initial state with a density that is a factor of 2 higher than the bosonic one. Second, the fermionic initial state consists of a band-insulator of doubly occupied sites (i.e., one atom of each species on a lattice site). Double occupancies carry an interaction energy of U, and thereby change the total energy of the expanding system. The interaction energy can be transformed into kinetic energy during the expansion, as the doubly occupied sites dissolve, and influence the dynamics. Such an effect is not present in the bosonic case, where the absence of double occupancies in the initial state ensures that the total energy of the initial state is always the same and independent of U. Third, in the limit of large $|U|$, the formation of double occupancies is strongly suppressed due to energetic constraints. The exact opposite is true in the fermionic case, where the double occupancies of the initial state become very stable for large interactions [146] and, due to their lower effective tunneling matrix element [27], exhibit only very slow dynamics. This can even lead to additional quantum distillation effects [83] that further inhibit the expansion of the core. While this effect only becomes relevant for large $|U|$, where an expansion is neither observed in the fermionic nor in the bosonic case, it could explain why we observe a shrinking core at large $|U/J|$ in the fermionic case, while we observe minimal, but always positive core expansion velocities in the bosonic case.

8.2 Expanding Bosons in 1D

We now turn to investigating the expansion dynamics of interacting bosons in one dimensional systems. As we have discussed in chapter 3.4.2, reducing the dimensionality of a system can strongly restrict the degrees of freedom available to its constituents and significantly change both its dynamical and equilibrium properties. In the limit of hard-core interactions, the 1D Bose-Hubbard model even becomes integrable, leading to the appearance of many integrals of motion that constrain the allowed relaxation dynamics as well as the evolution of its density distribution.

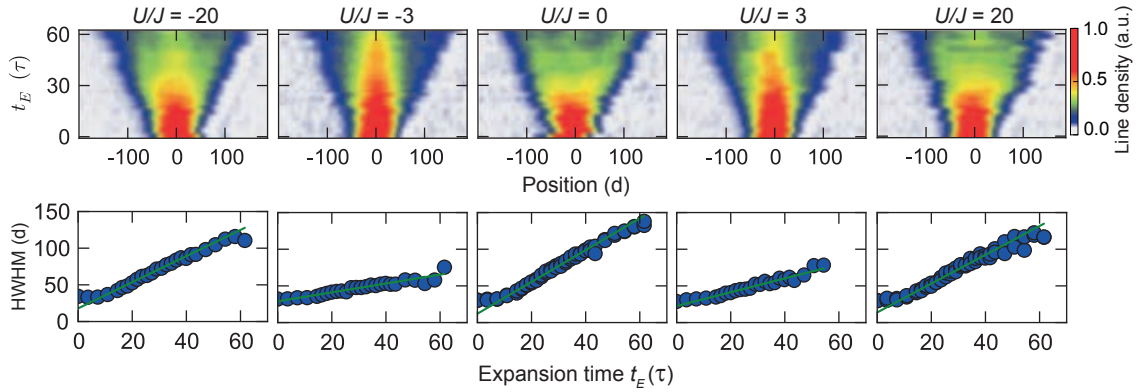

Figure 8.5: Top Row: Evolution of line densities $n_x(t_E)$ during expansions in 1D at various interactions U/J. Bottom row: corresponding evolution of the extracted HWHM (circles) and linear fits to extract the core expansion velocity v_c (solid lines).

In the top row of fig. 8.5, we show the evolution of the line density profiles $n_x(t_E)$ during expansion measurements for various interaction strengths U/J in a 1D lattice configuration with lattice depths $(8, 33, 33)\, E_r$ along (x, y, z), respectively. These line density profiles are again obtained by integrating the *in-situ* column densities, obtained by absorption imaging, along the y-direction. In these density plots, we can already see qualitative differences compared to the evolution of $n_x(t_E)$ in the 2D case (fig. 8.2).

In the non-interacting case ($U/J = 0$), the evolution of $n_x(t_E)$ behaves exactly as predicted. Each atomic wavefunction expands ballistically according to its initial group velocity distribution, as discussed in chapter 6.2. For $U/J = 0$, the evolution of these profiles in 1D is exactly the same as in 2D, as the dynamics along the x- and y-directions are completely decoupled. Integrating along the y-direction, as it is done to obtain $n_x(t_E)$, results in the exact same dynamics, regardless of whether an expansion takes place along the y-axis.

In the case of intermediate interaction strengths ($U/J = \pm 3$), we can observe a bimodal behavior that is qualitatively similar to that of the 2D profiles, namely a

slowly evolving central region of higher density atop a low density background of atoms with high velocity. However, this central core is not as stable as in the 2D case, and slowly disappears over the course of the expansion.

In the strongly interacting limit ($U/J = \pm 20$), the behavior of the 1D systems is very different from that of 2D systems. While in 2D, the stability of the high density core increases with increasing interactions, in the 1D case, the evolution becomes fully ballistic again, showing the characteristic shape expected for free atoms (see chapter 6.2). Note that there is indeed a region of slightly higher central density visible also in the strongly interacting case. However, this excess density in the center is most likely caused by a small fraction of higher occupancies in the initial state, the effect of which is discussed in section 8.4.4.

In the bottom row of fig. 8.5, we show the evolution of the HWHMs that were extracted from the line density profiles. The qualitative features discussed above manifest themselves in a significantly reduced expansion velocity for the $U/J = \pm 3$ cases, where the central region of higher density dominates the evolution. The reduction, however, is not as strong as in the 2D case, where v_c essentially becomes zero already around $U/J \pm 2$. For stronger interactions, the evolution of the HWHM becomes much faster again in the 1D case, due to the absence of the high density core which allows the evolution of the HWHM to be dominated by the ballistic wings of the cloud.

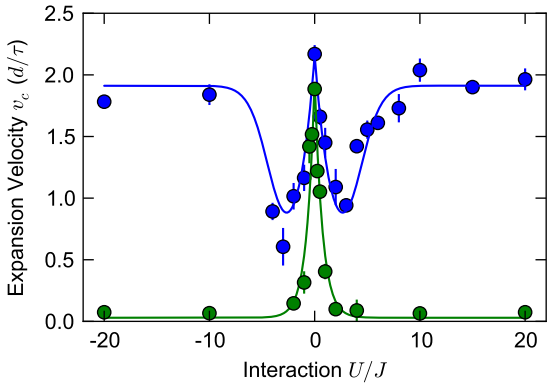

Figure 8.6: Core expansion velocity v_c (along x-direction) as a function of interaction U/J for expanding bosons in an $(8, 33, 33)\, E_r$ lattice (blue circles) and in an $(8, 8, 33)\, E_r$ lattice (green circles). Solid lines are guides to the eye. The error bars are the standard deviations of the linear fits used to determine v_c.

In fig. 8.6, we show the extracted core expansion velocities v_c for a range of interaction strengths in the 1D case (blue circles) and the 2D case (green circles). As a first observation, we note that the $U \leftrightarrow -U$ symmetry also holds in the 1D case. As both the initial state and the observable (i.e., the density distribution) are

the same in 1D as they are in 2D, the conditions for this symmetry are also fulfilled and the dynamics is expected to be invariant under a transformation $U \to -U$.

The core expansion velocity in the 1D case at $U = 0$ is consistent with the maximum group velocity in the lattice of $v_g = 2d/\tau$ (see chapter 6.4.2). For increasing interactions, v_c then decreases and reaches a minimum value between $|U/J| = 3$ and $|U/J| = 4$, before increasing again for even stronger interactions and reaching values consistent with $2d/\tau$ for $|U/J| > 10$. This increase in the expansion velocity for large U is a direct consequence of the mapping of hard-core bosons in 1D onto free fermions. In the limit of $|U/J| \to \infty$, the density distribution of a state of bosons in 1D evolves in exactly the same way as that of free, single component fermions, leading to the same v_c in our experiments (see chapter 3.4.2). This constitutes the first direct observation of a strongly interacting system exhibiting ballistic transport dynamics due to the approach of an integrable limit (see [226, 227] and [86] and references therein).

A more complex regime is that of intermediate interaction strengths, where the system is far away from the integrable limits. We will limit the following discussion to the case $U > 0$, but all results directly carry over to the $U < 0$ case, due to the aforementioned $U \leftrightarrow -U$ symmetry.

We can compare our experimental results to time-dependent density matrix renormalization group (t-DMRG) [74–76] calculations. These calculations were carried out by S. Langer et al. [225].

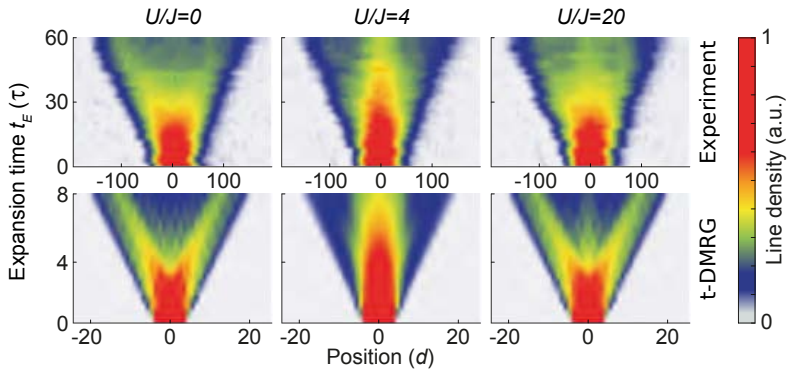

Figure 8.7: Top row: Experimental evolution of line densities $n_x(t_E)$ during expansions in 1D for various interactions (each line is individually normalized). Bottom row: Corresponding t-DMRG calculations for $N = 8$ atoms, plotted using cubic interpolation between the sites.

In fig. 8.7, we compare the results of t-DMRG calculations with our experimental results. The top row shows the evolution of the line density profiles for various U/J as in the top row of fig. 8.5. The bottom row shows the results of t-DMRG calculations carried out with an initial state of $N = 8$ atoms.

In the non-interacting ($U/J = 0$) and strongly interacting ($U/J = 20$) cases, the t-DMRG profiles exhibit the two peaks traveling with maximum group velocity $v_g = 2d/\tau$ that result from the flat n_q of the initial state (see chapter 6.4.2). In the non-interacting case, these peaks can be observed clearly, but are weaker than in the t-DMRG calculations. In the strongly interacting case, there is an additional peak in the center of the cloud. This peak is most likely caused by few higher occupancies in our initial state which we discuss in sect. 8.4.4. The qualitative change of the evolution of the line density when departing from the integrable limit at $U/J = 0$ and close to the integrable limit at $U/J = 20$, however, can be seen very clearly both in the t-DMRG calculations and in the experimental data. Instead of the fast ballistic dynamics, there is a high density core present throughout the complete expansion.

Note that the length scales and the time scales differ greatly between the experimental and the numerical data. As discussed in chapter 6.4.3, in the non-interacting case, larger sizes of the initial state lead to a linearly increasing time until the traveling peaks can be observed. The width of these traveling peaks also scales linearly with the initial size while their velocity is independent of it. Thus, by scaling the temporal and spatial axes accordingly, we expect the density profiles of experiment and theory to agree with each other. This is also the case for the strongly interacting atoms in 1D, where the density of the system behaves like that of non-interacting particles. The agreement in the intermediate interaction regime, however, is not *a priori* clear, as the evolution under the influence of scattering between atoms could depend non-linearly on the extension of the initial state. As we will see in the following discussion, the agreement between t-DMRG results and experiments turns out to be very good, which indicates that in 1D, the linear scaling also holds at least approximately in the regime of intermediately strong interactions.

We can extract the core expansion velocity from the profiles of the t-DMRG calculations in the same way as for the experimental data. Note that in some of the calculated profiles, the HWHM is not uniquely defined, as the density between the two fast moving peaks drops to very small values. In these cases, we define the HWHM as half the distance between the two outermost points where $n_x = n_{\max}/2$, which results in the expected large v_c in the $U = 0$ and $U \to \infty$ cases. In fig. 8.8a, we plot the v_c extracted from t-DMRG calculations with $N = 10$ atoms (green triangles) together with the experimentally observed v_c (blue circles). The solid line is a guide to the eye for the experimental data. The qualitative behavior of the decrease and increase of v_c for increasing U/J is very well reproduced by the t-DMRG calculations. The largest expansion velocities are reached in the non-interacting and strongly interacting limits, with a strong minimum of v_c between $U/J = 3$ and $U/J = 4$. Note that the calculated HWHM for fig. 8.8a suffer from rather large finite size effects of the calculations, given that they are done for rather small atom numbers. Another quantity that is less sensitive to finite size effects when investigating the evolution of the calculated line density profiles is the radius

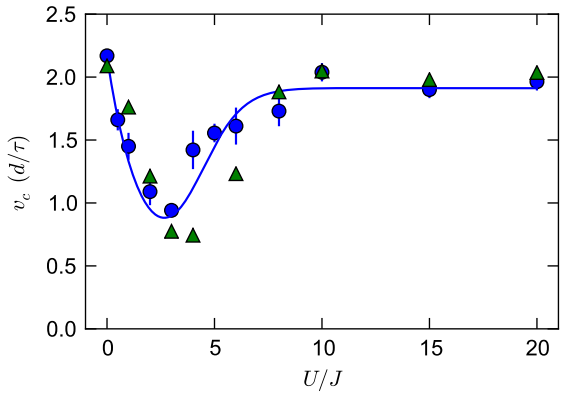

(a) Core expansion velocity v_c for experimental data of atoms expanding in 1D (blue circles) and t-DMRG calculations with $N = 10$ atoms in 1D (green triangles). The solid line is a guide to the eye for the experimental data.

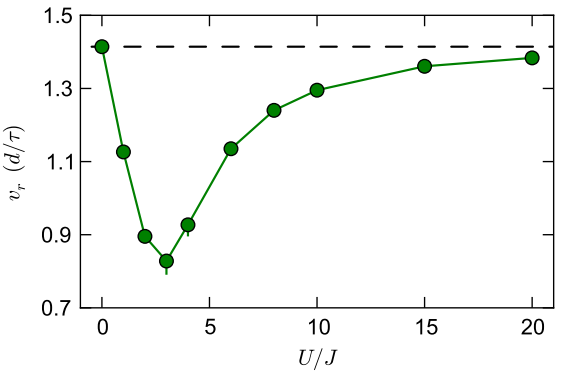

(b) Radius expansion velocity v_r for varying U/J from t-DMRG calculations, extrapolated to $N \to \infty$. The error bars show the uncertainty of the extrapolation [225]. The dashed line indicates $v_r = \sqrt{2}d/\tau$, the value for non-interacting atoms with $n_q = \text{const}$.

Figure 8.8

expansion velocity

$$v_r(t_E) = \frac{d\tilde{R}(t_E)}{dt_E} = \frac{d}{dt_E}\sqrt{R^2(t_E) - R^2(0)}, \tag{8.1}$$

with $R^2(t_E)$ given by

$$R^2\left(t_E\right) = \frac{1}{N}\sum_{i=1}^{L}\left\langle \hat{n}_i \right\rangle \left(t_E\right)\left(i - i_0\right)^2 d^2 \tag{8.2}$$

(see chapter 6.4.2 for details). This quantity is more robust against finite size effects, as $R^2(t_E)$ takes the full shape of the density distribution into account instead of relying on the position of two distinct values of n_x. By determining v_r for various N, it can also be extrapolated to infinite particle numbers [225].

In fig. 8.8b, we show the extracted v_r from the t-DMRG calculations extrapolated to infinite particle numbers for varying U/J. The error bars stem from the uncertainty in the extrapolation. For $U/J = 0$, v_r has a direct physical interpretation, as it is equal to the average velocity

$$v_{\text{av}}(t_E) = \sqrt{\frac{1}{N\hbar}\sum_k \left(\frac{\partial \epsilon_q}{\partial q}\right)^2 n_q(t_E)}, \tag{8.3}$$

with the tight-binding dispersion relation ϵ_q (see chapter 6).

With an $n_q(t_E = 0)$ that is flat over the first Brillouin zone, as given in the experimental realization, the average velocity is $v_{\mathrm{av}} = \sqrt{2}d/\tau$. This value is indicated by the dashed line, which intersects with the calculated v_r at $U/J = 0$. For large U/J, v_r approaches this value again and almost reaches it at $U/J = 20$, indicating that the system is already very close to the hard-core boson regime where it can be mapped to a system of free fermions that also expands with $v_r = \sqrt{2}(d/\tau)$. Note that in the strongly interacting limit, the relation $v_r = v_{\mathrm{av}}$ does not hold, because $n_q(t_E)$ can be significantly altered in this case while leaving $n_x(t_E)$ unchanged. This effect, which can give rise to quasi-condensation in 1D, is discussed in detail in chapter 9.

The evolution of v_r with changing U/J shows a very similar behavior to that of v_c. v_r reaches its maximum value for $U/J = 0$ and $U/J \to \infty$ and has a pronounced minimum around $U/J \approx 3$. Starting from the hard-core limit, we can qualitatively understand the appearance of a minimum in v_c and v_r by considering the formation of doubly (and higher) occupied sites during the expansion. At $U/J \gg 4$, their formation is energetically suppressed but at smaller U/J, the system can maximize its local entropy through the formation of higher occupancies. At $U/J > 4$, doubly occupied sites (doublons) in 1D can be seen as metastable objects [146] that propagate with an effective hopping matrix element on the order of J^2/U [27]. Thus, there are two counteracting processes influencing the expansion velocity. On the one hand, for decreasing U/J, more doublons are formed that slow down the expansion dynamics. On the other hand, decreasing U/J mitigates the effects of the doublons on the dynamics, as they become less stable and J^2/U increases. In the limit of $U/J \to 0$, the maximum amount of doublons can be formed, but they do not affect the dynamics at all, as there is no interaction energy associated with them. The effects of doublons in the system as well as the local relaxation leading to their formation are discussed in more detail in section 8.4. A second effect of the possibility of forming higher occupancies in the system is the increase in phase space for scattering. In the hard-core limit, the formation of doublons is fully suppressed but for smaller U/J, the possibility of creating higher occupancies increases the phase space available for scattering. At $U/J \to 0$, however, the scattering cross section completely vanishes. Thus, the effect of scattering events becomes maximal at some U/J where the formation of doublons is possible and the scattering cross section is finite.

As the expansion velocity is large in the integrable limits of $U/J = 0$ and $U/J \to \infty$ and the effects present at intermediate values of U/J can only decrease the expansion velocity, there has to be a minimum in v_c at finite U/J. This minimum turns out to be close to the critical $(U/J)_c \approx 3.4$ for the superfluid to Mott insulator transition in 1D [104]. The formation of higher occupancies as well as the redistribution of momentum in collisions rely on a local relaxation of the system towards a quasi-equilibrium after the quantum quench in U/J, and the behavior is thus consistent with other studies of quantum quenches, which observe the fastest

time scales for relaxation at the critical point [73, 79].

8.3 Expansion Dynamics in the Crossover Between 1D and 2D

After investigating the dynamics of expanding atoms in purely 1D and 2D systems, we can make use of the high flexibility of the experimental setup to investigate the effects of the dimensionality in even more detail. By controlling the intensities of the lattice laser beams along the x- and y-direction, we can continuously tune the system from 1D through an intermediate regime towards 2D. To do so, we keep the lattice along the x-direction at a constant depth of $8\,E_r$, which gives $J_x/\hbar = 1.8\,\mathrm{kHz}$, and change the tunneling along the y-direction, denoted by J_y. The quantitative analysis of expansion velocities is again conducted for the line density profiles $n_x(t_E)$. Thus, J_x sets the dynamical time scales for the expansion and the tunneling time τ is given by $\hbar/J_x$. The z-lattice is always kept at large intensities to suppress any dynamics along the vertical direction.

Due to the asymmetry of the lattice intensities in all cases where $J_x \neq J_y$, it is not possible to compensate the overall anti-confinement along both the x- and y-direction. As we are investigating the evolution of the HWHM of the clouds along the x-direction, we choose to adjust the intensity of the z-dipole beam for an optimal homogeneity along x. Only in the 2D configuration, where the lattice beams along x and y have approximately the same intensities, is it possible to compensate the anti-confining potentials along both axes, up to small imperfections caused by slight asymmetries in the beam sizes and their alignment (see section 8.1.1).

In fig. 8.9, we show the *in-situ* column density of the atoms after an expansion for $t_E \approx 36\,\tau$, obtained by imaging along the z-direction. The expansion takes place in lattice configurations characterized by the dimensionality ratio $\chi = J_y/J_x$. For $\chi = 1$, the system is in a purely two-dimensional configuration. The lower the values of χ are, the stronger the reduction of tunneling along the y-direction is, and for $\chi \to 0$, the system approaches the purely 1D regime.

In the top row, we show the densities after an expansion at a small value of $U/J_x = 0.5$. The changing dimensionality in this case mainly changes the extension of the cloud along the y-direction, due to the increasing tunneling for larger χ. Additionally, we can observe that the distribution becomes slightly more peaked in the center for larger χ, indicating an increasing tendency towards diffusive dynamics in the system. This effect is much more visible in the case of $U/J_x = 3$. For this interaction, we already observe a central peak close to the 1D regime ($\chi = 0.08$), but with increasing χ, this peak becomes more and more dominant and in the purely 2D case, the fast atoms at the edges of the cloud are hardly visible at all anymore. The strongest effect can be observed in the strongly interacting limit ($U/J_x = 20$). Close

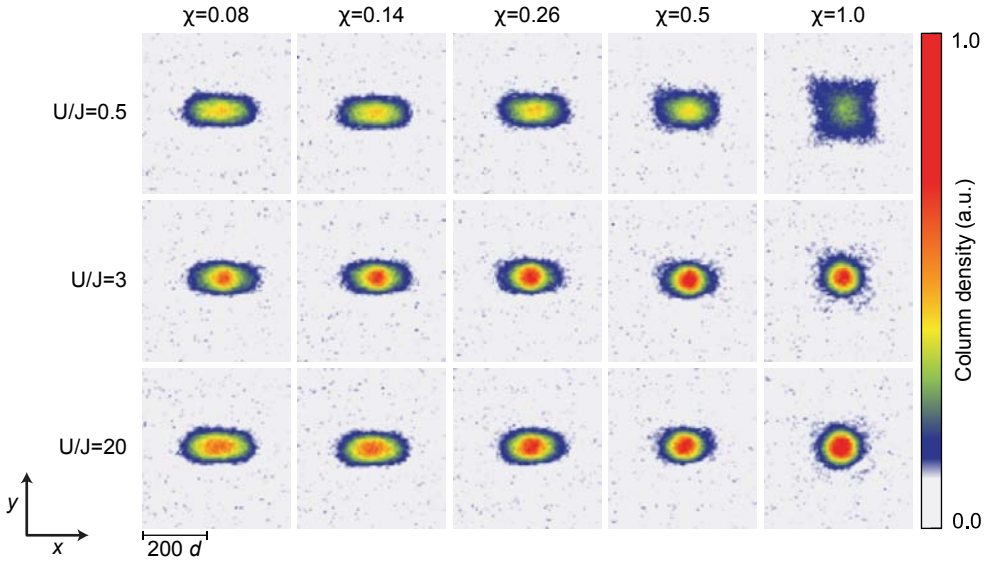

Figure 8.9: Column density of atoms after an expansion for $t_E \approx 36\,\tau$ in lattices with varying dimensionality $\chi = J_y/J_x$ at varying interaction U/J_x

to the 1D regime, the resulting cloud shapes are very flat along x, indicating that the system is close to the integrable regime of 1D hard-core bosons. For increasing χ, this flat shape becomes strongly peaked and more and more symmetric. Already at $\chi = 0.5$, there is hardly any dynamics observable along the x-axis anymore and the system appears to behave purely diffusively.

From the evolution of the density distribution in these varying geometries, we can again extract the core expansion velocities v_c, which are plotted in fig. 8.10a over U/J_x during the expansion. The colors of the circles indicate the respective geometry of the system, ranging from purely 1D ($\chi = 0.01$, black circles) to purely 2D ($\chi = 1.0$, red circles). The solid lines are guides to the eye. At $U/J_x = 0$, all curves start at approximately the same large $v_c \approx 2d/\tau$ that necessarily arises for non-interacting atoms starting from the same initial state with a flat n_q. For all χ, the core expansion velocity then decreases with increasing U/J_x. This decrease becomes stronger with increasing χ, highlighting the role that increasing degrees of freedom play in the formation of the high density cores.

For $U/J_x > 4$, the velocities for $\chi < 0.5$ increase again with increasing interactions. In the 1D case ($\chi = 0.01$), this was shown to be directly related to the approach of an integrable regime at $\chi \to 0$ and $U/J_x \to \infty$. It is very interesting that this behavior persists even for dimensionality ratios up to $\chi = 0.26$, but with strongly reduced v_c at large U/J_x. This shows the counteracting nature of increasing U/J_x and χ. While increasing U/J_x brings the system closer towards the hard-core regime, where the formation of higher occupancies is inhibited and the degrees of freedom are reduced, the increase of χ brings the system closer towards the 2D regime, where it does not

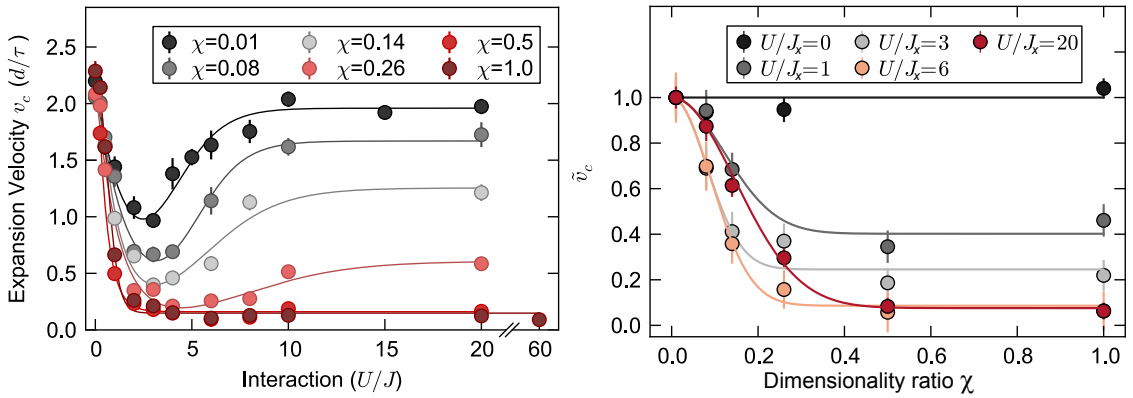

(a) Core expansion velocity v_c over interaction U/J_x for various dimensionalities $\chi = J_y/J_x$. Solid lines are guides to the eye and error bars show the standard deviation of the linear fits used to determine v_c.

(b) Normalized core expansion velocity $\tilde{v}_c = v_c(\chi)/v_c(\chi = 0.01)$ over dimensionality χ for various interactions U/J_x. Solid lines are guides to the eye, error bars are determined from the errors in fig. 8.10a.

Figure 8.10

become integrable even for $U/J_x \to \infty$. For $\chi \geq 0.5$, the expansion velocity does not increase anymore with increasing U/J_x, which we confirmed for interactions up to $U/J = 60$ in the 2D case.

In order to investigate the effect of changing χ more closely, it is instructive to plot the behavior of v_c with changing χ for different values of U/J_x. However, as v_c is already strongly dependent on U/J_x even in the case of $\chi = 0.01$, we show the normalized core expansion velocity

$$\tilde{v}_c(\chi) = v_c(\chi)/v_c(\chi = 0.01) \tag{8.4}$$

in fig. 8.10b. This quantity shows the relative change of v_c when going from a 1D towards a 2D system. The interaction is indicated by the different colors of the circles, the solid lines are guides to the eye. For $U/J_x = 0$, there is, as expected, no significant change in v_c when crossing over from 1D to 2D. Already at $U/J_x = 1$, however, we can observe a strong effect of the changing dimensionality resulting in decreasing $\tilde{v}_c$. This effect, as expected, becomes even stronger with increasing interactions. One peculiar aspect is that while the curves for $U/J_x = 3$ and $U/J_x = 6$ show a quite fast decay of $\tilde{v}_c$ with χ, the decay at $U/J_x = 20$ occurs for larger χ. A potential reason for this is that at large U/J_x, the system is still influenced by the proximity to the hard-core boson regime even at significant tunneling along the second axis, delaying the formation of diffusive high density cores.

A similar crossover between 1D and 2D systems is investigated numerically, using t-DMRG, in a recent publication [86] and compared to our experimental results.

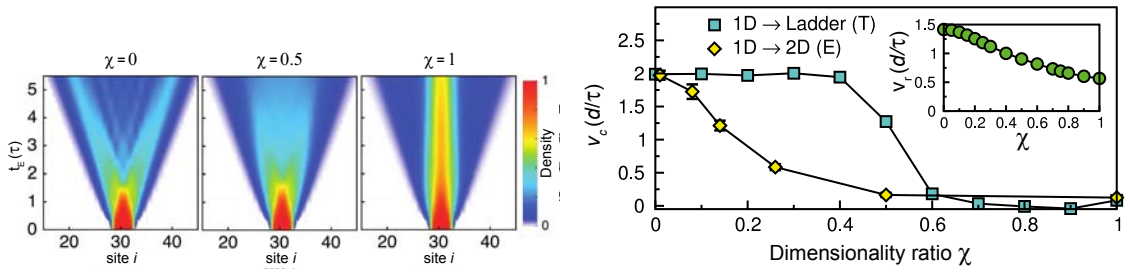

(a) (b)

Figure 8.11: (a): Density distribution in t-DMRG calculations of 8 hard-core bosons on ladders for different tunneling ratios $\chi = J_\perp/J_x$. (b): Comparison between experimentally measured v_c in the 1D-2D crossover (yellow diamonds) and those extracted from t-DMRG calculations of 12 hard-core bosons on ladders (blue squares). $\chi = J_y/J_x$ in the experiment and $\chi = J_\perp/J_x$ in the calculations. Inset: radius expansion velocity v_r for the same t-DMRG data. Figures adapted from [86] with kind permission of the author.

In this work, two 1D systems with tunneling J_x in the hard-core boson regime are coupled to each other via a perpendicular tunneling $J_\perp$, and the effects of changing $J_\perp/J_x$, which is analogous to $\chi = J_y/J_x$ in our experiment, on the core expansion velocity are investigated.

Figure 8.11a (reprinted from [86]) shows the density distribution during expansions for three different values of $\chi = J_\perp/J_x$. The case $\chi = 0$ is a simple 1D expansion of hard-core bosons, as already discussed in section 8.2, and shows the typical peaks traveling with large velocity. This behavior changes when χ is increased to 0.5. Now, instead of two traveling peaks, there is a region of larger density in the center of the system that dissolves slowly. For $\chi = 1$, the evolution exhibits a high density peak in the center of the cloud that, while decreasing in magnitude, is stable over the whole expansion duration. This behavior is qualitatively similar to the experimentally observed effects, where increased tunneling along the perpendicular direction leads to the formation of high density central cores. There are, however, quantitative differences which can be investigated by extracting the core expansion velocities v_c from the numerically calculated profiles and comparing them to the experimental results. This is done in figure 8.11b, which shows the v_c of 12 hard-core bosons on a ladder with varying χ (gray squares) in comparison to the v_c of expanding bosons in the experiments at $U/J_x = 20$. While the limits of small χ and large χ agree very well, the experimental data shows a much smoother transition between the two limits, while the numerical results indicate a rather sharp drop in v_c around $\chi = 0.5$. There are a few explanations for this discrepancy: First and foremost, a ladder system is not the same as a full 2D system and we should expect

the dynamics to be different. Second, the measure v_c is not particularly well suited for the investigation of the theoretical data, due to finite size effects and third, we always average over multiple systems of varying initial sizes in the experiment, given by the initial shape of the cloud before loading the lattice, which can be responsible for smearing out otherwise sharp features in the dynamical behavior. The inset of figure 8.11b shows the evolution of the radius expansion velocity v_r for the theoretical data, which captures changes in the evolution of the density distribution in more detail. Here, it can be clearly observed that as soon as $\chi > 0$, the expansion velocity decreases smoothly due to the breaking of the integrability of the system. We can conclude that the essential effects of breaking the integrability of a 1D system of hard-core bosons by allowing tunneling along a second direction can already be captured in a simple ladder system. Thus, the decrease in expansion velocity and the appearance of high density cores does not depend on an actual expansion along a second direction, but mainly on the additional degrees of freedom that allow for more complex relaxation dynamics.

8.4 Effects of Double Occupancies

In this section, we discuss the role of sites with occupancy $\eta_i > 1$ (higher occupancies). In our experiments, we detect the higher occupancy in the system after freezing out the distribution by rapidly increasing the lattice depth (see chapter 6.3.3). This freezing out leads to a dephasing of the wavefunctions on different sites and effectively localizes the atoms, resulting in a projection onto a mixture of products of local Fock states, where the individual terms have the form

$$|\Psi_F\rangle = \prod_i \frac{1}{\sqrt{\eta_i!}} \left(\hat{b}_i^\dagger\right)^{\eta_i} |0\rangle \,. \tag{8.5}$$

Thus, when talking about multiply occupied sites in the experimental context, we refer to all sites i where $\eta_i > 1$ after the projection onto $|\Psi_F\rangle$ that happens during our measurement process.

We first investigate the formation of these higher occupancies during the expansion from initial states with all initial $\eta_i = 0$ or 1, which proves to be an indication of fast relaxation dynamics after a quench in U/J. We also investigate, how the presence of higher occupancies in the initial state influences the dynamics during the expansion. This is particularly interesting for the expansions in one dimension at strong interactions, where the presence of higher occupancies breaks the near-integrability of the system and can be expected to significantly alter the dynamics.

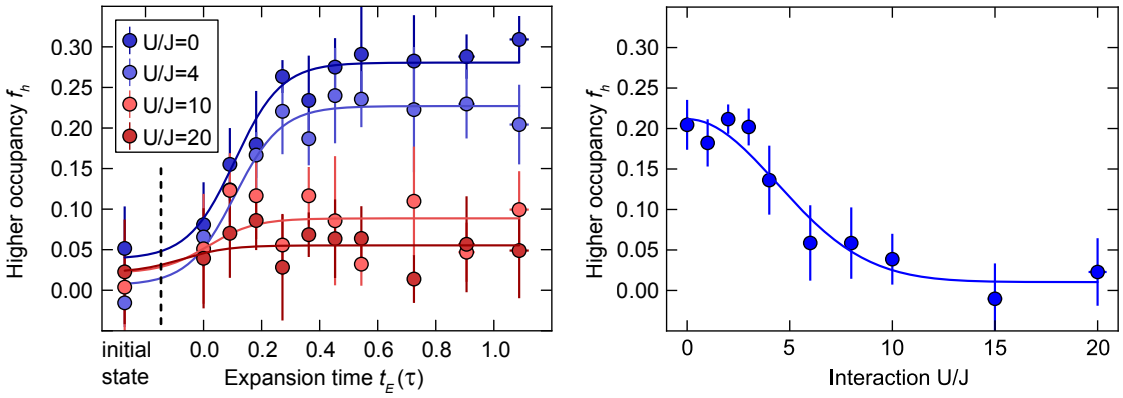

(a) Higher occupancy f_h during expansions in 1D for various interactions U/J. For the points labeled "initial state", the measurements were performed directly after the dephasing period in the deep lattice. Error bars show the standard deviation of averaging four data points, lines are guides to the eye.

(b) Higher occupancy f_h after an expansion for $t_E = 18\,\tau$ versus interaction U/J during the expansion. Error bars show the standard deviation of averaging four data points, the solid line is a guide to the eye.

Figure 8.12

8.4.1 Formation of Higher Occupancies

We measure the amount of higher occupancies in the system as outlined in chapter 6.3.3, by relying on the parity projection induced by near-resonant light pulses. As discussed, the measure f_h for the higher occupancies in the system does not give a completely accurate value for the ratio of atoms on sites with an occupation $\eta_i > 1$, due to the nature of the parity projection, but still serves as a good approximation in the experimentally relevant cases.

In fig. 8.12a, we show the evolution of the higher occupancy f_h during the first tunneling time τ of expansions in a 1D lattice. The initial state is created as described in chapter 6.1, and the lattice depth during the expansion is $(8, 33, 33)\,E_r$ along (x, y, z), respectively. For the points labeled "initial state", the measurement of f_h is performed directly after the dephasing period in the deep lattice. For the points at $t_E = 0$, the quench to small J that initiates the expansion is performed, but then directly succeeded by the second quench in J to freeze out the distribution for the determination of f_h. The time scale on which the higher occupancy forms and saturates in the system is very fast compared to the time scales of the expansion measurements. Already after approximately half of a tunneling time τ, the amount of double occupancies in the non-interacting and weakly interacting cases reaches a plateau. This short time scale indicates that the formation of higher occupancies in

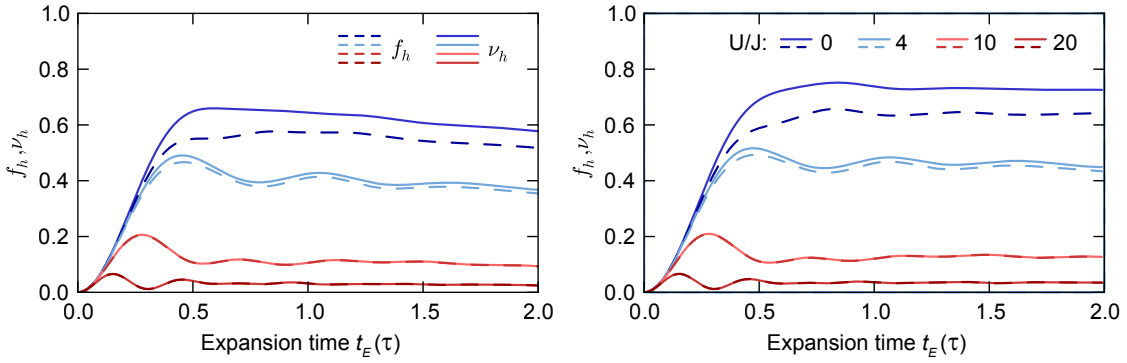

(a) Expansion in a homogeneous lattice

(b) Evolution in a homogeneous lattice, confined by a box potential

Figure 8.13: Buildup of higher occupancy f_h (dashed lines) and ν_h (solid lines, see text) for various interactions U/J in t-DMRG calculations with $N = 10$ atoms and $N_b = N$. The evolution is initiated by a quench to finite J, starting from an initial state of singly occupied sites. The calculations were conducted by S. Langer et al. [225].

the system is a purely local relaxation effect, and could indicate prethermalization, as observed in other systems [65, 81, 82, 145]. In the strongly interacting cases $U/J = 10$ and $U/J = 20$, no significant increase of f_h beyond the experimental uncertainty is observed.

After this fast initial relaxation to a local equilibrium state, the amount of higher occupancies decays only very slowly. In the asymptotic limit of very long expansion durations, however, the amount of higher occupancies is expected to decay to zero along with the average density. Figure 8.12b shows the higher occupancy f_h, measured after an expansion duration of $t_E = 18\,\tau$. While we can observe a reduction of f_h on the order of 30% at $U/J = 0$ and $U/J = 4$, this is a much slower process than the initial fast relaxation.

To further establish that the formation of double occupancies is a local relaxation process, we investigate the evolution of higher occupancies in t-DMRG calculations of the dynamics of $N = 10$ atoms on ten lattice sites, with all initial $\eta_i = 1$, in a homogeneous lattice after quenching from $U/J = \infty$ to a finite U/J. These calculations were performed by S. Langer et al. [225]. Figure 8.13a shows the evolution during an expansion in a homogeneous lattice for various interaction strengths. Here, the solid lines show the actual fraction of atoms on sites with higher occupancy, ν_h, while the dashed lines show the experimentally observable quantity f_h, which reflects the inaccuracies introduced by remaining atoms after a parity measurement on sites with odd atom number.

Numerically, ν_h is determined as

$$\nu_h = \frac{1}{N} \sum_i \sum_{m=2}^{N_b} m \langle \hat{n}_{m,i} \rangle \,, \tag{8.6}$$

where N is the total number of atoms and $\langle \hat{n}_{m,i} \rangle$ measures the probability of finding m bosons on site i. N_b is a numerical cutoff for the maximum number of bosons per site that is introduced in the numerics for computational efficiency. For interactions $U/J > 2$, $N_b = 3$ as contributions from sites with $n_i > 3$ are negligible. For interactions $U/J \leq 2$, fluctuations in the particle number per site are larger and $N_b = N$. To take the inaccuracies after the parity projection into account that are introduced by the remaining atoms on sites with odd particle numbers, f_h is numerically determined as

$$f_h = \frac{1}{N} \sum_i (2 \langle \hat{n}_{2,i} \rangle + 2 \langle \hat{n}_{3,i} \rangle + 4 \langle \hat{n}_{4,i} \rangle + \ldots). \tag{8.7}$$

Note that in figures 8.13a and 8.13b, the difference between ν_h and f_h is only significant for the smaller interactions. For larger U/J, the formation of sites with $\langle \hat{n}_{m,i} \rangle > 0$ is strongly suppressed for $m \geq 3$, and $f_h \approx \nu_h$.

The time scale, on which the higher occupancies form in figure 8.13a agrees very well with our experimental observations, even though the system sizes differ greatly. However, the value for the maximum f_h reached in the calculations does not match the observations. In the experiment, the measured values for f_h are consistently lower than those obtained from t-DMRG, reaching approximately half the predicted values. The main reason for this discrepancy is the existence of sites with $\eta_i = 0$ in our initial states. There are always regions with empty lattice sites at the outer edges of the cloud, and we can not rule out that we might also produce a significant fraction of empty lattice sites in the center of the cloud, as our main concern when preparing the initial states is to prevent the formation of double occupancies. Since the expected local relaxation dynamics are dominated by atoms tunneling to neighboring sites, any empty lattice site will result in the creation of fewer sites with $\eta_i > 1$.

In order to further establish that the fast creation of higher occupancies is due to local relaxation processes, while the long term evolution is governed by the global expansion dynamics, we compare the dynamics during an expansion with that of atoms after a quench in U/J without expansion. This is shown in figure 8.13b, where U/J is quenched to the same values as in figure 8.13a, but a box-potential is left on, which confines the atoms to their initially occupied ten lattice sites. The fast relaxation time scale remains the same in this case, but the slight long term decay of ν_h and f_h vanishes and the number of higher occupancies remains constant after the relaxation. The fraction of atoms on multiply occupied sites is similar in

both cases, which corroborates the notion that the formation of higher occupancies is a purely local process and not a consequence of the expansion.

8.4.2 Evolution of Dynamically Formed Higher Occupancies

In our experimental set up, we can not determine the exact distribution of sites with occupancies $\eta_i > 1$. We can neither differentiate between atoms on sites with $\eta_i = 2$ and atoms on sites with $\eta_i > 2$ nor determine their position precisely, due to the limited resolution of our imaging system. We can, however, investigate the distribution of higher occupancies in the system using t-DMRG results obtained by S. Langer et al. [225].

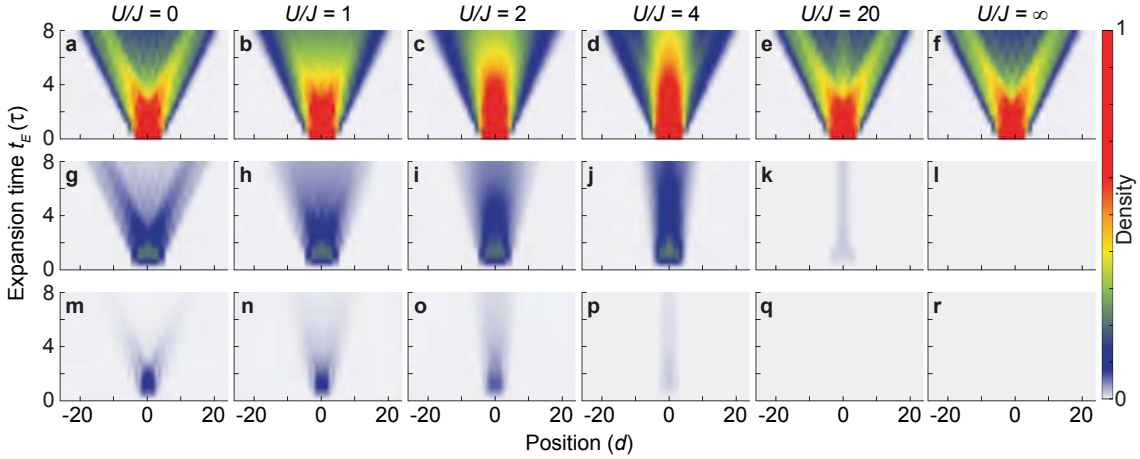

Figure 8.14: t-DMRG calculations of the evolution of line densities $n_x(t_E)$ (top row, (a)-(f)), of double occupancies $\langle \hat{n}_{2,i} \rangle$ (middle row, (g)-(l)) and of triple occupancies $\langle \hat{n}_{3,i} \rangle$ (bottom row, (m)-(r)). The calculations were conducted by S. Langer et al. [225] for the sudden expansion in a 1D lattice at various interactions U/J, starting from a product of local Fock states of $N = 8$ bosons with one boson per site.

Figure 8.14 shows the evolution of the density distribution as well as the evolution of higher occupancies for $N = 8$ bosons expanding from an initial Fock state with $\eta_i = 1$ on the central eight lattice sites. The panels (a)-(f) (top row) show the density $\langle \hat{n}_i(t_E) \rangle$, panels (g)-(l) (middle row) the doublon density $\langle \hat{n}_{2,i}(t_E) \rangle$ and panels (m)-(r) (bottom row) the density of triple occupancy $\langle \hat{n}_{3,i}(t_E) \rangle$

The density of multiply occupied sites is zero for all initial states and for the complete time evolution in the case of $U/J = \infty$, where their formation is energetically forbidden. In all cases with $U/J < \infty$, there is a dynamical generation of multiply occupied sites. This net production (resulting in the increase of ν_h and f_h observed in figure 8.13) results from initial relaxation dynamics following the quench in U/J,

because the initial state is not the ground state for any finite U/J. This is a notable difference to expansions starting from a system that is already in thermal equilibrium (compare [85, 90, 154]), where the non-trivial time evolution is only induced by the quench in the external trapping potential.

As already seen in fig. 8.13a and 8.13b, the main contribution to f_h is given by the doubly occupied sites, while triple occupancy $\langle \hat{n}_{3,i} \rangle$ is only visible for interactions $U/J \leq 4$ and is always significantly smaller than the double occupancy $\langle \hat{n}_{2,i} \rangle$.

Figure 8.14 demonstrates, how the dynamics of higher occupancies in the system is governed by the interaction. For $U/J = 0$, the evolution of $\langle \hat{n}_{2,i} \rangle$ and $\langle \hat{n}_{3_i} \rangle$ follows immediately from the overall density distribution $\langle \hat{n}_i \rangle$. When the interaction is increased, a slowing down of the evolution of $\langle \hat{n}_{2,i} \rangle$ and $\langle \hat{n}_{3_i} \rangle$ can be observed. At large U/J, the tunneling an isolated doubly occupancy becomes a second order process, with an effective hopping matrix element that is $\propto J^2/U$ [27] and this effect is reflected in the tunneling speed of higher occupancies at $U/J > 4$. At $U/J = 20$, we can also observe the effect of quantum distillation [83]. The doubly occupied sites move towards the center of the cloud and stay there for the whole duration of the simulation. For bosons in the strongly repulsive regime, there is even an additional attractive interaction between doubly occupied sites that further increases the stability of such a core of doubly occupied sites [147, 228].

8.4.3 Energetic Effects of the Formation of Higher Occupancies

For an initial state with all $\eta_i \leq 1$, the interaction energy, given by

$$E_{\text{int}} = \frac{U}{2} \sum_i \langle \hat{n}_i \left(\hat{n}_i - 1 \right) \rangle, \tag{8.8}$$

vanishes. Except in the cases of $U = 0$, where the atoms do not interact, and $U/J \to \infty$, where the formation of higher occupancies is energetically forbidden, the local relaxation after a quench in U/J leads to a buildup of higher occupancies (see previous section) and thus to a conversion of kinetic energy to interaction energy. This change of the kinetic energy is necessarily reflected in a changing quasimomentum distribution $n_q(t_E)$, which is shown in figure 8.15 for t-DMRG calculations of $N = 10$ bosons on 1D lattices after a quench in U/J. The calculations were performed by S. Langer et al. [225].

Panels (a) and (b) show the evolution of $n_q(t_E)$ during an expansion and during the relaxation in a box potential at $U/J = 0$. There is a shift of the weight of the density in quasimomentum space towards small values of q on a time scale $t_E \approx 0.5\,\tau$, consistent with the time scale for the formation of higher occupancy in the system that leads to a decreasing kinetic energy. For negative values of U, the interaction energy actually decreases while higher occupancies are formed. In panel (c), we show the evolution of $n_q(t_E)$ under the same conditions as in (b), but with $U/J = -1$.

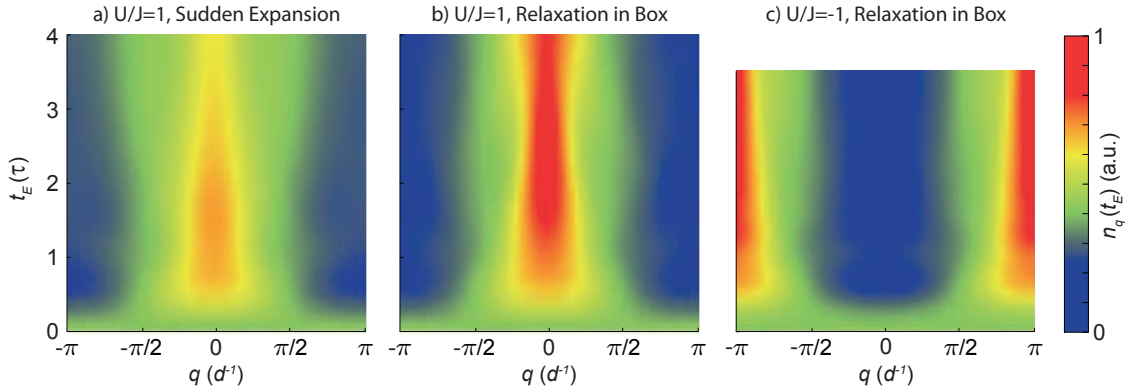

Figure 8.15: Evolution of the quasimomentum distribution $n_q(t_E)$ from t-DMRG calculations for $N = 10$ particles in various relaxation scenarios, starting from an initial product of Fock states with all $\eta_i = 1$. a) Expansion at $U/J = 1$ in a homogeneous lattice. b) Relaxation at $U/J = 1$ in a lattice with additional box potential, restricting the evolution to the initial 10 sites. c) Relaxation as in b), but with $U/J = -1$. The t-DMRG calculations were conducted by S. Langer et al. [225].

As expected, in this case the kinetic energy increases during the relaxation and the weight of the distributions shifts to larger q. This evolution of the quasimomentum distribution can have an effect on the expansion dynamics of atoms in a lattice, as their instantaneous group velocity directly depends on q. However, the effect is not very large, which can already be seen by observing that the main redistribution of weight in $n_q(t_E)$ takes place between large values of $|q|$ and very small ones. Around the points of largest group velocity, at $q = \pi/(2d)$, the density $n_q(t_E)$ changes only very little. Since $v_g(q = 0) = v_g(q = \pm\pi/d) = 0$, redistributing density between these points does not alter the average velocity v_{av}.

In fig. 8.16, we show the average velocities v_{av} calculated from $n_q(t_E)$ at time $t_E = \tau$ for expanding atoms (blue circles) and atoms after relaxation in a box potential (green circles), extracted from t-DMRG calculations conducted by S. Langer et al. [225]. In both cases, v_{av} decreases with increasing interaction up to a value of $U/J \approx 4$ and increases again for larger values. This qualitatively reflects the behavior observed in the experiment, where we also find a minimum of the expansion velocities in this region of interaction strengths. However, the effect on v_{av} is much weaker than the actual reduction of v_r, indicated by the red circles. In the limit of non-interacting particles, v_r and v_{av} are necessarily equal, but for interaction strengths on the order of $U/J \approx 4$, v_r is much lower than v_{av}. This is another clear indication that collisions during the expansion, in which further momentum exchange between individual atoms take place, are mainly responsible for the decrease in expansion velocity at intermediate interaction strengths, and energetic effects play only a minor

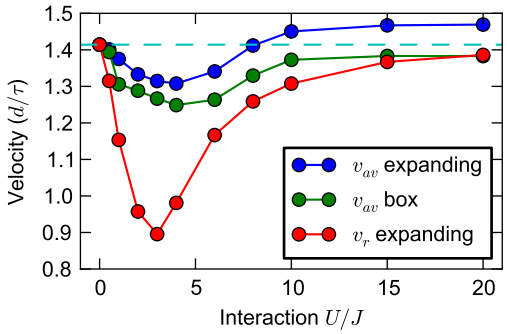

Figure 8.16: t-DMRG results ($N = 10$) for the radius expansion velocity v_r and the average velocity v_{av} at varying interaction strengths U/J. Blue circles: v_{av} for an expansion in a homogeneous 1D lattice. Green circles: v_{av} during a relaxation in a box potential, limiting the evolution to the initially occupied 10 sites. Red circles: v_r of expanding atoms in homogeneous 1D lattices. All calculations started from an initial product of Fock states with one boson per site and were conducted by S. Langer et al. [225].

role.

The increase of v_{av} above $\sqrt{2}d/\tau$ marks the onset of quasi-condensation in the system, where an accumulation in n_q around $q = \pi/(2d)$ occurs during the expansion of strongly interacting atoms in 1D. This effect is investigated in more detail in chapter 9.

8.4.4 Effects of Higher Occupancies in the Initial State

In order to investigate the effect of sites with $\eta_i > 1$ that are already present in the initial state, we change the preparation procedure. Instead of loading the lattice from low density clouds at a strongly repulsive interaction, we reduce the initial scattering length and increase the dipole trap frequencies during the loading (see chapter 6.3.4). The dephasing in the deep lattice remains effective in this preparation, and the resulting initial states of the expansion can still be described as products of local Fock states, but with randomly distributed sites with a higher occupancy $\eta_i > 1$.

In the top row of figure 8.17, we show the density distribution during expansion series in 1D lattices at an interaction of $U/J = 10$ for various initial values of f_h. To extract the f_h values, we start with the prepared initial states, in this case in a lattice of depth $(20, 20, 20)E_r$, and immediately increase the lattice depth to image the amount of higher occupancies as outlined in section 6.3.3. The lowest value, $f_h \approx 0.02$, is a value that is, within the margin of error, consistent with no double occupancies. In this case, the initial state is prepared in the same way

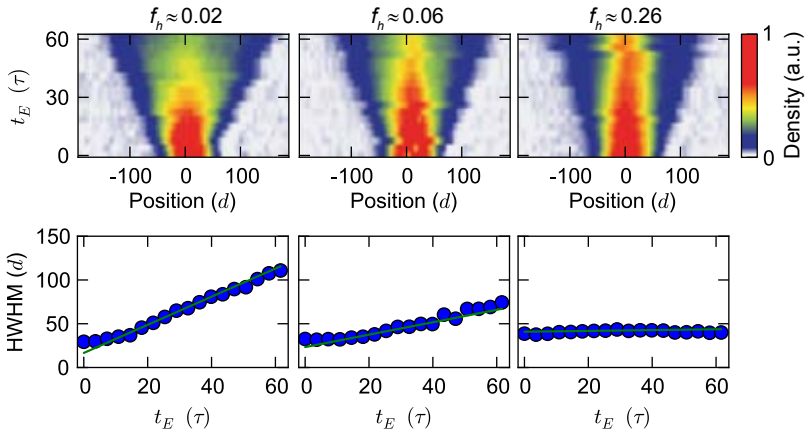

Figure 8.17: Top row: Experimental evolution of the line density distribution $n_x(t_E)$ during expansions in 1D at $U/J = 10$ with varying higher occupancy f_h in the initial states. Bottom row: Evolution of the HWHM extracted from the density profiles.

as those states associated with a negligible fraction of higher occupancies of the measurements described above. For all other values of f_h, we adapt the preparation to deliberately create larger amounts of higher occupancies.

In general, the addition of higher occupancies to a system of 1D hard-core bosons breaks its integrability, as it invalidates the assumption of hard-core interactions, which is fundamental to the mapping onto free fermions. Thus, we certainly expect significant changes in the dynamics of the system at large U/J. Dynamically, the main characteristics of higher occupancies at large U/J, as already discussed in 8.4.2, are their lower effective tunneling matrix elements, resulting in a slower expansion. This is reflected in the evolution of the density distributions over time. While $n_x(t_E)$ becomes rather flat in the case of no higher occupancies in the initial state ($f_h \approx 0.02$), a central core of higher density remains in the center of trap for larger Amounts of higher occupancies. In the lower panel of 8.17, we show the HWHM extracted from these density profiles. Even though there are some fast ballistic atoms present in the expansions, the evolution of the HWHM slows down drastically with added higher occupancies and comes to a complete stop for large initial f_h. The reason for this is that the HWHM is dominated by the central core of higher density, which remains essentially stable at large U/J.

In figure 8.18, we summarize the effects of larger f_h in the initial state for atoms expanding in one dimension at various interaction strengths. At $U/J = 0$, the expansion velocity is not significantly affected by an increase in the amount of higher occupancies. Since the addition of sites with $\eta_i > 1$ in the initial state does not alter the quasimomentum distribution of the atoms after the dephasing, it remains flat over the first Brillouin zone. Without interactions, each single particle wave func-

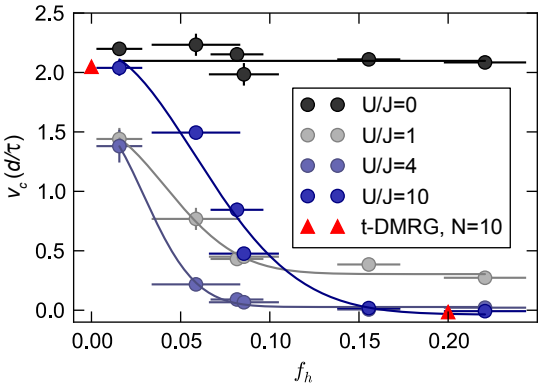

Figure 8.18: Core expansion velocity v_c in 1D when changing the higher occupancy f_h of the initial states (circles). The interaction U/J is indicated by the color of the circles. Vertical error bars are the standard deviation of the fits used to determine v_c, horizontal error bars the standard deviation of averaging 16 measurements. Red triangles are results from t-DMRG calculations with $N = 10$ atoms. Solid lines are guides to the eye.

tion then evolves independently of the others according to its initial group velocity distribution, regardless of the amount of atoms on a given site.

For $U/J = 10$, the effect of higher occupancies is very strong. In the limit of $f_h \to 0$, the atoms expand almost as fast as in the non-interacting case as they are already close to the hard-core boson regime. As soon as higher occupancies are introduced into the system, the assumption of hard-core bosons becomes invalid, as double or higher occupancies are forbidden in the hard-core regime and break the integrability of the system (see chapter 3.4.2). Without the additional (approximate) integrals of motion introduced by being close to the HCB regime, the system has more degrees of freedom for local relaxation, which can drive the system towards diffusive behavior and slow down the dynamics. Additionally, the stability of higher occupancies at large U/J along with their lower effective tunneling matrix element $\propto J^2/U$ contributes to the stability of the central high density region. Another effect of double occupancies at large U/J is an effectively attractive interaction between the doubly occupied sites [147, 228], which again increases the stability of a region of high density in the center of the cloud.

Already for intermediately strong interactions ($U/J = 4$), we observe a strong effect of higher occupancies in the initial state. The core expansion velocity here is already lower than that of non-interacting and strongly interacting atoms when there are only negligible amounts of higher occupancies present, due to the reasons outlined in section 8.2. As f_h is increased, the expansion velocity further decreases and reaches the same values as in the case of $U/J = 10$, consistent with $v_c = 0$.

This is surprising, given that the initial f_h introduced by the different preparation procedure is similar to the f_h that is dynamically created during the expansion, when starting from an initial state without higher occupancies. However, due to the sensitivity of the HWHM to the amount of atoms in higher density regions for bimodal cloud shapes, a small increase in atoms behaving diffusively instead of ballistically can already have a strong effect on v_c. Even for weak interactions at $U/J = 1$, a significant effect of the higher occupancy can be observed.

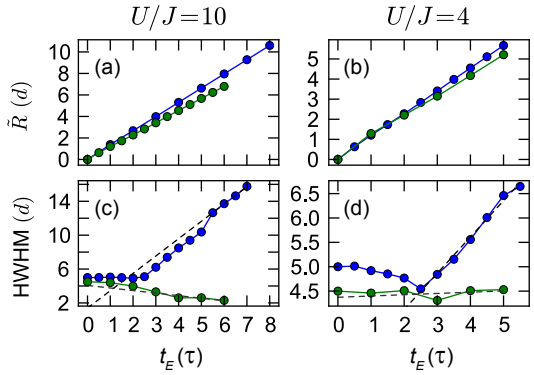

Figure 8.19: Evolution of the radius $\tilde{R}$ and the HWHM for $U/J = 4$ and $U/J = 10$ in t-DMRG calculations of $N = 10$ bosons conducted by S. Langer et al. [225]. For the blue circles, $f_h = 0$ in the initial state, while for the green circles, $f_h = 0.2$. For $f_h \neq 0$, the evolution is obtained by averaging over all possible distributions of sites with $\eta_i = 2$ in the initial states. The dashed lines in the lower plots show the fits used to determine v_c.

To investigate this effect, we can again turn to t-DMRG calculations, conducted by S. Langer et al. [225]. For the results in the case $f_h > 0$, the evolution of $n_x(t_E)$ is averaged over all realizations of initial states with the given f_h. The resulting v_c for two different initial f_h are also shown in figure 8.18 as the red triangles. In figure 8.19, we compare the evolution of the radius $\tilde{R}(t_E)$ to that of the HWHM for expansions without and with higher occupancies in the initial state.

The panels (a) and (b) show the evolution of $\tilde{R}(t_E)$ for $U/J = 10$ (a) and $U/J = 4$ (b) for $f_h = 0.0$ (blue data) and $f_h = 0.2$ (green data). The calculation were performed with $N = 10$ atoms. For the data at $f_h = 0.2$, averages were performed over all initial distributions with one site at $\eta_i = 2$ and all other occupied sites at $\eta_i = 1$. The presence of higher occupancies is visible in the evolution of $\tilde{R}(t_E)$, but the effect is not very strong. This is due to the fact that the evolution of $\tilde{R}(t_E)$ is dominated by the fast moving ballistic tails, which are largely unaffected by the presence of few doubly occupied site. The evolution of the HWHM reveals a much stronger effect of the higher occupancies. For $f_h = 0$, the HWHM stays

flat for the first tunneling times but then proceeds to evolve linearly in time, as we have observed before. In the cases with $f_h = 0.2$, however, there is no expansion visible at all and for $U/J = 10$, the HWHM even decreases over time. This strong effect is due to the high sensitivity of the HWHM to a maximum in the atomic density. A stable doublon surrounded by a low density background of fast atoms can completely dominate the evolution of the HWHM as soon as the background density drops below half the density at the position of the doublon.

8.5 Summary

In this chapter, we have shown how ultracold atoms in optical lattices can be used to investigate expansion dynamics in the Bose-Hubbard model for a wide range of parameters. The ability to tune the interaction between atoms using Feshbach resonances allowed for the direct observation of the onset of diffusive dynamics in 2D lattices, as well as for the observation of a dynamical symmetry between positive and negative U. The versatility of changing the lattice depth along individual axes made it possible to observe a second integrable regime in the 1D Bose-Hubbard Hamiltonian at large U, in addition to the non-interacting limit. In the regime of intermediate interactions, we found significantly slower dynamics of the density distributions and fast relaxation dynamics of the number of higher occupancies and of the quasimomentum distribution. By continuously transforming the system from the 1D regime into a 2D system, we could directly observe the effects of breaking the integrability of the Hamiltonian, that lead to local relaxation and diffusive dynamics.

In general, we found the fastest expansions in the integrable limits, namely the non-interacting limits in 1D and 2D and the strongly interacting limit in 1D. Any deviation from these limits, introduced by changing the interaction, the geometry, or the initial state, lead to a strong reduction of the expansion velocities and the appearance of bimodal cloud shapes that where interpreted as signaling the emergence of diffusive dynamics in the central regions of the clouds.

Chapter 9

Dynamics in Momentum Space

In this chapter, we investigate the dynamics of the quasimomentum distribution $n_q(t_E)$ of strongly interacting atoms during expansions in homogeneous lattices. First, we discuss the theoretical predictions for expanding hard-core bosons in 1D, which are shown to undergo a dynamical quasi-condensation. This quasi-condensation is signaled by the development of sharp peaks in $n_q(t_E)$ of the expanding atoms around quasimomenta $q = \pm\pi/(2d)$. We show experimental results, where we observe the formation of distinct peaks in the momentum distribution of strongly interacting atoms in time-of-flight (TOF) imaging. We then develop a method to reconstruct the approximate quasimomentum distribution $n_q(t_E)$ of the atoms during their evolution in the lattice and find that an accumulation of population indeed takes place around $q = \pm\pi/(2d)$. However, the peaks we observe in $n_q(t_E)$ are much broader than those predicted by theory, and we devote the final part of this chapter to a detailed discussion of experimental effects that can obscure and prevent the formation of quasi condensates and give suggestions for improvements to the experiment.

9.1 Quasi-Condensation during Expansion

Due to the exact mapping from 1D hard-core bosons (HCB) to free fermions [148], quantities like the total energy, the density distribution and density-density correlations are the same for both kinds of systems [154, 229]. This is not the case for quantities like the momentum distribution function $n_q(t_E)$ [149, 153] and the so-called natural orbits [230], which can show very different behavior in the two systems.

9.1.1 Hard-Core Bosons in 1D

Very interesting features that differ strongly from the behavior of non-interacting fermions arise in the context of hard-core bosons expanding from initially confined states into a homogeneous 1D lattice. For a system of HCB confined to the center of a lattice at rather low densities, the ground state quasimomentum distribution

is peaked around $q = 0$. In such a system, an expansion of the atoms, initiated by the removal of the external confinement, results in a fermionization of $n_q(t_E)$ which approaches the $n_q(t_E)$ of free fermions over time [154]. Quite the contrary effect can be observed for HCB that are initially described by a product of local Fock states with one atom per lattice site. In this case, $n_q(t_E = 0)$ is initially completely flat in the first Brillouin zone (BZ) and thus identical to the quasimomentum distribution of free fermions in the same initial state. During an expansion, it can then be observed that $n_q(t_E)$ acquires sharp peaks at momenta $q = \pm\pi/(2d)$, which signal a quasi-condensation of the atoms into the lowest natural orbits [90, 229].

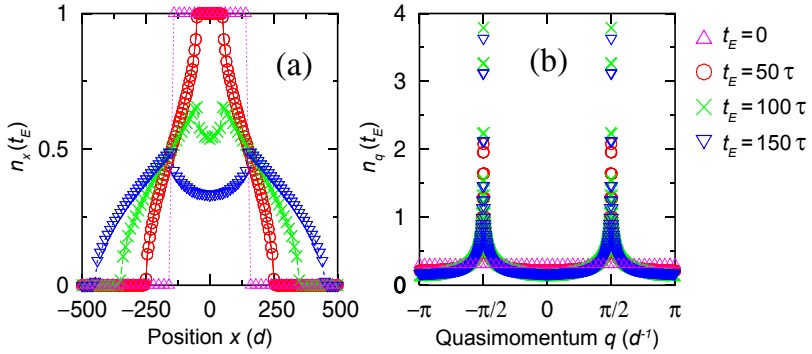

Figure 9.1: Evolution of density (a) and quasimomentum (b) profiles of N=300 HCB expanding in a 1D lattice at different evolution times t_E. Figure reprinted from [90] with kind permission of the author. The axis labeling has been adapted to match the conventions of this thesis.

Figure 9.1 shows the results of exact diagonalization calculations conducted by M. Rigol and A. Muramatsu [90] for the evolution of 300 HCB in a homogeneous lattice, starting from an initial Fock state with one atom per site. Figure 9.1a shows the evolution of the density distribution. This evolution has been discussed extensively in chapter 8 and shows the typical peaks given by the group velocity distribution for a state with $n_q(t_E = 0) = \text{const.}$ in the first BZ. Figure 9.1b shows the evolution of $n_q(t_E)$. It starts out completely flat at $t_E = 0$ (magenta triangles) but already at $t_E = 50\,\tau$ (red circles), sharp peaks have formed around $q = \pm\pi/(2d)$ that further increase in height for $t_E = 100\,\tau$ (green crosses) and then slightly decrease for $t_E = 150\,\tau$ (blue inverted triangles). For very long expansion durations, these peaks vanish completely and n_q approaches the initial flat distribution.

It was shown that the occupation λ_0 of the lowest natural orbit, which determines the peak height in momentum space, increases with the expansion duration as $\lambda_0 = 1.38\sqrt{t/\tau}$, independent of the number of atoms N in the initial state [90]. The maximum occupation of λ_0 scales with $\sqrt{N}$ and thus the time t_m at which the maximum occupation is reached, depends linearly on N as $t_m = 0.32N\tau$.

A quantity that is well-suited to analyze the formation of peaks in n_q is the average

velocity

$$v_{\mathrm{av}}(t_E) = \sqrt{\frac{1}{N\hbar}\sum_q \left(\frac{\delta\epsilon_q}{\delta q}\right)^2 n_q(t_E)}, \tag{9.1}$$

as discussed in chapter 6.4.2. For an n_q that is constant in the first BZ, the average velocity is $\sqrt{2}d/\tau$. If all density in momentum space accumulated at $q = \pm\pi/(2d)$, where the group velocity is maximal, v_{av} would be given by $v_{\mathrm{av}} = 2d/\tau$. Any observed increase in v_{av} to values larger than $\sqrt{2}d/\tau$ is thus an indication of redistribution in $n_q(t_E)$ towards large group velocities and a first sign of the onset of quasi-condensation. Figure 9.2a shows the evolution of v_{av} for initial states with

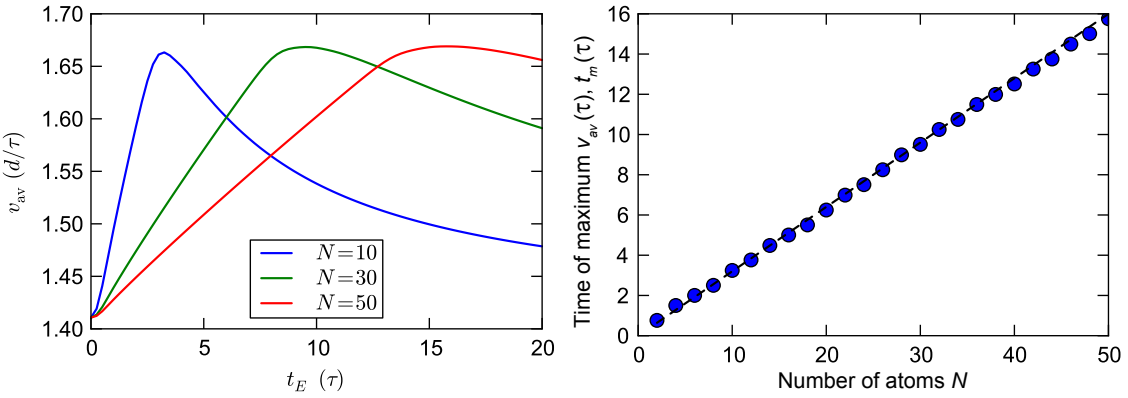

(a) Evolution of the average velocity $v_{\mathrm{av}}(t_E)$ during the expansion for initial states with varying atom numbers N, calculated by S. Langer [231] using exact diagonalization.

(b) Time at which the expanding atoms reach the largest average velocity v_{av} for varying numbers of atoms N (see panel a). The dashed line shows the time of maximum occupation of λ_0, $t_m = 0.32N\tau$, which coincides with the times of largest v_{av}.

Figure 9.2

varying N, obtained from exact diagonalization calculations conducted by S. Langer [231]. In all cases, the initial average velocity is $v_{\mathrm{av}}(t_E = 0) = \sqrt{2}d/\tau$, which then increases to values on the order of $v_{\mathrm{av}} \approx 1.67d/\tau$. The time scale for this increase, as discussed above, depends on the number of atoms in the initial state. In fig. 9.2b, we plot the time at which v_{av} is maximal for the different N (blue circles), which coincides with the time t_m of maximum occupation of λ_0. The dashed line shows the linear behavior of t_m. The fact that t_m depends on N has an effect on our experiment, as we always average over multiple realizations with varying N, which is discussed in section 9.5.1.

9.1.2 Quasi-Condensation at Finite U/J

As the hard-core bosons limit is only reached at $U/J \to \infty$, it is necessary to investigate whether the aforementioned effects persist also for finite U/J that can be reached in experimental realizations. This was done in [232] using t-DMRG calculations (for finite U/J, the mapping to free fermions is not valid anymore and the system cannot be diagonalized as easily). It was shown that for large $U/J > 40$, $n_x(t_E)$ and $n_q(t_E)$ are almost identical to those of real HCB. The peak height in $n_q(t_E)$ is slightly reduced for finite U/J. At $U/J = 20$, which is the interaction strength used in our experiments, the reduction amounts to approximately 5%. Interestingly, the formation of peaks in $n_q(t_E)$ persists for even much lower values of U/J, but with further decreasing peak amplitudes. At finite U/J, also the peak positions shift towards lower values of $|q|$ [232]. At $U/J = 20$, the peaks in $n_q(t_E)$ appear at $|q| \approx 0.95\pi/(2d)$, while at $U/J = 6$, they are shifted down to $|q| \approx 0.83\pi/(2d)$. This effect can easily be understood by considering the conservation of energy in the system. At finite U/J, a system released from a Fock state of singly occupied sites dynamically generates higher occupancies, which increase its interaction energy (cf. chapter 8.4). This increased interaction energy has to be compensated by a decrease in kinetic energy, which results in a shift of the peaks in $n_q(t_E)$ towards lower values of $|q|$.

9.1.3 Quasi-Condensation in Higher Dimensions

Calculations were also performed for systems with tunneling along two lattice axes within a Gutzwiller mean-field approximation [233]. Here, it was observed that by increasing the tunneling along a second axis, the positions of the peaks in $n_q(t_E)$ were shifted towards larger values of $|q|$. The Gutzwiller approximation reproduces the exact diagonalization results of the 1D case when no tunneling is present along the second axis. In the case of equal tunneling along both axes, it predicts quasi-condensation analogous to that in 1D, but into many different momentum modes lying on a rotated square in the first BZ. We do not observe such effects in our experiments. As discussed in chapter 8.1.2, the expansion in 2D at large U/J becomes purely diffusive, with a high density core region and very few atoms in the ballistic wings. These observed bimodal density distributions disagree with the predictions of [233] and we do not observe any signs for quasi-condensation in momentum space. As the validity of the Gutzwiller approximation cannot be taken for granted in the investigated system [233], our experimental results suggest that such a quasi-condensation does not occur in 2D. There are, however, some experimental imperfections present in our system (see section 9.5) and it is not clear how sensitive the theoretically predicted effects are to these imperfections. Thus, we cannot completely rule out that quasi-condensation in 2D may occur, but the observed diffusive nature of the expansion dynamics is a strong argument against it.

9.2 Experimental Procedure

9.2.1 Initial State and Expansion

The preparation of the initial states for the measurements discussed in this section is identical to that for the experiments investigating expansion velocities of Bosons in 1D lattices, discussed in chapters 6 and 8. A detailed description of the optimization of the expansion can be found in chapter 6.3. As we are mainly concerned with the dynamics of bosons close to the hard-core regime, we again take special care to avoid the formation of higher occupancies in the initial state. We prepare the initial state in a lattice of depth $(20\,E_r, 20\,E_r, 20\,E_r)$ along the (x, y, z)-axes, respectively. The expansion in 1D is then initiated by linearly ramping down the intensity of the lattice beam along the x-axis within $150\,\mu$s to reach a final lattice depth of $8\,E_r$ along this axis, while the other two lattice axes remain at a depth of $20\,E_r$. The intensity of the dipole trap beam along the z-direction, which provides confinement along the x- and y-axes, is simultaneously adjusted to compensate the anti-confinement along the expansion direction (x-axis) that is caused by the blue-detuned lattice beams. The main difference to the experiments of chapters 6, 7 and 8, which are concerned with the expansion dynamics of density distributions, is the imaging technique. To observe quasi-condensation, we have to gain insight into the evolution of the quasimomentum distribution of the atoms during the expansion.

9.3 TOF Measurements of Momentum Distributions

In order to investigate the evolution of the quasimomentum distribution during the expansion, we use time-of-flight imaging after a band-mapping procedure. For the band-mapping, instead of switching off the lattice instantaneously, we lower the intensity of the lattice beams linearly over a time of $50\,\mu$s, which leads to a mapping of quasimomenta onto momenta in real space (see chapter 5.2.3). We then switch off the optical dipole trap and the magnetic field and let the atoms drop down under the influence of gravity for a time t_{TOF} before taking an absorption image using the imaging system along the y-direction.

Figure 9.3 shows the density distribution after TOF when releasing the atoms after expanding in the 1D lattice at $U/J = 20$ for durations of $t_E = 0\,\tau$ (fig. 9.3(a)) and $t_E \approx 36\,\tau$ (fig. 9.3(b)). The TOF duration for these images is $t_{\mathrm{TOF}} = 8\,\mathrm{ms}$. We can clearly observe qualitative differences between the distributions after a long evolution in the lattice and those directly after the quench in U/J that initiates the expansion. To see the qualitative changes in the momentum distribution more clearly, we sum the images along the z-axis to obtain line density profiles shown in fig. 9.3(c). While the profile at $t_E = 0\,\tau$ (green line), where no expansion has taken place, does not show any sharp features, the profile after $t_E \approx 36\,\tau$ (blue line)

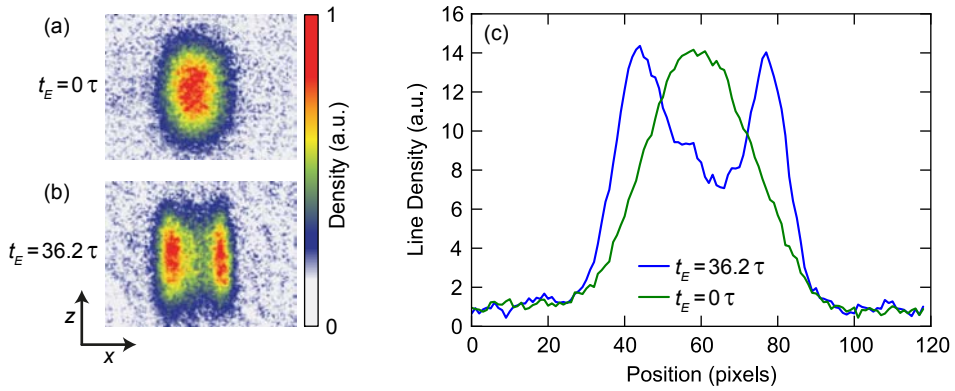

Figure 9.3: (a),(b): Density distribution in TOF imaging with $t_{\mathrm{TOF}} = 8\,\mathrm{ms}$ after no expansion (a) and after an expansion for $t_E = 36.2\,\tau$ (b), both at $U/J = 20$. (c): Line density plots obtained by integrating along the vertical (z) axis for both density profiles. The x-axis denotes pixels on the camera.

exhibits two distinct peaks. These peaks indicate that a redistribution in $n_q(t_E)$ has indeed taken place during the expansion and that there are two distinct values for q, around which density in momentum space has accumulated.

To illustrate this accumulation of density in momentum space during the expansion, we show the line density profiles after various expansion durations in fig. 9.4.

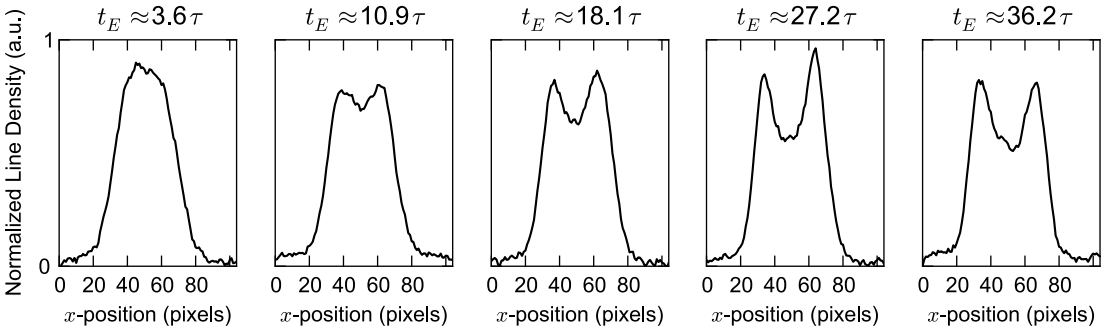

Figure 9.4: Density profiles after $t_{\mathrm{TOF}} = 8\,\mathrm{ms}$ for varying expansion durations t_E at $U/J = 20$. Each profile is obtained by averaging images from two experimental realizations and integrating along the z-direction. All profiles are individually normalized and the x-axis denotes pixels on the camera.

Starting from the left panel, after a short expansion of $t_E \approx 3.6\,\tau$, where only one broad peak is visible in the density profile, we can observe how two peaks emerge and become stronger for longer expansion durations. Already at $t_E \approx 18.1\,\tau$, they

are quite pronounced and reach their highest visibility around $t_E \approx 27.2\,\tau$. They remain clearly visible even for long expansion durations.

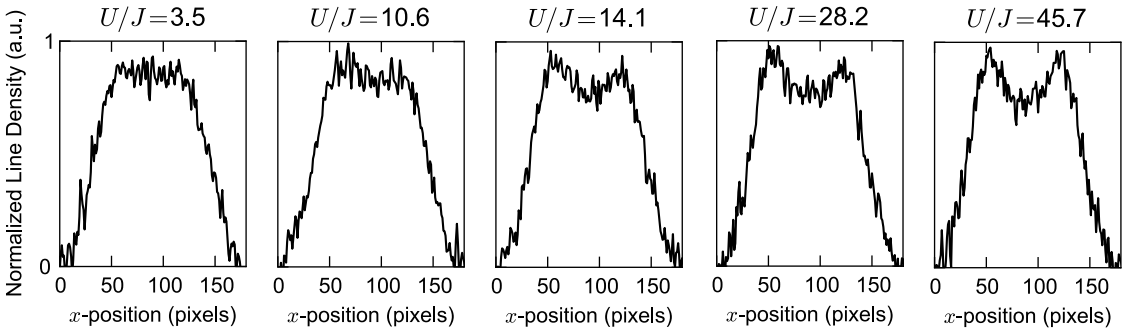

Figure 9.5: Density profiles with $t_{\mathrm{TOF}} = 15\,\mathrm{ms}$ after expanding for $t_E \approx 18.1\,\tau$ at varying interaction U/J. The profiles are obtained as in fig. 9.4. All profiles are individually normalized and the x-axis denotes pixels on the camera.

As a further indication that these peaks are indeed signs of the expected behavior for HCB, we show in fig. 9.5 how the structure of the TOF profiles changes with changing interaction during the expansion. In this case, the expansion duration is always $t_E \approx 18\,\tau$ and the TOF duration is $t_{\mathrm{TOF}} = 15\,\mathrm{ms}$. We expect a much weaker accumulation of quasimomentum for weakly interacting atoms and indeed, the TOF profiles remain rather flat for interactions $U/J = 3.5$ and $U/J = 10.6$. At $U/J = 14.1$, two peaks emerge at the edges of the flat distribution which become more pronounced for even stronger interactions.

In the following, we will investigate the formation of these peaks more closely to extract more information about the actual quasimomentum distribution of the atoms during expansions in 1D.

9.4 Extracting Momentum Profiles from TOF Images

The evolution of the atoms during TOF is, in the ideal case, completely determined by their initial momentum, but the resulting density distribution after a time t_{TOF} is always given by a convolution of the initial density distribution and the evolution during TOF. In the limit of infinitely large t_{TOF}, the effect of the *in-situ* density distribution on the distribution after TOF becomes negligible. However, in our experiments we are limited to a maximum t_{TOF} of about 16 ms. This limitation is partly due to constraints in the optical setup, which could be overcome by changing some of the beam paths, but mainly due to the dilution that takes place during TOF. While expanding, the density at each point of the image becomes lower, reducing the signal-to-noise ratio on the camera. This effect can already be observed in

the comparison of the profiles obtained after $t_{\mathrm{TOF}} = 8\,\mathrm{ms}$ shown in fig. 9.4 and those after $t_{\mathrm{TOF}} = 15\,\mathrm{ms}$ (fig. 9.5), which show a much stronger noise. Despite this limitation, we can extract additional information about the momentum distribution by recording images after several different t_{TOF}.

9.4.1 Calibrating the TOF Imaging

In order to be able to equate positions on the camera after a given t_{TOF} with initial momenta, we need to calibrate the relation between the two. In principle, the information where an atom with momentum p (corresponding to a quasimomentum $q = p/\hbar$ before band-mapping) should arrive after a given t_{TOF} can be deduced directly from the magnification of the imaging system and the initial position of the atom. However, this only works under ideal conditions. In the experiment, additional effects can influence the behavior of the atoms during TOF. First, it is possible that the imaging axis is not directly perpendicular to the directions of gravity and of the lattice beam along which we want to determine the quasimomentum. Second, since the atoms are released from a state at strong interactions, there is a significant magnetic field present before the TOF is initiated, used to set the interactions via a Feshbach resonance (see chapter 4.5). Ideally, this magnetic field should be homogeneous and there should be no forces exerted on the atoms in its presence. However, switching off a strong magnetic field can induce eddy currents in nearby metal parts, which in turn create inhomogeneous magnetic fields that can exert forces on the atoms.

In order to measure the relationship between the position after TOF and the initial quasimomentum, we measure the evolution of atoms during TOF after subjecting a Bose-Einstein condensate to a very short (on the order of a few μs) pulse of the lattice at large lattice intensities. This leads to Raman-Nath diffraction from the lattice, creating groups of atoms traveling with momenta $0, \pm 2\hbar k, \pm 4\hbar k$, where $k = \pi/d$ is the lattice momentum, that show up as distinct peaks during TOF.

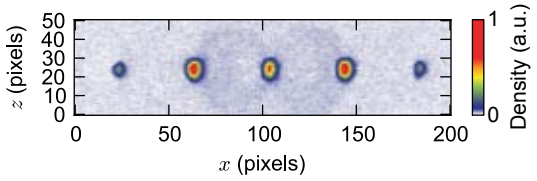

Figure 9.6: Bragg peaks after a short lattice pulse and 7 ms TOF, imaged along the y-direction.

Figure 9.6 shows a typical picture of these peaks after a short lattice pulse and TOF imaging with $t_{\mathrm{TOF}} = 7\,\mathrm{ms}$. We apply a fit function to these peaks, consisting of the sum of five Gaussian peaks, and use a least-squares fitting algorithm to extract their positions.

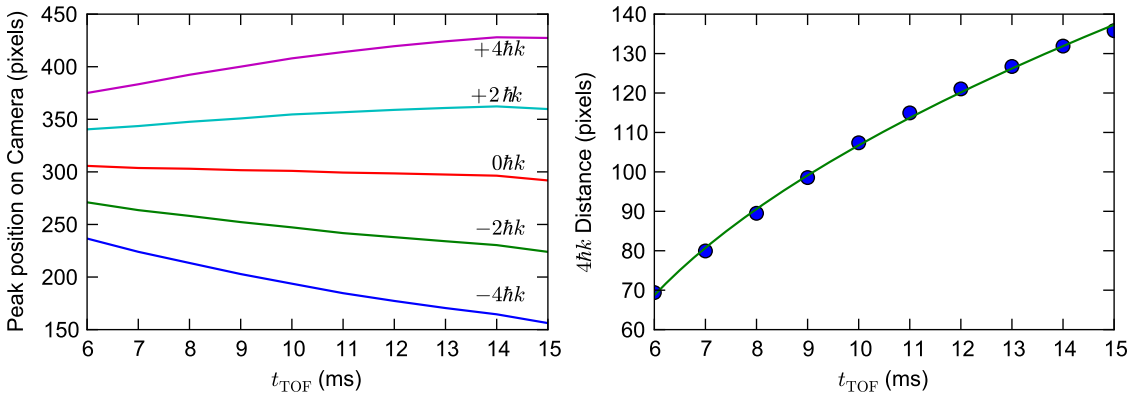

(a) Positions of Bragg peaks on the camera during TOF. The central peak is identified with a momentum $p = 0$, the others with the respective higher order lattice momenta.

(b) Distance between the $-2\hbar k$ peak and the $+2\hbar k$ peak in pixels on the camera during TOF. The solid line is given by eq. 9.2 with parameters obtained by a least-squares fitting method.

Figure 9.7: Calibration of the distance traveled by Bragg peaks during TOF

In figure 9.7a, we plot the evolution of the position of these Bragg peaks during TOF. We identify the central peak with the atoms at momentum $p = 0$, while the peaks to the left and right of the central peaks are identified with the higher order momenta. The evolution does not show the linear dependence of the position on t_{TOF} that is expected for an ideal free evolution with constant momenta, which indicates that there are indeed additional effects present during TOF. For our measurements, we are mainly concerned with the evolution of momenta in the first Brillouin zone, as we apply the aforementioned band-mapping procedure to a state that occupies only the lowest band in the lattice. Thus, we use the evolution of the distance $D_{4\hbar k}$ between the two peaks corresponding to $+2\hbar k$ and $-2\hbar k$ to calibrate the relation between position x on the camera and momentum p in the TOF measurements. Figure 9.7b shows this evolution during TOF, and we can fit it with a function

$$D_{4\hbar k}(t_{\mathrm{TOF}}) = a + b\sqrt{t_{\mathrm{TOF}} - c}, \tag{9.2}$$

where a is an initial distance that corrects for effects during the first 6 ms of TOF and b and c are two more parameters, determined by the least-squares fitting routine, to approximately describe the evolution of the Bragg peaks during TOF. The result of this fitting is shown as the solid line in fig. 9.7.

9.4.2 Calculating the Evolution During TOF

Equation 9.2 describes the distance traveled by an atom with a hypothetical momentum of $p = 4\hbar k$, corresponding to an initial $q = 4\pi/d$. Assuming a linear

scaling of this distance with the quasimomentum of an atom at a fixed t_{TOF}, we can then derive a function that maps an atom starting at the initial position x_{in} with a quasimomentum q to a final position $x_f\,(q, t_{\mathrm{TOF}}, x_{\mathrm{in}})$:

$$x_f\,(q, t_{\mathrm{TOF}}, x_{\mathrm{in}}) = x_{\mathrm{in}} + f_{\mathrm{TOF}}\,(q, t_{\mathrm{TOF}}) \tag{9.3}$$

$$= x_{\mathrm{in}} + \frac{qd}{4\pi}\left(a + b\sqrt{t_{\mathrm{TOF}} - c}\right) \tag{9.4}$$

Note that in the simplest case of a perfect band-mapping procedure, ideal imaging conditions, and no forces acting on the atoms during TOF, the function $f_{\mathrm{TOF}}\,(q, t_{\mathrm{TOF}})$ would simply be given as

$$f_{\mathrm{TOF}}(q, t_{\mathrm{TOF}}) = \frac{\hbar q}{m} t_{\mathrm{TOF}}, \tag{9.5}$$

where m is the atomic mass. In our experimental case, however, we clearly observe deviations from this linear behavior and use the function of eq. 9.4.

Inverting eq. 9.4 gives a mapping that describes from what position in the initial state atoms with a given quasimomentum q arrive at a final position x_f after time t_{TOF}:

$$x_{\mathrm{in}}(q, t_{\mathrm{TOF}}, x_f) = x_f - f_{\mathrm{TOF}}(q, t_{\mathrm{TOF}}). \tag{9.6}$$

The total density n_f arriving at a point x_f after t_{TOF} is then given by the sum over the initial density at all possible starting points $n_{\mathrm{in}}(x_{\mathrm{in}}(q, t_{\mathrm{TOF}}, x_f))$, weighted with the density in momentum space n_q at quasimomenta q. For simplicity, we assume that n_q is the same over the full extension of the cloud.

$$n_f(x_f, t = t_{\mathrm{TOF}}) = \sum_q n_{\mathrm{in}}\left(x_{\mathrm{in}}\left(q, t_{\mathrm{TOF}}, x_f\right)\right) \cdot n_q(q) \tag{9.7}$$

$$= \sum_q n_{\mathrm{in}}\left(x_f - f_{\mathrm{TOF}}\left(q, t_{\mathrm{TOF}}\right)\right) \cdot n_q(q). \tag{9.8}$$

In fig. 9.8, we show exemplary evolutions of the density distribution during TOF for various initial quasimomentum distributions, calculated using eq. 9.8 with the simple f_{TOF} of eq. 9.5. We always start these calculations with a Gaussian shaped initial density distribution of the form:

$$n_{\mathrm{in}}(x) = e^{\frac{-x^2}{2\sigma_x^2}}, \tag{9.9}$$

where σ_x is $10\,\mu$m and then calculate the density distributions after various times t_{TOF}, which are shown in the density plots (bottom row of fig. 9.8). The assumed

n_q for the respective evolutions are shown in the panels above.

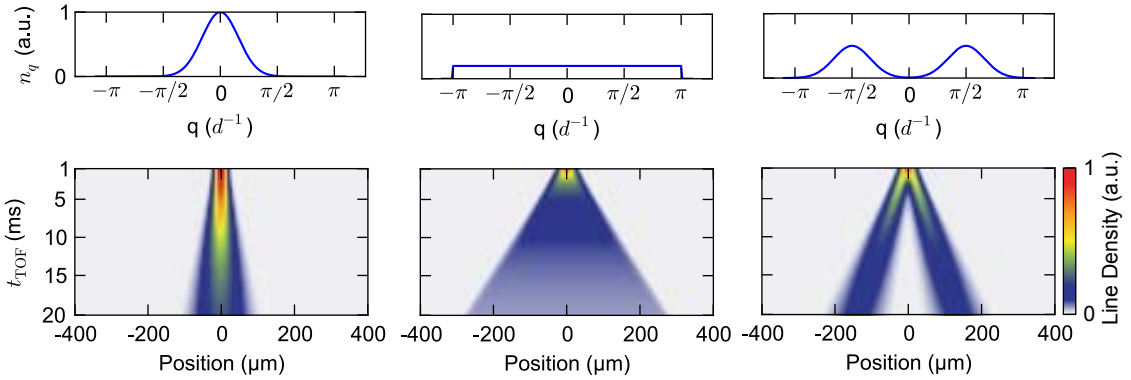

Figure 9.8: Evolution of the line density observed in TOF imaging for various initial n_q. The upper row shows the n_q used for the calculation of the evolution of the line density during TOF shown in the lower row.

The left column shows the evolution of a state with an n_q that is peaked around $q = 0$. Releasing this state results in a slow spreading of the atomic cloud during TOF, caused by the spread in momentum space of the initial state. The center column shows the evolution of a state with an n_q that is completely flat over the first Brillouin zone, which is the case for a state of completely localized atoms. In this case, the density distribution during TOF becomes completely flat and the velocity of the edges of this distribution is equal to the maximum possible velocity after band-mapping, $v_{\mathrm{max}} = \hbar k/m$. The initial shape of the cloud will in this case only change the steepness of the edges of the final distribution.

A more interesting evolution results from initial n_q that include extra features. In the right column of fig. 9.8, we show the TOF evolution of an initial state with a quasimomentum distribution that has two peaks around $q = \pm\pi/(2d)$. This initial quasimomentum distribution leads to the formation of two distinct peaks evolving in opposite directions during TOF. The width of these peaks is given by a convolution of the width of the initial density distribution in real space and the width of the peaks in n_q, which causes a spreading over time during the free evolution in TOF. For true quasi-condensation, we expect the peaks in momentum space to be very narrow (see section 9.1).

9.4.3 Determining Momentum Distributions from TOF Evolutions

Our goal is to extract an approximate quasimomentum distribution for states of strongly interacting atoms during the expansion in the 1D lattice geometry. We let the atoms expand in a 1D lattice with a lattice depth of $(8, 20, 20)\, E_r$ along (x, y, z)

at $U/J = 20$ for a given expansion duration t_E and then initiate the TOF procedure. The atoms proceed to fall down and after various t_{TOF}, we image the atoms along the y-direction and extract line density profiles by integrating along the z-direction.

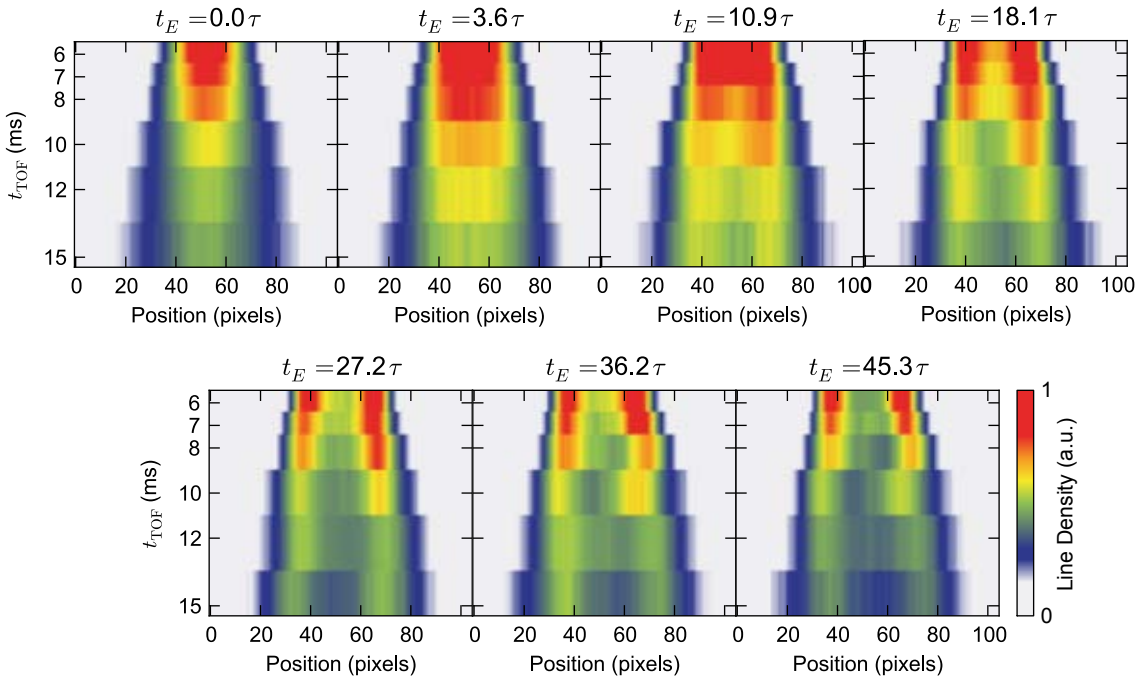

Figure 9.9: Line density profiles during TOF for various expansion durations t_E, averaged over multiple realizations, individually normalized and shifted to a common center.

In fig. 9.9, we show the evolution of the density distributions during TOF after various expansion durations t_E. Each horizontal line shows the line density at the indicated t_{TOF}, which is averaged over multiple experimental realizations. For the short $t_{\mathrm{TOF}} = 6\,\mathrm{ms}$, $7\,\mathrm{ms}$, and $8\,\mathrm{ms}$, we average over two images, for $t_{\mathrm{TOF}} = 10\,\mathrm{ms}$, we average over three images and for $t_{\mathrm{TOF}} = 12$ and $15\,\mathrm{ms}$, we use four or five images. Again, we clearly see how an increasing evolution time in the lattice leads to the formation of two peaks. At $t_E = 0\,\tau$ and $t_E = 3.6\,\tau$, we do not observe any distinct features in the density distributions during TOF. At $t_E = 10.9\,\tau$, we can notice the first hint of two distinct peaks with a lower density in the center. For $t_E = 18.1\,\tau$, we can already clearly observe the two peaks traveling in opposite directions at $t_{\mathrm{TOF}} = 6\,\mathrm{ms}$, and the signal becomes even stronger for larger t_E.

We can now use the method outlined in sect. 9.4.2 to calculate the evolution during TOF of an assumed $n_q(t_E)$ and compare it to the experimental results. For these calculations, we use the independently measured *in-situ* densities $n_x(t_E)$ as the initial density distributions $n_{\mathrm{in}}(x_{\mathrm{in}})$ in eq. 9.8. We then employ a least-squares fitting

procedure to optimize the free parameters of our assumed $n_q(t_E)$. This heavily relies on the model used to approximate an initial quasimomentum distribution. Here, we will limit the discussion to a rather simple model that allows to easily identify key characteristics of the momentum distribution. In section 9.5.4, we will present a more general method that yields similar results. As we expect $n_q(t_E)$ to develop two distinct peaks, we start with a simple trial function of the form

$$n_q = A_c \exp\left(-q^2/(2\sigma_c^2)\right) + A_d \left(\frac{\sigma_d^2}{\sigma_d^2 + (q - q_d)^2} + \frac{\sigma_d^2}{\sigma_d^2 + (q + q_d)^2} \right), \tag{9.10}$$

with $q \in [-\pi/d, \pi/d]$, i.e., limited to the first Brillouin zone.

This function describes a momentum distribution consisting of a Gaussian peak centered around $q = 0$ with a standard deviation σ_c, which can in principle be very broad and thus also describe a flat momentum distribution. The weight of this peak is given by A_c. To this, we add two Lorentzian peaks, displaced by variable $\pm q_d$, where σ_d defines the width of the peaks and A_d is their amplitude. These peaks can describe the accumulation of density in quasimomentum space at specific points in the Brillouin zone that have the same distance from the center of the Brillouin zone, but are displaced in opposite directions.

In fig. 9.10, we show the experimental density distributions during TOF (top row) for various evolution times in the lattice t_E, along with the simulated density distributions for the parameters of eq. 9.10 that result in the best matches between experiment and simulation (center row). In the lower row of fig. 9.10, we show $n_q(t_E)$ for the fitted parameters. The three dashed lines are the individual terms of eq. 9.10, i.e. the broad central peak and the two displaced peaks. Note that we only take into account the distributions after large t_{TOF} for the fitting procedures. Taking smaller t_{TOF} into account results in an increase of the fitted q_d towards large values of $|q|$, which is an indication for imperfections in our band-mapping and TOF imaging procedure that we address in section 9.5.4.

While at $t_E = 0$, $n_q(t_E)$ is given by a very broad function that is peaked at the center, at $t_E = 10.9\,\tau$, two distinct peaks of $n_q(t_E)$ have formed around $q = \pm\pi/(2d)$, as expected during quasi-condensation. These peaks become even more pronounced after $t_E = 18.1\,\tau$. The peaks persist for longer t_E, but they remain rather broad compared to the expected sharp peaks indicative of quasi-condensation.

To investigate the behavior of the peaks in n_q more closely, we first plot their displacement q_d over expansion duration t_E in figure 9.11a. For $t_E \gtrsim 10\,\tau$, which is the time at which two distinct peaks can first be observed, their displacement is close to the predicted value of $q_d = \pi/(2d)$.

From the fitted quasimomentum distributions, we can calculate the average velocity v_{av} (eq. 9.1), which we plot over t_E in figure 9.11b. We see that during the first part of the expansion, v_{av} shows the behavior expected during quasi-condensation,

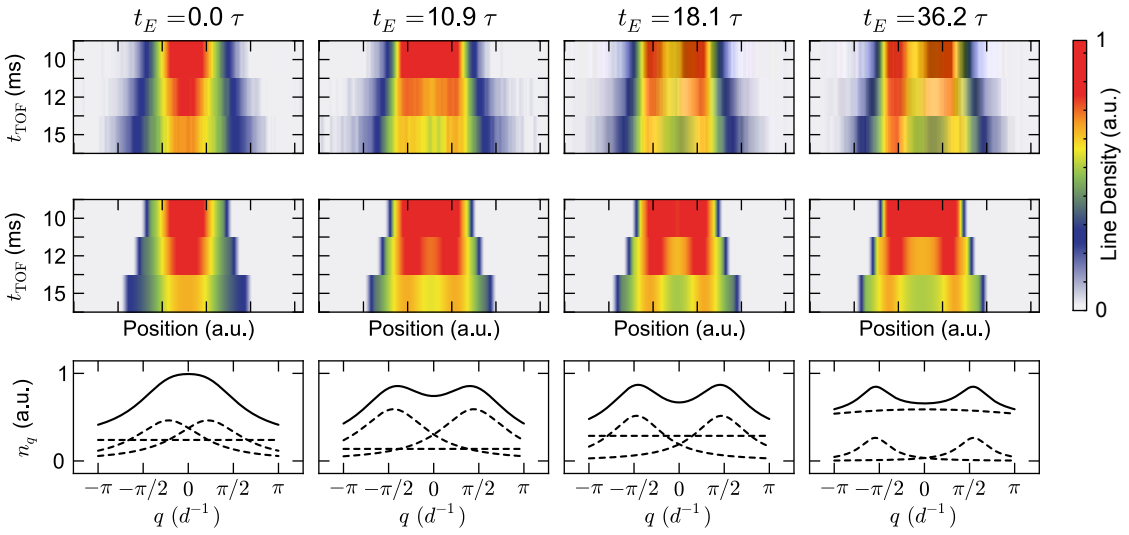

Figure 9.10: Top Row: Experimental TOF line density profiles for various expansion durations for $t_{\mathrm{TOF}} = 10\,\mathrm{ms}, 12\,\mathrm{ms}$ and $15\,\mathrm{ms}$, all line densities individually normalized. Middle Row: Simulated TOF profiles after obtaining the best parameters for n_q from least squares fitting. Bottom Row: The fitted quasimomentum profiles. The dashed lines show the three contributing peaks of eq. 9.10 and the solid line shows n_q, which is the sum of the three peaks. Note that the fits result in very large widths for the central peak, which then corresponds to a flat background.

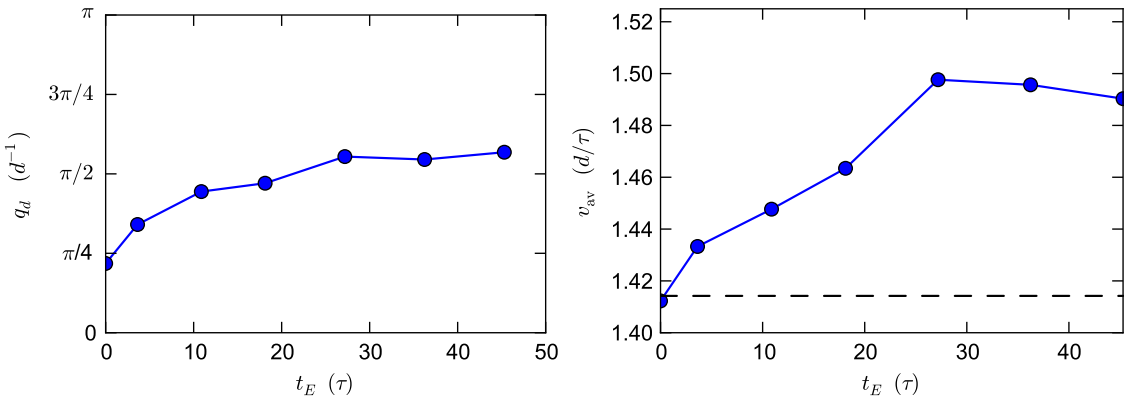

(a) Evolution of the displacement q_d of the additional peaks in eq. 9.10 during the expansion.

(b) Evolution of v_{av}, calculated from the fitted n_q of fig. 9.11b, during the expansion.

Figure 9.11

as discussed in section 9.1. At $t_E = 0$, v_{av} is close to $v_{\mathrm{av}} = \sqrt{2}d/\tau$, the average velocity of a state in 1D that has a completely flat quasimomentum distribution. Even though the fitted n_q for this state (see fig. 9.10) is not completely flat, the symmetry of the group velocity distribution (see fig. 6.4a) ensures that v_{av} does not differ significantly from $\sqrt{2}d/\tau$. For increasing expansion durations, v_{av} then increases, reaching a maximum of $v_{\mathrm{av}} \approx 1.5d/\tau$, which is about 6% larger than $\sqrt{2}d/\tau$. This is directly related to the accumulation of n_q around $|q| = \pm\pi/(2d)$, where the absolute group velocity is largest. For even larger expansion durations, however, v_{av} stops to increase and remains significantly lower than the values of $v_{\mathrm{av}} \approx 1.67d/\tau$ predicted by the calculations shown in fig. 9.2a.

9.5 Effects Limiting the Formation and Detection of Quasi-Condensates

As discussed in the previous section, we do observe an accumulation in $n_q(t_E)$ around $q = \pm\pi/(2d)$, in agreement with theoretical predictions. However, the peaks forming in $n_q(t_E)$ during the expansion are much broader than those expected for quasi-condensation of hard-core bosons in 1D, and the increase of v_{av} is not as strong as expected.

The theoretical predictions discussed in section 9.1 are given in the context of a single defect-free 1D chain of hard-core bosons evolving in a perfectly homogeneous 1D lattice. This is naturally quite far from the experimental situation we encounter, which involves averaging over multiple tubes, imperfect initial states and residual global potentials. In the following, we discuss the effects of these imperfections in the experimental situation, as well as ways to circumvent them and to improve the experiments.

9.5.1 Averaging of 1D Systems with Varying Atom Numbers

The theoretical predictions for quasi-condensation of hard-core bosons discussed in section 9.1 are mainly concerned with the evolution of an initial state consisting of a fixed number of atoms N expanding in a 1D tube. In our experiment, the realizable systems are quite different from this situation.

Even if the initial state created before the dephasing period in the deep lattice were a perfect and pure Mott insulator, it would nevertheless consist of a multitude of 1D tubes with chains of atoms of varying length l_t. As an example, figure 9.12a shows a visualization of the chain lengths in an ellipsoidal density distribution. In this case, we assumed that the number of atoms per site is $\eta_i = 1$ for every site within an ellipsoid with half axes of length $(5\,\mu m, 5\,\mu m, 2\,\mu m)$ along (x, y, z), respectively. The outermost tubes of the state can contain only very few atoms, while the most central tubes in this example can contain up to 27 atoms. Note

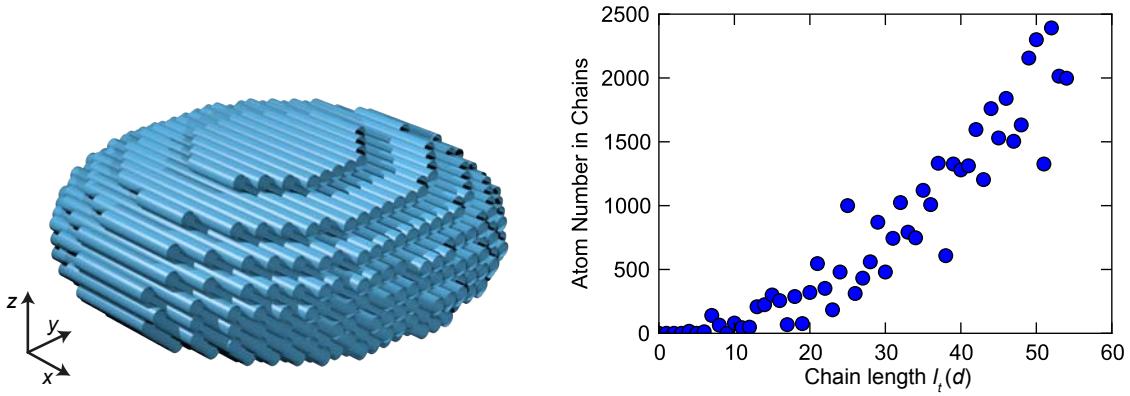

(a) Visualization of chains of atoms in an exemplary ellipsoidal density distribution with half-axes $(5\,\mu m, 5\,\mu m, 2\,\mu m)$. The chain lengths are rounded off to integer numbers of sites.

(b) The total number of atoms in chains with a given length l_t for an experimentally more realistic ellipsoidal density distribution with half-axes $(10\,\mu m, 10\,\mu m, 5\,\mu m)$.

Figure 9.12

that in such ellipsoidal states, the number of tubes N_{l_t} of length l_t is approximately proportional to l_t (aside from finite size effects and rounding to integer numbers of l_t, which becomes important in small systems).

In the experimental TOF images, we measure the averaged momentum distribution for all atoms from tubes with varying l_t. Thus, it is instructive to investigate the total number of atoms in chains of length l_t, given by $N_{l_t} \cdot l_t$, which is approximately proportional to l_t^2. We show this quantity in fig. 9.12b for an experimentally more realistic assumption of a state with half-axes $(10\,\mu m, 10\,\mu m, 5\,\mu m)$ along (x, y, z), respectively. The quadratic dependence on l_t can be observed, although there are strong fluctuations present stemming from finite size effects. Due to this quadratic behavior, the dynamics in momentum space that can be observed in TOF images are dominated by atoms in chains of length $l_t \gtrsim 30$, while atoms in shorter chains contribute only very little.

As discussed in sect. 9.1, the formation time of the quasi-condensate in a tube depends approximately linearly on the length of the chain of atoms in this tube. For every single chain with a given l_t, there is a point in time at which the occupation of the lowest natural orbit is maximal and the peaks in $n_q(t_E)$ are the narrowest. If we now include the evolution of tubes with fewer and more atoms, this will lead to a broadening of the peaks at the given time, because of the differing time scales for the formation of the quasi-condensates. To investigate this effect, we average over calculated quasimomentum profiles for the expansion of HCB with varying atom numbers in the initial state. The evolution of the quasimomentum profiles was calculated by S. Langer [231] using exact diagonalization. We use the occupation of

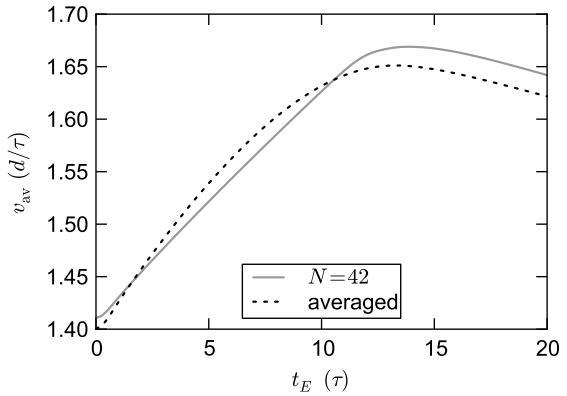

(a) Evolution of v_{av} during the expansion for an initial ellipsoidal density distribution with half-axes $(10\,\mu m, 10\,\mu m, 5\,\mu m)$ along (x, y, z) (black dotted line), compared to the evolution of initial states with $N = 42$ atoms (gray solid line).

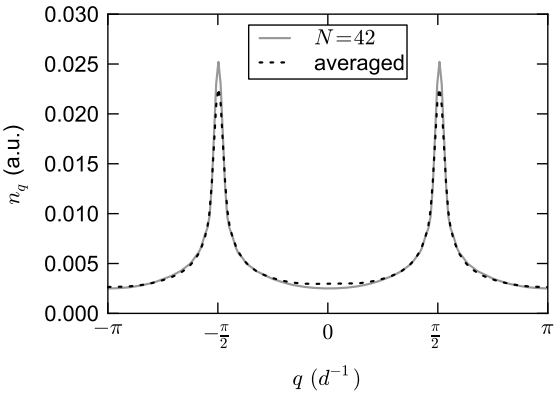

(b) The quasimomentum profiles n_q for a state with 42 atoms after $t_E = 13.75\,\tau$ (gray solid line) and for the averaged case at $t_E = 13.25\,\tau$ (black dotted line).

Figure 9.13

tubes with length l_t, as shown in fig. 9.12b, as weights in the averaging and calculate v_{av} for every time step. The evolution of v_{av} for the averaged quasimomentum profiles is shown in fig. 9.13a in comparison to that of a state with a fixed $l_t = 42$, which corresponds to the average tube length of the ellipsoidal density distribution with half axes $(10\,\mu m, 10\,\mu m, 5\,\mu m)$ along (x, y, z), respectively, when weighted by the number of atoms per tube. Note that only the evolution of quasimomentum distributions for atom numbers $N \leq 50$ was calculated. For the averaging of the quasimomentum profiles, we thus introduce a cutoff at $N = 50$ and discard the contributions of the tubes with $l_t > 50$.

There are two main effects of the averaging over varying tube lengths. The first effect is a slight reduction of the maximum v_{av} that is reached during the expansion. While for a single tube with a fixed atom number, the average velocity reaches values between $v_{\mathrm{av}} = 1.66\,d/\tau$ and $v_{\mathrm{av}} = 1.67\,d/\tau$ for atom numbers $N > 10$ in the initial state, v_{av} does not exceed $1.65\,d/\tau$ for the averaged momentum profiles. The reason for this effect can be observed in fig. 9.13b, where we compare the shape of the averaged quasimomentum profile with that of atoms in a single tube with an initial $l_t = 42$. The profiles plotted are taken at the respective times t_E where the maximum v_{av} is reached. We can observe that the peaks in the averaged profile are slightly lower than in the state with $l_t = 42$. Conversely, n_q is slightly higher around $q = 0$ for the averaged state. As the group velocity v_g is maximal around $q = \pm\pi/(2d)$ and minimal around $q = 0$ (and $q = \pm\pi/d$), this results in a slightly

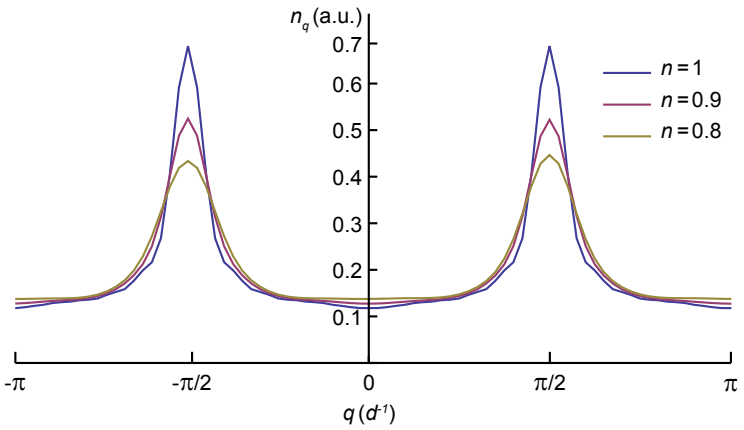

Figure 9.14: Quasimomentum distribution n_q of initial products of Fock states with mean density n after an expansion for $t_E = 10\,\tau$, calculated using exact diagonalization. All n_q are normalized individually. For $n < 1$, 70 configurations of randomly distributed holes were included in the initial states, and the resulting n_q averaged. Figure adapted from [231] with kind permission of the author.

lower v_{av} for the averaged profiles.

It is nevertheless quite remarkable how well the shapes of the two profiles agree. This shows that the averaging over tubes with varying length should not be a limiting factor for the observation of quasi-condensation in HCB systems. Even though the height of the peaks in momentum space is slightly reduced after averaging, the peaks still remain very narrow. The second effect that can be observed is a slight broadening of the maximum in v_{av} with respect to t_E in the averaged case, compared to the case of $l_t = 42$. This broadening, however, should only facilitate the observation of the peaks in n_q, as it increases the time span of high visibility.

9.5.2 Effects of Holes and Higher Occupancies in the Initial State

The theoretical calculations published to date on quasi-condensation of 1D hard-core bosons all assume an initial state of a chain of singly occupied lattice sites with no empty sites in between. In the experiment, there are always regions of lower density with empty lattice sites at the outer edges of the cloud, but as our greatest concern is to prevent the formation of higher occupancies when loading the lattice, it is certainly possible that we also produce a significant fraction of empty lattice sites even closer to the center. To investigate the effects of holes in the initial state, calculations using exact diagonalization were conducted by L. Vidmar [231] for various configurations of holes in the initial states.

Figure 9.14 shows the results of calculations for a varying number N of atoms initially in a product of local Fock states, expanding from a box of size $L_B = 20\,d$ into a homogeneous lattice. The initial density n is given by $n = N/L_B$. For $n < 1$, multiple calculations were performed with the position of the empty sites in the initial states chosen randomly according to a probability distribution that mimics the assumed distribution of holes in the experimental situation [231]. The three lines are the resulting quasimomentum distributions n_q after an expansion duration $t_E = 10\,\tau$. There is a clear tendency of decreasing peak height and increasing width as more holes are introduced into the initial state. With 20% holes in the initial state, the height of the peaks is almost reduced to half of the height in the $n = 1$ case. Such effects could certainly be present in our experiments and inhibit the formation of sharp peaks in n_q. In future experiments, we should thus pay close attention to creating initial Mott insulators that contain as few holes as possible, which could be assessed by monitoring the peaks in momentum space while optimizing the loading procedure.

The investigation of doubly occupied sites in the initial state is more complex, as the presence of these doublons breaks the integrability of the system and the exact diagonalization method cannot be applied anymore. In this case, one has to resort again to t-DMRG calculations, which are limited to smaller system sizes. In [234], the formation of peaks in n_q during expansions was investigated for $N = 10$ atoms with varying admixtures of holes and doubly occupied sites, starting from initial products of Fock states. At $U/J = 20$, the presence of such defects was found to slightly shift the position of the peaks, but did not significantly reduce their visibility. However, finite size effects might play a larger role for these calculations and we should also make sure that there are as few double occupancies as possible in the initial state of future experiments. A more extensive numerical analysis of the combined effects of holes and doubly occupied sites in the initial state is currently being conducted [231].

9.5.3 Effects of Global Potentials

In chapter 6.3.1, we discuss the effects of uncompensated global potentials on the expansion velocity and our method of optimizing the homogeneity of the system. We are able to reach a homogeneity that is good enough to observe undisturbed dynamics of the density distributions for non-interacting and strongly interacting atoms in agreement with the theoretical predictions. The presence of a global harmonic potential, however, does not only affect the expansion velocity but also the evolution of the quasimomentum distribution, and for states with a flat initial n_q in the first Brillouin zone, it is quite possible that these changes are significant in $n_q(t_E)$ without strongly altering the overall evolution of the density distribution.

To show the effects of additional potentials on $n_q(t_E)$ in more detail, we again investigate the dynamics of non-interacting atoms in a Hubbard Hamiltonian of the

form

$$H = -J \sum_{\langle i,j \rangle} \hat{b}_i^\dagger \hat{b}_j + \sum_i \frac{\omega^2}{2} (i - i_0)^2 \, d^2 \hat{n}_i, \tag{9.11}$$

where i_0 is the index of the site in the center of the harmonic potential with trap frequency ω (given in units of $J^{1/2}$). As discussed in chapter 6.3.1, to calculate the evolution of atoms in such a system we use our knowledge about the dispersion relation of atoms in a lattice potential in the tight binding regime, which is given by

$$\epsilon_q = -2J \cos(qd), \tag{9.12}$$

and the resulting group velocity relation

$$v_g(q) = \frac{1}{\hbar} \frac{\partial \epsilon_q}{\partial q} = 2 \frac{d}{\tau} \sin(qd). \tag{9.13}$$

From these relations, we can obtain simple differential equations for the evolution of single atoms under the influence of external potentials and solve them numerically (see also chapter 6.2).

Effects of Harmonic Potentials

We have already shown in sect. 6.3.1 that for strong enough external potentials, the expansion velocity of the *in-situ* density distribution in the lattice can be strongly reduced. As we experimentally optimize the intensity of the dipole trap beams to maximize the cloud size after large expansion durations t_E, we do not expect such strong harmonic confinements to be present. In order to demonstrate the effects of the harmonic confinement on the evolution of $n_q(t_E)$, we thus choose a harmonic confinement that is small enough to leave the evolution of the HWHM of the cloud largely unperturbed. In figure 9.15, we demonstrate the effects of a small harmonic confinement on the evolution of atoms in a 1D lattice. Here, we assume all atoms to be initially localized on a single lattice site and their quasimomentum to be completely flat within the first Brillouin zone and zero elsewhere. Panel a) shows the unperturbed ($\omega = 0$) time evolution of the line density $n_x(t_E)$ of such an initial state, dominated by the fast ballistic atoms with group velocities $v_g = 2d/\tau$. Panel b) shows an evolution of the same initial state, but with an added harmonic confinement of $\omega = 0.03 J^{1/2}$. The difference between the evolutions can only be observed for large t_E, where a slight inward bending of the trajectories of the fastest atoms takes place. The effect of this bending on our experimental observable, the HWHM of the clouds, is shown in panel c). We plot the HWHM of the evolution without external potential as the dashed gray line and that of the evolution with $\omega = 0.03 J^{1/2}$ as the solid black line. A significant deviation of the HWHM can only be observed for $t_E > 30\tau$. In such an expansion, harmonic confinements on

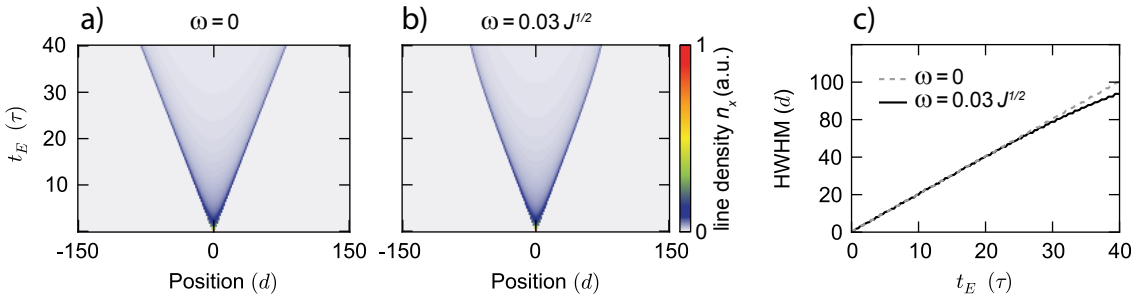

Figure 9.15: a): Evolution of the line density $n_x(t_E)$ of atoms starting at $x = 0$ with $n_q(t_E = 0) = \text{const}$ for $q \in [-\pi/d, \pi/d]$ and no external confinement present ($\omega = 0$). b): The same evolution as in a), but with a harmonic confinement of $\omega = 0.03J^{1/2}$ present. c): The evolution of the HWHM for the expansion without confinement and with confinement.

the order of $\omega \lesssim 0.03J^{1/2}$ would thus not be easily detected by investigating the HWHM of the clouds, but they could still have strong effects on the evolution of the momentum distributions.

During quasi-condensation, we expect that the quasimomentum distribution $n_q(t_E)$ acquires sharp peaks at quasimomenta $q = \pm\pi/(2d)$. Thus, we first investigate how the presence of the harmonic potential affects the evolution of an initial state that exhibits sharp peaks in $n_q(t_E)$. We again choose the initial position of all atoms to be at $x = 0$, but this time, the initial n_q is given by

$$n_q(t_E = 0) = e^{-\frac{(x-\pi/(2d))^2}{2(\pi/(10d))^2}} + e^{-\frac{(x+\pi/(2d))^2}{2(\pi/(10d))^2}}. \tag{9.14}$$

This distribution has two distinct peaks at $q = \pm\pi/(2d)$, shown as the dashed line in fig. 9.16e). Without any additional potentials present, the evolution of the density distribution $n_x(t_E)$ now consists only of two density lobes, traveling with maximum velocity $2d/\tau$ in opposite directions, as shown in fig. 9.16 a). During the evolution, a small broadening of the two lobes takes place, determined by the width of the two peaks in n_q. The peaks in n_q themselves, however, do not change during the evolution, shown in fig. 9.16 c), as there are no forces acting on the atoms.

When an additional harmonic potential with $\omega = 0.03J^{1/2}$ is added, we can already observe some changes in the time evolution of $n_x(t_E)$, as shown in fig. 9.16 b). The trajectories of the atoms again bend inwards for large t_E and the broadening of the traveling density lobes is more severe than without the external potential. A much stronger effect, however, can be observed in the evolution of $n_q(t_E)$ (fig. 9.16 d). As expected for a confining potential, the absolute value of the peak position is reduced during the expansion, since a state with an n_q peaked around $q = \pi/(2d)$

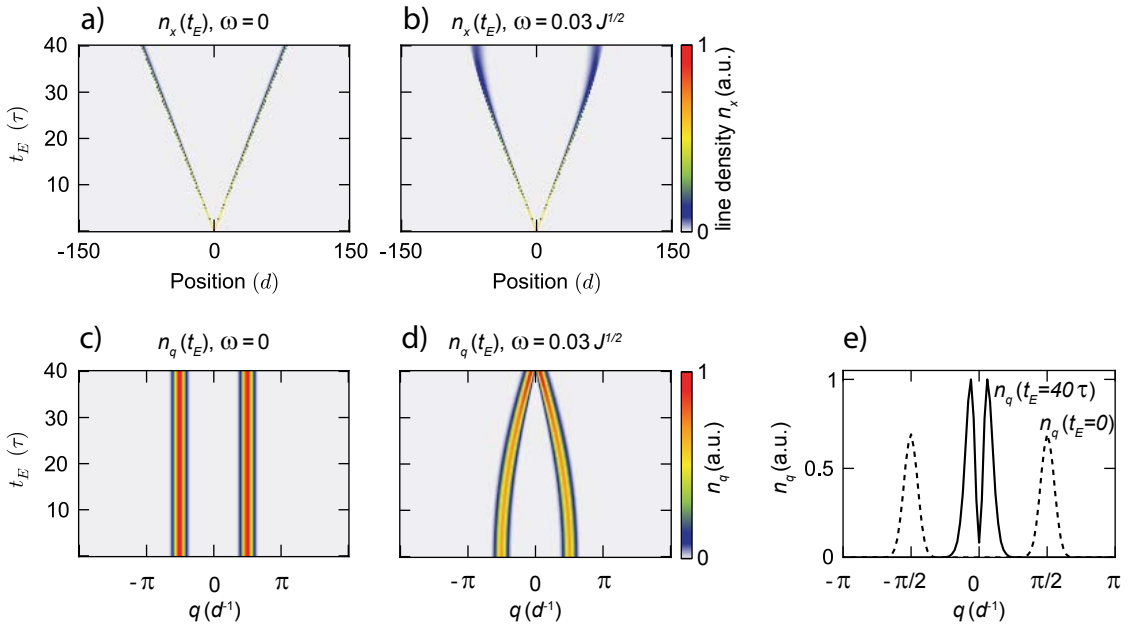

Figure 9.16: a),b): Evolution of the line density $n_x(t_E)$ during an expansion of atoms starting at $x = 0$ with $n_q(t_E = 0)$ given by eq. 9.14 for $\omega = 0$ and $\omega = 0.03J^{1/2}$. c),d): Evolution of the quasimomentum distribution $n_q(t_E)$ for the same parameters. e): Comparison between $n_q(t_E = 0)$ (dashed line) and $n_q(t_E = 40\,\tau)$ (solid line)

has a large group velocity and travels in the direction of increasing potential, which results in a decreasing quasimomentum. The magnitude of this effect is very large, and after $t_E \approx 40\tau$, the peak position in quasimomentum space has been shifted almost to $q = 0$.

The same effect, but with an opposite sign, can be observed for anti-confining potentials, where the peaks are shifted towards larger values of $|q|$. This is shown in fig. 9.17 for $\omega = 0.03\mathrm{i}J^{1/2}$. The evolution of the density distribution (fig. 9.17a) is identical to the evolution in the case $\omega = 0.03J^{1/2}$ (fig. 9.16b), due to the symmetry of the group velocity relation. The evolution of $n_q(t_E)$, shown in fig. 9.17b, is also analogous to the $\omega = 0.03J^{1/2}$ case, but with an opposite sign. Due to the anti-confining nature, the peaks are now shifted towards larger values of $|q|$ and after $t_E = 40\,\tau$, they reach $q = \pm\pi/d$. Note that for even longer evolution times, the position of the peaks in n_q would increase even further in $|q|$. As the quasimomentum is limited to the first Brillouin zone, the atoms would then be reflected, $\pm q \to \mp q$, and then continue their evolution, oscillating in the lattice.

In both cases ($\omega = 0.03J^{1/2}$ and $\omega = 0.03\mathrm{i}J^{1/2}$), the peaks do not only move in momentum space, but even become slightly narrower during the evolution. This effect, however, is caused by the focusing nature of the harmonic potential in com-

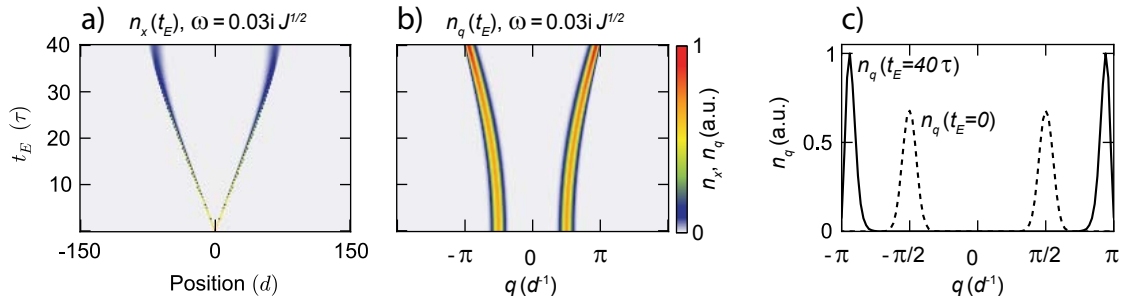

Figure 9.17: a) Evolution of the line density $n_x(t_E)$ during an expansion of atoms starting at $x = 0$ with $n_q(t_E = 0)$ given by eq. 9.14 for $\omega = 0.03\mathrm{i}J^{1/2}$. b): Evolution of the quasimomentum distribution $n_q(t_E)$ for the same parameters. c): Comparison between $n_q(t_E = 0)$ (dashed line) and $n_q(t_E = 40\,\tau)$ (solid line)

bination with the very small spatial extension of the initial state. It cannot be expected to occur under realistic experimental conditions with larger initial states, as we will discuss in the next section.

Effects on Expanded Distributions

In the examples above, we discuss the effects of global harmonic confining and anti-confining potentials on states that have strongly peaked momentum distributions. This leads to shifts in the peak position in quasi-momentum space, but also to an overall narrowing of the peaks. The main reason for this narrowing is the fact that these states were considered to be originating from a very small region in real space, which facilitates the focusing due to harmonic potentials. In the following, we will consider realistic states that are expected to be present during the expansion in our experiments.

In fig. 9.18, we discuss the evolution of the density distribution of an initial state with a constant density in the region $x \in [-30d, 30d]$ and no atoms outside of this region. This corresponds to the typical HWHM of the initial states used in the experiment. Here, the initial quasimomentum distribution $n_q(t_E = 0)$ of the atoms is again assumed to be constant over the first Brillouin zone.

Figure 9.18a shows the evolution of the line density $n_x(t_E)$ during the expansion without an additional harmonic potential, which has already been discussed extensively in chapter 6. Figure 9.18b shows the same evolution, but with an external harmonic confinement of $\omega = 0.015J^{1/2}$. The changes of $n_x(t_E)$ when adding the harmonic confinement are indeed almost negligible. A very slight bending of the outermost flanks of the expanding distribution can be observed in the density profiles, which leads to a vary small reduction of the HWHM after long evolution times. This becomes more clear by comparing the evolution of the HWHM directly in figure

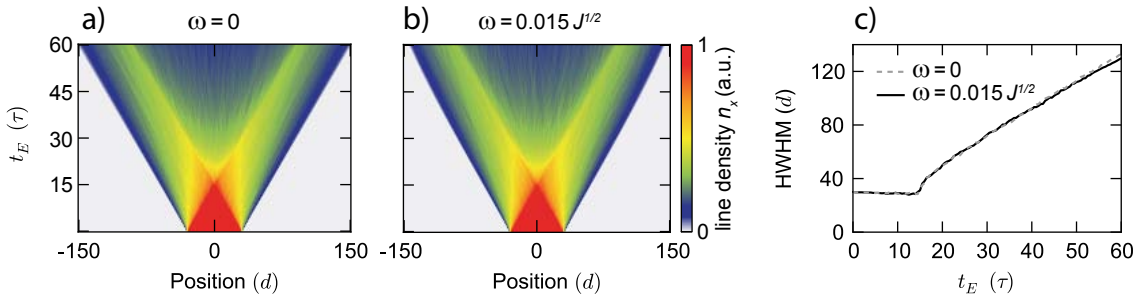

Figure 9.18: a) Evolution of the line density $n_x(t_E)$ during an expansion of atoms with $n_x(t_E = 0) = \text{const.}$ for $x \in [-30d, 30d]$ and $n_q(t_E = 0) = \text{const.}$ for $q \in [-\pi/d, \pi/d]$. b): Same as a), but with an additional harmonic potential with $\omega = 0.015J^{1/2}$. c): The evolution of the HWHM for the expansion without confinement (dashed gray line) and with confinement (solid black line)

9.18c. The gray dashed line shows the HWHM without an external potential, the black solid line those with the harmonic potential present. Both curves lie almost exactly on top of each other and only for very large $t_E > 50\,\tau$ can we observe that the HWHM is indeed slightly smaller when the confinement is present. Thus, such a small harmonic confinement would certainly go undetected in our experimental optimization.

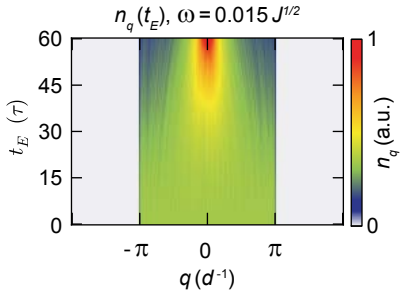

Figure 9.19: Evolution of the momentum distribution of the initial state of fig. 9.18 under the influence of an external harmonic potential with $\omega = 0.015J^{1/2}$.

Even though we do not observe any obvious deviations in comparison to the free case when looking at the density distributions, we can nevertheless observe a clear effect when investigating the evolution of the momentum distribution. This is shown in fig. 9.19 for the same initial conditions and external potential. The effect of the harmonic potential can be seen in the redistribution of n_q from higher absolute values of q towards the center of the Brillouin zone. The fact that the evolution of the HWHM of the density distribution is not affected strongly by this redistribution

in quasimomentum space can be explained by considering that the highest absolute group velocities are associated with quasimomenta $q = \pm\pi/(2d)$. Even though n_q decreases strongly at $q = \pi/d$ and increases at $q = 0$, both these points are anyway associated with $v_g = 0$. Thus, in the time span investigated here, the changes in n_q cause only small changes in the average velocity, as n_q at $q = \pi/(2d)$ is not strongly affected by the redistribution.

Since we are interested in the effects of the confinement on the signatures of quasi-condensation, we repeat this calculation for a state similar to those that would be expected after quasi-condensation has happened in the experiment. We expect strong peaks in n_q to be visible after an evolution time of $t_E \approx 20\,\tau$, after which our experimental systems typically reach a HWHM of $\approx 50d$. Thus, we assume an initial state that, for the sake of simplicity, has a flat density distribution in the range $x \in [-50d, 50d]$ and no atoms outside of this region. The initial quasimomentum distribution, however, is now again assumed to be strongly peaked around $q = \pm\pi/(2d)$ according to eq. 9.14 (dashed line in fig. 9.20c).

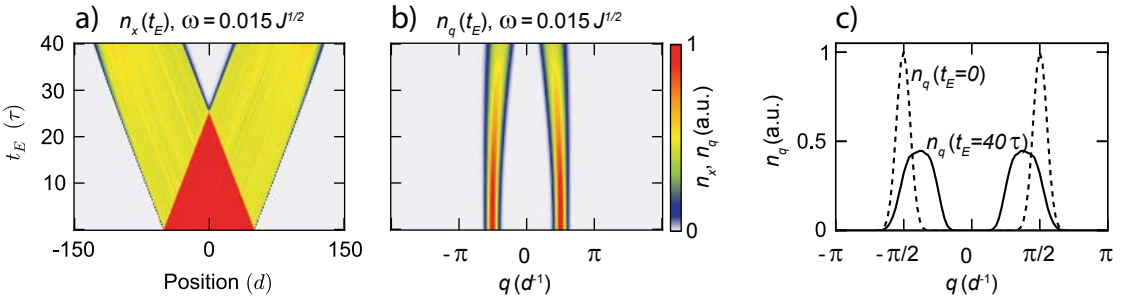

Figure 9.20: Evolution of the line density $n_x(t_E)$ during an expansion of atoms starting with $n_x(t_E = 0) = \text{const.}$ for $x \in [-50d, 50d]$ with $n_q(t_E = 0)$ given by eq. 9.14 for $\omega = 0.015J^{1/2}$. b): Evolution of the quasimomentum distribution $n_q(t_E)$ for the same parameters. c): Comparison between $n_q(t_E = 0)$ (dashed line) and $n_q(t_E = 40\,\tau)$ (solid line).

Figure 9.20a shows the evolution of the density distribution for such an initial state. Due to the distinct peaks of n_q, instead of the spreading observed in regular expansions, the evolution is now clearly separated into a left-moving and a right-moving portion, both moving with maximum group velocity v_g. Note that such an evolution is certainly not what we expect to occur in the experiment. The reason for this is that, while n_q is indeed expected to become strongly peaked during the formation of quasi-condensates, there will always be scattering processes that lead to an exchange of momentum between two particles and can thus transfer an atom from the left-moving portion of the cloud to the right moving. These scattering processes cannot be taken into account in our simple model calculation, but we can nevertheless use it to estimate what kinds of effects can be expected for the evolution of the quasimomentum distribution. The evolution of $n_q(t_E)$ during the

expansion is shown in fig. 9.20b. Starting with two peaks at $q = \pm\pi/2$, there are two clear effects of the external harmonic potential. First, the center of the peaks shifts again to smaller values of $|q|$ during the evolution, as already observed in fig. 9.16. Second, the fact that we started from a broad initial state mitigates the otherwise focusing nature of the harmonic potential. As atoms starting at different positions experience the effects of the harmonic potential with varying strength, the influence of the potential leads to an overall broadening of the peaks in momentum space.

To show this broadening more clearly, we show the initial momentum profile $n_q(t_E = 0)$ as the dashed gray line in fig. 9.20c and the final $n_q(t_E = 40\tau)$ as the solid black line. The effect is indeed quite strong, the peak heights are reduced by more than a factor of two while the width of the peaks increases by a similar amount.

This serves as an example of the strong effects global potentials can have on the evolution in quasimomentum space. Experimentally, we use the evolution of the HWHM as a measure for the homogeneity of our global potentials. However, as we have seen in fig. 9.18, this measure is less precise than investigating the evolution of the quasimomentum distribution. Note that the effects on the dynamics during the actual formation of quasi-condensates are more intricate, since the peaks in $n_q(t_E)$ are not present in the initial state, as assumed in our examples, but instead dynamically form during the evolution. Such an evolution is certainly more complicated than what is presented in this section. However, the qualitative effects that can arise from the presence of external potentials are shown to range from shifts in the position of peaks in quasimomentum space to a broadening as well as a narrowing of the peaks, while being undetected in observations of the HWHM of the clouds.

A further investigation of these effects is needed to rule out such strong effects on the evolution of $n_q(t_E)$ during expansion measurements. This could easily be done by varying the intensity and position of the dipole trap laser in expansion measurements and investigating the effects this has on the peaks observed after TOF.

9.5.4 Imperfect Band Mapping Procedure

As mentioned in sect. 9.4.3, the fitting of quasimomentum distributions to our TOF data did not work very well, when taking the whole range of t_{TOF} from 6 ms to 15 ms into account. It is not entirely clear, what the exact reason for this is, but we do observe that the fitted distributions tend to show excess weight at large q for large values of t_E and small values of t_{TOF}, which indicates that the mapping of position to quasimomentum is not completely accurate.

One effect that could possibly influence the behavior of the atoms during TOF is an imperfect band mapping procedure. In order to faithfully convert all quasimomenta q into real momenta $p = \hbar q$, it is required to ramp down the lattice intensity

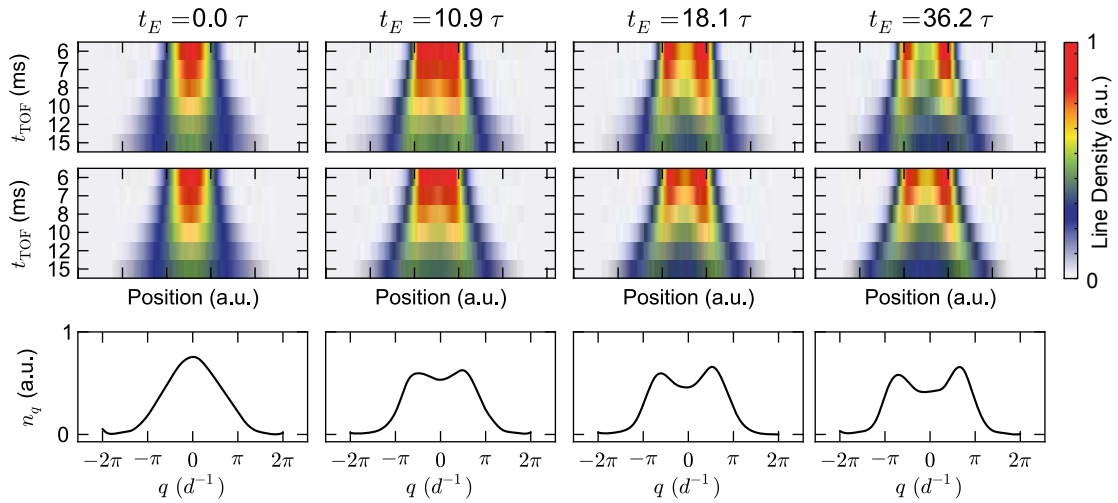

Figure 9.21: Top row: Experimental TOF line density profiles for various expansion durations. Middle row: Simulated TOF profiles after obtaining the best parameters for n_q from least squares fitting. Bottom row: The fitted quasimomentum profiles.

slowly enough to adiabatically stay in the lowest band of the lattice during the complete ramp [51, 203] but also fast enough so that the quasimomentum distribution cannot change significantly during this ramp. For strongly interacting atoms, these two conditions are hard to fulfill at the same time. In our experiments, we used a linear ramp of the lattice intensity over a time span of 50 μs, which is rather fast and could potentially lead to some atoms being promoted to the next higher band during the band mapping. These atoms would then be mapped onto real momenta $p = \hbar(q \pm 2\pi/d)$, and in TOF, would travel further than possible under the assumption of perfect band mapping.

In order to investigate this effect, we can modify the fitting procedure of sect. 9.4.3. Instead of limiting the real space momenta of the atoms after the band mapping procedure to $p \in [-\hbar k, \hbar k]$, which corresponds to all atoms being adiabatically transferred from the lowest band of the lattice, we allow for momenta in the range of $p \in [-2\hbar k, 2\hbar k]$. This can accommodate for a slightly too fast band-mapping procedure that promotes few atoms into higher bands.

In fig. 9.21, we show fit results for momentum distributions with this relaxed constraint on the possible momenta. In this case, we do not make an initial assumption about the shape of n_q, as we did in sect. 9.4.3. Instead, we simply use the value of n_q at thirty points in q, evenly spaced over the interval $[-2\pi/d, 2\pi/d]$, as the free parameters of the fitting algorithm, using a cubic interpolation between these points. In the bottom row of fig. 9.21, we show the resulting fitted n_q. The behavior for n_q to acquire two distinct peaks during the expansion is reproduced in this case, without explicitly including them in the ansatz. We can also observe that the

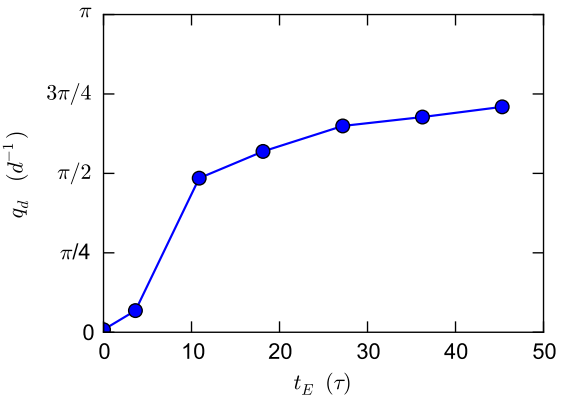

(a) Evolution of the peak position $\overline{|q_{\max}|}$ in the fitted $n_q(t_E)$.

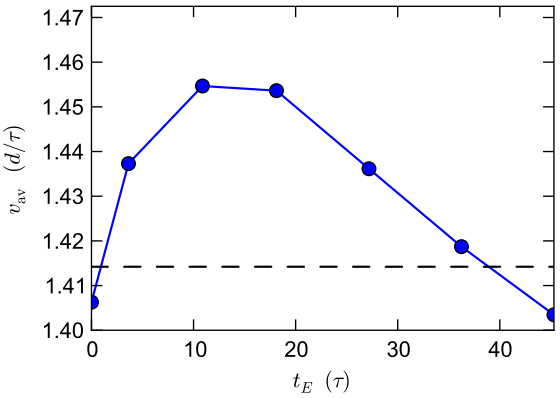

(b) Evolution of v_{av}, calculated from the fitted $n_q(t_E)$.

Figure 9.22

fitted momentum distributions indeed tend to extend slightly beyond $\pm\pi/d$. This supports our hypothesis of imperfections either during the band mapping or in our TOF calibration of the camera.

However, in addition to a contribution to the n_q at large quasimomenta, we also observe that the developing peaks themselves are shifted to higher momenta for large t_E. This is shown in fig. 9.22a, where we extract the average distance $\overline{|q_{\max}|}$ of the two maxima of the distributions from the center of the Brillouin zone, where $q_{\max}$ are the positions of the local maxima in momentum space. for small t_E, the distribution has not developed clearly distinguishable peaks, but after $t_E \approx 10\,\tau$, the two peaks are distinguishable and their positions are close to $\overline{|q_{\max}|} \approx \pi/(2d)$. For increasing t_E, these positions also increase, and approach values of $3\pi/(4d)$ for large t_E. This is also reflected in the average velocities, calculated from the fitted n_q and shown in fig. 9.22b. The average velocity first increases with t_E, while the peaks in n_q form around the points of large v_g. For longer times, however, the displacement of these peaks towards even larger values of q, where the group velocity is smaller, results in an overall decreasing v_{av} for large t_E.

As discussed in sect. 9.5.3, it is physically possible to observe such a continued shift in the peak positions under the influence of additional potentials acting on the atoms during their expansion. However, we see this effect disappear when only including data for large t_{TOF} in the fitting routine which indicates that it is caused by the experimental profiles after small t_{TOF}. This can be seen by repeating the above fitting procedure, but only taking data for $t_{\mathrm{TOF}} = 10\,\mathrm{ms}, 12\,\mathrm{ms}$ and $15\,\mathrm{ms}$ into account. We do not show the fitted profiles for this case, which look similar to the ones shown in fig. 9.21, but the results for the evolution of $\overline{|q_{\max}|}$ and v_{av} are shown in figs. 9.23a and 9.23b, respectively.

Here, the peak positions stay much longer in a range around $q \approx \pi/(2d)$ and only

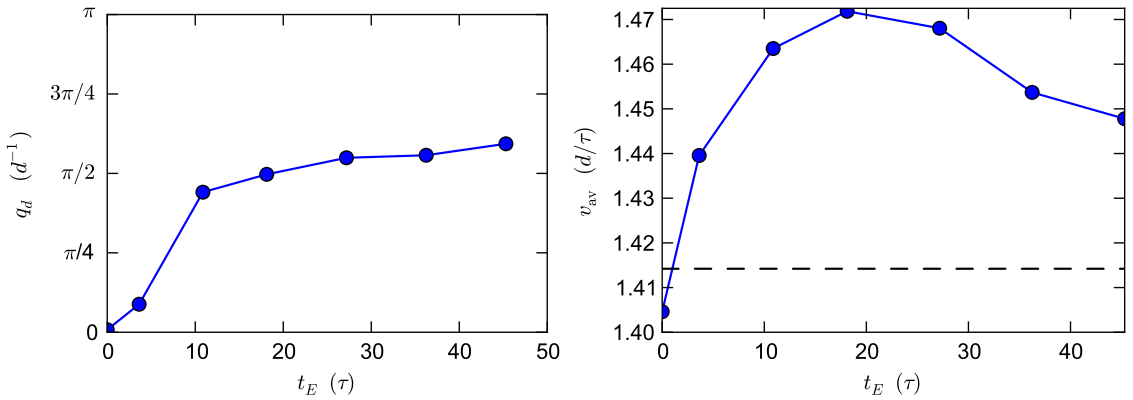

(a) Evolution of the peak position $\overline{|q_{\max}|}$ in the fitted $n_q(t_E)$, when only taking data with $t_{\mathrm{TOF}} = 10\,\mathrm{ms}, 12\,\mathrm{ms}$, and $15\,\mathrm{ms}$ into account.

(b) Evolution of v_{av}, calculated from the fitted $n_q(t_E)$ when only taking data with $t_{\mathrm{TOF}} = 10\,\mathrm{ms}, 12\,\mathrm{ms}$, and $15\,\mathrm{ms}$ into account.

Figure 9.23

increase slightly for larger t_E. Also the average velocity, while still showing a decay for large t_E, does not decrease as drastically as in the previous case.

We conclude that there are indeed some imperfections present in either the TOF data or our calibration of the dynamics during TOF. This is reflected in the presence of momenta with absolute values $|q| > k$ in the best fits for n_q as well as in the difference between fitted n_q when taking data for different ranges of t_{TOF} into account. While an imperfect band mapping procedure can lead to the appearance of atoms with too large momenta in TOF, it is not expected to lead to a broadening and shifting of the observed peaks in momentum space. Spatially dependent field gradients during the first few ms of TOF could, however, have adverse effects on the sharpness of the observed peaks, as well as on their position. Our method of calibrating the relationship between quasimomentum q of an atom and its position after TOF relied on Bragg pulses applied to a condensate in the center of the trap (see sect. 9.4.2). Thus, inhomogeneous effects that have a stronger influence on atoms at different positions can go unnoticed in this procedure and these effects should thus be investigated more closely in future experiments.

9.6 Summary

In this chapter, we presented our experimental results towards the realization and observation of quasi-condensation of strongly interacting atoms in 1D. We did indeed observe an accumulation in n_q around quasimomenta consistent with theoretical predictions. However, these peaks were much broader than the expected ones, and we

discussed several sources of errors and deviations from the ideal case that could be responsible for this. We showed that the averaging over individual experimental realizations with varying atom numbers, as it always happens in our experiments, only leads to a small broadening. While imperfections in the band mapping procedure or the calibration of the TOF imaging should have negligible effects on the width of the observed peaks, spatially dependent magnetic field gradients during the first ms of TOF could lead to a broadening and should be investigated more carefully. The most probable causes that inhibit the formation of quasi-condensates in our experiments are uncompensated global potentials and empty sites in the initial state. Both these aspects could be addressed in future experiments. The effects of global potentials could easily be detected by varying the dipole trap properties and monitoring the density distribution in TOF to detect changes in n_q. The number of holes in the initial state could be reduced by optimizing the initial state preparation while monitoring TOF images.

Chapter 10

Conclusions and Outlook

In this thesis, we have shown that ultracold atoms in optical lattices can be used as a highly flexible model system to study the non-equilibrium dynamics of quantum systems. Using blue detuned lattices along with magnetic Feshbach resonances and additional dipole traps, we were able to control all parameters of the Hubbard Hamiltonians independently and in real-time, which allowed us to conduct a series of experiments on the expansion dynamics of ultracold atoms in homogeneous lattices.

One of the main investigated aspects was the influence of the dimensionality of the systems on their expansion dynamics. We found clear indications of diffusive dynamics for interacting fermions in 2D and 3D geometries, as well as for interacting bosons in 2D. The diffusive behavior resulted in very small expansion velocities in the regime of moderate to large interactions, combined with characteristic bimodal density distributions consisting of a diffusive core and a ballistic background. In 1D, however, the behavior was found to be fundamentally different. Instead of vanishing expansion velocities, we observed a minimum between $|U/J| = 3$ and $|U/J| = 4$ and reincreasing velocities for larger interactions. This was found to be a direct consequence of approaching the 1D hard-core boson limit, where the system is integrable and can be mapped onto free fermions, leading to an identical behavior of the density distributions of non-interacting and strongly interacting atoms. This constitutes the first direct observation of a strongly interacting system exhibiting ballistic transport dynamics due to the approach of an integrable limit (see [226, 227] and [86] and references therein). Our experimental results for 1D bosons were found to be in excellent agreement with t-DMRG calculations.

Using the flexibility of tuning individual lattice axes independently and thereby changing the ratio of tunneling along the two axes, we were able to map out the crossover between 1D and 2D systems for a wide range of interactions and tunneling ratios. This served as a demonstration of how increasing the degrees of freedom of a system can slow down its expansion and highlighted the counter-acting effects of strong interactions driving the system towards integrability when being close to the 1D regime, while driving it towards diffusive behavior close to the 2D regime.

Furthermore, we investigated the formation and evolution of higher occupancies in the system, when starting from an initial state without higher occupancies. We

found a fast local relaxation towards quasi-stationary amounts of higher occupancies on the time scale of the tunneling time τ, consistent with the time scales observed in t-DMRG calculations. Finally, we introduced higher occupancies already into the initial state of the system and found that already at small interactions, these higher occupancies significantly slowed down the expansion dynamics and brought them to an almost complete stop in the strongly interacting regime.

The final part of this thesis was devoted to studying the evolution of the momentum distribution of strongly interacting atoms expanding from initial states consisting of localized atoms. While we did not observe the sharp peaks in momentum space predicted in [90, 233], we did observe the formation of a non-thermal quasimomentum distribution with broad peaks around quasimomenta predicted by theory. We discussed multiple possible effects that could hinder the formation or detection of quasi-condensation in our experiments, as well as methods to investigate and mitigate these issues experimentally.

Outlook

The field of non-equilibrium dynamics in quantum systems offers a broad range of uncharted territory and cold atoms in optical lattices provide a great tool for its investigation.

Regarding the expansion dynamics, there are many more interesting situations that can be investigated in our setup. The initial state of the expanding fermions investigated in chapter 7 was that of a band insulator with one fermion of each species per lattice site. For a better comparison of their expansion dynamics to the bosonic case, it would be interesting to investigate expansion dynamics in 1D of interacting fermions starting in a Mott insulator ground state. According to [85], such an initial state should always result in the same fast expansion velocities, independent of the interaction. If a dephasing procedure like the one used in our experiments is applied, however, an interaction dependence of the expansion velocity similar to the bosonic case should emerge [86], even though the system is integrable for all U. This would also allow for the observation of the 1D-2D crossover between ballistic and diffusive dynamics in the fermionic case.

By making small changes to the experimental setup, we should be able to reach a higher resolution when imaging the *in-situ* density distributions in the lattice. Starting expansion measurements with initial states that contain a large fraction of doubly occupied sites, this increased resolution could allow for an observation of quantum distillation effects in the lattice for bosons [147, 228] as well as for fermions [83]: An expansion of such initial states at large interactions is expected to lead to a contracting core of double occupancies while atoms on singly occupied sites leave the system, effectively reducing the overall entropy of the atoms in the center of the lattice.

A quantitative theoretical analysis of the expansion dynamics in 2D is computa-

tionally very challenging, but the analysis of ladder systems using t-DMRG already showed that they can qualitatively reproduce aspects of the dynamics in 2D [86]. In our experiment, we are currently setting up a bichromatic superlattice along one of the lattice axes, which will allow for the creation of arrays of decoupled ladder systems with tunable coupling between the individual legs of the ladders [235]. In future experiments, we could use this setup as a simple model system to study integrability breaking and directly compare the experiments to theoretical predictions.

So far, we have not been able to observe clear indications of quasi-condensation of expanding strongly interacting atoms. However, we already discussed multiple sources of errors that could be responsible for preventing the formation of quasi-condensates and obscuring our measurements. In future experiments, these could be investigated in more detail by directly measuring the effects of different initial state preparation schemes, optimized potential compensation, and imaging techniques on the appearance of peaks in momentum space, which would hopefully lead to the observation of clear signs of quasi-condensation. Another interesting situation to investigate would be the expansion of strongly interacting atoms starting from their ground state at low filling factors. Here, measurements of their momentum distribution should reveal the dynamical fermionization predicted in [154].

In an ideal realization of expansions in homogeneous lattices, the atoms can tunnel outwards indefinitely and their density vanishes for long expansion durations. Thus, although we do observe fast local relaxation dynamics, we cannot investigate long-term relaxation and thermalization dynamics on global scales in these systems. By inducing a quantum quench in the tunneling and interaction strength of the system without changing the harmonic confinement, however, we could directly study long-term relaxation dynamics. Using Bose-Fermi mixtures or patterned initial density distributions, and measuring the evolution of densities, higher occupancies or momentum distributions, this would provide an interesting approach to studying how relaxation and thermalization depends on dimensionality and interaction strength.

Bibliography

[1] R. P. Feynman, "Simulating physics with computers", International Journal of Theoretical Physics **21**, 467–488 (1982).

[2] J. I. Cirac and P. Zoller, "Goals and opportunities in quantum simulation", Nature Physics **8**, 264–266 (2012).

[3] I. Buluta and F. Nori, "Quantum Simulators", Science **326**, 108–111 (2009).

[4] I. Bloch, J. Dalibard, and S. Nascimbène, "Quantum simulations with ultracold quantum gases", Nature Physics **8**, 267–276 (2012).

[5] A. Aspuru-Guzik and P. Walther, "Photonic quantum simulators", Nature Physics **8**, 285–291 (2012).

[6] R. Blatt and C. F. Roos, "Quantum simulations with trapped ions", Nature Physics **8**, 277–284 (2012).

[7] A. A. Houck, H. E. Türeci, and J. Koch, "On-chip quantum simulation with superconducting circuits", Nature Physics **8**, 292–299 (2012).

[8] M. H. Anderson, J. R. Ensher, M. R. Matthews, C. E. Wieman, and E. A. Cornell, "Observation of Bose-Einstein Condensation in a Dilute Atomic Vapor", Science **269**, 198–201 (1995).

[9] C. C. Bradley, C. A. Sackett, J. J. Tollett, and R. G. Hulet, "Evidence of Bose-Einstein Condensation in an Atomic Gas with Attractive Interactions", Physical Review Letters **75**, 1687–1690 (1995).

[10] K. B. Davis, M.-O. Mewes, M. R. Andrews, N. J. van Druten, D. S. Durfee, D. M. Kurn, and W. Ketterle, "Bose-Einstein Condensation in a Gas of Sodium Atoms", Physical Review Letters **75**, 3969–3973 (1995).

[11] M. R. Andrews, C. G. Townsend, H.-J. Miesner, D. S. Durfee, D. M. Kurn, and W. Ketterle, "Observation of Interference Between Two Bose Condensates", Science **275**, 637–641 (1997).

[12] I. Bloch, T. W. Hänsch, and T. Esslinger, "Measurement of the spatial coherence of a trapped Bose gas at the phase transition", Nature **403**, 166–170 (2000).

[13] M. R. Matthews, B. P. Anderson, P. C. Haljan, D. S. Hall, C. E. Wieman, and E. A. Cornell, "Vortices in a Bose-Einstein Condensate", Physical Review Letters **83**, 2498–2501 (1999).

[14] K. W. Madison, F. Chevy, W. Wohlleben, and J. Dalibard, "Vortex Formation in a Stirred Bose-Einstein Condensate", Physical Review Letters **84**, 806–809 (2000).

[15] J. R. Abo-Shaeer, C. Raman, J. M. Vogels, and W. Ketterle, "Observation of Vortex Lattices in Bose-Einstein Condensates", Science **292**, 476–479 (2001).

[16] M. R. Andrews, D. M. Kurn, H.-J. Miesner, D. S. Durfee, C. G. Townsend, S. Inouye, and W. Ketterle, "Propagation of Sound in a Bose-Einstein Condensate", Physical Review Letters **79**, 553–556 (1997).

[17] D. M. Stamper-Kurn, A. P. Chikkatur, A. Görlitz, S. Inouye, S. Gupta, D. E. Pritchard, and W. Ketterle, "Excitation of Phonons in a Bose-Einstein Condensate by Light Scattering", Physical Review Letters **83**, 2876–2879 (1999).

[18] D. Jaksch, C. Bruder, J. I. Cirac, C. W. Gardiner, and P. Zoller, "Cold Bosonic Atoms in Optical Lattices", Physical Review Letters **81**, 3108–3111 (1998).

[19] M. P. A. Fisher, P. B. Weichman, G. Grinstein, and D. S. Fisher, "Boson localization and the superfluid-insulator transition", Physical Review B **40**, 546–570 (1989).

[20] M. Greiner, O. Mandel, T. Esslinger, T. W. Hänsch, and I. Bloch, "Quantum phase transition from a superfluid to a Mott insulator in a gas of ultracold atoms", Nature **415**, 39–44 (2002).

[21] T. Stöferle, H. Moritz, C. Schori, M. Köhl, and T. Esslinger, "Transition from a Strongly Interacting 1D Superfluid to a Mott Insulator", Physical Review Letters **92**, 130403 (2004).

[22] I. B. Spielman, W. D. Phillips, and J. V. Porto, "Mott-Insulator Transition in a Two-Dimensional Atomic Bose Gas", Physical Review Letters **98**, 080404 (2007).

[23] R. Jördens, N. Strohmaier, K. Günter, H. Moritz, and T. Esslinger, "A Mott insulator of fermionic atoms in an optical lattice", Nature **455**, 204–207 (2008).

[24] U. Schneider, L. Hackermüller, S. Will, T. Best, I. Bloch, T. A. Costi, R. W. Helmes, D. Rasch, and A. Rosch, "Metallic and Insulating Phases of Repulsively Interacting Fermions in a 3D Optical Lattice", Science **322**, 1520–1525 (2008).

[25] B. Paredes, A. Widera, V. Murg, O. Mandel, S. Fölling, I. Cirac, G. V. Shlyapnikov, T. W. Hänsch, and I. Bloch, "Tonks–Girardeau gas of ultracold atoms in an optical lattice", Nature **429**, 277–281 (2004).

[26] T. Kinoshita, T. Wenger, and D. S. Weiss, "Observation of a One-Dimensional Tonks-Girardeau Gas", Science **305**, 1125–1128 (2004).

[27] S. Fölling, S. Trotzky, P. Cheinet, M. Feld, R. Saers, A. Widera, T. Müller, and I. Bloch, "Direct observation of second-order atom tunnelling", Nature **448**, 1029–1032 (2007).

[28] M. Anderlini, P. J. Lee, B. L. Brown, J. Sebby-Strabley, W. D. Phillips, and J. V. Porto, "Controlled exchange interaction between pairs of neutral atoms in an optical lattice", Nature **448**, 452–456 (2007).

[29] S. Trotzky, P. Cheinet, S. Fölling, M. Feld, U. Schnorrberger, A. M. Rey, A. Polkovnikov, E. A. Demler, M. D. Lukin, and I. Bloch, "Time-Resolved Observation and Control of Superexchange Interactions with Ultracold Atoms in Optical Lattices", Science **319**, 295–299 (2008).

[30] C Becker, P Soltan-Panahi, J Kronjäger, S Dörscher, K Bongs, and K Sengstock, "Ultracold quantum gases in triangular optical lattices", New Journal of Physics **12**, 065025 (2010).

[31] P. Soltan-Panahi, J. Struck, P. Hauke, A. Bick, W. Plenkers, G. Meineke, C. Becker, P. Windpassinger, M. Lewenstein, and K. Sengstock, "Multi-component quantum gases in spin-dependent hexagonal lattices", Nature Physics **7**, 434–440 (2011).

[32] H. Feshbach, "Unified theory of nuclear reactions", Annals of Physics **5**, 357–390 (1958).

[33] U. Fano, "Effects of Configuration Interaction on Intensities and Phase Shifts", Physical Review **124**, 1866–1878 (1961).

[34] S. Inouye, M. R. Andrews, J. Stenger, H.-J. Miesner, D. M. Stamper-Kurn, and W. Ketterle, "Observation of Feshbach resonances in a Bose–Einstein condensate", Nature **392**, 151–154 (1998).

[35] E. Tiesinga, B. J. Verhaar, and H. T. C. Stoof, "Threshold and resonance phenomena in ultracold ground-state collisions", Physical Review A **47**, 4114–4122 (1993).

[36] C. A. Regal, C. Ticknor, J. L. Bohn, and D. S. Jin, "Creation of ultracold molecules from a Fermi gas of atoms", Nature **424**, 47–50 (2003).

[37] M. Greiner, C. A. Regal, and D. S. Jin, "Emergence of a molecular Bose–Einstein condensate from a Fermi gas", Nature **426**, 537–540 (2003).

[38] S. Jochim, M. Bartenstein, A. Altmeyer, G. Hendl, S. Riedl, C. Chin, J. H. Denschlag, and R. Grimm, "Bose-Einstein Condensation of Molecules", Science **302**, 2101–2103 (2003).

[39] M. W. Zwierlein, C. A. Stan, C. H. Schunck, S. M. F. Raupach, S. Gupta, Z. Hadzibabic, and W. Ketterle, "Observation of Bose-Einstein Condensation of Molecules", Physical Review Letters **91**, 250401 (2003).

[40] C. A. Regal, M. Greiner, and D. S. Jin, "Observation of Resonance Condensation of Fermionic Atom Pairs", Physical Review Letters **92**, 040403 (2004).

[41] M. W. Zwierlein, C. A. Stan, C. H. Schunck, S. M. F. Raupach, A. J. Kerman, and W. Ketterle, "Condensation of Pairs of Fermionic Atoms near a Feshbach Resonance", Physical Review Letters **92**, 120403 (2004).

[42] M. W. Zwierlein, J. R. Abo-Shaeer, A. Schirotzek, C. H. Schunck, and W. Ketterle, "Vortices and superfluidity in a strongly interacting Fermi gas", Nature **435**, 1047–1051 (2005).

[43] C. Gross, T. Zibold, E. Nicklas, J. Estève, and M. K. Oberthaler, "Nonlinear atom interferometer surpasses classical precision limit", Nature **464**, 1165–1169 (2010).

[44] T. Kraemer, M. Mark, P. Waldburger, J. G. Danzl, C. Chin, B. Engeser, A. D. Lange, K. Pilch, A. Jaakkola, H.-C. Nägerl, and R. Grimm, "Evidence for Efimov quantum states in an ultracold gas of caesium atoms", Nature **440**, 315–318 (2006).

[45] S. Knoop, F. Ferlaino, M. Mark, M. Berninger, H. Schöbel, H.-C. Nägerl, and R. Grimm, "Observation of an Efimov-like trimer resonance in ultracold atom–dimer scattering", Nature Physics **5**, 227–230 (2009).

[46] M. Zaccanti, B. Deissler, C. D'Errico, M. Fattori, M. Jona-Lasinio, S. Müller, G. Roati, M. Inguscio, and G. Modugno, "Observation of an Efimov spectrum in an atomic system", Nature Physics **5**, 586–591 (2009).

[47] M. J. Mark, E. Haller, K. Lauber, J. G. Danzl, A. J. Daley, and H.-C. Nägerl, "Precision Measurements on a Tunable Mott Insulator of Ultracold Atoms", Physical Review Letters **107**, 175301 (2011).

[48] M. J. Mark, E. Haller, K. Lauber, J. G. Danzl, A. Janisch, H. P. Büchler, A. J. Daley, and H.-C. Nägerl, "Preparation and Spectroscopy of a Metastable Mott-Insulator State with Attractive Interactions", Physical Review Letters **108**, 215302 (2012).

[49] W. Ketterle, D. S. Durfee, and D. M. Stamper-Kurn, "Making, probing and understanding Bose-Einstein condensates", arXiv e–print cond–mat/9904034 (1999).

[50] N. Gemelke, X. Zhang, C.-L. Hung, and C. Chin, "*In situ* observation of incompressible Mott-insulating domains in ultracold atomic gases", Nature **460**, 995–998 (2009).

[51] M. Greiner, I. Bloch, O. Mandel, T. W. Hänsch, and T. Esslinger, "Exploring Phase Coherence in a 2D Lattice of Bose-Einstein Condensates", Physical Review Letters **87**, 160405 (2001).

[52] S. Fölling, F. Gerbier, A. Widera, O. Mandel, T. Gericke, and I. Bloch, "Spatial quantum noise interferometry in expanding ultracold atom clouds", Nature **434**, 481–484 (2005).

[53] T. Rom, T. Best, D. van Oosten, U. Schneider, S. Fölling, B. Paredes, and I. Bloch, "Free fermion antibunching in a degenerate atomic Fermi gas released from an optical lattice", Nature **444**, 733–736 (2006).

[54] G. K. Campbell, J. Mun, M. Boyd, P. Medley, A. E. Leanhardt, L. G. Marcassa, D. E. Pritchard, and W. Ketterle, "Imaging the Mott Insulator Shells by Using Atomic Clock Shifts", Science **313**, 649–652 (2006).

[55] P. T. Ernst, S. Götze, J. S. Krauser, K. Pyka, D.-S. Lühmann, D. Pfannkuche, and K. Sengstock, "Probing superfluids in optical lattices by momentum-resolved Bragg spectroscopy", Nature Physics **6**, 56–61 (2010).

[56] T. Gericke, P. Würtz, D. Reitz, T. Langen, and H. Ott, "High-resolution scanning electron microscopy of an ultracold quantum gas", Nature Physics **4**, 949–953 (2008).

[57] W. S. Bakr, J. I. Gillen, A. Peng, S. Fölling, and M. Greiner, "A quantum gas microscope for detecting single atoms in a Hubbard-regime optical lattice", Nature **462**, 74–77 (2009).

[58] J. F. Sherson, C. Weitenberg, M. Endres, M. Cheneau, I. Bloch, and S. Kuhr, "Single-atom-resolved fluorescence imaging of an atomic Mott insulator", Nature **467**, 68–72 (2010).

[59] C. Weitenberg, M. Endres, J. F. Sherson, M. Cheneau, P. Schauß, T. Fukuhara, I. Bloch, and S. Kuhr, "Single-spin addressing in an atomic Mott insulator", Nature **471**, 319–324 (2011).

[60] A. Polkovnikov, K. Sengupta, A. Silva, and M. Vengalattore, "Colloquium: Nonequilibrium dynamics of closed interacting quantum systems", Reviews of Modern Physics **83**, 863–883 (2011).

[61] J. Hubbard, "Electron Correlations in Narrow Energy Bands", Proceedings of the Royal Society of London. Series A. Mathematical and Physical Sciences **276**, 238–257 (1963).

[62] I. Bloch, J. Dalibard, and W. Zwerger, "Many-body physics with ultracold gases", Reviews of Modern Physics **80**, 885–964 (2008).

[63] T. Kinoshita, T. Wenger, and D. S. Weiss, "A quantum Newton's cradle", Nature **440**, 900–903 (2006).

[64] S. Hofferberth, I. Lesanovsky, B. Fischer, T. Schumm, and J. Schmiedmayer, "Non-equilibrium coherence dynamics in one-dimensional Bose gases", Nature **449**, 324–327 (2007).

[65] M. Gring, M. Kuhnert, T. Langen, T. Kitagawa, B. Rauer, M. Schreitl, I. Mazets, D. A. Smith, E. Demler, and J. Schmiedmayer, "Relaxation and Prethermalization in an Isolated Quantum System", Science **337**, 1318–1322 (2012).

[66] H. Ott, E. de Mirandes, F. Ferlaino, G. Roati, G. Modugno, and M. Inguscio, "Collisionally Induced Transport in Periodic Potentials", Physical Review Letters **92**, 160601 (2004).

[67] C. D. Fertig, K. M. O'Hara, J. H. Huckans, S. L. Rolston, W. D. Phillips, and J. V. Porto, "Strongly Inhibited Transport of a Degenerate 1D Bose Gas in a Lattice", Physical Review Letters **94**, 120403 (2005).

[68] J.-P. Brantut, J. Meineke, D. Stadler, S. Krinner, and T. Esslinger, "Conduction of Ultracold Fermions Through a Mesoscopic Channel", Science **337**, 1069–1071 (2012).

[69] D. Stadler, S. Krinner, J. Meineke, J.-P. Brantut, and T. Esslinger, "Observing the drop of resistance in the flow of a superfluid Fermi gas", Nature **491**, 736–739 (2012).

[70] N. Strohmaier, Y. Takasu, K. Günter, R. Jördens, M. Köhl, H. Moritz, and T. Esslinger, "Interaction-Controlled Transport of an Ultracold Fermi Gas", Physical Review Letters **99**, 220601 (2007).

[71] U. Schneider, L. Hackermüller, J. P. Ronzheimer, S. Will, S. Braun, T. Best, I. Bloch, E. Demler, S. Mandt, D. Rasch, and A. Rosch, "Fermionic transport and out-of-equilibrium dynamics in a homogeneous Hubbard model with ultracold atoms", Nature Physics **8**, 213–218 (2012).

[72] D. Chen, M. White, C. Borries, and B. DeMarco, "Quantum Quench of an Atomic Mott Insulator", Physical Review Letters **106**, 235304 (2011).

[73] S. Trotzky, Y.-A. Chen, A. Flesch, I. P. McCulloch, U. Schollwöck, J. Eisert, and I. Bloch, "Probing the relaxation towards equilibrium in an isolated strongly correlated one-dimensional Bose gas", Nature Physics **8**, 325–330 (2012).

[74] G. Vidal, "Efficient Simulation of One-Dimensional Quantum Many-Body Systems", Physical Review Letters **93**, 040502 (2004).

[75] A. J. Daley, C. Kollath, U. Schollwöck, and G. Vidal, "Time-dependent density-matrix renormalization-group using adaptive effective Hilbert spaces", Journal of Statistical Mechanics: Theory and Experiment **2004**, P04005 (2004).

[76] S. R. White and A. E. Feiguin, "Real-Time Evolution Using the Density Matrix Renormalization Group", Physical Review Letters **93**, 076401 (2004).

[77] M. Rigol, V. Dunjko, and M. Olshanii, "Thermalization and its mechanism for generic isolated quantum systems", Nature **452**, 854–858 (2008).

[78] C. Kollath, A. M. Läuchli, and E. Altman, "Quench Dynamics and Nonequilibrium Phase Diagram of the Bose-Hubbard Model", Physical Review Letters **98**, 180601 (2007).

[79] M. Cramer, A. Flesch, I. P. McCulloch, U. Schollwöck, and J. Eisert, "Exploring Local Quantum Many-Body Relaxation by Atoms in Optical Superlattices", Physical Review Letters **101**, 063001 (2008).

[80] A. Flesch, M. Cramer, I. P. McCulloch, U. Schollwöck, and J. Eisert, "Probing local relaxation of cold atoms in optical superlattices", Physical Review A **78**, 033608 (2008).

[81] M. Moeckel and S. Kehrein, "Interaction Quench in the Hubbard Model", Physical Review Letters **100**, 175702 (2008).

[82] M. Moeckel and S. Kehrein, "Crossover from adiabatic to sudden interaction quenches in the Hubbard model: prethermalization and non-equilibrium dynamics", New Journal of Physics **12**, 055016 (2010).

[83] F. Heidrich-Meisner, S. R. Manmana, M. Rigol, A. Muramatsu, A. E. Feiguin, and E. Dagotto, "Quantum distillation: Dynamical generation of low-entropy states of strongly correlated fermions in an optical lattice", Physical Review A **80**, 041603 (2009).

[84] J. Kajala, F. Massel, and P. Törmä, "Expansion Dynamics in the One-Dimensional Fermi-Hubbard Model", Physical Review Letters **106**, 206401 (2011).

[85] S. Langer, M. J. A. Schuetz, I. P. McCulloch, U. Schollwöck, and F. Heidrich-Meisner, "Expansion velocity of a one-dimensional, two-component Fermi gas during the sudden expansion in the ballistic regime", Physical Review A **85**, 043618 (2012).

[86] L. Vidmar, S. Langer, I. P. McCulloch, U. Schneider, U. Schollwoeck, and F. Heidrich-Meisner, "Sudden expansion of Mott insulators in one dimension", arXiv e–print 1305.5496 (2013).

[87] M. Rigol, V. Dunjko, V. Yurovsky, and M. Olshanii, "Relaxation in a Completely Integrable Many-Body Quantum System: An *Ab Initio* Study of the Dynamics of the Highly Excited States of 1D Lattice Hard-Core Bosons", Physical Review Letters **98**, 050405 (2007).

[88] M. Rigol, "Breakdown of Thermalization in Finite One-Dimensional Systems", Physical Review Letters **103**, 100403 (2009).

[89] S. Mandt, A. E. Feiguin, and S. R. Manmana, "Relaxation towards negative temperatures in bosonic systems: generalized Gibbs ensembles and beyond integrability", arXiv e–print 1307.7188 (2013).

[90] M. Rigol and A. Muramatsu, "Emergence of Quasicondensates of Hard-Core Bosons at Finite Momentum", Physical Review Letters **93**, 230404 (2004).

[91] M. Greiner, "Ultracold quantum gases in three-dimensional optical lattice potentials", PhD thesis (Ludwig-Maximilians-Universität München, 2003).

[92] T. Rom, "Bosonische und fermionische Quantengase in dreidimensionalen optischen Gittern: Präparation, Manipulation und Analyse", PhD thesis (Ludwig-Maximilian-Universität München, 2009).

[93] N. W. Ashcroft and N. D. Mermin, *Solid state physics* (Harcourt College Publishers, New York; London, 1976).

[94] C. Kittel, *Introduction to solid state physics* (Wiley, Hoboken, NJ, 2005).

[95] J. C. Slater, "A Soluble Problem in Energy Bands", Physical Review **87**, 807–835 (1952).

[96] D. Jaksch, "Bose-Einstein Condensation and Applications", PhD thesis (Leopold-Franzens-Universität Innsbruck, 1999).

[97] S. Will, T. Best, U. Schneider, L. Hackermüller, D.-S. Lühmann, and I. Bloch, "Time-resolved observation of coherent multi-body interactions in quantum phase revivals", Nature **465**, 197–201 (2010).

[98] R. J. Glauber, "Coherent and Incoherent States of the Radiation Field", Physical Review **131**, 2766–2788 (1963).

[99] S. Sachdev, *Quantum Phase Transitions* (Cambridge University Press, Cambridge, 1999).

[100] K. Sheshadri, H. R. Krishnamurthy, R. Pandit, and T. V. Ramakrishnan, "Superfluid and Insulating Phases in an Interacting-Boson Model: Mean-Field Theory and the RPA", EPL (Europhysics Letters) **22**, 257 (1993).

[101] J. K. Freericks and H. Monien, "Phase diagram of the Bose-Hubbard Model", EPL (Europhysics Letters) **26**, 545 (1994).

[102] D. van Oosten, P. van der Straten, and H. T. C. Stoof, "Quantum phases in an optical lattice", Physical Review A **63**, 053601 (2001).

[103] V. A. Kashurnikov and B. V. Svistunov, "Exact diagonalization plus renormalization-group theory: Accurate method for a one-dimensional superfluid-insulator-transition study", Physical Review B **53**, 11776–11778 (1996).

[104] T. D. Kühner, S. R. White, and H. Monien, "One-dimensional Bose-Hubbard model with nearest-neighbor interaction", Physical Review B **61**, 12474–12489 (2000).

[105] C. Kollath, U. Schollwöck, J. von Delft, and W. Zwerger, "Spatial correlations of trapped one-dimensional bosons in an optical lattice", Physical Review A **69**, 031601 (2004).

[106] B. Capogrosso-Sansone, Ş. G. Söyler, N. Prokof'ev, and B. Svistunov, "Monte Carlo study of the two-dimensional Bose-Hubbard model", Physical Review A **77**, 015602 (2008).

[107] B. Capogrosso-Sansone, N. V. Prokof'ev, and B. V. Svistunov, "Phase diagram and thermodynamics of the three-dimensional Bose-Hubbard model", Physical Review B **75**, 134302 (2007).

[108] S. Fölling, A. Widera, T. Müller, F. Gerbier, and I. Bloch, "Formation of Spatial Shell Structure in the Superfluid to Mott Insulator Transition", Physical Review Letters **97**, 060403 (2006).

[109] W. S. Bakr, A. Peng, M. E. Tai, R. Ma, J. Simon, J. I. Gillen, S. Fölling, L. Pollet, and M. Greiner, "Probing the Superfluid–to–Mott Insulator Transition at the Single-Atom Level", Science **329**, 547–550 (2010).

[110] J. M. Deutsch, "Quantum statistical mechanics in a closed system", Physical Review A **43**, 2046–2049 (1991).

[111] M. Srednicki, "Chaos and quantum thermalization", Physical Review E **50**, 888–901 (1994).

[112] Y. G. Sinai, "Dynamical systems with elastic reflections", Russian Mathematical Surveys **25**, 137 (1970).

[113] L. D. Landau and E. M. Lifshitz, *Statistical Physics*, 3rd ed., Vol. 5, Course of theoretical physics (Elsevier, Oxford, 1980).

[114] M. V. Berry, "Regular and irregular motion", AIP Conference Proceedings **46**, 16–120 (1978).

[115] E. Fermi, J. R. Pasta, S. Ulam, and M. Tsingou, "Studies of nonlinear problems", Los Alamos Internal Report LA-1940 (1955).

[116] J. Ford, "The Fermi-Pasta-Ulam problem: Paradox turns discovery", Physics Reports **213**, 271–310 (1992).

[117] G. Galvalotti, *The Fermi-Pasta-Ulam Problem - A Status Report*, Vol. 728, Lecture Notes in Physics (Springer, Berlin, 2008).

[118] G. P. Berman and F. M. Izrailev, "The Fermi–Pasta–Ulam problem: Fifty years of progress", Chaos: An Interdisciplinary Journal of Nonlinear Science **15**, 015104–015104–18 (2005).

[119] A. N. Kolmogorow, "On the conservation of conditionally periodic motions for a small change in Hamilton's function", Doklady Akademii Nauk SSSR **98**, 527–530 (1954); (English translation in *Stochastic behavior in classical and quantum Hamiltonian systems*, Volta Memorial conference, Como, 1977, Lecture Notes in Physics **93**, Springer, 1979).

[120] J. Moser, "On invariant curves of area-preserving mappings of an annulus.", Nachrichten der Akademie der Wissenschaften in Göttingen. II. Mathematisch-Physikalische Klasse **1962**, 1–20 (1962).

[121] V. I. Arnol'd, "Proof of a Theorem of A. N. Kolmogorov on the Invariance of Quasi-Periodic Motions under small Perturbations of the Hamiltonian", Russian Mathematical Surveys **18**, 9 (1963).

[122] F. Jin, T. Neuhaus, K. Michielsen, S. Miyashita, M. A. Novotny, M. I. Katsnelson, and H. D. Raedt, "Equilibration and thermalization of classical systems", New Journal of Physics **15**, 033009 (2013).

[123] J. v Neumann, "Beweis des Ergodensatzes und des H-Theorems in der neuen Mechanik", Zeitschrift für Physik **57**, 30–70 (1929).

[124] S. Goldstein, J. L. Lebowitz, R. Tumulka, and N. Zanghì, "Long-time behavior of macroscopic quantum systems: Commentary accompanying the English translation of John von Neumann's 1929 article on the quantum ergodic theorem", The European Physical Journal H **35**, 173–200 (2010).

[125] P. Reimann, "Foundation of Statistical Mechanics under Experimentally Realistic Conditions", Physical Review Letters **101**, 190403 (2008).

[126] A. Peres, "Ergodicity and mixing in quantum theory. I", Physical Review A **30**, 504–508 (1984).

[127] E. J. Heller and B. R. Landry, "Statistical properties of many particle eigenfunctions", Journal of Physics A: Mathematical and Theoretical **40**, 9259 (2007).

[128] J.-S. Caux and J. Mossel, "Remarks on the notion of quantum integrability", Journal of Statistical Mechanics: Theory and Experiment **2011**, P02023 (2011).

[129] B. Sutherland, *Beautiful Models: 70 Years of Exactly Solved Quantum Many-body Problems* (World Scientific Publishing, Singapore, 2004).

[130] G. P. Brandino, R. M. Konik, and G. Mussardo, "Energy level distribution of perturbed conformal field theories", Journal of Statistical Mechanics: Theory and Experiment **2010**, P07013 (2010).

[131] K. Sengupta, S. Powell, and S. Sachdev, "Quench dynamics across quantum critical points", Physical Review A **69**, 053616 (2004).

[132] W. H. Zurek, U. Dorner, and P. Zoller, "Dynamics of a Quantum Phase Transition", Physical Review Letters **95**, 105701 (2005).

[133] M. Cramer, C. M. Dawson, J. Eisert, and T. J. Osborne, "Exact Relaxation in a Class of Nonequilibrium Quantum Lattice Systems", Physical Review Letters **100**, 030602 (2008).

[134] E. T. Jaynes, "Information Theory and Statistical Mechanics", Physical Review **106**, 620–630 (1957).

[135] A. C. Cassidy, C. W. Clark, and M. Rigol, "Generalized Thermalization in an Integrable Lattice System", Physical Review Letters **106**, 140405 (2011).

[136] T. Barthel and U. Schollwöck, "Dephasing and the Steady State in Quantum Many-Particle Systems", Physical Review Letters **100**, 100601 (2008).

[137] P. Calabrese, F. H. L. Essler, and M. Fagotti, "Quantum quenches in the transverse field Ising chain: II. Stationary state properties", Journal of Statistical Mechanics: Theory and Experiment **2012**, P07022 (2012).

[138] M. A. Cazalilla, "Effect of Suddenly Turning on Interactions in the Luttinger Model", Physical Review Letters **97**, 156403 (2006).

[139] J.-S. Caux and R. M. Konik, "Constructing the Generalized Gibbs Ensemble after a Quantum Quench", Physical Review Letters **109**, 175301 (2012).

[140] D. Fioretto and G. Mussardo, "Quantum quenches in integrable field theories", New Journal of Physics **12**, 055015 (2010).

[141] M. Eckstein and M. Kollar, "Nonthermal Steady States after an Interaction Quench in the Falicov-Kimball Model", Physical Review Letters **100**, 120404 (2008).

[142] M. Kollar and M. Eckstein, "Relaxation of a one-dimensional Mott insulator after an interaction quench", Physical Review A **78**, 013626 (2008).

[143] J. De Nardis, B. Wouters, M. Brockmann, and J.-S. Caux, "Variational solution for the interaction quench in the Lieb-Liniger Bose gas", arXiv e–print 1308.4310 (2013).

[144] S. R. Manmana, S. Wessel, R. M. Noack, and A. Muramatsu, "Strongly Correlated Fermions after a Quantum Quench", Physical Review Letters **98**, 210405 (2007).

[145] T. Langen, R. Geiger, M. Kuhnert, B. Rauer, and J. Schmiedmayer, "Local emergence of thermal correlations in an isolated quantum many-body system", Nature Physics **9**, 640–643 (2013).

[146] K. Winkler, G. Thalhammer, F. Lang, R. Grimm, J. Hecker Denschlag, A. J. Daley, A. Kantian, H. P. Büchler, and P. Zoller, "Repulsively bound atom pairs in an optical lattice", Nature **441**, 853–856 (2006).

[147] D. Muth, D. Petrosyan, and M. Fleischhauer, "Dynamics and evaporation of defects in Mott-insulating clusters of boson pairs", Physical Review A **85**, 013615 (2012).

[148] M. Girardeau, "Relationship between Systems of Impenetrable Bosons and Fermions in One Dimension", Journal of Mathematical Physics **1**, 516–523 (1960).

[149] A. Lenard, "Momentum Distribution in the Ground State of the One-Dimensional System of Impenetrable Bosons", Journal of Mathematical Physics **5**, 930–943 (1964).

[150] H. G. Vaidya and C. A. Tracy, "One-Particle Reduced Density Matrix of Impenetrable Bosons in One Dimension at Zero Temperature", Physical Review Letters **42**, 3–6 (1979).

[151] M. Olshanii, "Atomic Scattering in the Presence of an External Confinement and a Gas of Impenetrable Bosons", Physical Review Letters **81**, 938–941 (1998).

[152] P. Jordan and E. Wigner, "Über das Paulische Äquivalenzverbot", Zeitschrift für Physik **47**, 631–651 (1928).

[153] M. Rigol and A. Muramatsu, "Universal properties of hard-core bosons confined on one-dimensional lattices", Physical Review A **70**, 031603 (2004).

[154] M. Rigol and A. Muramatsu, "Fermionization in an Expanding 1D Gas of Hard-Core Bosons", Physical Review Letters **94**, 240403 (2005).

[155] J. Berges, S. Borsányi, and C. Wetterich, "Prethermalization", Physical Review Letters **93**, 142002 (2004).

[156] H. J. Metcalf and P. V. D. Straten, *Laser Cooling and Trapping* (Springer, 1999).

[157] S. Will, "Interacting bosons and fermions in three-dimensional optical lattice potentials", PhD thesis (Johannes Gutenberg-Universität Mainz, 2011).

[158] T. Best, "Interacting Bose-Fermi mixtures in optical lattices", PhD thesis (Johannes Gutenberg-Universität Mainz, 2011).

[159] C. Adams and E. Riis, "Laser cooling and trapping of neutral atoms", Progress in Quantum Electronics **21**, 1–79 (1997).

[160] M. Meucci, E. Mariotti, P. Bicchi, C. Marinelli, and L. Moi, "Light-Induced Atom Desorption", EPL (Europhysics Letters) **25**, 639 (1994).

[161] E. L. Raab, M. Prentiss, A. Cable, S. Chu, and D. E. Pritchard, "Trapping of Neutral Sodium Atoms with Radiation Pressure", Physical Review Letters **59**, 2631–2634 (1987).

[162] A. M. Steane, M. Chowdhury, and C. J. Foot, "Radiation force in the magneto-optical trap", Journal of the Optical Society of America B **9**, 2142–2158 (1992).

[163] T. G. Tiecke, "Feshbach resonances in ultracold mixtures of the fermionic quantum gases ^{6}Li and ^{40}K", PhD thesis (University of Amsterdam, 2009).

[164] D. A. Steck, "Rubidium 87 D Line Data", available online at http://steck.us/alkalidata (revision 2.1.4, 23 December 2010).

[165] C. B. Alcock, V. P. Itkin, and M. K. Horrigan, "Vapour Pressure Equations for the Metallic Elements: 298–2500K", Canadian Metallurgical Quarterly **23**, 309–313 (1984).

[166] A. L. Schawlow, "Spectroscopy in a new light", Reviews of Modern Physics **54**, 697–707 (1982).

[167] A. L. Migdall, J. V. Prodan, W. D. Phillips, T. H. Bergeman, and H. J. Metcalf, "First Observation of Magnetically Trapped Neutral Atoms", Physical Review Letters **54**, 2596–2599 (1985).

[168] H. F. Hess, "Evaporative cooling of magnetically trapped and compressed spin-polarized hydrogen", Physical Review B **34**, 3476–3479 (1986).

[169] N. Masuhara, J. M. Doyle, J. C. Sandberg, D. Kleppner, T. J. Greytak, H. F. Hess, and G. P. Kochanski, "Evaporative Cooling of Spin-Polarized Atomic Hydrogen", Physical Review Letters **61**, 935–938 (1988).

[170] L. De Sarlo, P. Maioli, G. Barontini, J. Catani, F. Minardi, and M. Inguscio, "Collisional properties of sympathetically cooled ^{39}K", Physical Review A **75**, 022715 (2007).

[171] G. Roati, M. Zaccanti, C. D'Errico, J. Catani, M. Modugno, A. Simoni, M. Inguscio, and G. Modugno, "^{39}K Bose-Einstein Condensate with Tunable Interactions", Physical Review Letters **99**, 010403 (2007).

[172] K. B. Davis, M.-O. Mewes, M. A. Joffe, M. R. Andrews, and W. Ketterle, "Evaporative Cooling of Sodium Atoms", Physical Review Letters **74**, 5202–5205 (1995).

[173] S. Bize, Y. Sortais, M. S. Santos, C. Mandache, A. Clairon, and C. Salomon, "High-accuracy measurement of the ^{87}Rb ground-state hyperfine splitting in an atomic fountain", EPL (Europhysics Letters) **45**, 558 (1999).

[174] E. Majorana, "Teoria Relativistica di Particelle Con Momento Intrinseco Arbitrario", Il Nuovo Cimento **9**, 335–344 (1932).

[175] W. Petrich, M. H. Anderson, J. R. Ensher, and E. A. Cornell, "Stable, Tightly Confining Magnetic Trap for Evaporative Cooling of Neutral Atoms", Physical Review Letters **74**, 3352–3355 (1995).

[176] V. S. Letokhov, "Narrowing of the Doppler Width in a Standing Wave", ZhETF Pisma Redaktsiiu **7**, 348 (1968).

[177] G. A. Askaryan, "Effect of the field gradient of an intense electromagnetic beam on electrons and atoms", Soviet Phsics JETP **15**, 1088 (1962).

[178] S. Chu, J. E. Bjorkholm, A. Ashkin, and A. Cable, "Experimental Observation of Optically Trapped Atoms", Physical Review Letters **57**, 314–317 (1986).

[179] R. Grimm, M. Weidemüller, and Y. B. Ovchinnikov, "Optical Dipole Traps for Neutral Atoms", in *Advances In Atomic, Molecular, and Optical Physics*, Vol. 42, edited by Benjamin Bederson and Herbert Walther (Academic Press, 2000), pp. 95–170.

[180] J. Ye, S. Swartz, P. Jungner, and J. L. Hall, "Hyperfine structure and absolute frequency of the ^{87}Rb $5P_{3/2}$ state", Optics Letters **21**, 1280–1282 (1996).

[181] G. P. Barwood, P. Gill, and W. R. C. Rowley, "Frequency measurements on optically narrowed Rb-stabilised laser diodes at 780 nm and 795 nm", Applied Physics B **53**, 142–147 (1991).

[182] S. Falke, E. Tiemann, C. Lisdat, H. Schnatz, and G. Grosche, "Transition frequencies of the D lines of ^{39}K, ^{40}K, and ^{41}K measured with a femtosecond laser frequency comb", Physical Review A **74**, 032503 (2006).

[183] J. J. Sakurai, *Modern Quantum Mechanics* (Addison-Wesley Publishing Company, Inc, 1994).

[184] T. Köhler, K. Góral, and P. S. Julienne, "Production of cold molecules via magnetically tunable Feshbach resonances", Reviews of Modern Physics **78**, 1311–1361 (2006).

[185] R. Duine and H. Stoof, "Atom–molecule coherence in Bose gases", Physics Reports **396**, 115–195 (2004).

[186] F. Ferlaino, C. D'Errico, G. Roati, M. Zaccanti, M. Inguscio, G. Modugno, and A. Simoni, "Feshbach spectroscopy of a K-Rb atomic mixture", Physical Review A **73**, 040702 (2006).

[187] P. F. Bedaque, E. Braaten, and H.-W. Hammer, "Three-body Recombination in Bose Gases with Large Scattering Length", Physical Review Letters **85**, 908–911 (2000).

[188] C. D'Errico, M. Zaccanti, M. Fattori, G. Roati, M. Inguscio, G. Modugno, and A. Simoni, "Feshbach resonances in ultracold ^{39}K", New Journal of Physics **9**, 223 (2007).

[189] C. A. Sackett, J. M. Gerton, M. Welling, and R. G. Hulet, "Measurements of Collective Collapse in a Bose-Einstein Condensate with Attractive Interactions", Physical Review Letters **82**, 876–879 (1999).

[190] J. M. Gerton, D. Strekalov, I. Prodan, and R. G. Hulet, "Direct observation of growth and collapse of a Bose–Einstein condensate with attractive interactions", Nature **408**, 692–695 (2000).

[191] E. A. Donley, N. R. Claussen, S. L. Cornish, J. L. Roberts, E. A. Cornell, and C. E. Wieman, "Dynamics of collapsing and exploding Bose–Einstein condensates", Nature **412**, 295–299 (2001).

[192] S. Braun, J. P. Ronzheimer, M. Schreiber, S. S. Hodgman, T. Rom, I. Bloch, and U. Schneider, "Negative Absolute Temperature for Motional Degrees of Freedom", Science **339**, 52–55 (2013).

[193] R. Jáuregui, N. Poli, G. Roati, and G. Modugno, "Anharmonic parametric excitation in optical lattices", Physical Review A **64**, 033403 (2001).

[194] J. H. Denschlag, J. E. Simsarian, H. Häffner, C. McKenzie, A. Browaeys, D. Cho, K. Helmerson, S. L. Rolston, and W. D. Phillips, "A Bose-Einstein condensate in an optical lattice", Journal of Physics B: Atomic, Molecular and Optical Physics **35**, 3095 (2002).

[195] K. Burnett, P. S. Julienne, and K.-A. Suominen, "Laser-Driven Collisions between Atoms in a Bose-Einstein Condensed Gas", Physical Review Letters **77**, 1416–1419 (1996).

[196] U. Schneider, "Interacting Fermionic Atoms in Optical Lattices - A Quantum Simulator for Condensed Matter Physics", PhD thesis (Johannes Gutenberg-Universität Mainz, 2010).

[197] M. O. Scully and M. S. Zubairy, *Quantum optics* (Cambridge University Press, Cambridge; New York, 1997).

[198] G. Reinaudi, T. Lahaye, Z. Wang, and D. Guéry-Odelin, "Strong saturation absorption imaging of dense clouds of ultracold atoms", Optics Letters **32**, 3143–3145 (2007).

[199] R. Darius, "Die Effekte von Sättigung und optischem Pumpen auf die Atomzahl-Kalibrierung in Absorptionsabbildungen", Bachelor's thesis (Ludwig-Maximilians-Universität München, 2013).

[200] F. Gerbier, A. Widera, S. Fölling, O. Mandel, T. Gericke, and I. Bloch, "Interference pattern and visibility of a Mott insulator", Physical Review A **72**, 053606 (2005).

[201] F. Gerbier, A. Widera, S. Fölling, O. Mandel, T. Gericke, and I. Bloch, "Phase Coherence of an Atomic Mott Insulator", Physical Review Letters **95**, 050404 (2005).

[202] T. Best, S. Will, U. Schneider, L. Hackermüller, D. van Oosten, I. Bloch, and D.-S. Lühmann, "Role of Interactions in ^{87}Rb-^{40}K Bose-Fermi Mixtures in a 3D Optical Lattice", Physical Review Letters **102**, 030408 (2009).

[203] A. Kastberg, W. D. Phillips, S. L. Rolston, R. J. C. Spreeuw, and P. S. Jessen, "Adiabatic Cooling of Cesium to 700 nK in an Optical Lattice", Physical Review Letters **74**, 1542–1545 (1995).

[204] S. E. Braun, "In preparation", PhD thesis (Ludwig-Maximilians-Universität München).

[205] N. F. Ramsey, "Thermodynamics and Statistical Mechanics at Negative Absolute Temperatures", Physical Review **103**, 20–28 (1956).

[206] M. J. Klein, "Negative Absolute Temperatures", Physical Review **104**, 589–589 (1956).

[207] E. M. Purcell and R. V. Pound, "A Nuclear Spin System at Negative Temperature", Physical Review **81**, 279–280 (1951).

[208] A. S. Oja and O. V. Lounasmaa, "Nuclear magnetic ordering in simple metals at positive and negative nanokelvin temperatures", Reviews of Modern Physics **69**, 1–136 (1997).

[209] P. Medley, D. M. Weld, H. Miyake, D. E. Pritchard, and W. Ketterle, "Spin Gradient Demagnetization Cooling of Ultracold Atoms", Physical Review Letters **106**, 195301 (2011).

[210] A. P. Mosk, "Atomic Gases at Negative Kinetic Temperature", Physical Review Letters **95**, 040403 (2005).

[211] A. Rapp, S. Mandt, and A. Rosch, "Equilibration Rates and Negative Absolute Temperatures for Ultracold Atoms in Optical Lattices", Physical Review Letters **105**, 220405 (2010).

[212] Y. Aharonov, L. Davidovich, and N. Zagury, "Quantum random walks", Physical Review A **48**, 1687–1690 (1993).

[213] E. Farhi and S. Gutmann, "Quantum computation and decision trees", Physical Review A **58**, 915–928 (1998).

[214] M. Karski, L. Förster, J.-M. Choi, A. Steffen, W. Alt, D. Meschede, and A. Widera, "Quantum Walk in Position Space with Single Optically Trapped Atoms", Science **325**, 174–177 (2009).

[215] C. Zener, "A Theory of the Electrical Breakdown of Solid Dielectrics", Proceedings of the Royal Society of London. Series A **145**, 523–529 (1934).

[216] M. Ben Dahan, E. Peik, J. Reichel, Y. Castin, and C. Salomon, "Bloch Oscillations of Atoms in an Optical Potential", Physical Review Letters **76**, 4508–4511 (1996).

[217] M. T. DePue, C. McCormick, S. L. Winoto, S. Oliver, and D. S. Weiss, "Unity Occupation of Sites in a 3D Optical Lattice", Physical Review Letters **82**, 2262–2265 (1999).

[218] J. Weiner, V. S. Bagnato, S. Zilio, and P. S. Julienne, "Experiments and theory in cold and ultracold collisions", Reviews of Modern Physics **71**, 1–85 (1999).

[219] L. Hackermüller, U. Schneider, M. Moreno-Cardoner, T. Kitagawa, T. Best, S. Will, E. Demler, E. Altman, I. Bloch, and B. Paredes, "Anomalous Expansion of Attractively Interacting Fermionic Atoms in an Optical Lattice", Science **327**, 1621–1624 (2010).

[220] T. Loftus, C. A. Regal, C. Ticknor, J. L. Bohn, and D. S. Jin, "Resonant Control of Elastic Collisions in an Optically Trapped Fermi Gas of Atoms", Physical Review Letters **88**, 173201 (2002).

[221] S. Mandt, A. Rapp, and A. Rosch, "Interacting Fermionic Atoms in Optical Lattices Diffuse Symmetrically Upwards and Downwards in a Gravitational Potential", Physical Review Letters **106**, 250602 (2011).

[222] M. Eckstein, M. Kollar, and P. Werner, "Thermalization after an Interaction Quench in the Hubbard Model", Physical Review Letters **103**, 056403 (2009).

[223] J. L Vazquez, *Smoothing and decay estimates for nonlinear diffusion equations: equations of porous medium type* (Oxford University Press, Oxford, 2006).

[224] O. Romero-Isart, K. Eckert, C. Rodó, and A. Sanpera, "Transport and entanglement generation in the Bose–Hubbard model", Journal of Physics A: Mathematical and Theoretical **40**, 8019 (2007).

[225] J. P. Ronzheimer, M. Schreiber, S. Braun, S. S. Hodgman, S. Langer, I. P. McCulloch, F. Heidrich-Meisner, I. Bloch, and U. Schneider, "Expansion Dynamics of Interacting Bosons in Homogeneous Lattices in One and Two Dimensions", Physical Review Letters **110**, 205301 (2013).

[226] X. Zotos, F. Naef, and P. Prelovsek, "Transport and conservation laws", Physical Review B **55**, 11029–11032 (1997).

[227] F. Heidrich-Meisner, A. Honecker, and W. Brenig, "Transport in quasi one-dimensional spin-1/2 systems", The European Physical Journal Special Topics **151**, 135–145 (2007).

[228] D. Petrosyan, B. Schmidt, J. R. Anglin, and M. Fleischhauer, "Quantum liquid of repulsively bound pairs of particles in a lattice", Physical Review A **76**, 033606 (2007).

[229] M. Rigol and A. Muramatsu, "FREE EXPANSION OF IMPENETRABLE BOSONS ON ONE-DIMENSIONAL OPTICAL LATTICES", Modern Physics Letters B **19**, 861–881 (2005).

[230] O. Penrose and L. Onsager, "Bose-Einstein Condensation and Liquid Helium", Physical Review **104**, 576–584 (1956).

[231] L. Vidmar, S. Langer, J. P. Ronzheimer, M. Schreiber, S. Braun, S. S. Hodgman, I. Bloch, U. Schneider, and F. Heidrich-Meisner, *In preparation*.

[232] K. Rodriguez, S. R. Manmana, M. Rigol, R. M. Noack, and A. Muramatsu, "Coherent matter waves emerging from Mott-insulators", New Journal of Physics **8**, 169 (2006).

[233] M. Jreissaty, J. Carrasquilla, F. A. Wolf, and M. Rigol, "Expansion of Bose-Hubbard Mott insulators in optical lattices", Physical Review A **84**, 043610 (2011).

[234] S. M. Langer, "Transport and real-time dynamics in one-dimensional quantum magnets and ultra-cold atomic gases", PhD thesis (Ludwig-Maximilians-Universität München, 2012).

[235] Y.-A. Chen, S. D. Huber, S. Trotzky, I. Bloch, and E. Altman, "Many-body Landau-Zener dynamics in coupled one-dimensional Bose liquids", Nature Physics **7**, 61–67 (2011).

Danksagung

Viele Menschen haben in den letztzen Jahren direkt oder indirekt zum Gelingen dieser Doktorarbeit beigetragen. Ganz besonders bedanken möchte ich mich bei

- Prof. Immanuel Bloch für die Möglichkeit, hier in München an spannenden physikalischen Themen arbeiten zu können, für die großartigen Bedingungen für wissenchaftliches Arbeiten in seiner Gruppe und dafür, dass er immer Zeit für Fragen und Dikussionen gefunden hat.

- Prof. Ulrich Schollwöck für die Übernahme der Zweitkorrektur dieser Arbeit.

- Ulrich Schneider für all die Hilfe während der letzten Jahre, den unerschütterlichen Glauben an unser Experiment und all die Ideen, wie sich damit spannende Physik betreiben lässt.

- meinen Laborkollegen in München: Simon Braun, Sean Hodgman, Michael Schreiber und Tim Rom. Es gibt sehr wenige Menschen, mit denen ich in den letzten Jahren mehr Zeit verbracht habe. Wir haben all die Höhen und Tiefen erlebt, die einem ein solches Experiment bescheren kann und es war eine Freude, diese Erfahrung mit ihnen zu teilen.

- Stephan Langer, Lev Vidmar und Fabian Heidrich-Meisner für die gute Zusammenarbeit, die konstruktiven Diskussionen und ihre Hilfe beim Verstehen unserer Experimente und Fabian Heidrich-Meisner im Speziellen für das geduldige Beantworten all meiner Fragen.

- meinen ehemaligen Kollegen Kin Chung Fong, Lucia Hackermüller und Sebastian Will für die gute Zusammenarbeit in Mainz und die Hilfe beim Umzug und in der Anfangsphase hier in München.

- Daniel Garbe für all den Kuchen.

- allen weiteren Mitgliedern der Bloch Gruppe für das gute Klima, interessante Diskussionen und das ein oder andere gemeinsame Bier.

- Zorah Hauck, Marianne Kargl und Ildiko Kecskesi für all die Hilfe in organisatorischen Fragen und dafür, dass alles in der Gruppe so reibungslos funktioniert.

- Bodo Hecker für seine Hilfestellung beim Entwerfen und Reparieren der Laborelektronik.
- Juergen Aust, Thomas Großhauser und den Mitarbeitern der Werkstatt der Fakultät für Physik dafür, dass sie trotz der gefüllten Auftragsbücher immer wieder die Zeit gefunden haben, unsere ganz dringenden Wünsche zu erfüllen.
- dem Max-Planck-Institut für Quantenoptik für die finanzielle Unterstützung am Anfang der Doktorarbeit und dem Exzellenzcluster Nanosystems Initiative Munich für die Förderung während der letzten zwei Jahre.
- meinen Eltern und Geschwistern für ihre bedingungslose Unterstützung seitdem ich denken kann.
- Anika Pflanzer dafür, dass sie immer für mich da ist und für eine wunderbare gemeinsame Zeit, die hoffentlich noch sehr lange anhält.